Geophysical characterization of the Crustal structures from Equatorial to North-East Brazilian margins

Susana Ferreira D. S. Gonçalves

To cite this version:

Susana Ferreira D. S. Gonçalves. Geophysical characterization of the Crustal structures from Equatorial to North-East Brazilian margins. Geophysics [physics.geo-ph]. Université de Bretagne occidentale - Brest, 2023. English. NNT : 2023BRES0080 . tel-04619710

HAL Id: tel-04619710

https://theses.hal.science/tel-04619710v1

Submitted on 21 Jun 2024

THÈSE DE DOCTORAT DE

L'UNIVERSITE
DE BRETAGNE OCCIDENTALE

ECOLE DOCTORALE N° 598
Sciences de la Mer et du Littoral
Spécialité : *Géosciences Marines*

Par
Susana Ferreira D. S. GONÇALVES

Geophysical characterization of Crustal structures from Equatorial to North-East Brazilian margins

Thèse présentée et soutenue à Brest, le 20/12/2023
Unité de recherche : GIPS - GEO-OCEAN

Rapporteurs avant soutenance :

Donatienne LEPAROUX	Directrice de Recherche, HDR, BOUGUER, Université Gustave Eiffel
Luís PINHEIRO	Professor, Universidade de Aveiro, Portugal

Composition du Jury :

Président :	Pascal TARITS	Professeur CNAP, HDR, Laboratoire Geosciences Ocean, Institut Universitaire de la Mer
Examinateurs :	Milena MARJANOVIC	Chargée de Recherche, CNRS, Institut de Physique du Globe, Paris
	Boris MARCAILLOU	Directeur de Recherche, HDR, Maître de Conference, UMR Géoazur
	Donatienne LEPAROUX	Directrice de Recherche, HDR, BOUGUER, Université Gustave Eiffel
	Luís PINHEIRO	Professor, Universidade de Aveiro, Portugal
Dir. de thèse :	Maryline MOULIN	Chargée de Recherche, HDR, UMR Geo-Ocean, Ifremer Centre Bretagne
Co-dir. de thèse :	Philippe SCHNÜRLE	Chargée de Recherche, UMR Geo-Ocean, Ifremer Centre Bretagne
	Alexandra AFILHADO	Chargée de Recherche, Instituto Dom Luiz, Lisbonne, Portugal

PhD Thesis

Marine Geosciences

Geophysical characterization of Crustal structures from Equatorial to North-East Brazilian margins

Susana Ferreira Duarte dos Santos Gonçalves

Brest, October 2023

GEO-OCEAN
|CNRS | Ifremer | UBO | UBS|

INSTITUTO
DOM LUIZ

fct
Fundação
para a Ciência
e a Tecnologia

Abstract

A better knowledge about the geologic and physical properties of deeper crustal layers and discontinuities is crucial to understand the process on the formation of passive margins and their evolution. During the last decade, an intense collaborative focus on the Brazilian continent, passive margins, and deep-sea basins has been conducted by Brazilian, French and Portuguese research groups. The complexity of these systems and the time scale of their development makes the characterization of these structures often hard. The availability of field samples are limited in depth and number of locations. This means that we need to rely on remote sensing/indirect methods in order to retrieve the information about those deeper layers. The development of new methods to analyze jointly these data sets is common way to move forward in science. But the adaptation and improvement of existing ones in terms of efficiency, scale or data sets, is also a useful way to contribute to scientific knowledge.

The studied area in this project is the Northwest part of Brazil. In spite of the geologic and geodynamic complexity, the area fits well the aims of the project because there are several previous studies completed, from different sources and data sets allowing to test the developed methods. For instance, three Wide-Angle Seismic (WAS) profiles were acquired in the area. Two offshore – to the North-West and South-East of the Borborema province – and one onshore, in between. The profiles are sub-parallel meaning that the merge of this profiles can give a unique and regional perspective on the formation of Northwest Brazilian passive margins and the opening of the Equatorial and South Atlantic Ocean. Two main geophysical methods will be described in this study.

The first method is the 3D gravity inversion with seismic data constraint, first developed and applied by Uieda and Barbosa (2017) for the entire South American continent. This method was adapted so it can be applied to an area of any size and to investigate the depth and geometry of any layer/discontinuity, given that there is a density contrast between the targeted layer and the above layer(s) and also a pool of seismic depth information in that same area. We will shown that the 3D gravity method can be applied in the context of the study of passive margins, bringing new and spatially extended knowledge in areas where several previous studies were completed. The method also shown coherence and robustness that allow to be applied as a first approach for new data acquisitions for different goals.

The second method developed was the Reverse Time Migration (RTM) applied to WAS data. This method was first developed in the 80's and has as main goal to map the subsurface

reflectivity using recorded seismic waveform. There are several applications of the RTM to different data sets, acquisition footprints, and geological environments. However, there are very few applications to WAS data due to the wide spacing between the instruments and consequently the low resolution of the obtained image. We are able to show that the application of the RTM is not only possible to these type of data, is also capable to retrieve essential information about crustal layers and the Moho discontinuity and that the traveling wavefield is of crucial importance in this method. The RTM was applied to WAS data in Marine and Land environments and also to both vertical and radial components in order to test the full reach of the method. A comparison with different migration methods and velocity analysis was performed to evaluate the usefulness and robustness of the RTM.

We were also able to show that the RTM can be applied as a complement to other methods (PSDM or P-wave velocity modeling) and confirm or not the obtained results, and is capable to retrieve the main structures of the subsurface reaching depths that other migration technics are not capable of. The RTM

The results retrieved from both methods are coherent with the geologic and geodynamic context of the research area and also bring new knowledge on the formation of the passive margins. The merged wide-angle seismic profile of almost 1800 km in length brings to light a striking similarity between the Equatorial and the Central margin of the South Atlantic Ocean.

Résumé

Une meilleure connaissance des propriétés géologiques et physiques des couches crustales profondes et des discontinuités est essentielle pour comprendre le processus de formation des marges passives et leur évolution. Au cours de la dernière décennie, des groupes de recherche brésiliens, français et portugais se sont concentrés sur le continent brésilien, les marges passives et les bassins associés. La complexité de ces systèmes et l'échelle de temps de leur développement rendent la caractérisation de ces structures souvent difficiles. Les échantillons disponibles sur le terrain sont limités en profondeur et en nombre de sites. Cela signifie que nous devons nous appuyer sur des sondages indirectes pour obtenir des informations sur ces couches profondes. Le développement de nouvelles méthodes pour analyser ces ensembles de données est un moyen courant de faire progresser la science. Mais l'adaptation et l'amélioration des méthodes existantes en termes d'efficacité, d'échelle ou de traitements de données conjointes est également un moyen utile de contribuer à la connaissance scientifique.

La zone étudiée dans ce projet est la partie nord-est du Brésil. Malgré sa complexité géologique et géodynamique, la région correspond bien aux objectifs du projet car plusieurs études antérieures ont été réalisées, à partir de sources et de jeux de données différents, permettant de tester les méthodes développées. Par exemple, trois profils de sismique grand-angle ont été acquis dans la région. Deux au large - au nord-ouest et au sud-est de la province de Borborema - et un à terre, entre les deux. Les profils sont subparallèles, ce qui signifie que la fusion de ces profils peut donner une perspective unique et régionale sur la formation des marges passives du nord-est du Brésil et sur l'ouverture des océan Atlantique Equatorial et Sud. Deux méthodes géophysiques principales seront décrites dans cette étude.

La première méthode est l'inversion gravimétrique 3D avec contrainte de données sismiques, développée et appliquée pour la première fois par Uieda et Barbosa (2017) pour l'ensemble du continent sud-américain. Cette méthode a été adaptée pour pouvoir être appliquée à une zone de n'importe quelle taille et pour étudier la profondeur et la géométrie de n'importe quelle couche/discontinuité, étant donné qu'il existe un contraste de densité entre la couche ciblée et la (les) couche(s) supérieure(s) et également un pool d'informations sur la profondeur sismique dans cette même zone. Nous avons montré que la méthode de gravité 3D peut être appliquée dans le contexte de l'étude des marges passives, apportant de nouvelles connaissances même dans les zones où plusieurs études antérieures ont été réalisées. La méthode a également montré une cohérence et

une robustesse qui lui permettent d'être appliquée comme première approche pour de nouvelles acquisitions de données pour différents objectifs.

La deuxième méthode mise au point est la migration temporelle inverse (RTM) appliquée aux données sismiques grand angle (WAS). Cette méthode a été développée pour la première fois dans les années 80 et a pour objectif principal de cartographier la réflectivité du sous-sol à l'aide des formes d'ondes sismiques enregistrées. Il existe plusieurs applications de la RTM à différents ensembles de données, types d’acquisition, et environnements géologiques. Cependant, il y a très peu d'applications aux données WAS en raison du grand espacement entre les instruments et, par conséquent, de la faible résolution de l'image obtenue. Nous sommes en mesure de montrer que l'application de la méthode n'est pas seulement possible à ce type de données, mais qu'elle permet également de récupérer des informations essentielles sur les couches de l'écorce terrestre et la discontinuité du Moho, et que le champ d'ondes progressives est d'une importance cruciale dans cette méthode. La méthode a été appliquée aux données WAS dans des environnements marins et terrestres, ainsi qu'aux composantes verticales et radiales afin de tester la portée totale de la méthode. La RTM peut être appliquée en complément d'autres méthodes (PSDM ou modélisation de la vitesse des ondes P) et confirmer ou non les résultats obtenus, et d’être capable de retrouver les principales structures de la subsurface et d'atteindre des profondeurs que d'autres techniques de migration ne sont pas capables d'atteindre ou elle peut être appliquée comme outil pour retrouver les caractéristiques des couches plus profondes lorsque seules les données WAS sont disponibles.

Les résultats obtenus par les deux méthodes sont cohérents avec le contexte géologique et géodynamique de la zone de recherche et apportent également de nouvelles connaissances sur la formation des marges passives. Le profil sismique grand angle fusionné, d'une longueur de près de 1800 km, met en évidence une similitude frappante entre la marge équatoriale et la marge centrale de l'océan Atlantique Sud.

“Five hundred twenty-five thousand, six hundred minutes
Five hundred twenty-five thousand moments so dear
Five hundred twenty-five thousand, six hundred minutes
How do you measure, measure a year?

In daylights, in sunsets
In midnight's, in cups of coffee
In inches, in miles
In laughter, in strife
In five hundred twenty-five thousand, six hundred minutes
How do you measure a year in the life?

How about love?”

(Jonathan D. Larson; from “Rent”, 1996)

Acknowledgments

The path which allowed me to arrive to this stage, of defending a PhD degree, was quite long and the number of persons involved in it is high. People in the form of individuals, people representing institutions, family, friends, teachers, supervisors, etc. When you start to think about it and try to make a list, you find that the chance of forgetting someone becomes increasingly high as you move into your professional and personal life. But even if it happens that I do forget to mention someone in this text, I hope you will understand that there is “five hundred twenty-five thousand, six hundred minutes” in a year and consequently a much higher number of memories and moments within that time and I do try to “measure my life in love” and recognize it.

I will start by leaving my greatest thanks to Dr. Philippe Schnürle, one of my supervisors, who accompanied this PhD project since the very beginning, no matter the form in which he did so: from the teaching, advising, suggesting, criticizing, always in a positive way, and from whom I have learned an almost immeasurable amount of knowledge.

I also leave a big thank you to Dr. Maryline Moulin, Dr. Alexandra Afilhado and Dr. Marina Rabineau, the remaining members of main official supervising team. I take with me the knowledge of their different fields and how they helped me to build my thesis and my work. By either the warm reception when I first arrived in Brest and helping me to get around and take notice of this nice town, by taking the time to discuss with me the different results and how to move forward, helping on the revision of texts and making suggestions; by teaching me about concepts on their own fields that were essential to my work, by pushing me to move forward and helping me to make my work known to others, with a first-author published paper at JSAES for instance, and how those exchanges are valuable.

I would like to extend my thanks to all the Géodynamique: Interactions Profond/Surface team (GIPS) at GEO-OCEAN, Ifremer. Namely Dr. Daniel Aslanian, Dr. Mickael Evain and Dr. Estelle Leroux. The balance between formal work environment and informal human relationships is absolutely extraordinary. Here, I found what, for me, is the true sense of team work, where each one actually takes part on helping each others projects and makes their personal concern to ensure that you improve everyday. From the formal meeting presentations to the informal lunches at Minou where all the PhD students, Post-Docs and researchers would come together and share their knowledge with others, was crucial for my personal growth and I will take this lesson with me.

Thank you to the team in Portugal, in the additional persons of Dr. Nuno Afonso Dias and Dr. Afonso Loureiro, that also accompanied this work and were the ones that encouraged be since the very beginning to apply to the PhD scholarship and to pursue this path.

Thank you to the two external elements of the Comité de Suivi Individuel (CSI), Dr. Luis Matias and Dr. Jordi Juliá, who each year accompanied the evolution of the project and helped to improve the course of the project.

Thank you to the Institutions that were part of this project, Université de Bretagne Occidental (UBO), Institut Français de Recherche et Exploitation de la MER (Ifremer), Instituto Dom Luis (IDL), Fundação para a Ciência e Tecnologia (FCT) and ISBlue, for all the formal and financial support, without what would be impossible to bring the project to its fulfillment.

I would also like to thank to Dr. José Soares from Universidade de Brasília, for his effort to maintain a long partnership with the French and Portuguese groups and welcoming me in Brasilia two times and for all the profitable discussions, that were essential to bring the results of this project together.

One last word of thank you to a particular Teacher, my primary school Teacher. It may seem strange to do it and it is not the first time that I formally want to leave a word of thanks. However, it was Professora Fátima (in Portuguese and without surname because it will be always like that I will remember her) that first opened the world for me. By teaching me not only to read and write but also about how passionate you can be about your work and life and how that can be passed on to others.

To all the other colleagues, students, researchers and people which paths we have crossed, I am thankful to have met you and shared moments.

I will finish by thanking my family and friends. The core family, mom, sister and niece that always supported me and were always there either in the form of very complicated questions for a five year old child, or by simply being there for me all the time. Hope that you know how important that has been to me and it will always be. My friends, I will not name each of you because I am sure that you all know who you are. Your support was essential. The simple fact that you know me, and always knew where to be and what to say, had been more then enough. But you all know that you have done much more than that.

With a final thanks to everyone and with the hope that we will work and see each other again, I wish you all the best!!

Table of Contents

List of Figures

List of Acronyms

AFZ – Ascension Fault Zone

AVL – Anomalous Velocity Layer

Bar – Barreirinhas

Bo – Borborema

CAR – Central African Republic

Cea – Ceará

CFZ – Chain Fracture Zone

CTJ – Camamú Triple Junction

ICGEM – Center for the Global Earth Models

Jac – Jacuípe

JFZ – Jaguaribe Fault Zone

LSS – Land Seismic Station

MAGIC – Margins of brAzil, Ghana and Ivory Coast

MCS – Multi-Channel Seismic

OBS – Ocean Bottom Seismic

Pa – Parnaíba

PAM – Pernambuco-Alagoas Massif

PbFZ – Pernambuco Fault Zone

PM – Pará-Maranhão

Pot – Potiguar

PP – Pernambuco-Paraiba

PSDM – PreStack Depth Migration

PtFZ – Patos Fault Zone

RMZ or RomFZ – Romanche Fracture Zone

RTJ – Recôncavo-Tucano-Jatoba

RTM – Reverse Time Migration

SA – Sergipe-Alagoas

SALSA – Sergipe-ALagoas Seismic Acquisition

SFB – Sergipiano Fold Belt

SFC – São Francisco Craton

SPdFZ – São Paulo double Fault Zone

SPFZ – Senador Pompeu Fault Zone

TBFZ – TransBraziliano Fault Zone

VBFZ – Vaza-Barris Fault Zone

WAS – Wide Angle Seismic

ZT – Zona Transversal

1. Scope of the PhD project

This PhD project has at its core the development of two geophysical methods that can help to automatize and improve the analysis and interpretation of a given data set – 3D gravity data inversion with the seismic constraint and Reverse Time Migration (RTM) applied to Wide-Angle Seismic (WAS) data.

The application of both methods had at their core the deeper crustal structures from the Northwest of Brazil, comprising two crucial passive margins – the Equatorial and North-East Brazilian margin with two different geodynamical settings.

The 3D gravity inversion will focus on the recovery of the Moho discontinuity depth and geometry for an area comprising the two margins and the Borborema province ([45º; 30º]W; [1ºN; 12ºS]), enabling the capability of the method to recover the geometry of the Moho discontinuity in an area with a complex geology and sharp variations of the Moho depth as in passive margins.

The RTM method will be applied on two different WAS data profiles in the same area (MC5 and SL04 – Data description chapter) with stations onshore and offshore, where the capacity and limitations of the method to obtain an image of the deeper crustal layers for this type of data is tested. Also acoustic P to shear-wave S conversions have been investigated in both reflection and transmission modes

The integration of the obtained results of each method with the previous geologic and geodynamics knowledge of the research area is done in order to contextualize these geophysical methods and show their purpose and usefulness.

The merge of three WAS data profiles – MC5, INCT-NE (NW) and SL04 – is also presented giving a uncommon regional perspective on the geodynamics of the study area, connecting two passive margins related with the opening of the South Atlantic Ocean.

2. Geologic setting

The research area is composed mostly by the Borborema province in the Northwest Brazil and its offshore surroundings, limited by the São Paulo fracture zone in the North and the Jacuípe basin in the South (Figure 2.1).

The Borborema province is a region of great structural complexity, with superposition of distinct deformational, metamorphic, and magmatic events and final structural configuration in the collisional and post-collisional (trans-current) stages of the Brasiliano/Pan-African Orogeny (625-510 Ma) (Caxito et al., 2020). The geologic history of the area, being so long and complex, we will focus on the formation and consolidation of the West-Gondwana super-continent from the geodynamic point of view and in the sections of this chapter we will focus on the geology and geodynamics of the two margins surveyed by MAGIC and SALSA experiments, respectively (sections 2.1 and 2.2). In section 2.3, a more detailed geological description on the Borborema province is given, along with the geological setting integration of the three areas.

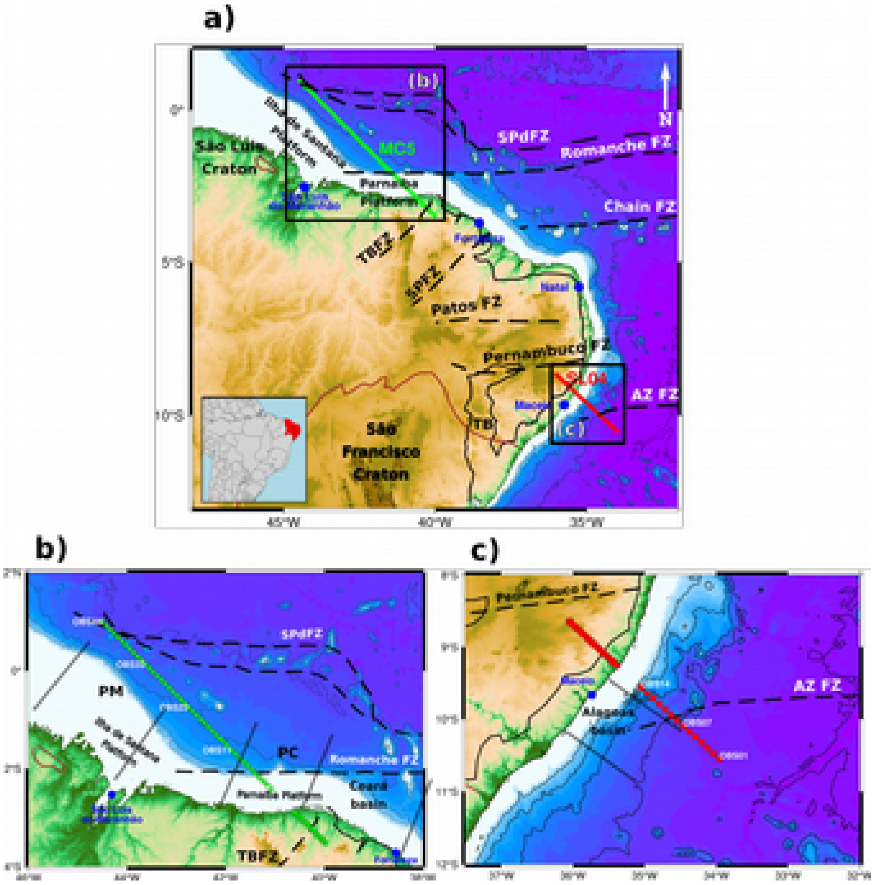

Figure 2.1 – Location of the study area. a) full study area – North-West Brazil – with the major fracture zones; black squares – location of the MAGIC (green) and SALSA experiments; b) detail of the major geological features of the MAGIC experiment area; c) detail of the major geological features of the SALSA experiment area

The formation and consolidation of the West Gondwana

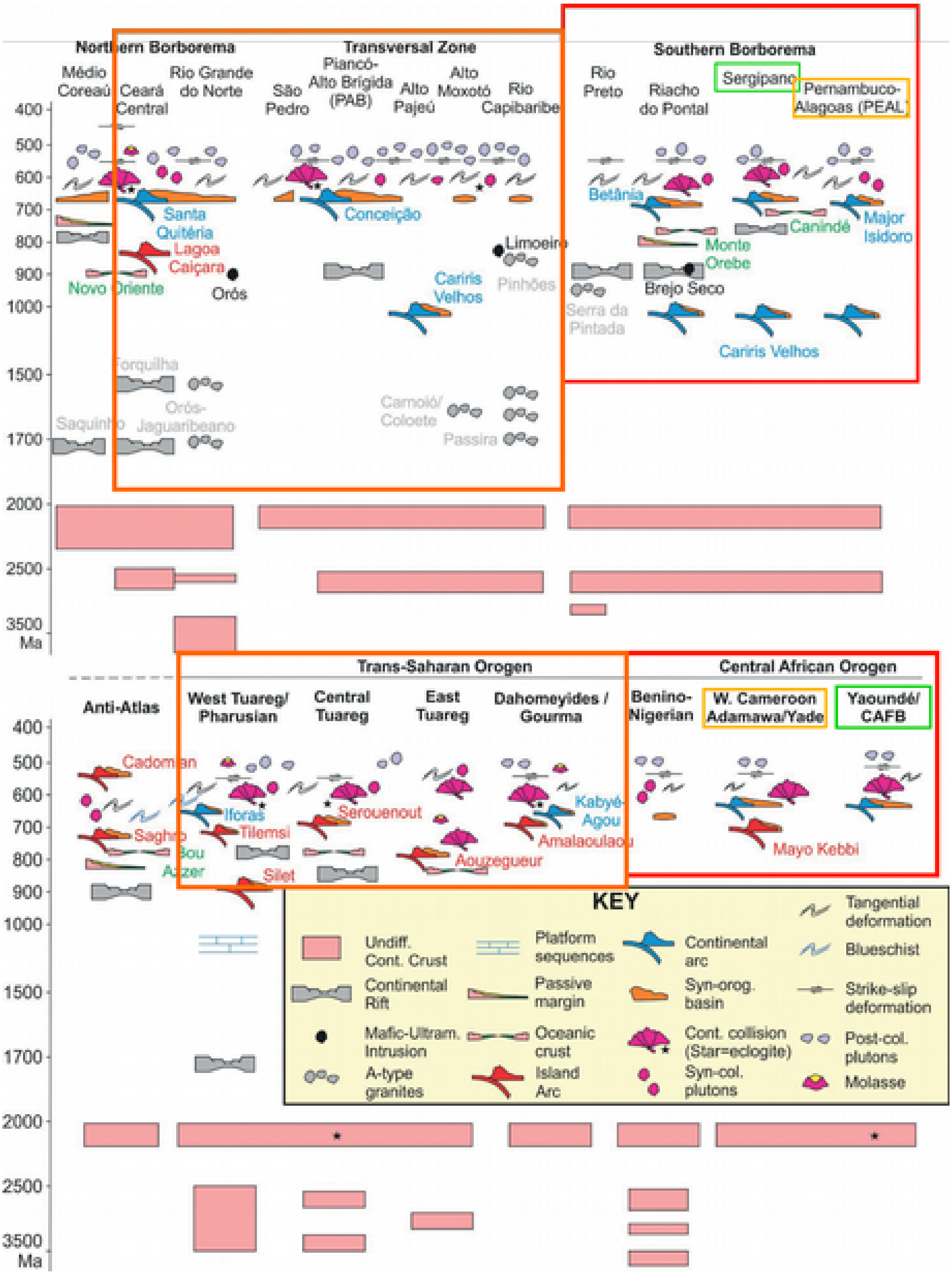

Figure 2.2 – Simplified chart of the chronology, from Rodínia break-up to West-Gondwana formation, of the main geodynamic events in each geological domains of NE Brazil and NW Africa with highlighted (colored squares) areas/structures that have links/connections between the two conjugated margins (adapted from Caxito et al., 2020)

In Figure 2.2 we presented a resume of the major geodynamic events for each domain of both NE Brazil and NW Africa with same color highlighted squares where the same type of structures and tectonics can be found on either side, correlating both margins and showing the chronological events that explain the evolution of the paleo-continents from Rodínia to the formation of the West Gondwana.

At present there are several proposed models for the geological evolution of the Borborema province (Brazil) area and its conjugate margin, the NW Africa. Figure 2.3 presents the simplified geological features of the West-Gondwana super continent (Caxito et al., 2020), where the major structures composing and linking the two conjugated margins are presented. The NW Africa provinces comprise (Figure 2.3): the Benino-Nigerian Shield, the Tuareg Shield of Algeria, Niger and Mali, the Dahomeyides-Gourma Orogen of Togo, Benin and Mali (the former composing the Trans-Saharan Orogen) and the Oubanguides Orogen of Cameroon and Chad continuing into the Central African Fold Belt in the Central African Republic (CAR).

Along with the Borborema Province, these major orogenic areas represent the site of agglutination of the West African-São Luís, São Francisco-Congo and Saharan paleo-continents.

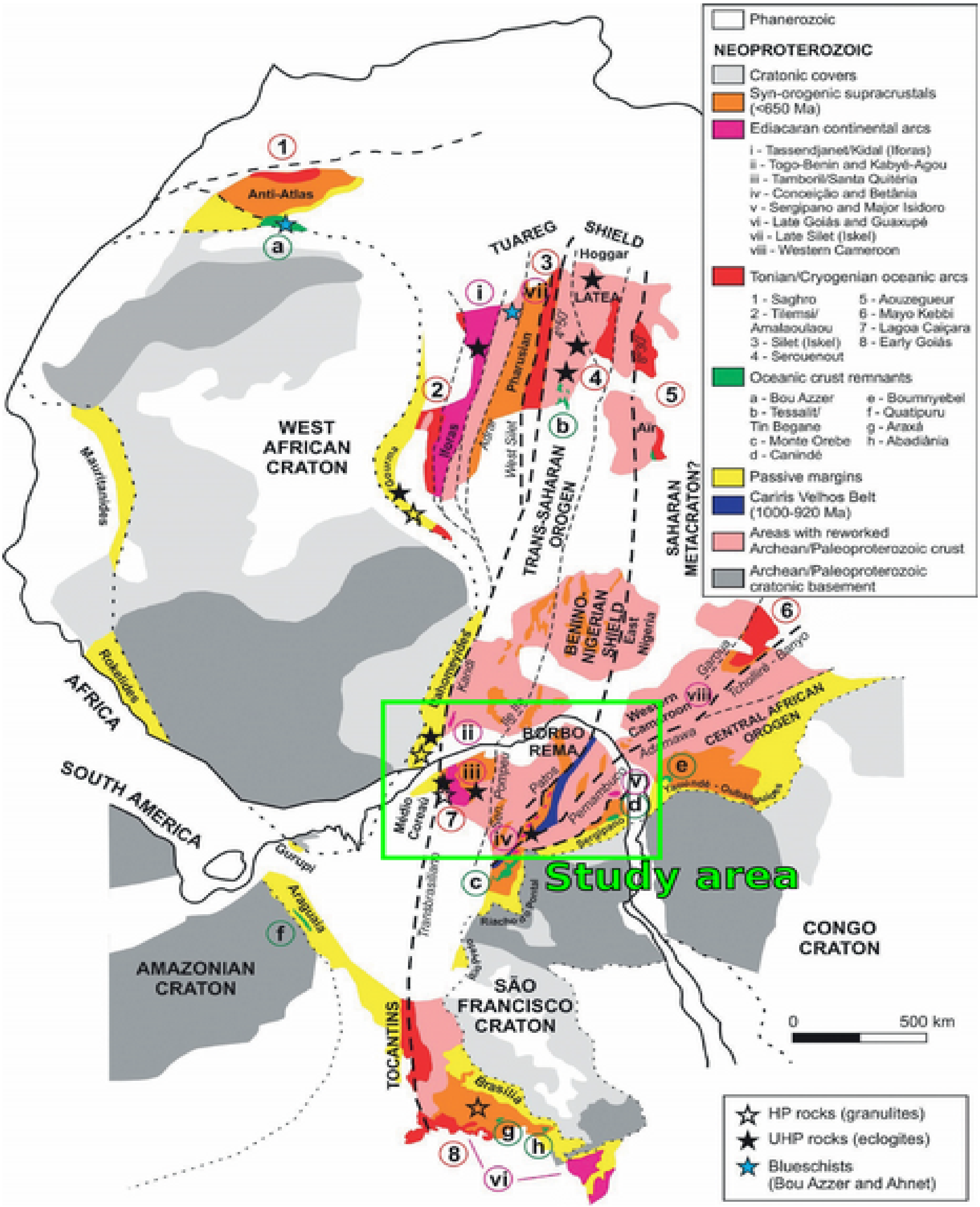

Figure 2.3 – Simplified geological features of the West-Gondwana super continent; Present conjugated margins – NE Brazil and NW Africa (adapted from Caxito et al., 2020)

For the Borborema province area, we can split the different proposed models in two groups:

I) hypothesis that suggests the development of the plate tectonic processes during the Neoproterozoic, either involving: progressive accretion of exotic terrains (dos Santos et al., 2008; Neves et al., 1999); complete Wilson cycles involving crustal rifting, opening and closing of oceans, installation of subduction zones and continental collision (Basto et al., 2019; Caxito et al., 2014); or a combination of complete tectonic cycles at the province's borders and reworking of pre-Neoproterozoic crust in an intracontinental setting at its core (Oliveira et al., 2010; Caxito et al., 2014b).

II) the province involves the reworking of a single continental block, which remained relatively stable from approximately 2.0 Ga and was then affected by the installation and further inversion of mainly intracontinental basins throughout the remaining time of the Proterozoic. In this second group of hypothesis, the metamorphism, deformation and magmatism associated with the Brasiliano Orogeny in this region would have been essentially caused by intracontinental processes, although locally, subduction and common plate convergence processes are not completely ruled out (Ganade De Araujo et al., 2014).

In the context of the amalgamation of the Gondwana paleo-continent, the Borborema Province represents the orogenic region between the São Francisco–Congo and West African-São Luís cratons (Figure 2.3), structured by the collisional interaction between these two major lithospheric fragments and other possible smaller intervening fragments during the Proterozoic, such as the Parnaíba block, concealed below the Phanerozoic sedimentary rocks of the Parnaíba Basin (Kröner and Cordani, 2003). The region comprised between these two cratonic land masses also involves part of the geological domains of NW Africa, which are bound to the east by the Saharan metacraton.

The regional shear zones that crosscut both conjugated margins are the key to understand the correlation between these to areas. We find in the majority of the literature on this issue, the following connections (Figure 2.3):

I) continuation of the TransBrasiliano (Sobral/Pedro II) shear zone into the Kandi–4º50' shear zone seems well established (Cordani et al., 2013)

II) continuation between the Senador Pompeu and Ile Ife shear zones

III) some authors suggest continuation of the Patos Shear Zone into the Garou Shear Zone of NW Cameroon (Bley De Brito Neves, 2002), while others suggest that the region between the Patos and Pernambuco shear zones opens in a wedge-like geometry toward NW Africa, and thus the Patos Shear Zone would continue through the limit between the East and West Nigeria provinces to the

8º30’ Shear Zone separating East from Central Tuareg Shield as shown in Figure 2.3 (Van Schmus et al., 2011).

The break-up of West Gondwana

After the formation and consolidation of West Gondwana super-continent, it was in the early Cretaceous (133-112 Ma) that a new major break-up event started, debuting the opening of the South Atlantic ocean.

The South Atlantic Ocean can be divided into four, approximately, 2000 km-long segments (Figure 2.4). Going from North to South: I) the Equatorial segment; II) the Central segment; III) the Austral Segment; IV) the Falkland Segment.

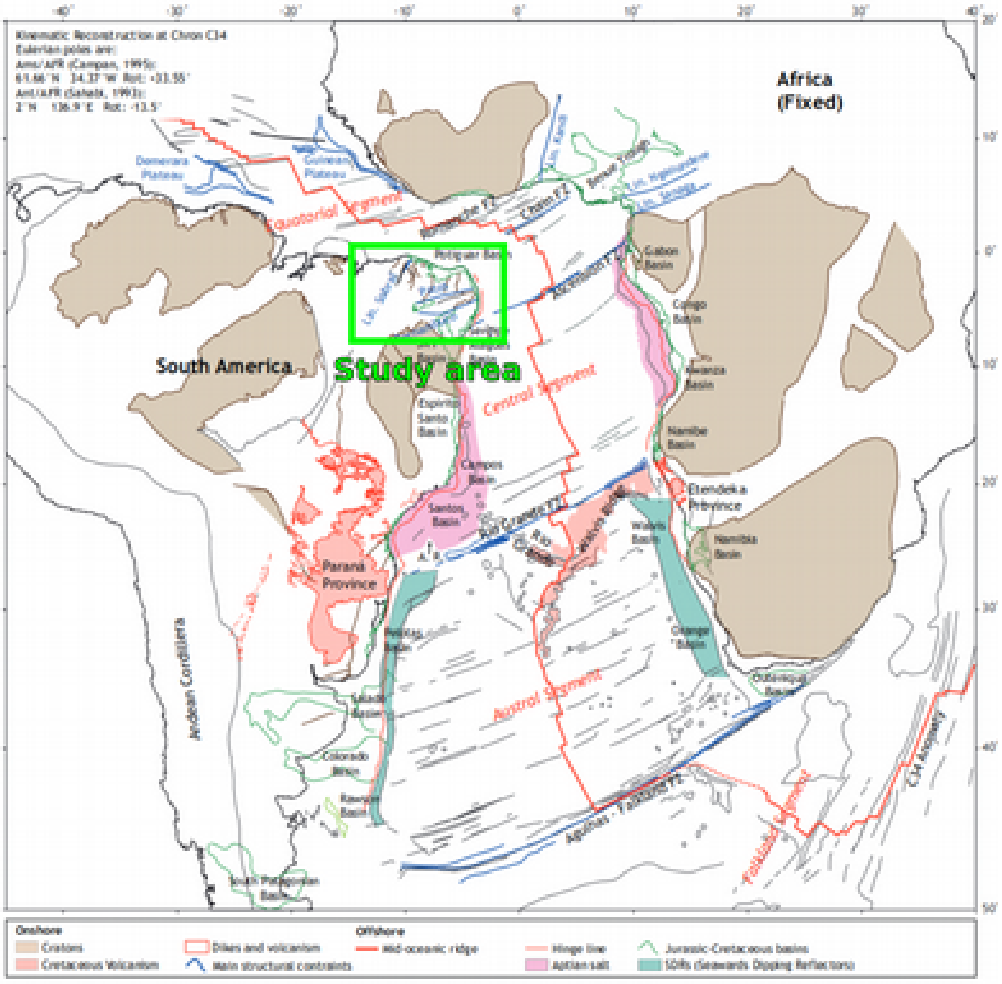

Figure 2.4 - General structural map of the South Atlantic Ocean at Chron 34 (84 Ma). For this well-constrained reconstruction, the Eulerian pole from Campan (1995) for the Equatorial and South Atlantic oceans and the Eulerian pole from Sahabi (1993) for the South Western Indian Ocean. Fracture zones and seamounts are based on interpretation of satellite derived gravity 1 mn x 1 mn grid (Sandwell & Smith, 2014). Mercator projection. (from Moulin et al., 2010a)

The geodynamic context of these different 2000 km-long segments has tremendous influence on the morphology and the genesis of the passive margins. Their kinematic evolution happened between the Hauterivian-Barremian (132-128 Ma) to Campanian (82-73 Ma) and four different stages can be highlighted – Figure 2.5 (Aslanian et al., 2015; Moulin et al., 2010a):

1) The Austral Segment: Between LMA and M4 the opening of this segment started after the massive outpouring of basalt lavas in the Paraná-Etendeka province;

2) The Santos "Buffer" block: Between M4 up to Aptian (125-113 Ma), the Santos block started to follow the general westward movement of the southern part of South America, whilst the Rio de la Plata block and the Argentine-Salado block were connected between M4 and M2;

3) The central segment: The Late Aptian/Early Albian (125-110 Ma) limit corresponds to the end of salt deposition and the opening of the central segment and coincides with the second stage of African deformation of Guiraud & Maurin (1992).

4) The Equatorial Segment: In Albian (113-100 Ma) time, the Equatorial Atlantic Ocean opened, allowing the definitive water connection between the Central Atlantic and the South Atlantic oceans.

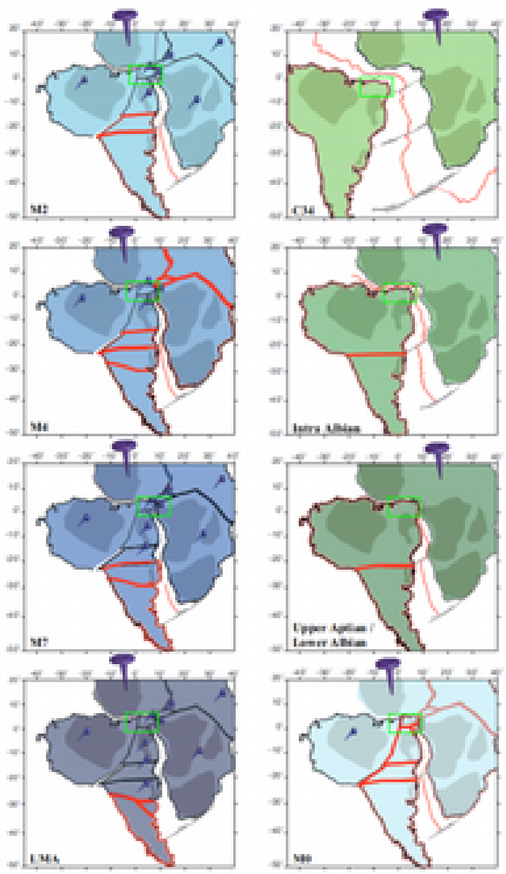

Figure 2.5 - Initial evolution of the Equatorial and South Atlantic Oceans from M9 to C34 proposed by Moulin et al. (2010): from LMA (~133 Ma), M7 (~132 Ma), M4 (130 Ma), M2 (127.5 Ma), M0 (125 Ma), Late Aptian (112 Ma), Intra-Albian (106 Ma) and C34 (84 Ma). The West Africa block is considered as the

fixed plate (large mauve nail). The small mauve nails symbolize that the block does not move, in respect to the West Africa Block, for this period. Large red lines give the location of the intra-plate deformation between two chrons. Study area represented by green square.

As show in Figure 2.4, the study area comprises the equatorial and beginning of the central segments in what concerns the passive margins and offshore geological environments, along with the Borborema province. In the next sections of this chapter, a more detailed description of these three particular areas will be presented.

2.1. The Equatorial segment (MAGIC experiment)

The Equatorial Atlantic ocean is separated from the Central Atlantic Ocean, to the north, by the Guinea Fracture Zone and, to the south, from the Central Segment of South Atlantic Ocean by the Chain Fracture Zone (Aslanian et al., 2015; Moulin et al., 2010a, 2021; Schnürle et al., 2023). The ocean spans, approximately, NS-ward 2000 km in length and can be divided into three 600–800 km long major sub-segments, separated by main fracture zones:

I) The northern segment is bounded by the Sierra Leone Fracture Zone to the north and the São Paulo double Fracture Zone (SPdFZ) to the south and consists in two ~400 km-large segments separated by the 4◦N Fracture Zone and fringed by the Demerara plateau-Sierra Leone conjugate passive margins system and the Foz do Amazonas-Liberian conjugate passive margins system.

II) The central segment is bounded by the São Paulo double Fracture Zone to the north and the Chain Fracture Zone (CFZ). It comprises two segments, about 300 km wide: the Ceará-Potiguar and the East Ghana basin-Togo-Benue conjugate passive margins system and the Para-Maranhão-Barreirinhas and the Deep Ivory Basin-Ghana conjugate passive margins system, separated by the Romanche Fracture Zone (RFZ).

The SPdFZ, RFZ and CFZ have offset magnitude of about 600, 920 and 320 Km, respectively. The RFZ can be traced 3200 km from South America to West Africa and is the second longest active fracture zone in the world. Thus, the breakup of northwestern Gondwana occurred in a sequence of several distinct pull-apart basins connected by strike-slip/transform faults in three Mesozoic extensional events. Hence, a trans-tensional shear corridor with dextral sense of displacement was developed along the present-day northern, equatorial continental margin of Brazil, which formed the Pará-Maranhão and Barreirinhas marginal basins.

In 2012, a set of five Wide-Angle/MSC Seismic (WAS) data profiles, the Magic experiment (Margins of brAzil, Ghana and Ivory Coast), was conducted in order to investigate the structure of the North-East equatorial Brazilian margin. With this large data set (which details are presented in the Data location chapter), it was possible to better understand the kinematics and geodynamics of the opening of this segment of the ocean. In Figure 2.1.1, the geological interpretation of the area concerning these five profiles is presented.

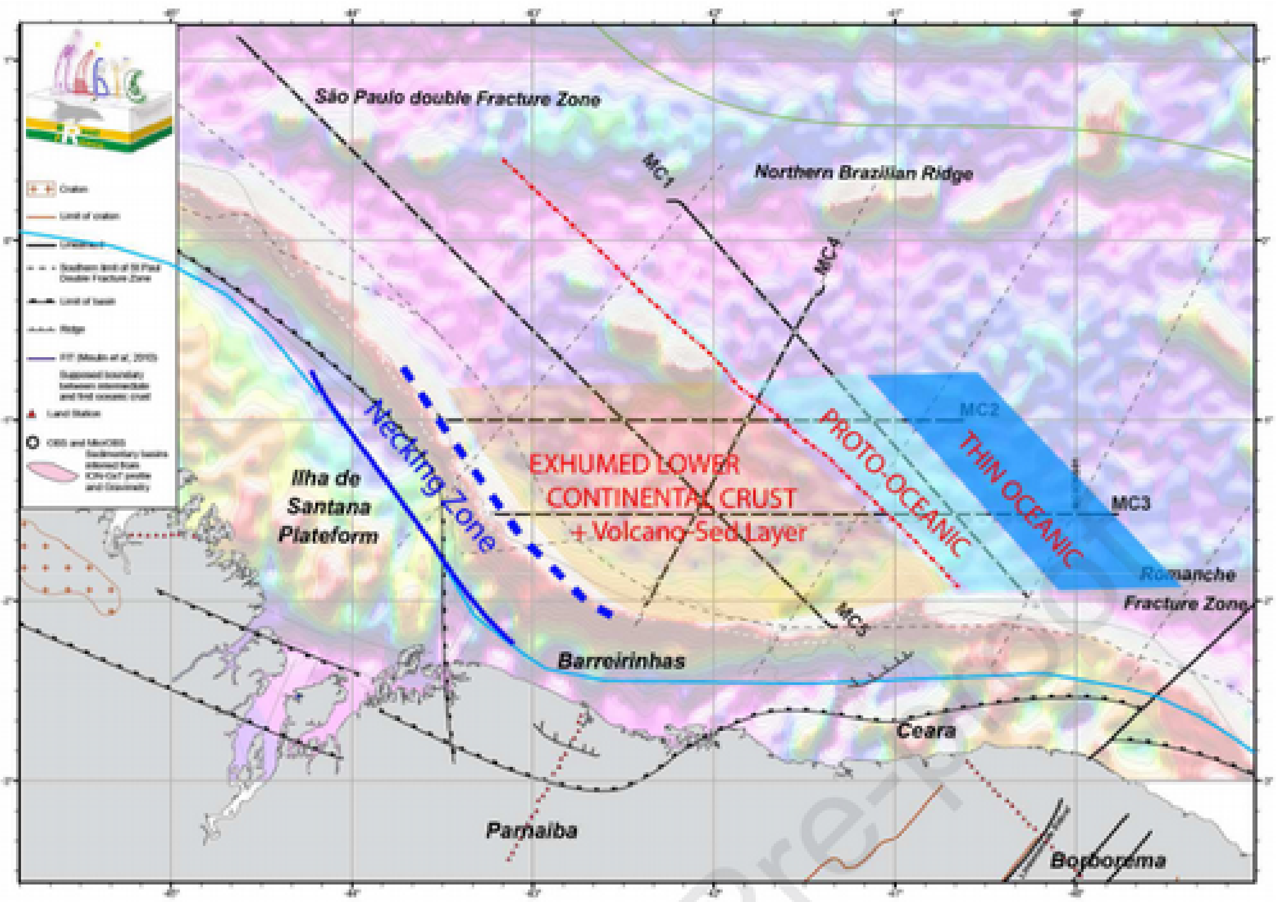

Figure 2.1.1 - Geological interpretation of the basement of the central segment of the Equatorial passive margin on the Brazilian side. Gravity map from Sandwell & Smith (2009). The map also depicts location of MAGIC wide-angle seismic profiles (thin black lines), OBS (small white circles), Land Seismic Stations (LSS) (red triangles) and the geological crustal interpretation proposed. Color polygons: orange = exhumed lower crust; light blue = proto-oceanic crust; blue = thin oceanic crust; thick and dashed blue lines = necking zone. MAGIC experiment profiles location (black full thin lines) (from Aslanian et al., 2015, 2021a)

There is a very strong E-W segmentation of the Pará-Maranhão/Barreirinhas passive margin composed, from West to East by (Aslanian et al., 2015, 2021a; Moulin et al., 2021; Schnürle et al., 2023): I) sharp Necking zone; ii) Exhumed lower continental crust plus a volcano sediment layer; iii) Proto-Oceanic Crust; iv) thin oceanic crust. Above the crustal layers, and within the limits of the necking zone (dashed blue line in Figure 2.1.1) and the proto-oceanic limit (dashed red line in Figure 3.1.1) and in the SE-NW direction, three different basins where identified in this area (Aslanian et al., 2021a; Moulin et al., 2021; Schnürle et al., 2023): I) Basin I – the one closer to the shore, on the continental shelf, close to the Romanche FZ, is a 8 km thick sedimentary basin that thins rapidly inland up to 5 km; ii) Basin II – an intermediate basin, with a 8 km thickness, similar to Basin I apart from being already affect by the NW volcano structures, but the deepest one of the three; iii) Basin III – a shallower, southward tilted basin highly marked by the volcano structures further NW, with a sedimentary layer that goes from 7 km to 3 km in the North.

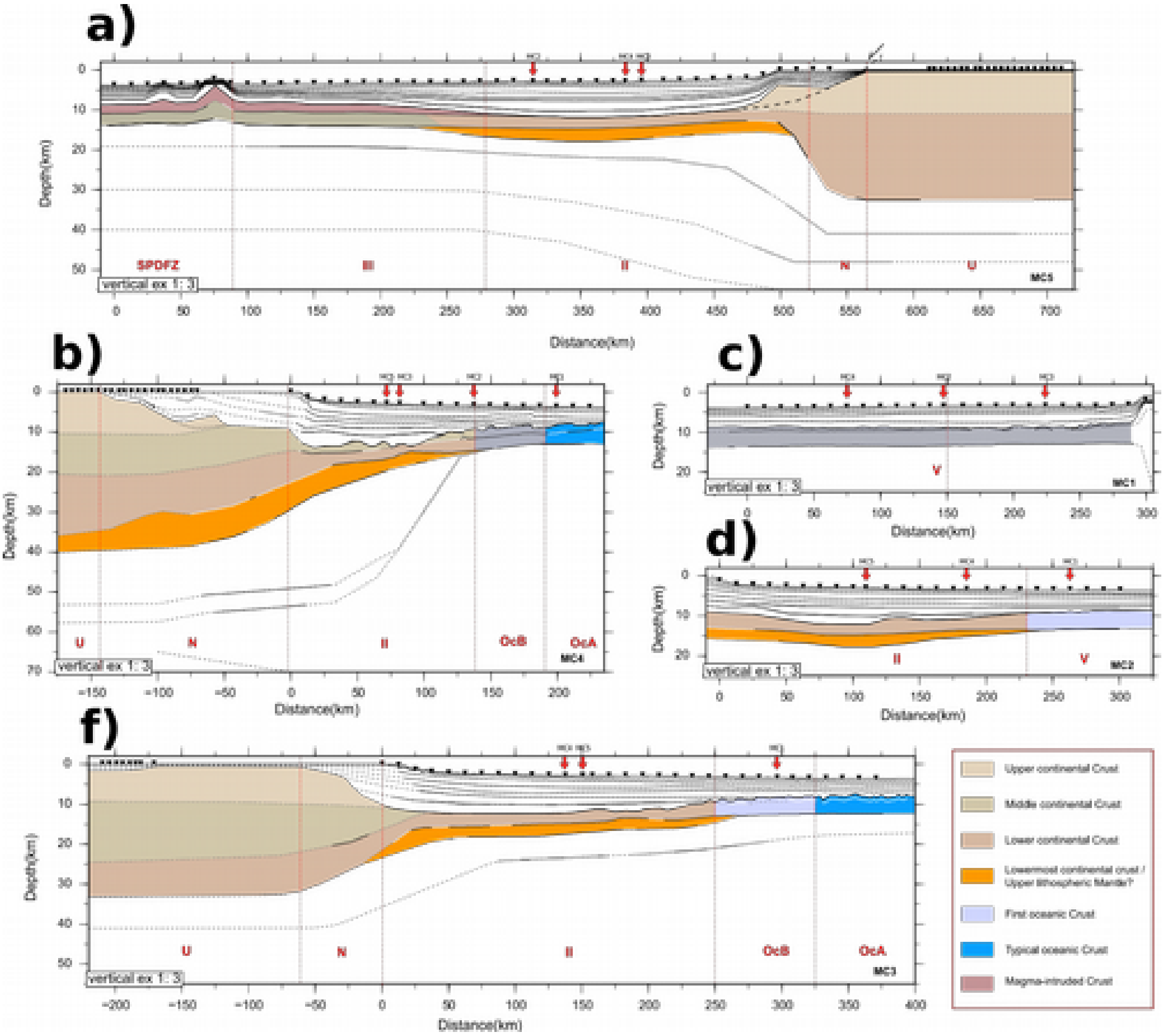

Figure 2.1.2 – Geologic interpretation of the crustal nature of the MAGIC experiment profiles. a) MC5 profile; b) MC4 profile; c) MC1 profile; d) MC2 profile; f) MC3 profile. (from Aslanian et al., 2015; Schnürle et al., 2023)

Looking into the geological interpretations of the WAS data profiles (Figure 2.1.2) we better understand the geological context of this area. There is a horizontal and vertical segmentation within all the profiles that describe the nature of the crust in the area, meeting the one of the main purposes of the experiment. This goal suits well the purpose of this PhD project since it concerns a regional scale and the analysis of deeper crustal layers.

According with Aslanian et al. (2021), where profiles MC2 (Figure 2.1.2-d) and MC3 (Figure 2.1.2-f) were analyzed (and MC4 to some extend – Figure 3.1.2-b), a 33 km thick unthinned continental crust in interpreted below São Luis craton (Profile MC3) and the Parnaíba basin (Profile MC4). In Schnürle et al (2023) where the MC5 profile (Figure 2.1.2-a) is discussed, the same unthinned continental crust is found under the Medio Coreaú onshore structure. This unthinned crust is split in two or three different continental layers depending on the profile depending on the velocities found for each profile.

Following this unthinned continental crust, for the same profiles a very sharp necking zone extends horizontally for approximately 60 km and this continental crust thins to values that vary between 5 km and 8 km depending on the profile. After this necking zone, for MC2, MC3 and MC4 profiles, only a thinned lower continental crust remains and extends up until the marked limit of the Basin II. For MC5 profile, this lower crust extends up until the beginning of the Basin III.

Apart of MC1 profile, located entirely offshore (Figure 2.1.1), an anomalous velocity layer is identified and the two possible interpretations were put in place - lowermost continental crust or lithospheric mantle. This anomalous velocity layer is described as having higher velocity then the lower crust but the values are neither of typical lithospheric mantle. This layer extends within the necking zone and the North limit of the Basin I for MC3, MC2 and MC5. For MC4 profile, It passes the necking zone into the continental environment.

All the profiles, with the exception of MC5, identify what is interpreted as two different oceanic crusts (Aslanian et al, 2021, Moulin et al., 2021). One transitional (Ocean B – Figure 2.1.2) or proto-oceanic crust (Figure 2.1.1) and another as typical oceanic crust (Ocean A – Figure 3.1.2). As exposed by Moulin et al. (2021), the MC1 profile (Figure 2.1.2-c) presents a crustal layer with invariable characteristics that can be interpreted as proto-oceanic crust and that as a correspondence in profiles MC2, MC3 and MC4 after the North limit of Basin II. The typical but thin oceanic crust is identified at the end of profiles MC2, MC3 and MC4.

Within the MC5 profile (Figure 2.1.2-a), Schnürle et al. (2023), analyses and interpret the crust within the Basin III as middle/lower continental crust underneath a magma intruded crust due to the presence of the volcanic structures in the area.

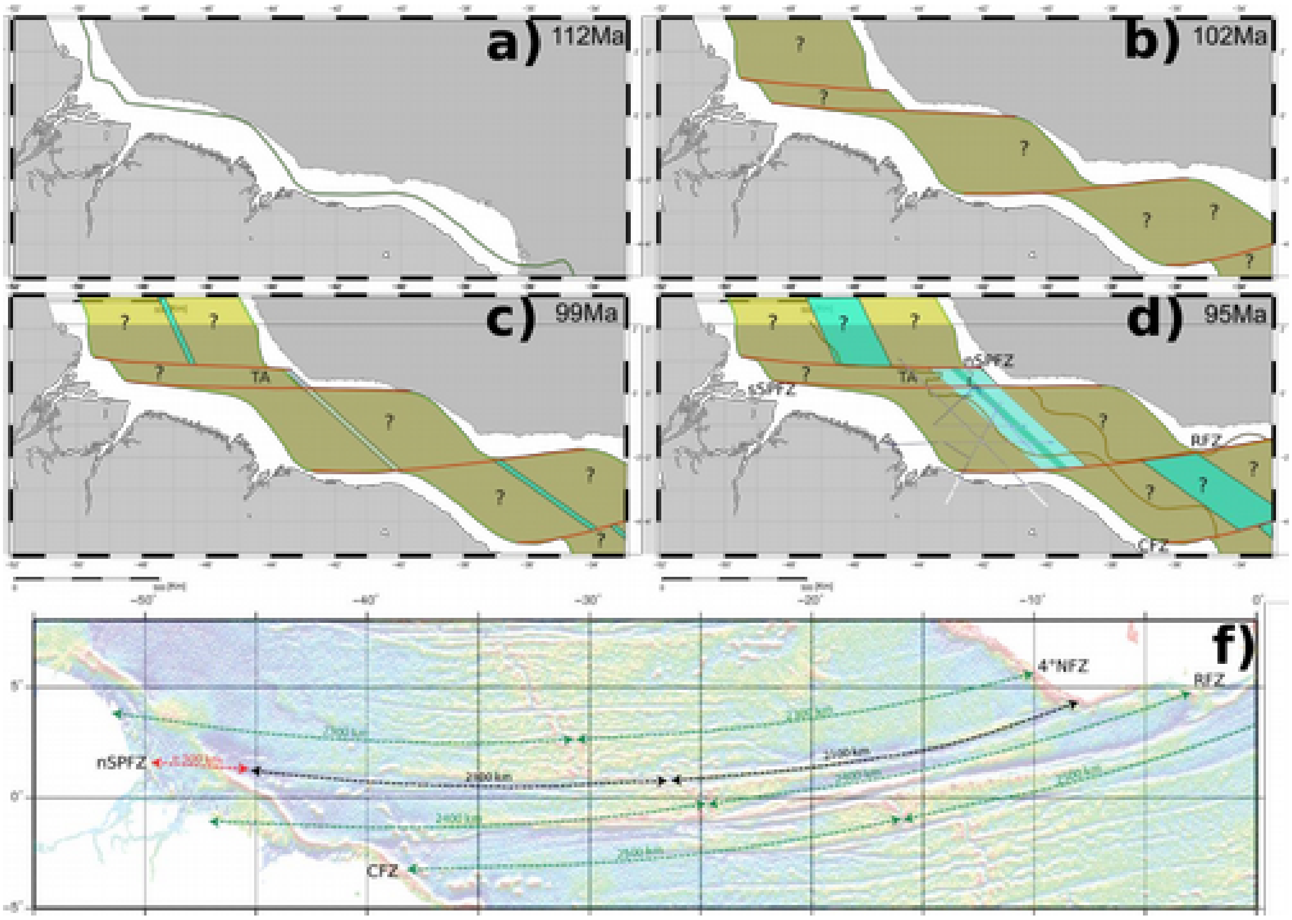

Figure 2.1.3 – Schematic kinematic evolution of the central Equatorial opening with fixed South American plate: a) 112 Ma; b) 102 Ma; c) 99 Ma; d) 95 Ma. f) present day free-air gravimetric map of the central Atlantic Equatorial Ocean and length of the main fracture zones (from: Schnürle et al., 2023)

To finalize the geologic, geodynamic and kinematic context of the Equatorial segment, Figure 2.1.3 presents a schematic evolution of the Central Equatorial Ocean, given by Schnürle et al. (2023). The evolution is presented along 4 stages during rifting and oceanic spreading phases, extrapolated from the fit of Moulin et al. (2010) at 112 Ma and the intermediate pole at C34 of Campan (1995) considering a constant spreading rate. Furthermore, our reconstruction initially assumes both relative symmetrical and cylindrical rifting of the 3 divergent segments of the Central Equatorial Atlantic. The COBs of Tamara et al. (2019), Tavares et al (2020) and Aslanian et al. (2021) on the South American side and of Antobreh et al. (2009) on the African side delimit the domains of continental hyper-extension/exhumation, and inset of “mid”-oceanic crust accretion (Figure 2.1.3-c near 99 Ma). The location of this onset within the SPdFZ is matter of debate. The relatively small width of the SPdFZ in the Parã-Maranhão transform segment favors an accretion center aligned with either the Amazone or Barreirinhas segments. The observed COB of Tamara et al. (2019), together with the present-day NE-SW oriented continental coast-lines that spur a favorable mechanical week line extending from the RFZ to the SPdFZ. In this scenario, the entire African continental hyper extended/exhumation domain of the Pará-Maranhão transfer margin would have been trapped with the Brazilian one, and would explain our findings at the NW end of our MC5 survey. This hypothesis is confirmed by the present-day ~500 km in length asymmetry of the mid-oceanic ridge at the SPdFZ between its South-American and African sides (Figure 2.1.3-f).

2.2. The Central margin (SALSA experiment)

The Southeast limit of the research area is located at the edge of the Central segment, the second segment shown in Figure 2.3., after the Equatorial one.

The process of break-up of the West Gondwana and the opening of the South Atlantic Ocean is composed by several rifts systems that developed during the Cretaceous. Not all of those systems were successful and some were abandoned in different periods but there were other cases were rifting jumped from one axis to an other. This type of behavior culminated in a very complex geologic and geodynamic area, where the Northeast Brazilian margin is a good example (Aslanian et al., 2016).

The northern part of the Central Segment represents also a peculiar kinematic-buffer situation, due to its position, at the connection between the equatorial Atlantic Ocean and the Central Segment of the South Atlantic. This peculiar kinematic-buffer situation gives some very specific characteristics to the North - Eastern Brazilian margins: i) The presence of an aborted first rift, the Recôncavo-Tucano-Jatoba Rift (RTJR) system, in the direction of the main central break-up, south of Camamú (Evain et al., 2023); ii) The presence of a triple junction (Camamú area) due to the eastward jump of the opening to the Jacuípe-SergipeAlagoas areas (Pinheiro, 2018; Loureiro et al., 2018; Loureiro et al., 2023; Evain et al., 2023; Aslanian et al., 2023); iii) A drastic change of the coast direction on both sides of the Camamú Triple junction; iv) and the presence of a short wavelength segmentation (< 200 km) on the margins. The NE Brazilian margin is highly segmented with different tectonic heritages and geodynamic settings (divergent or oblique). The question of segmentation (wavelength, direction, heritage and connection with the on-land rifts system and the oceanic part) is of crucial importance (Evain et al., 2023; Aslanian et al., 2016, 2023, Pinheiro et al., 2018 ,Loureiro et al., 2018, 2023).

The Cretaceous extension disrupted both cratonic cores and orogenic belts that were amalgamated during Brasiliano/Pan African orogenies (Almeida et al., 2000; Brito Neves et al., 2014). In the south of the SALSA experiment, the Brazilian basement is composed of Archean and

Paleoproterozoic metamorphic rocks (Itabuna-Salvador-Curaçá Belt or Itabunas Belt) that belong to the southern São Francisco Craton (SFC) (Barbosa and Sabaté, 2004; Mascarenhas et al., 1984). In the north, the Recôncavo-Tucano-Jatobá (RTJ) rift system partly cuts through the SFC, with partial outcrops of Archean basement (Aporá and Salvador-Jacuípe horsts) bounding the Recôncavo basin. But the RTJ further extends northward through the Proterozoic metamorphic rocks of the Sergipano Fold Belt (SFB) and the Mesoproterozoic to Neoproterozoic granite gneisses of the Pernambuco-Alagoas Massif (PAM).

Further south, the Camamu-Almada-Jequitinhonha basins have NNE-SSW basement fabrics directly inherited from deformation trends of the SFC Itabunas Belt (Barbosa & Sabaté, 2004; Ferreira et al., 2013; Gordon et al., 2013). The triple junction within the Camamú segment also coincides with a point where two perpendicular trends of foliations exist within the SFC granulite belt (Blaich et al., 2008; Mascarenhas et al., 1984; Milani and Davison, 1988). Northward, the RTJ rift geometry was controlled by a network of NE-trending normal fault that followed most of the foliations within the northern SFC basement. The rift system also exhibits a segmentation clearly controlled by NW-trending transfer faults reactivated from Precambrian trans-current shear zones (Chang et al., 1992; Matos, 1992; Milani and Davison, 1988). The main depocenters are bounded by such features. Among them, the NE Vaza-Barris/Itaporanga transfer fault (VBFZ, Figure 1a), which localizes the transition between the SFC and SFB, marks a flip in geometry between the Central and South Tucano basins (Milani and Davison, 1988). Further north, in the PAM, the Jatobá basin developed along the already mentioned NE trending Pernambuco lineament, which acted as a barrier to the northward propagation of the RTJ rift system (Milani and Davison, 1988; Szatmari and Milani, 1999).

Finally, recent investigations of this network of Precambrian inherited structures showed how they were reactivated as normal faults controlling the rift architecture of the Sergipe-Alagoas basins, at least for its sub-aerial and near shore parts (Vasconcelos et al., 2019). Extending their analysis of potential field and seismic data offshore, Vasconcelos et al. (2019) further showed how they directly influenced the localization of transfer and fracture zones during break-up and early seafloor spreading.

In 2014, a set of 11 WAS data profiles (SALSA experiment – more detailed in the SALSA experiment section) were acquired in this area where, among of the purposes of the experiment, were the of study the segmentation of the area and characterization of the nature of the crust (Aslanian et al., 2016). These profiles location and the main geologic and tectonic features are described in Figure 2.2.1.

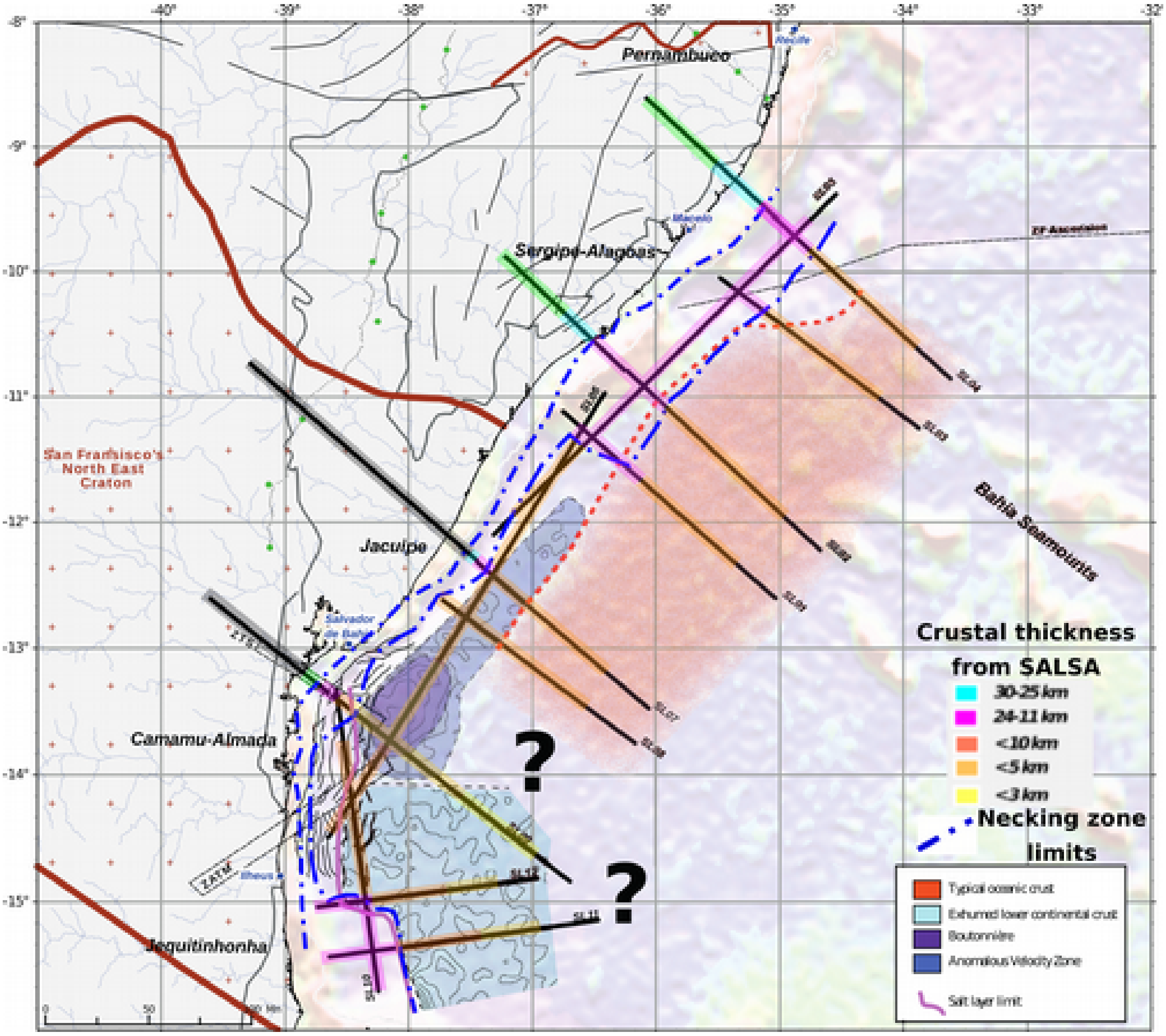

Figure 2.2.1 – Location of the 12 profiles comprising the SALSA experiment. Proposed segmentation and crustal geologic interpretation for the SALSA experiment study area with crustal thicknesses obtained from the SALSA data profiles. (adapted from: Evain et al., 2023 and Loureiro et al., 2023)

According with the interpretation done for the SALSA experiment area (Aslanian et al., 2015, 2023; Loureiro et al., 2018, 2023; Pinheiro et al., 2018; Evain et al., 2023), there are two clearly different segments:

I) In the South part, the Jequitinhonha-Almada segment (Figure 2.2.1 - profiles SL09, SL10, SL11, SL12 and the end part of profile SL06), presenting a wide transitional domain with a 150 km wide band of exhumed lower continental crust (light blue polygon in Figure 2.2.1) and where the oceanic crust was not reached by the SALSA profiles in the area.

II) The Northern part, the Jacuípe-Sergipe-Alagoas segment (Figure 2.2.1 – profiles SL01 to SL08). Within these margins, the oceanic crust is quickly reached (red polygon – oceanic crust -

Figure 3.2.1), in less then 80 km to the coast. The limit between the continental and oceanic crust is parallel to the coast (red dashed line in Figure 2.2.1). This segment can be divided into two sub-domains where the Vaza-Barris Transfer zone represents the limit between those two sub-domains (Loureiro et al., 2018; Evain et al., 2023). The south sub-domain (Jacuípe Basin) presents a continuation of the domain observe to the South and described in the previous point. As for the North domain, composed by the Sergipe and Alagoas Basins, is characterized by a thinned continental crust overlain by a 1.5 km thick volcanic layer. The segmentation on the Jacuípe-Sergipe-Alagoas margins and their adjacent oceanic crust has a NW-SE direction , oblique to the relative movement of the plates, being evidence of strong tectonic heritage. Also, further offshore, this segmentation seems to continue with the presence of the NW-SE oriented Bahia Seamount alignments in the Sergipe and Alagoas sub-segment (Aslanian et al., 2015).

The study area concerning this PhD project concerns the Northern part of the SALSA experiment – profiles SL01, SL02, SL03, SL04, SL05 and SL07. In the next figures, the available interpretation for each of these profiles will be presented, with a focus on the nature of the crust, as it was done for the Equatorial margin, since the deeper crustal layers are the focus of this project.

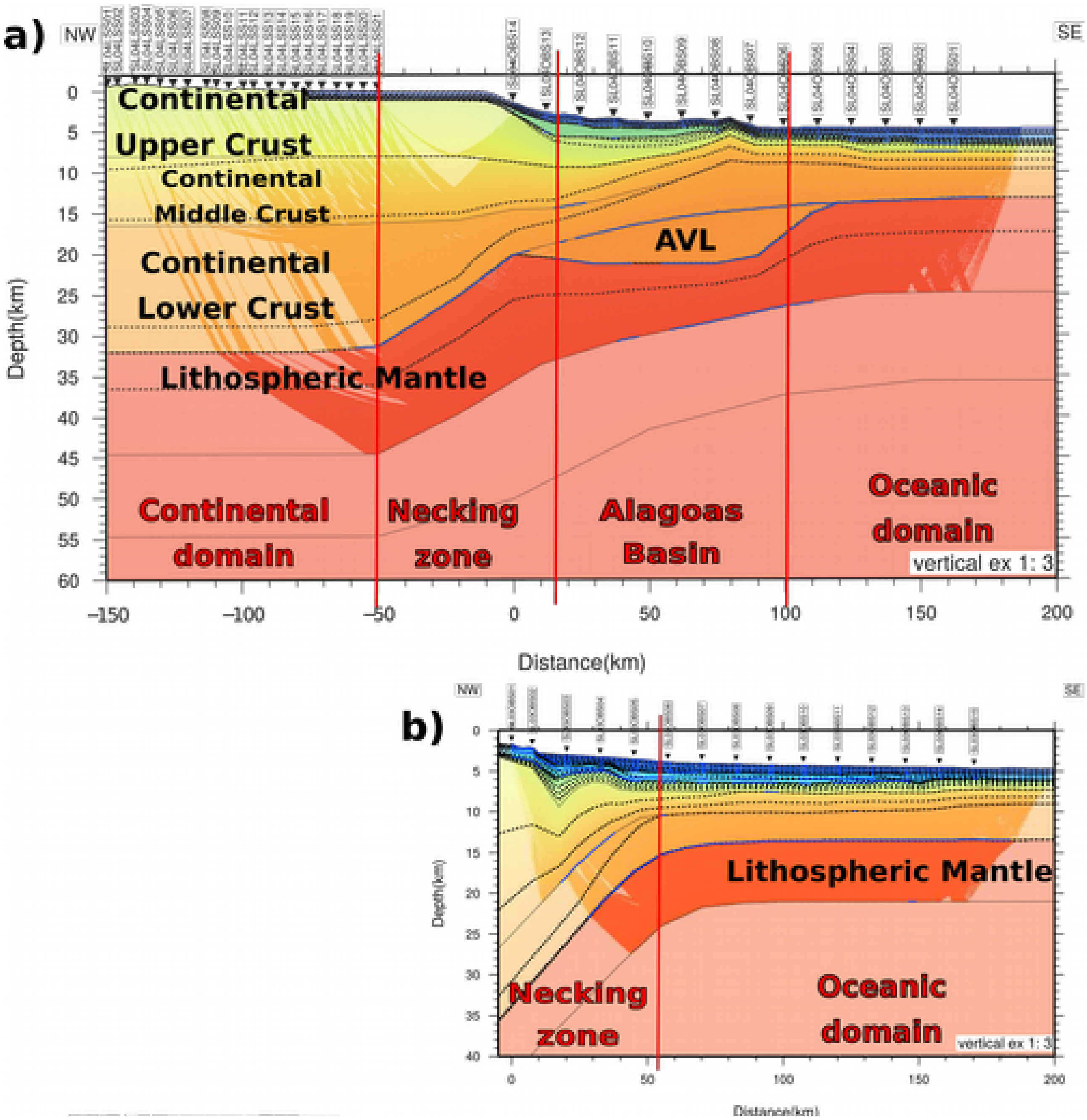

Figure 2.2.2 – Geologic interpretation of the crustal nature of two most Northern SALSA experiment profiles: a) SL04; b) SL03; AVL – Anomalous Velocity Layer (adapted from: Aslanian et al., 2016)

The SL04 and SL03 profiles are the two profiles located in the most northern part of the SALSA experiment and they concern the Alagoas basin. One of the profiles is extended in land (SL04) and the other one (SL03) only comprises OBS stations – Figure 2.2.2-a and b, respectively.

Both profiles share two common domains – Necking zone and Oceanic crust domain (in SL04 profile composed by the offshore part of the Alagoas Basin and the Oceanic domain). Because

SL04 is extended on land, the Continental Crust Domain can be found within this profile (Aslanian et al., 2016).

The complex nature of the extended continental and the oceanic crust, is emphasized in these profiles, by the relatively thin sedimentary sequence resting on top of the three layered crust. The distinction between the continental and oceanic crust is based on the variations of velocity values and gradients where the continental crust is typically faster and, as it transitions to typical oceanic crust, the velocity values decrease. Also, there is the thickness variation of the crust from land to ocean (NW-SE in the case of the profiles), that progressively thins as we move ocean-ward (Aslanian et al., 2016).

The thinning of the crust in the necking zone is quite abrupt (SL04, Figure 2.2.2-a), where in 70 km horizontal distance, the crust goes from 33 km thick to 18 km. This profile is also marked by the presence of a volcanic edifice, at 75 km horizontal distance, that affects the geometry of the layer up until the middle crust.

There is also the presence of an Anomalous Velocity Layer (AVL) in SL04 profile that extends landward for 90 km profile distance between the lower crust and the lithospheric mantle. This layer has a higher velocity value then the crust above it but not quite the typical values for lithospheric mantle and is interpreted as possibly reworked continental crust or mantle intruded crust since part of it is just bellow the volcanic structure (Aslanian et al., 2015).

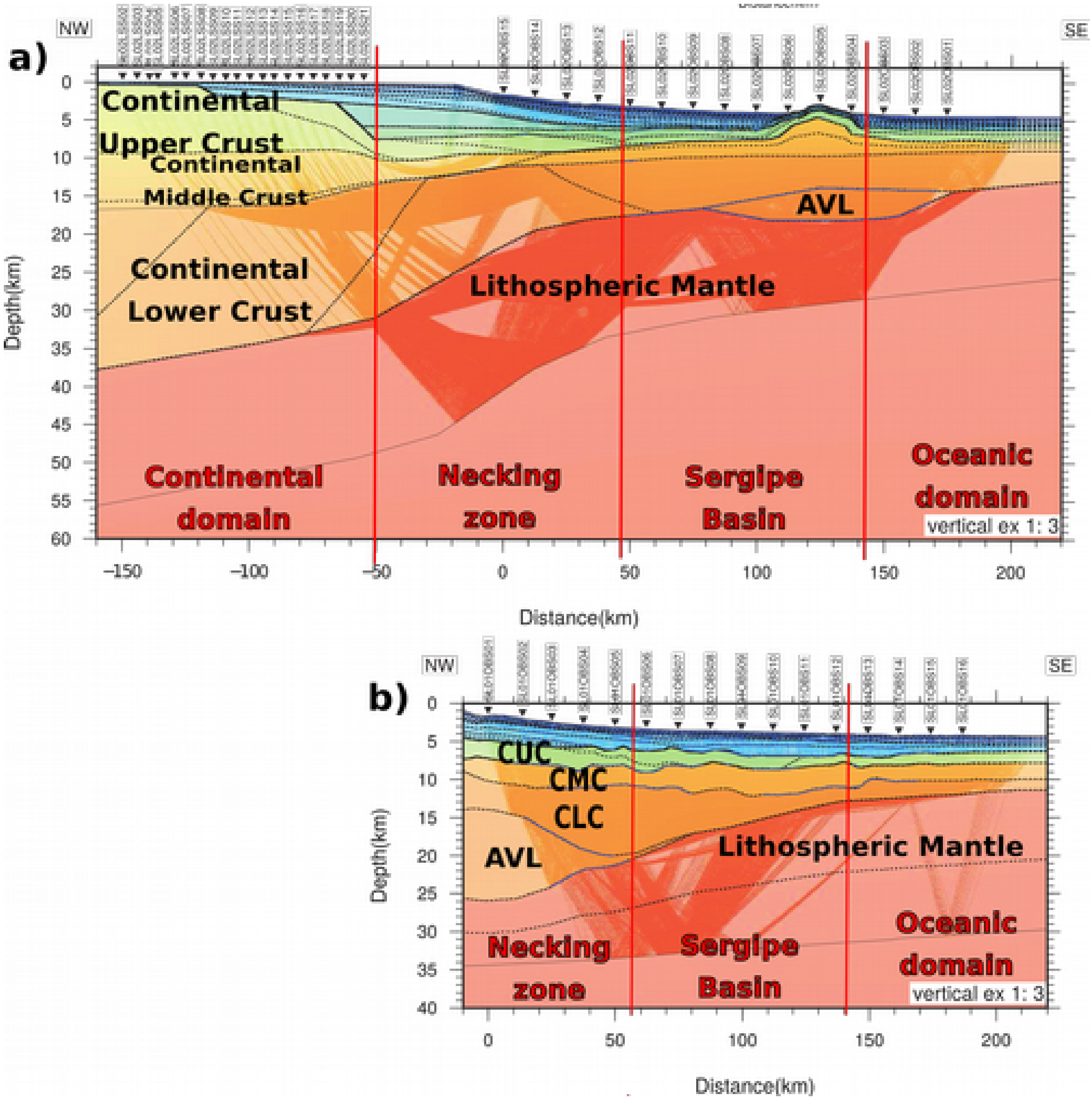

Figure 2.2.3 – Geologic interpretation of the crustal nature of two profiles of the SALSA experiment profiles: a) SL02; b) SL01; CUC – Continental Upper Crust; CMC – Continental Middle Crust; CLC – Continental Lower Crust; AVL – Anomalous Velocity Layer (adapted from: Pinheiro et al., 2018; Aslanian et al., 2016)

Moving South, into the Sergipe basin, profiles SL02 and SL01 were deployed. As for the previous profiles, SL02 profile (the northern of the two) is extended inland while SL01 only comprises OBS stations.

As for the previous pair of profiles, three domains were identified and interpreted for the profile that extends on land (SL02) and two for the other (SL01): Continental domain, Necking zone and Oceanic domain (that includes the offshore part of the Sergipe Basin). In spite of the seemingly domains with SL03 and SL04, in terms of the geometry of the structures the differences are clear (comparison between Figure 2.2.2 – SL04 and SL03 – and Figure 2.2.3 – SL02 and SL01).

The continental crust for SL02 is 35 km thick and in SL01, already in the necking zone, the thickness of the crust is 25 km. Three different continental crustal layers are distinguished, where the contrast between middle and lower crust is quite clear (Aslanian et al., 2016, Pinheiro et al., 2018).

Both necking zones are much smoother then the previous profiles, where the crustal layers get thinner and deeper along a horizontal range of approximately 100 km. At the same time and distance, the Moho discontinuity and Mantellic layers get shallower but in an asymmetric fashion, were the mantellic layer rises more then the amount that the crustal layers get deeper. Also, between the two profiles, the thinning processes are different, where a step like thinning is seen for SL02 profile and a more smooth thinning for SL01 profile (Aslanian et al., 2016).

The Sergipe-Alagoas basin (profile SL02) and the Sergipe basin (profile SL03) are interpreted with thin sedimentary layers overlaying also a set of three thin crustal layers that are interpreted as oceanic crust due to the slower velocities.

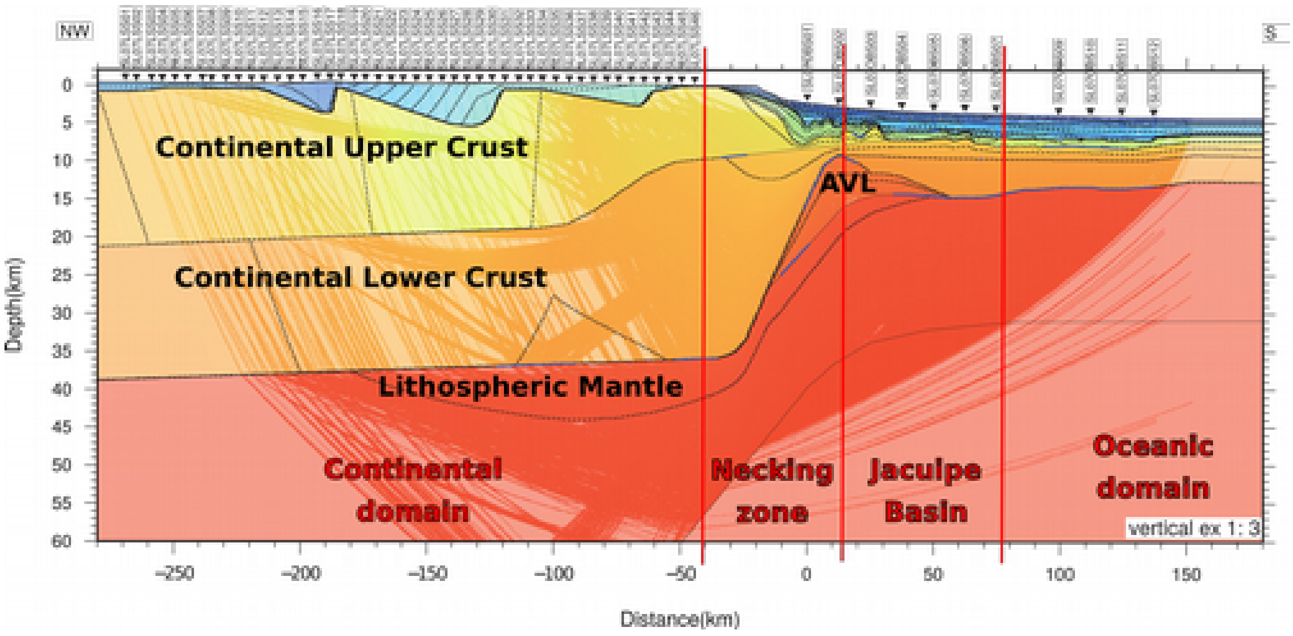

Figure 2.2.4 - Geologic interpretation of the crustal nature of SL07 profile of the SALSA experiment (after Aslanian et al., in press).

Moving again South, the SL07 profile was deployed. This is the last profile that is within the research area of the PhD project, where only the land stations and the first part of the ocean stations are considered.

Once again, this profile comprises three interpreted domains: the continental domain (including the São Francisco craton, the South Tucano basin, the Aporá High, the Recôncavo basin and the Salvador High), the Necking domain and the Oceanic domain (composed by the offshore part of the Jacuípe Basin an oceanic domain further offshore).

In the Jacuípe margin, the continental crust is 38 km thick composed of 2 layers with low gradients. Along the SL07 profile, in the Necking zone, the thick continental crust thins abruptly over a distance of less than 50 km. The top of the basement deepens from 0 to 5 km, whilst the Moho rises from 40 km to, approximately,15 km SW of the Necking zone (Figure 2.2.4).

In the oceanward end of the Necking zone, a lens shaped Anomalous Velocity Layer is interpreted, with velocities that are within crust and lithospheric mantle and a maximum thickness of 7 km.

The crust beneath the Jacuípe basin is interpreted as oceanic crust due to the progressive smooth of the crust and decrease in velocity. Beyond the Jacuípe basin, the crustal environment become quite homogeneous and is also interpreted as typical oceanic crust (Aslanian et al., 2016).

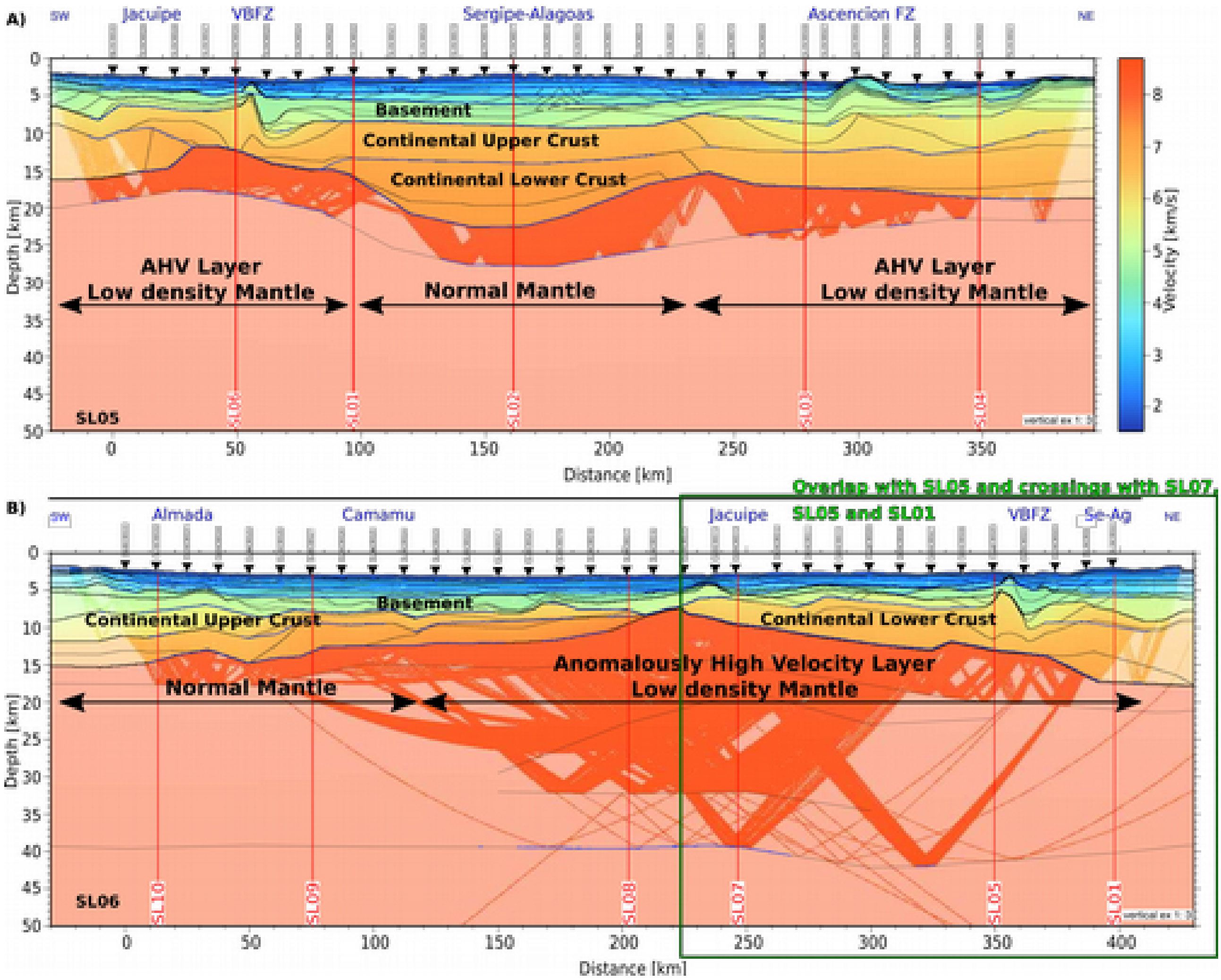

Figure 2.2.5 - Geologic interpretation of the crustal nature the two profiles along the coast line from SALSA experiment: a) SL05; b) SL06 (adapted from: Evain et al., 2023)

The last profiles within the research area are the entire length of the SL05 profile (Figure 2.2.5-a) and the overlapping portion of SL06 (Figure 2.2.5-b, green square). Both of these profiles were acquired along the coast line, as marked in Figure 2.2.1.

Both profiles present a strong topographic basement followed by also strong depth variations of the crustal layers and the Moho discontinuity. This topography has a clear effect over the sedimentary layers, where the Sergipe-Alagoas basins have a significant higher sediment thickness from the Vaza-Barris Fault Zone to the NE, when compared with the basins to the South (Figure 2.2.5-b). This sediment packages also thins as they approach the Ascension Fault Zone (Figure 2.2.5-a) (Evain et al., 2023).

The basement is characterized by a fairly constant and narrow velocity range but with a highly variable depth from one basin to another (Figure 2.2.5). It is deep in the Camamú basin at 6.5-7.5 km, rises abruptly up to 4.4 km depth at the transition with the Jacuípe basin to stabilize around 6 km within the basin itself. Crossing the VBFZ, it deepens abruptly to 6.5-7 km depth in the Sergipe-Alagoas basin to slightly rise again at 6 km within the AFZ (Evain et al., 2023).

Along SL06, the two crustal layers form together a 7 km thick crustal unit beneath the Almada basin reducing to a 4 km thick unit in the Camamú basin. The crust progressively thins until it completely vanishes at 210-220 km and a drastic increase in the crustal velocities is characterized in the NE direction. From Almada to this point, the Moho depth decreases from 15 km deep to only 8 km. From this point toward the NE crustal thickness and mantle velocities have probably been overestimated due to out of plane wave propagation and/or anisotropy. Instead very thin crust (only a few kilometers as suggested along SL07/SL08) may overlay an anomalously high velocity body.

SL05 velocity model and companion models along SL01/SL02 (J. M. Pinheiro et al., 2018) and SL04/SL03 (Aslanian et al., 2016) reveal an intermediate crustal architecture in the Sergipe-Alagoas basin and AFZ area starting from the offshore prolongation of the VBFZ toward the NE. The Moho has a concave shape beneath the Sergipe-Alagoas basin which reach 22 km at its center. It then varies between 15-18 km beneath the AFZ. The Sergipe-Alagoas crust is 14 km thick at most with average velocities that are higher then the crustal layers within the AFZ, with 8-9 km thickness.

Anomalously high velocity zones between the crust and mantle are again suggested beneath the Sergipe-Alagoas and the AFZ based on the velocity and density models as well as crossing models (Pinheiro et al., 2018; Aslanian et al., 2016).

When velocity-depth profiles of SL06, SL07, SL08 and SL09 were combined for the Camamú and Jacuípe basins, similarities were found with the Para-Maranhão-Barreirinhas margins in northern Brazil and in the aborted rift interpreted at the center of the Santos basin (Aslanian et al., this issue; Aslanian et al., 2021; Evain et al., 2015). The authors of Evain et al. (2023) suggest that exhumed and/or intruded continental crust lies above a layer of either highly intruded continental crust and/or serpentinized mantle, since the trend of these velocity profiles clearly diverge from the typical values for oceanic crust even if those values are found just a few kilometers oceanward according to SL07 and SL08 models (Aslanian et al., 2023). The Camamu-Jacuípe margins' narrow architecture, the nature of their transitional domains and the abrupt transition towards oceanic crust greatly diverge from the architecture just described for the Jequitinhonha-Almada margins and imply that the Camamú Triple Junction marks a first order major segmentation in NE Brazilian margins.

The crossing of SL05 and SL06 profiles near the offshore prolongation of the VBFZ marks a large change in sedimentary and crustal architecture between the Jacuípe and Sergipe-Alagoas basins. SL05 velocity model complement previously published models by Pinheiro et al. (2018) providing an along-strike view of the seaward extremity of the necking zone where the crust is considerably thicker (up to 16 km) than in the Jacuípe basin. The most striking observation is the thick and high velocity crust of the Sergipe-Alagoas basins which is underlain by normal mantle velocities. Such architecture is different beneath the AFZ where the crust is thinner, with lower velocities. However, an anomalous velocity layer is also suggested by crossing SL03/SL04 profiles (Aslanian et al., 2016). By compiling velocity-depth profiles in the Sergipe-Alagoas basin and in the AFZ area, Evian et al. (2023) highlight the low gradient of the crust which is intermediate between normal continental and oceanic crust as shown by Pinheiro et al. (2018). Such characteristics is again close to what was observed in the Santos basin (Evain et al., 2015) and suggest the presence of thinned, probably exhumed, continental crust modified by intrusions of mafic materials. Compared to Camamu-Jacuípe, the transition toward oceanic crust is also steep within the Sergipe-Alagoas and the AFZ segments (Pinheiro et al., 2018) but the width of the necking zone is larger and the continental crust thinned more gradually with lower inputs of mafic materials.

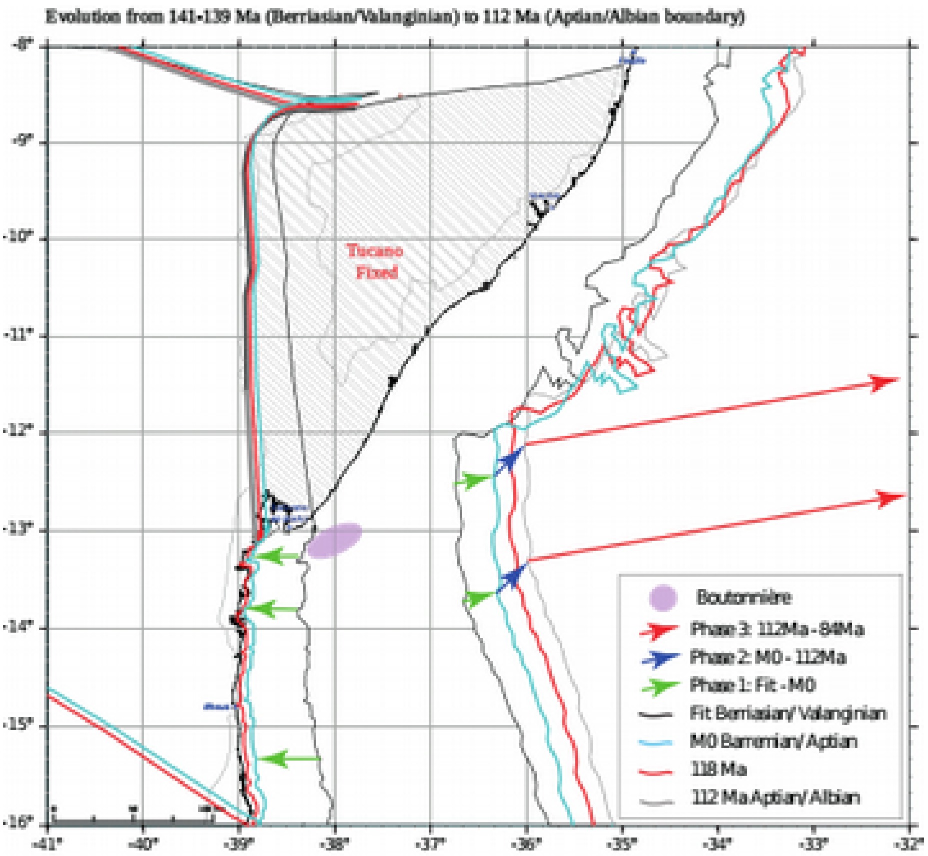

Figure 2.2.6 – Refined evolution of the regional plate motions relative to the Tucano micro-plate (considered as fixed) (from Evain et al., 2023)

From the vast area of exhumed continental crust evidenced in the Jequitinhoha-Almada segments to the steep thinning and sharp transition toward oceanic crust observed in the Camamu-Jacuipe-Sergipe-Alagoas segments these models are consistent with a geodynamic framework where purely divergent extension occurred to the south of the CTJ while trans-tension shaped the margins to the north. Integrating these results and building on the kinematic model of Moulin et al. (2010) and the stratigraphic synthesis of Chaboureau et al. (2013), Evain et al. (2023) presents the evolution of regional plate motions relative to the Tucano micro-plate (Figure 2.2.6). Its suggested three distinct stages characterized the region:

1) From the Berriasian-Vallanginian boundary (141-139 Ma) to the Barremian-Aptian (125 Ma) boundary, rifting occurred on each side of the Tucano plate, forming the Tucano rift and half grabens on its western edge and the RTJ basins and initiating the Jacuípe-Sergipe-Alagoas margins on the eastern edge. During this first phase the São Francisco Craton moved WSW with respect to the Tucano micro plate, while the African plate moved ENE. For the Jatoba-Jacuibe-Sergipe-Alagoas margins, a 45º oblique margin was initiated.

2) From the Barremian-Aptian (125 Ma) boundary to the Aptian-Albian boundary (112 Ma) a major kinematic change occurred. The movement of San Francisco plate ended and the RTJ rift aborted. The African plate movement also changes in direction, to a NE direction. Overall this implied strike-slip movement between Camamu-Jacuípe-Sergipe-Alagoas and North Gabon margins. This kinematic change was probably related to African intra-plate deformation, which also ended around the Aptian-Albian boundary (Guiraud and Maurin, 1992; Moulin et al.,2010).

3) Posterior to the Aptian-Albian boundary (112 Ma) and contemporary of the beginning of plate separation in the Equatorial Atlantic ocean, formation of the first oceanic crust in the Central Segment of the South Atlantic and the end of the African intra-plate deformation, the African Plate movement came back to the previous ENE direction, parallel to the Ascension Fracture Zone.

2.3. Integrating the geology context in the research area

The continental part of the research area, the Borborema Province, is mainly described by the events occurred upon the formation and consolidation of the West Gondwana, that were described previously. In this section, we present a fairly simplified map of the geologic and tectonic structures that compose the research area, along with the location of the three profiles that are at the core of the PhD project in order to obtain a rare and integrated view over an approximately 1800 km long transect that crosses two passive margins and one of the most complex and old continental geological settings.

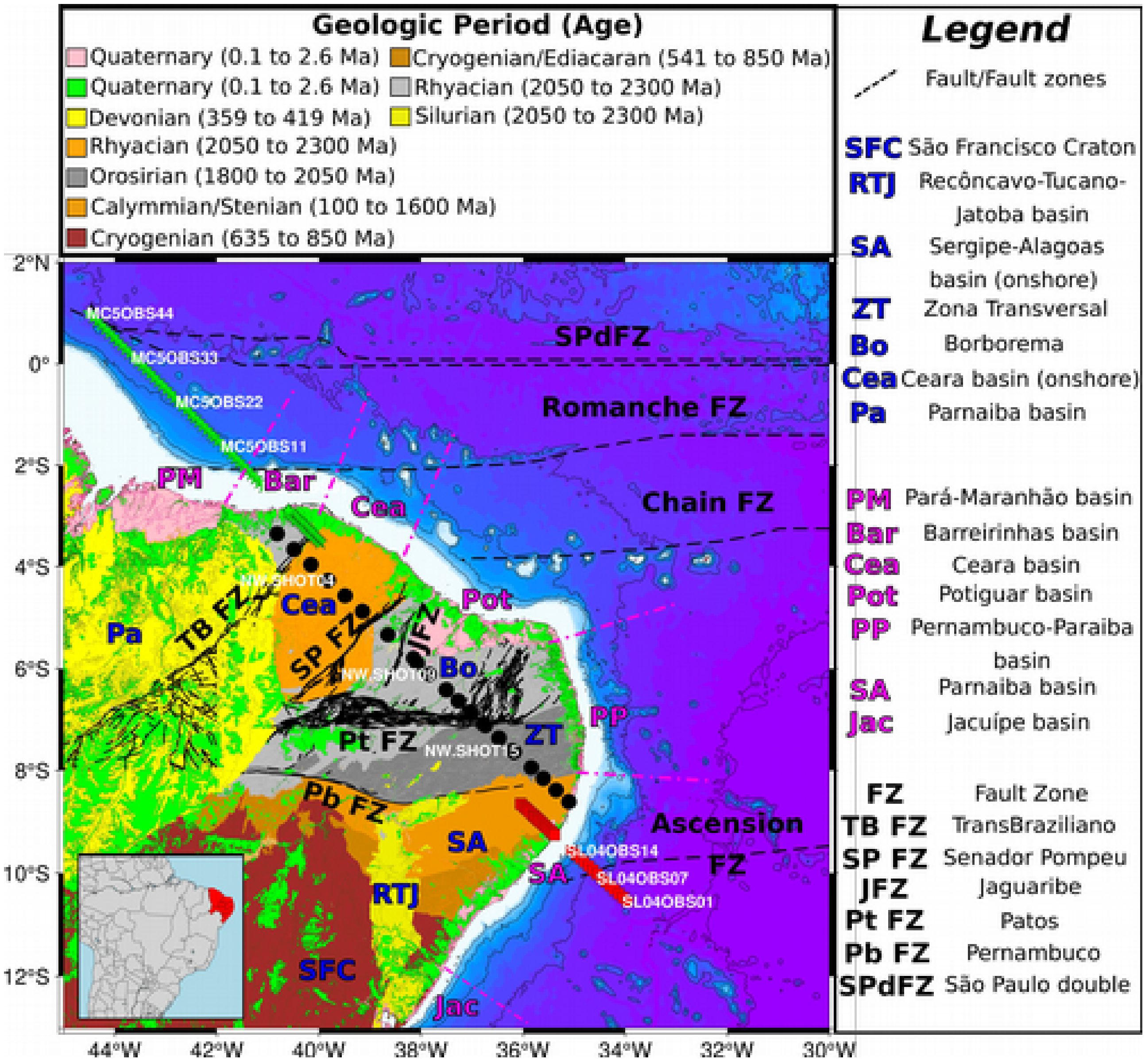

Figure 2.3.1 - Geology of the research area and studied profiles. (Green stars – MC5 profile from the MAGIC experiment; Black dots – NW profile of the INCT-ET project; red squares – SL04 profile from the SALSA experiment)

A detailed geologic/geodynamic description concerning the MC5 ans SL04 profiles (green stars and red squares, respectively – Figure 2.3.1) offshore areas was presented in the previous sections since these two profiles are part of two different experiments.

The large scale tectonic structures in the Borborema province are mainly right-lateral strike-slip shear zones (PbFZ, PtFZ, JFZ, SPFZ and TBFZ – Figure 2.3.1), with mostly Northeast-

Southwest and East-West directions, that limit the fold belts and basement inlines in the province and date from the end of the Neoproterozoic and Early Paleozoic (Caxito et al., 2020; Neves et al., 2012; Van Schmus et al., 2011).

The province is covered westwards by Phanerozoic sedimentary rocks and volcanic of the Parnaíba basin (Pa and light yellow in Figure 3.3.1) and northwards and eastwards by coastal Meso-Cenozoic deposits (green color in Figure 2.3.1) (Lima et al., 2015).

Three different geological domains can be distinguished within the province (Van Schumus et al., 2011), bounded by different tectonic structures and comprising multiple geologic facies. From Northwest to Southeast:

1) Northern domain – bounded to the Northwest by the Parnaíba basin and TransBrasiliano Fault zone and to the Southeast by the Patos Fault Zone. Within, the Médio Coreaú (light gray between the Barreirinhas basin and the TransBrasiliano Fracture Zone), the Ceará basin (orange, between the TBFZ and the JFZ), the onshore Potiguar basin (light pink, close to the East end of the PtFZ), part of the Borborema plateau (Bo, light gray in the PtFZ) and part of the Pernambuco-Paraiba basin.

2) Transverse domain (ZT in Figure 2.3.1) – bounded to the North by the Patos Fracture zone (PtFZ) and to the South by the Pernambuco Fracture Zone (PbFZ). Within, the Pernambuco-Paraiba basin (light pink closer to the shore and extending offshore).

3) Southern domain – bounded to the North by the PbFZ and to the South by the São Francisco craton. Within The Sergipe-Alagoas basin (dark orange – SA) and the central and northern part of the Recôncavo-Tucano-Jatoba (RTJ) basin (Yellow color).

In 2008, a NW-SE WAS data profile was acquired within the Borborema province area by INCT-ET (Instituto Nacional de Ciência e Tecnologia em Estudos Tectônicos), which acquisition details will be described in the Data description chapter.

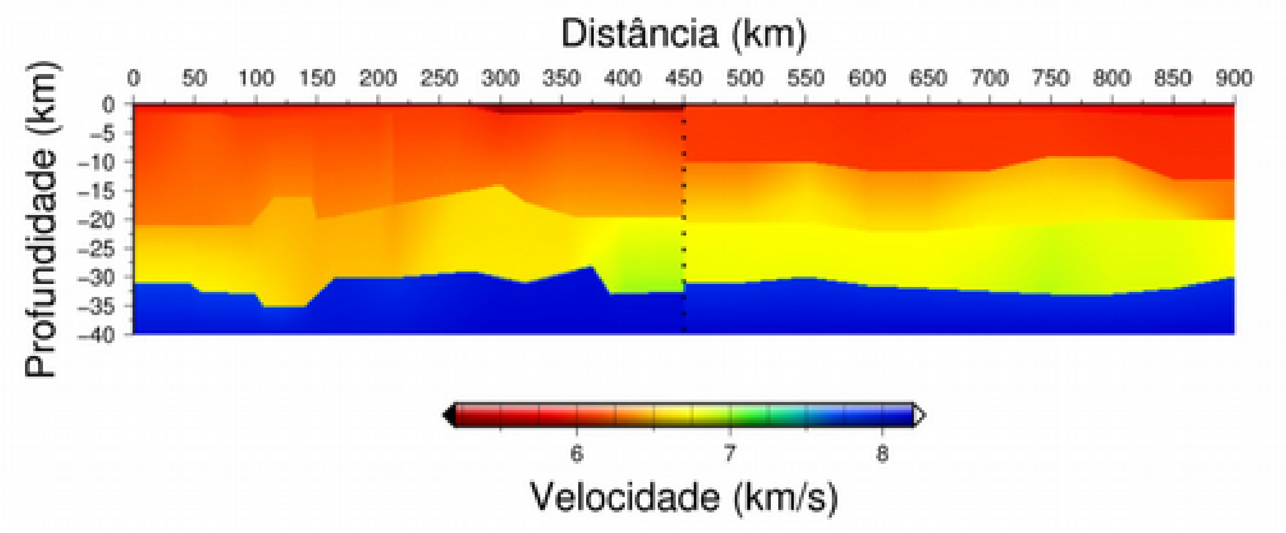

Figure 2.3.2 – 2D NW-SE seismic profile model of the Borborema province lithosphere (from Soares et al., 2010)

The model for the NW-SE profile is presented in Figure 2.3.2. The obtained model is a four layered model with a very thin sediment layer (dark red distinguishable between 300 and 450 km horizontal distance), two crustal layers (red-orange-yellow) and one lithospheric mantle layer (dark blue).

The upper crust layer has an average thickness of 22 km and the lower crust average thickness is 10 km, reaching 33 km depth. This crustal depth is in agreement with what was described in the two previously sections for the profiles that were extended onshore (like MC5 and SL04). The vertical velocity gradient is fairly smooth along the model with two exceptions for the bottom of the crust between 400-450 km and 700-800 km, where the gradient is sharper due to a faster lower crust.

The lithospheric mantle layer, which boundary with the lower crust corresponds to the Moho discontinuity, has an average depth of 33 km.

Both the lower crust and the lithospheric mantle have significant geometry variations, in particular for the first half of the profile (between 0 km and 450 km), roughly matching the major tectonic events – the TBFZ, the SPFZ and JFZ. For the second part of the profile (between 450 km to 900 km) this geometry becomes smoother for both layers and where the main structures within this part of the profile are the PtFZ, the Borborema Plateau, the PbFZ and the Sergipe-Alagoas onshore basin (Lima et al., 2015; Soares et al., 2011, 2010).

3. Data description

This PhD project comprises data sets with different origins and from diverse sources. Three of those data sets were part of three different WAS data acquisition projects and are at the core of the PhD. The details of these three data sets will be presented within the sections of this chapter.

Apart from those WAS data sets, a compilation of Moho depth from seismic station points was originally done by Assunção et al. (2013) and updated by Rivadeneyra-Vera et al. (2019) for the entire South American continent. That compilation comprises seismic refraction experiments, receiver function analyses and surface-wave dispersion.

The raw gravity data and topographic source used in this project was downloaded from the International Center for the Global Earth Models (ICGEM) web-service (Barthelmes & Köhler, 2012), with a regular grid of 0.1° spacing.

3.1. MAGIC experiment

The MAGIC (Margins of brAzil, Ghana and Ivory Coast) research experiment was a join project of the Department of Marine Geosciences (IFREMER: Institut Français de Recherche pour l'Exploitation de la MER, France), the Laboratory of Oceanic Geosciences (IUEM: Institut Universitaire et Européen de la Mer, France), the Faculdade de Ciências da Universidade de Lisboa (IDL, Portugal), the Universidade de Brasília (Brazil) and PETROBRAS (Brazil). The MAGIC survey was conducted first on the Brazilian side in order to verify the segmentation of the Pará-Maranhão basin and to determine the crustal nature of its domains (Aslanian et al., 2021b, 2015; Moulin et al., 2021; Schnürle et al., 2023).

The IFREMER's Marine Geosciences . OBS (Ocean Bottom Seismometer) pool (OldOBS and MicrOBS instruments) was used for offshore wide-angle acquisition. Each OBS is equipped with a three-component geophone and hydrophone. Onshore, portable seismic 150 stations (Reftex 125A-01 acquisition system and seismic sensor L-4C) from the Brazilian Geophysics instrument pool (Observatório Nacional, Rio de Janeiro) were used to record the airgun shots of the R/V Pourquoi Pas? (Aslanian et al., 2021b, 2015; Moulin et al., 2021; Schnürle et al., 2023). In the year 2000's high quality seismic profiles from ION-GXT were acquired off Brazil's coast, and a some of these profiles have been published, particularly in the Brazilian southeastern margin (e.g., Henry et al., 2009; Kumar et al., 2012 ; Romito & Mann, 2021). The location of MAGIC profiles follows when possible some of the ION-GXT profiles.

The seismic source consisted of a 7589 in3 array of 18 airguns, towed 25 m below the sea level and fired every 60 s. Shots were also recorded by a 4.5 km long, 360-channel solid streamer towed at 12-15 m depth, 275 m behind the ship. During the MAGIC seismic cruise, 143 Ocean Bottom Seismometers (OBS), a 4.5 seismic streamer and 50 land-stations were deployed along 5 profiles at sea and 3 on-land (Figure 2.1.1). Bathymetry, Chirp, multi-channel seismic (MCS) and wide-angle data were acquired on the 5 marine profiles (MC1, 332 km, MC2, 203 km, MC3, 404 km, MC4, 268 km and MC5, 528 km) between August and October 2012 by the French R/V Pourquoi Pas?. Additionally, six cores and one 160 piezometer were deployed during the experiment (Aslanian et al., 2021b, 2015; Moulin et al., 2021; Schnürle et al., 2023).

3.2. SALSA experiment

The SALSA experiment, was conducted in 2014 by the Department of Marine Geosciences (IFREMER: Institut Français de Recherche pour l'Exploitation de la MER, France) and PETROBRAS (Brazil), in collaboration with the Laboratory of Oceanic Domain (IUEM: Institut Universitaire et Européen de la Mer, France), the Faculdade de Ciências da Universidade de Lisboa (IDL, Portugal) and the Universidade de Brasilia (Brazil), was aimed at constraining the crustal structure, the segmentation and the geodynamical setting of the Jequitinhonha-Almada-Camamu-Jacuípe-Alagoas-Sergipe margin segments. In the year 2000's high quality seismic profiles from ION-GXT were acquired off Brazil's coast, and a some of these profiles have been published, particularly in the Brazilian southeastern margin (e.g., Henry et al., 2009; Kumar et al., 2012 ; Romito & Mann, 2021). The location of the SALSA profiles follows some of the ION-GXT profiles. Seismic shots, Multi-Channel Seismic (MCS) acquisition and Ocean Bottom Seismometers (OBS) deployments were performed by the French R/V L'Atalante (IFREMER) along twelve profiles (Figure 3.2.1) (Aslanian et al., 2016).

The 12 profiles comprised the deployment of 222 OBS (Ocean Bottom Seismometers) stations and 124 LSS (Land Seismic Stations). The OBS were deployed at 7 nautical miles intervals (approximately 12.5 km) , and were capable of recording on four channels (1 hydrophone and a 3 component geophone). A 4.5 km long digital seismic streamer ensured near-offset multi-channel seismic (MCS) recording of the shots with hydrophones. The seismic source was a tuned array of 16 air guns with a combined volume of 6544 in^3.

Two legs have been realized, the first one is devoted to six wide-angle/MCS profiles: four perpendicular (SL01 to SL04) to the coast, and two parallel (SL05/SL06) to the presumed ocean-continent boundary, whereas the second one is devoted to six additional profiles: five perpendicular (SL07 to SL09, SL11/SL12) to the coast, and one parallel (SL10) to the coast. Each pair of profile is devoted to a supposed specific basin, segmented of the Northeast Brazilian margin.

Bathymetry, Chirp, MCS and wide-angle data were acquired on the twelve profiles (Figure II.13): SL01 (177 km), SL02 (169 km), SL03 (155 km), SL04 (158km), SL05 (334 km), SL06 (377 km), SL07 (137 km), SL08 (149 km), SL09 (212 km), SL10 (223 km), SL11 (114 km) and SL12 profiles (216 km). Five profiles (SL02, SL04, SL07, SL09 and SL12) have been prolongated onshore by land stations acquisition (Loureiro et al., 2018, 2023; J. M. Pinheiro et al., 2018; Evain et al., 2023, Aslanian et al., 2023). .

The research area concerning the PhD project concerns half of the profiles within the SALSA experiment – SL01, SL02, SL03, SL04, SL05 and SL07.

3.3. INCT-NE project

In 2008 and 2011, two deep seismic refraction experiments were conducted and two WAS data profiles were acquired in the Borborema province area, NE Brazil. One of the profiles was acquired in the NW-SE directions and the other in the N-S direction (Figure 3.3.1).

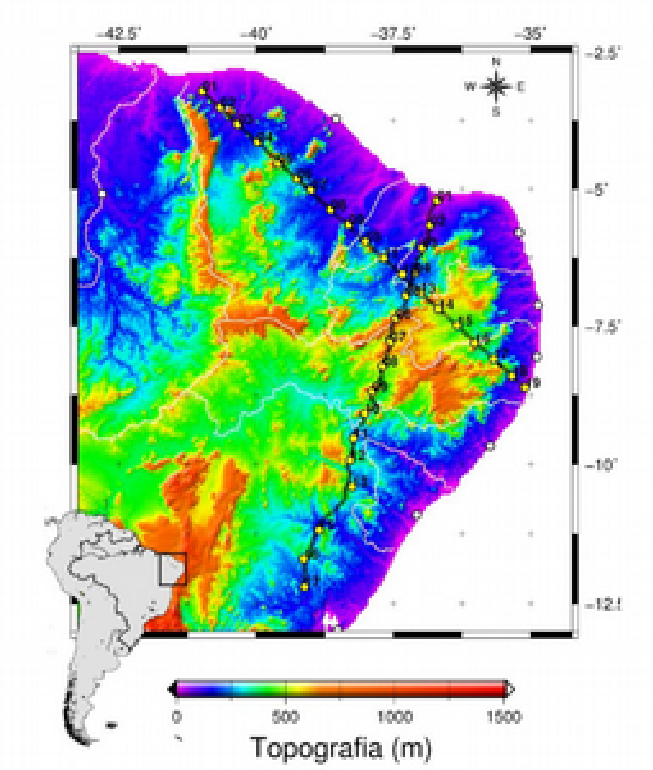

Figure 3.3.1 – Topographic map with the location of the two profiles acquired within the INCT-NE project (from Soares et al., 2011)

The NW-SW profile has a length of 880 km, extending from the Médio Coreau (to the NW) to the Sergipe-Alagoas basin (to the SE). This line was acquired with the deployment of 400 sensors, spaced each 2.2 km. As source, 19 shot locations (yellow circles in Figure 3.3.1) where designed, spaced by 50 km along the profile. Each intermediate shot was composed by 1.4 tons of explosives placed in boreholes of 0.25 m in diameter and 45 m in depth. The shots at each end of the profile were also composed by explosives but a 4 ton quantity was used (Soares et al., 2010).

The N-S profile has a length of 820 km, extending from Pendências-RN (North edge) and Anguera-BA (South edge). The distribution of the sensors was similar to the previous mentioned profile and 17 shots were performed with the same characteristics as the NW-SE profile (Soares et al., 2011)

4. Geophysical methods

We live in a world where the rhythm at which everything that surrounds us moves faster and faster, constantly evolving and changing. It was always like so, and certainly many researchers had the same feeling before. Working in science and research implies, in a certain way, to be always on the edge and keep up with technology and the new hypothesis and theories. In the past 30 years, the boom of the internet and computation, the capacity of having the world on our virtual hands, can be a double-edged sword. As it is important to use the new technologies, in order to improve our science in general, it is also important to keep in mind the already existing knowledge and build on top of that knowledge instead of simply dismiss it as hold or outdated. Working with Geophysics and Geology has the great advantage of not being able to dismiss that previous knowledge easily because the Earth history works in a million years scale and Physics basic laws and rules are quite stable also.

The purpose of this work is to take advantage of the technology evolution where we have the capacity of developing and test complex methods, handle large data sets and have them accessible on a laptop. On one hand, develop and/or improve methods that permits any researcher to save time on processing a large data set and obtain results that helps to better understand the geodynamics of the Earth sub-surface, is definitely something that takes advantage of the technological evolution. On the other hand, it is required from the researcher to document the previous knowledge on the subject and the understanding on how the method works in order to properly analyze, understand and integrate the obtained results into a positive contribution on the research of a certain subject.

This PhD project has two main branches – the 3D gravity inversion with a seismic constraint and the Reverse Time Migration (RTM) applied to Wide-Angle Seismic (WAS) data.

The first method was primarily developed by (Uieda and Barbosa, 2017) for the entire continent of South America. It was developed with the goal of obtaining the Moho discontinuity depth and geometry by combining satellite gravity data processing and inversion with a compiled list of seismic stations that provide constraint regarding the depth of the Moho discontinuity. Since its development and application to the South American continent, parts of the method have been applied. For example, Haas et al. (2021), used the calculation of the sediment layers gravitational effect to calculate Bouguer anomaly for the African continent. However, after its development, the method was not fully applied in other research areas.

The 3D gravity inversion method, as it was first developed, had the potential to be applied to any area in the world, given that one is able to gather the satellite gravity data for that particular area along with a compilation of seismic stations that can provide sufficient information concerning the depth of the Moho discontinuity and constrain the gravity inversion. Working on a very large scale and with a main focus on the continental Moho discontinuity, the original method gives a quite interesting perspective and contribution on how it is possible to combine gravity and seismic data in order to retrieve results that can actually add up to the already existing knowledge of the deeper crustal/mantellic layers. Given the potential of the method, this project used it as foundation and tried to improve it, so it could be applicable to smaller areas and where the land/ocean contrasting environments are relevant. More specifically, improve the method so it could help to characterize the Moho discontinuity depth and geology, or any other layer, along passive margins, structures quite important to understand, from the geophysical and geological point of view, since they help us to build knowledge on the tectonics and geodynamics of the continents drift in the past, and then be able to model different hypothesis on how the continent drift can happen in the future and what are the potential consequences on that.

The second method, the Reverse Time Migration (RTM), first developed in the 1980’s years by Baysal et al. (1983), has as main purpose to retrieve an image of the sub-surface through the correlation of the downward and upward propagating acoustic wavefields generated from seismic sources and records.

The main purpose of the RTM method within this PhD project was to apply it to WAS data, something that was scarcely done in the past (Schnürle et al., 2006; Shiraishi et al., 2022), in spite of 40 years of existence. Surely the method was changed and adapted along those years to different scales, purposes and data sets. However, in what concerns the WAS data, the main argument against the application of the RTM to WAS data is the wide spacing between stations in the acquisition of this data type and consequently the low resolution that would impair the method to be successfully applied. Within this PhD project we show not only that is possible to successfully apply the method to this type of data but also to retrieve encouraging results that definitely contributes to the interpretation of the seismic data on a given region. The application of the method could be useful in a incipient stage of a project of data acquisition in order to have a first image of the sub-surface structure or applied in the perspective of verifying different hypothesis on the structure and geodynamics of a certain sub-surface area.

Finally the retrieved results from each method need to be integrated in the geodynamical context of the research area and evaluate how they contribute to the knowledge and understanding built from previous studies and projects. The strengths and weaknesses of each method will be analyzed and discussed so they can be applied in other areas and how they can be improved in the near future.

4.1. Gravity

The classical gravitational potential theory has its roots in the XVII century with Issac Newton’s law of gravitation. With the studies developed by Pierre Louis Moreau de Maupertis and Alexis-Claude Clairaut and independently by Pierre Bouguer, Louis Godin and Charles Marie de la Condamine, and the first geodetic measurements were successfully conducted (Herring and Schubert, 2015). The use of the gravitational potential theory remained as a geodesy subject for a long time and only in the XX century, with the technological evolution, the modern gravimeters and satellites, capable of measuring in time the gravity acceleration, became a relevant tool in the geophysical subject.

We can simply define the gravity force as the attractive force exerted by the Earth to its center over another body mass. Being the Earth interior a complex system composed by the most diverse structures and materials and supplied of movement, this apparently simple concept become more complex.

To study the gravitational force exerted by a particular body within the Earth, we need to isolate that particular body from the surroundings. In order to do that, we need to understand the concept of gravity anomaly. For a particular point at the Earth surface, the amount of gravitational force that attracts a body to the Earth center is given by the vertical mass that is between the Earth surface and its center, multiplied by its density. If we consider a layered Earth with average density values for each layer, the total gravity force measured at the surface should be the sum of the gravitational force for each layer. However, due to variations of density and geometry within a particular layer, that does not happen. This means that, by removing the average gravitational effect of a particular layer, we are left with the anomalous gravitational effects and, consequently, a gravity anomaly.

Another important concept to understand is the one of gravitational potential. We can define this concept as a surface which geometry varies depending on the amount of potential energy that a certain body within the Earth exerts over that surface. One known example of the potential surface is the geoid that is the surface of constant potential that coincides with mean sea level over the ocean (Herring and Schubert, 2015). This means that surfaces at different altitudes are affected by different structures and there is a clear link between the size and depth of those structures. That leads us to the concept of wavelength of an anomaly where potential surfaces at higher altitudes are more affected by bigger and deeper structures while potential surfaces at lower altitudes are more affected by smaller and shallower structures.

4.2. Reverse Time Migration (RTM)

The study and interest in the seismology field is ancient and goes back to the Ancient Greece where Thales of Miletus or Aristotle included in their writings the interest and the relevance of understanding of earthquakes. However, it was the 1755 Lisbon earthquake that set in motion, along with the generalization of the scientific method in Europe, that more intensive studies started to be developed. Since that time the seismology field largely grow and the industrialization of society and the need of resources to produce energy made the field grow even more. At present day, the concerning with the environment and climate change, oblige seismology to diversify even more in order to be able to contribute for the urgent solutions needed.

The RTM method grew along within the seismology field and, even being a small element of a vast field, is an essential tool to image the subsurface by using seismic waves.

Seismic imaging is one of the most effective means to map the sub-surface structures and properties using seismic data, and reverse time migration is one of the most efficient seismic methods (Zhou et al., 2018). This type of tool is so powerful that, in little more then 40 years, the diversification of the method was huge. In spite of that, we still must to keep in mind that seismic imaging is a remote sensing method with uncertainty, an the quality of the resultant images is subjected to the influences from data noise and limitations in the acquisition and imaging methodology.

The concept of seismic migration involves the extrapolation of seismic data from the recording receivers to sub-surface reflectors. The data is extrapolated in reversed direction with respect to the direction of the wave propagation from the source. Treating the recorded wavefield as time-dependent secondary source distribution along the receivers, RTM extrapolates each data trace of time-reversed seismic record from the data space to an image space, where the output images of the sub-surface reflectors are achieved based on a imaging condition (Levin, 1984; Zhou et al., 2018). Of various seismic conditions for seismic migration, the common goal is to optimize the fitness in the image space between the extrapolated waveforms from the data space and the predictions based on estimated reference velocity model and source parameters in the model space.

At present day, the RTM methods can be divided into two groups: 1) a first generation RTM methods taking primary reflections as the only signals (Edip Baysal et al., 1983; Baysal et al., 1984; Whitmore, 1983); 2) second generation RTM methods making a full use of the all computable wavefield types (Youn and Zhou, 2001). A detailed and full description of the two groups was proposed by Zhou et al. (2018). The RTM method applied within this PhD project can be fitted in the second group since no assumptions are done regarding the type of waves that propagate within the wavefields. For instance, acoustic P to shear-wave S conversions have been investigated in both reflection and transmission modes.

5. Methodology

The study of deep earth structures is always a challenge as insights are only provided by indirect methods. In this chapter we present the three independent but complementary approaches we used to study the deeper crustal layers of the research area and describe their underlying principles.

First, there is the description of the 3D inversion of gravity data with seismic constraints in order to recover the depth and geometry of the Moho discontinuity for our research area. The method was presented by Uieda and Barbosa (2017) where the Moho discontinuity depth is estimated, for the entire South America. The original source code is available in GitHub (https://github.com/pinga-lab/paper-moho-inversion-tesseroids). The Bouguer anomaly associated with the Moho discontinuity is retrieved from satellite gravity data and topography. Here, we further use the model CRUST1.0 as reference for depth and density values of each crustal layer above the Moho discontinuity. The compilation file of seismic depths for the Moho discontinuity that is used to constrain the 3D gravity inversion incorporates values recently determined from wide-angle experiments. Half of the Bouguer anomaly data grid is used to evaluate the inversion parameters and the other half to perform the actual inversion. We obtain two main results: (i) maps of predicted and observed Bouguer anomaly; (ii) estimated depth of the Moho discontinuity by gravity inversion with seismic constraint. This method was chosen since it allows to minimize the non-uniqueness problem. By inverting a gravity data set with a seismic constraint, the method integrates two different data sets to solve a similar object within the Earth. This improves the result by itself and reduces the hypothetical models that would explain the geometry of the Moho discontinuity and the geodynamic processes responsible.

Secondly, the application of Reverse Time Migration (RTM) method to wide-angle seismic (WAS) data is described. Originally developed as one of the tools of Seismic Unix (SU) software, the method is composed by five steps: 1) the Forward problem, where the wavefield travels from the Earth sources to a set of receivers in the surface, recording amplitude and travel time for each time step; 2) The Backward problem, where the same time interval is reverse and the wavefield is restored to the Earth sources; 3) Correlation of the two wavefields, for each time step, retrieving an image of the subsurface of the target area. The method was applied to OBS and LSS stations of two profiles within this research project – MC5 and SL04.

To work with already existing methods and making adaptations/changes to those methods, is often disregarded. We have taken two of those methods and worked on their adaptation so they would fit a larger scope. The original gravity method was applied to the entire South American continent, aiming to study the geometry of the Moho discontinuity, only in the continental domain. In our study we also studied the geometry on the Moho discontinuity but in the passive margins context. In order to do this, a different altitude and higher resolution gravity grid was used along with an updated pool of seismic points. Instead of only consider the sediment layers in the calculation of the Bouguer anomaly, the crustal layers were also considered along with the analyses of the densities used. As for the RTM, the application of the method to WAS data without making any assumptions of the type of waves that propagate, is scarcely done, and it can be a efficient way to image the deeper crustal layers complementing other existing methods, or giving new insights to previous knowledge of the structure of the subsurface.

5.1. 3D Moho Gravity Inversion with seismic constraints

5.1.1. Concepts and principles

Two of the most used geophysical methods to study the deep crustal layers is Gravity and Seismic.

Gravity is a potential field that varies both spatially and temporally. It is a versatile geophysical technique to detect and identify subsurface bodies that generates anomalies within this field. Retrieving the structure of these bodies is not straightforward and there are several corrections and processes that should be taken into account.

Seismic instruments measure deformations generated by waves propagating through the different materials that compose the Earth. The sources of those waves can be natural (earthquakes) or controlled (air-gun shots, for example). There are several types of propagating waves and their behavior depends on the material that they propagate trough. As in gravity method, retrieving the complex structure of the Earth from the application of seismic methods requires careful processing and the interpretation may not straightforward .

Following the Newton’s law for gravity, every particle with mass attracts every other particle in the universe with a force that is proportional to the product of their masses and inversely proportional to the square of the distance between their center. That force of attraction can be measured on every point on Earth. However, the measured value is influenced by several factors since the Earth structure is not homogeneous, it has translation and rotation movement and is not a perfect sphere.

The Bouguer anomaly (named after Pierre Bouguer) is the gravitational attraction that remains after correcting the measured raw gravity value for the elevation at which it is measured and a theoretically calculated attraction. It allows to study the effect/contribution of a particular mass in the subsurface and characterize its structure, in our case the Moho at the base of Earth's crust.

In the methodology of Uieda and Barbosa (2017) the first calculation to be done is the removal of a theoretical scalar gravity calculated at the point P of measurement but for an ellipsoidal reference Earth – ɣ(P). This effect is calculated according to the closed-form solution presented in (Li and Götze, 2001):

$$\delta(P)=g(P)-\gamma(P) \qquad (5.1.1.1)$$

$$\delta_{bg}(P)=\delta(P)-g_{topo}(P) \qquad (5.1.1.2)$$

Equation (5.1.1.1) gives the gravity disturbance (δ(P)) by subtracting measured raw gravity value (g(P)) and calculated gravity for a reference Earth (ɣ(P)) at the point P. Equation (5.1.1.2) then gives the full Bouguer anomaly (δ_{bg}(P)) – gravity disturbance (δ(P)) minus gravitational effect of the topography (g_{topo}(P)).

To calculate gravitational effects to be removed such as the topography or any other layer the equation used is similar to the Bouguer simple reduction:

$$g_{layer}(P)=2\pi\rho GH \qquad (5.1.1.3)$$

where the thickness (H) and density (ρ) of a layer is multiplied by the gravity constant (G).

The code by Uieda and Barbosa (2017) takes into account the sphericity of the Earth using spherical prisms called tesseroids (Figure 5.1.1.1) in a geocentric coordinate system.

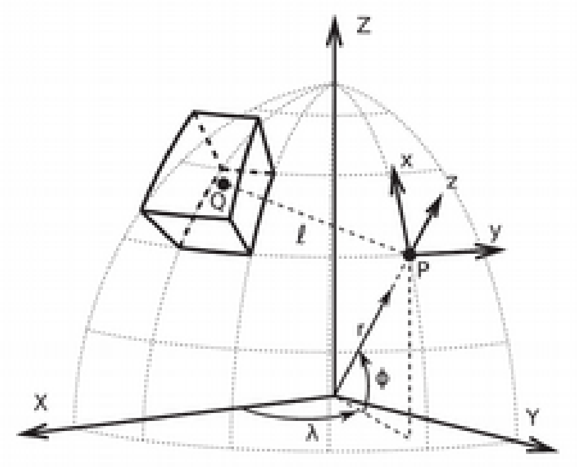

Figure. 5.1.1.1 - Sketch of a tesseroid (spherical prism) in a geocentric coordinate system (X, Y, Z). Observations are made at point P with respect to its local north-oriented coordinate system (x, y, z). After Uieda, L & Barbosa, V., 2017

The tesseroids used to calculate the gravitational effects are calculated numerically using Gauss-Legendre quadrature integration – GLQ – (Asgharzadeh et al., 2007). The accuracy of the GLQ integration is improved by the adaptive discretization scheme of Uieda et al. (2016).

Forward Problem

To solve the forward problem the Moho is discretized into a grid of M_{lon} X M_{lat} = M of juxtaposed tesseroids(Uieda and Barbosa, 2017). The depth of the true Moho varies with respect to the depth of the Moho of reference(zref). If the true Moho is above the reference level, the top of the kth tesseroid is the Moho depth z_k, the bottom is z_{ref}, and the density contrast (Δρ) is positive. Reversely, if the true Moho is below z_{ref}, the top of the tesseroid is z_{ref}, the bottom is z_k, and Δρ is negative.

Taking into account that the absolute value of the density contrasts of the tesseroids is a fixed parameter, the predicted Bouguer gravity anomaly disturbance of the Moho is a nonlinear function of the parameters z_k, k=1, 2, …, M that can be written as:

$$d_i = f_i(\mathbf{p}) \qquad (5.1.1.4)$$

where d_i is the ith element of the N-dimensional predicted data vector d, **p** is the M-dimensional parameter vector containing the M Moho depths (z_k), and f_i is the ith nonlinear function that maps the parameters onto the data. The function f_i are the radial component of the gravitational attraction of the tesseroid Moho model.

Inverse Problem

The inverse problem consists in estimating the parameter vector **p** from a set of observed gravity data d_0. It uses a least-squares scheme that minimizes the data-misfit function:

$$\phi(\mathbf{p}) = [\mathbf{d}^0-\mathbf{d}(\mathbf{p})]^T[\mathbf{d}^0-\mathbf{d}(\mathbf{p})] \qquad (5.1.1.5)$$

The function $\phi(\mathbf{p})$ is nonlinear with respect to **p**. Thus, the determination of its minimum can be done by using a gradient-base iterative optimization methods like Gauss-Newton or Steepest Descent. These methods start from an initial approximation to the model parameter vector $\mathbf{p}^0$ and estimate a parameter perturbation vector $\Delta\mathbf{p}^0$. The procedure is repeated until a minimum of the function $\phi(\mathbf{p})$ is reached. For the Gauss-Newton method, the parameter perturbation vector is obtained by solving a linear system including the gradient vector and the Hessian matrix both dependent of the Jacobean or sensitivity matrix.

Bott's method, regularization and tesseroids

To estimate the Moho depth in spherical coordinates, Uieda and Barbosa (2017) use a regularized version of Bott's method (Bott, 1960) to invert gravity data. The adaptation to spherical coordinates passes by the replacement of the right-rectangular prisms with tesseroids in the forward modeling . The tesseroid forward modeling uses the adaptive discretization algorithm of Uieda et al. (2016) to achieve accurate results. The inverse formulation minimizes a goal function using the Gauss-Newton method but replaces the full Jacobean matrix with the Bouguer plate approximation while stabilizing the solution through the well-established formalism of Tikhonov regularization (see Uieda and Barbosa, 2017). The inverse problem in implemented iteratively until the inversion residuals $\mathbf{r}^k = \mathbf{d}^o - \mathbf{d}(\mathbf{p}^k)$ fall below an assumed noise level of the data.

Estimating the inversion hyper-parameters

There are three hyper-parameters described by (Uieda et al., 2016) that influence the inversion problem: the regularization parameter (μ), the density contrast ($\Delta\rho$) and the depth of the reference Earth Moho or reference level (z_{ref}). The first one is related with the Cost-function that balances the obligation for a certain degree of smoothness of the result model and the fit of that same result to the real data. The second one is the density difference between the two layers in analyses. The third is the depth that is considered as Normal Earth Moho depth, meaning that is the depth considered as reference and at which the Moho depth anomalies revolve. These hyper-parameters are estimated in two steps: first μ is estimated by using fixed values for Δρ and z_{ref} and preform a hold-out cross validation procedure (Handsen, 1992); Secondly, the estimated μ is used to preform a validation procedure to estimate the other two parameters.

Uieda and Barbosa suggest a procedure to estimate hyper-parameters in two steps. The first one is to perform a hold-out cross-validation procedure (Hansen, 1992) to estimate an optimal value for μ, by assuming fixed values for z_{ref} and Δρ. The second step is to use the estimated μ to perform a validation procedure to estimate z_{ref} and Δρ.

To estimate μ, the hold-out method of cross-validation (Kim, 2009) is applied. The method consists of splitting the observed data set into two independent parts: a training set and a testing set. The training set is used in the inversion while the testing set is kept back and used to judge the quality of the chosen value of μ. For a value of the regularization parameter μ_n, the training set is inverted using μ_n to obtain an estimate $\mathbf{p}^n$. This estimate is used to calculate predicted data on the same points as the testing set via forward modeling:

$$\mathbf{d}^n_{test}=\mathbf{f}(\mathbf{p}^n) \qquad (5.1.1.6)$$

μ_n, is evaluated by the mean square error (MSE) of the misfit between the observed and predicted testing data sets:

$$MSE_n=\frac{\|\boldsymbol{d}^0_{test}-\boldsymbol{d}^n_{test}\|^2}{N_{test}} \qquad (5.1.1.7)$$

in which N_{test} is the number of data in the testing set. The optimal value of μ will be the one that minimizes the MSE, that is, the one that best predicts the testing data.

The other two hyper-parameters – z_{ref} and Δρ – need to be estimated too. This can be done also by the cross-validation procedure described before. The estimation of these two parameters should be tested with respect to information independent of the gravity data, such as knowledge of Moho depths at certain points. These points will generally come from seismologic studies, like receiver functions, surface wave dispersion, and deep refraction experiments.

The algorithm for estimating z_{ref} and Δρ is the following (Uieda et al., 2016):

1. For every combination of $z_{ref,l} \in [z_{ref,1}, z_{ref,2}, \ldots, z_{ref,Nz}]$ and $\Delta\rho_m \in [\Delta\rho_1, \Delta\rho_2, \ldots, \Delta\rho_{Np}]$:

1.1. Perform the inversion on the training data set $\mathbf{d}^0_{inv}$ using $z_{ref,l}$, $\Delta\rho_m$, and the previously estimated value of μ. The inversion output is the vector $\mathbf{p}^{l,m}$.

1.2. Interpolate $\mathbf{p}^{l,m}$ on the known points to obtain the predicted depths, $\mathbf{z}_s^{l,m}$

1.3. Calculate the MSE between z^0_s and $z^{l,m}_s$ using:

$$MSE = \frac{\|\boldsymbol{z}_s^{\boldsymbol{0}} - \boldsymbol{z}_s^{(\boldsymbol{l},\boldsymbol{m})}\|^2}{N_s} \qquad (6.1.1.8)$$

2. The final solution is the $\mathbf{p}^{l,m}$ corresponding to the smallest MSE.

5.1.2. CRUST 1.0 model

Regarding the crustal model, we used the same one as in (Uieda et al., 2016), the CRUST1.0 model (Laske et al., 2013). This model has a 1.0x1.0º resolution and is the most recent global model of the sediment and crust layers of the Earth. The model is composed by 3 sediment layers, 3 crustal layers and 1 mantellic layer. For each layer there is a thickness value with exception to the last one. The model also contains the Moho discontinuity depth, Vp and Vs values and density values that correspond to each layer.

In Uieda and Barbosa code (2107) the Moho depth provided as input for the forward problem, can be given in two different ways: (i) as in (Uieda and Barbosa., 2017), as a Moho depth variable or (ii) as a set of thickness values corresponding to each layer above the Moho.

The research area in Uieda and Barbosa (2017) was the entire South American continent which makes the Moho variable a good approximation for the purpose of their study. However, for the present work, the research area is much smaller. We have chosen to work with the sum of the layers given by the model. Also, in order to match the resolution of the gravity data we over-sampled with a linear interpolation each of those layers to a 0.1x0.1 degrees grid. To understand the effects of summing up the layer thicknesses and/or interpolate the given values to obtain a finer grid, the following tests were developed:

- Plot of the sum of the thickness of each layer in CRUST1.0, without any interpolation – Figure 5.1.2.1;
- Plot of the sum of every layer thickness given in CRUST1.0 and interpolate over the sum – Figure 5.1.2.2;
- Plot of the sum of each interpolated layer thickness given in CRUST1.0 that match the Moho discontinuity depth – Figure 5.1.2.3;

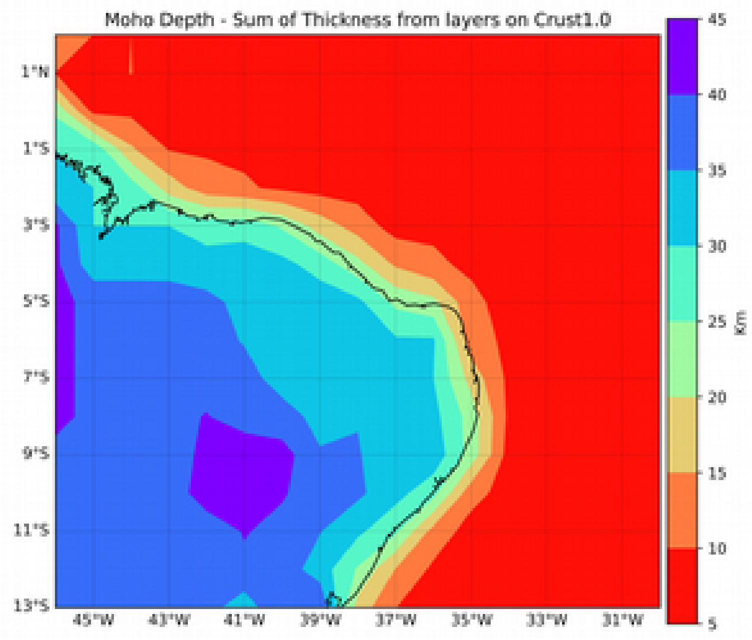

Figure 5.1.2.1 – Sum of layer thickness from Crust1.0 without interpolation.

If we do the sum of the thicknesses of each layer above the Moho discontinuity, as presented in Figure 5.1.2.1, we retrieve a range from 5 km to 45 km, going from deeper to shallower values with a trend SW-NE direction. The sharpness of the Land/Ocean transition, from 25/30 km to 5/10 km depth, in a few kilometers and such shallow depths for the Moho discontinuity in the marine environment are the two most concerning elements.

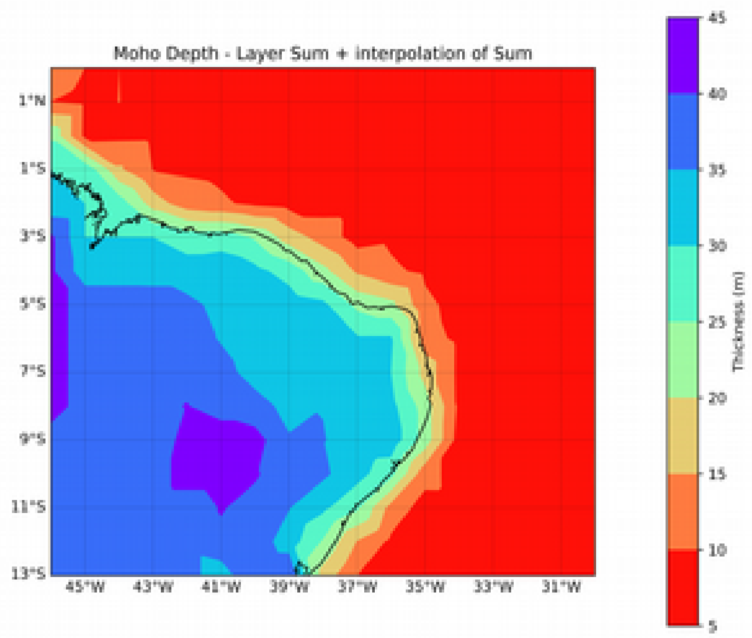

Figure 5.1.2.2 – Sum of each layer thickness given by CRUST1.0 and interpolation of the sum to obtain the Moho depth

By making the sum of the thicknesses of each layer and doing the interpolation over that sum, we obtain the result presented in Figure 5.1.2.2. The ranges and trends described for Figure 5.1.2.1 also apply to this Figure. The transition Land/Ocean extends a little more oceanward with Moho depths of 10-15 km.

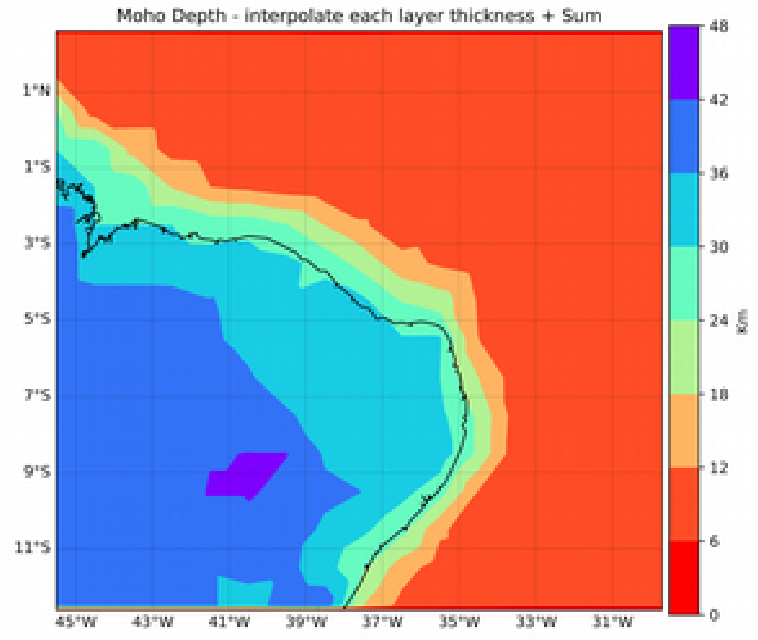

Figure 5.1.2.3 – Interpolation of each layer thickness given by CRUST1.0 and sum of the interpolated layers to obtain the Moho Depth

Finally, if we interpolate each layer and sum their values after, as presented in Figure 5.1.2.3, we obtain results for the Moho discontinuity depth that is quite similar to the original. The trend SW-NE is kept and the range is the same. The geometry and the transition Land/Ocean is smoother and extend for a larger horizontal distance. The values in the marine environment vary between [6 and 18] km which is a range that allows a smoother transition Land/Ocean. From this result it is clear that the interpolation has some effect over the original values. However it does not create artifacts or structures that are not present in the original model.

Being aware of the limitations of the original model and also the effects of the interpolations, we have chosen to work with the interpolation of each layer to a grid of 0.1x0.1 degrees and their summation in the end. From the analysis previously done, this is the one that keeps the major features of the original model grid but also have a smoother geometry without introducing artifacts related with the interpolation. However, it is necessary to keep in mind that the

Land/Ocean transition is still quite sharp and that the values for the marine environment are also probably too shallow.

5.1.3. Seismic data source for Moho depths

We used seismic Moho depths published by (Rivadeneyra Vera et al., 2019) that update an initial compilation made by (Assumpção et al., 2013). They come from several sources: (i) seismic refraction experiments; (ii) receiver function and (iii) surface-wave dispersion analyses. We included in this this set of points with values coming from our marine seismic refraction experiments – MAGIC and SALSA.

The compiled file structure has the following variables: 1) station ID; 2) Longitude (degrees); 3) Latitude (degrees); 4) Elevation (m); 5) Moho discontinuity depth (km); 6) Error associated (m). This file includes points for the entire South American continent. The points that concern the research area of this project are presented in Figure 6.1.3.1.

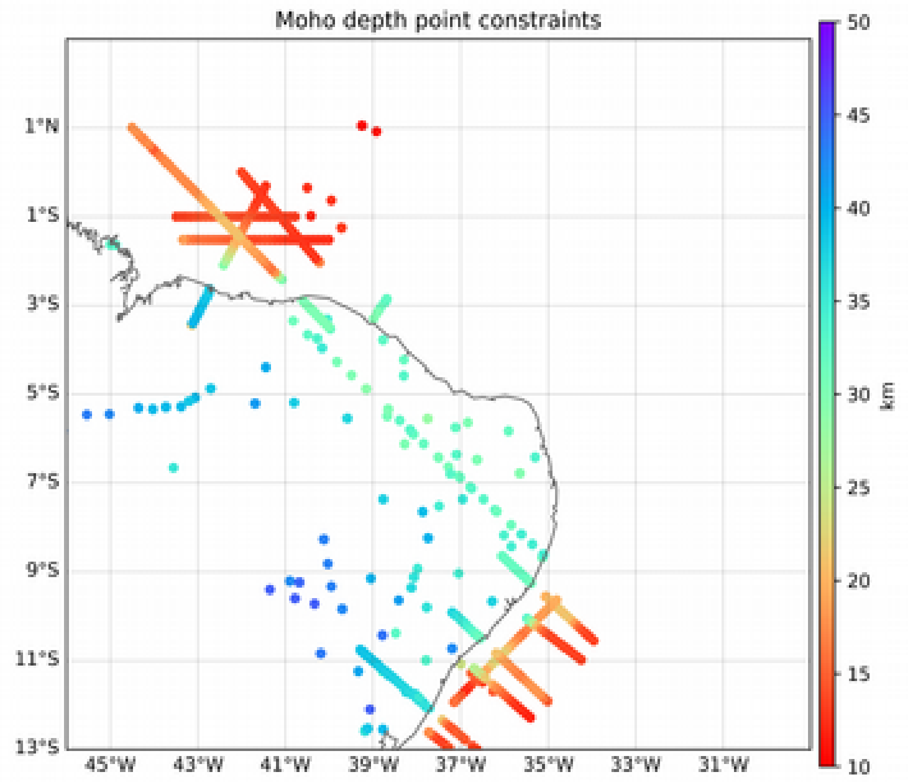

Figure 5.1.3.1 - Moho depths point constrains given by seismic experiments

5.1.4. Gravity data source

We used raw gravity data from the high-resolution gravity model SGG-UGM-2 (Liang et al., 2020), downloaded from the International Center for Global Earth Models (ICGEM) web-service (Barthelmes & Köhler 2012, http://icgem.gfz-potsdam.de/ICGEM/), in the form of the complete gravity field on a regular grid with 0.1° spacing for a square research area of 1666.5x1666.5 km.

As a potential field data set, a gravity grid includes both a high frequency content where signal from shallow structures dominates and lower frequency signal coming from deeper structures. Depending on the targeted structure, the height of the chosen gravity grid is essential since the frequency bandwidth that dominates is related with the targeted structures. Four different grids were tested – 0 km, 25 km, 50 km and 75 km – that are represented on Figure 5.1.4.1.

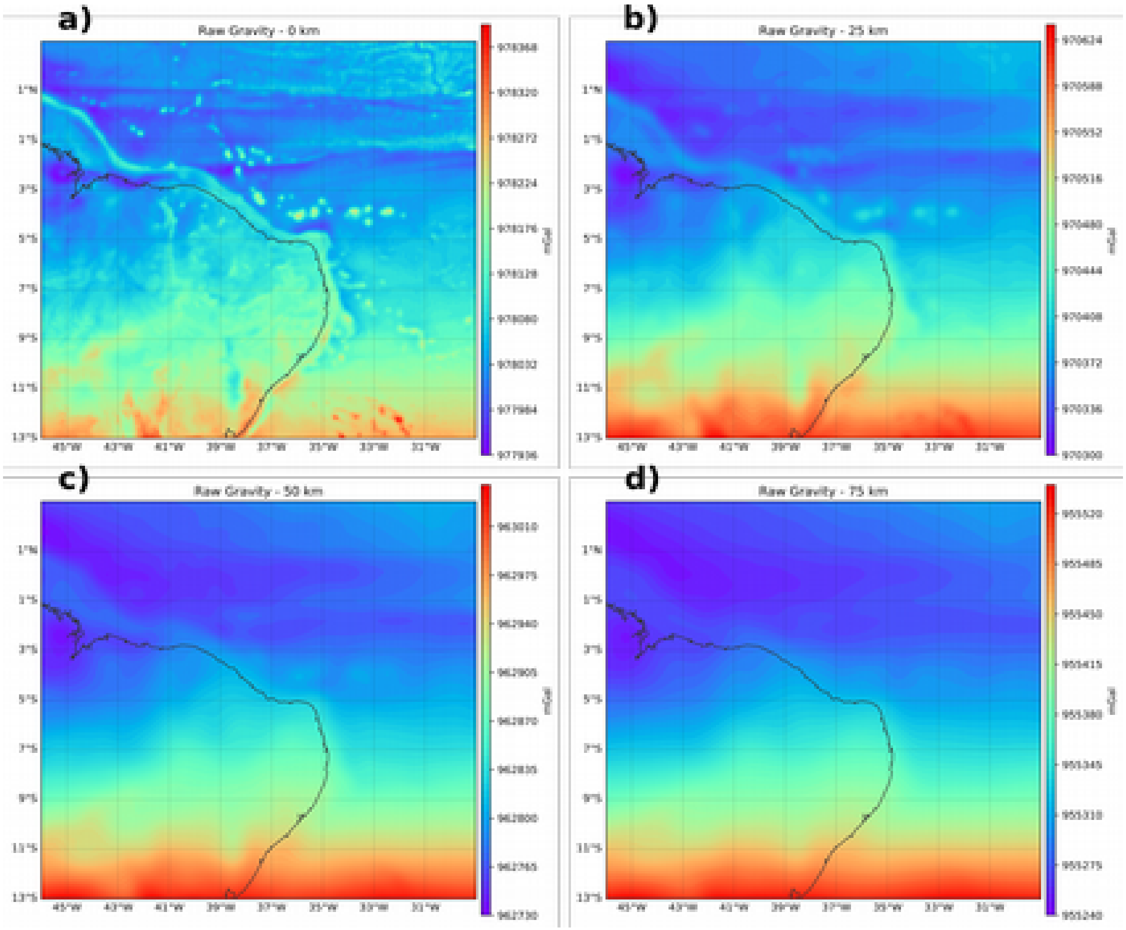

Figure 5.1.4.1 – Different raw gravity data grids at: a) Ground level – 0km b) 25km altitude; c) 50km altitude; d) 75 km altitude

Comparing the different gravity grids in Figure 5.1.4.1 illustrates the relationship between the dominant frequency band and the structures at the subsurface. The 0 km grid has a high frequency content related with smaller and shallower structures and, as we move in altitude, the frequency content becomes lower and related with deeper and larger structures. In Figures 5.1.4.2 and 5.1.4.3 we present the obtained results for the hyper-parameters for each gravity grid in order to test their potential influence on the gravity inversion.

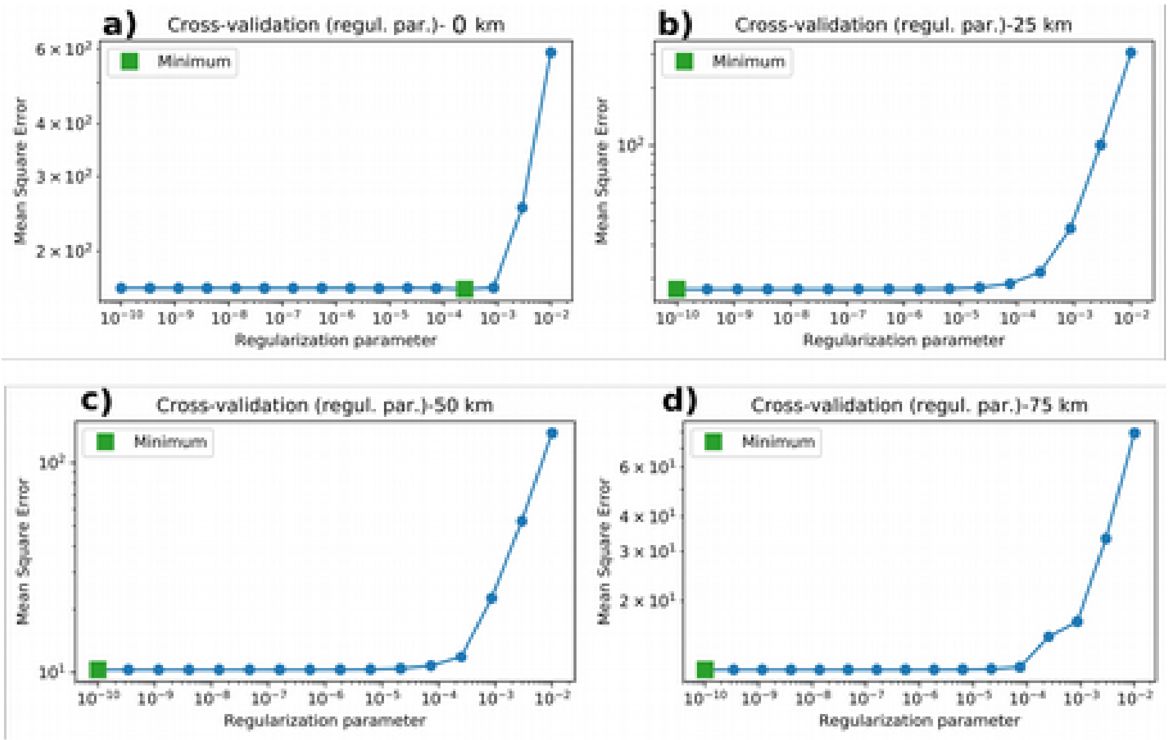

Figure 5.1.4.2 – Results for the regularization parameter (μ) for each gravity grid tested: a) 0 km; b) 25 km; c) 50 km and d) 75 km

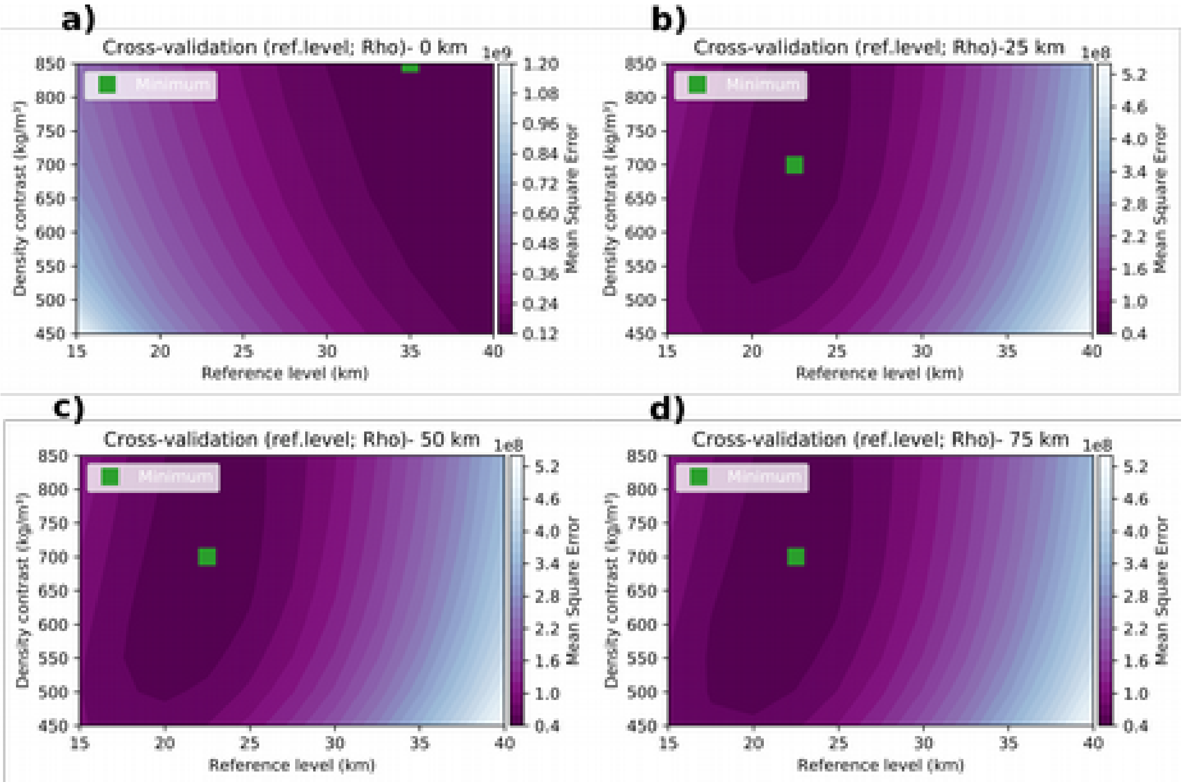

Figure 5.1.4.3 – Results for the reference level (Δz_{ref}) – horizontal axis – and density contrast (ρ) – vertical axis – for each gravity grid tested: a) 0 km; b) 25 km; c) 50 km and d) 75 km

Regarding the regularization parameter (µ) we obtain an asymptotically convergence of the mean square error for all the grids but the error associated to the 0 km grid (Figure 5.1.4.2-a) is higher then the others, that contain the same error range. Regarding the reference level (Δz_{ref}) and the density contrast (Δρ), the 0 km grid returns values completely out of the considered range, making this grid unfitted for the method. For the other 3 grids (Figure 5.1.4.3-b – 25 km; Figure 5.1.4.3-c – 50 km; Figure 5.1.4.3-d – 75 km) we obtain the same reference level (Δz_{ref}) – 22.5 km – and the same density contrast – 700 kg/m³. In spite of returning a specific value for the density contrast, these plots shows similar error value for a large range of density contrasts - 475 kg/m³ to 850 kg/m³. This can be explained by the complex geology of our research area that include different structures of variable densities. Also, further in this chapter, we will show the variability of the density contrast associated with the model used (CRUST1.0) that contributes to this uncertainty.

Given the results for the hyper-parameters, apart from the 0 km grid, we can not exclude any of the others based on the quality of those hyper-parameters. In this case and given the already exposed explanation that as we move in altitude the gravity signal is filtered and consequently correlates with progressively bigger and deeper structures, we have chosen to work with the grid at 25 km altitude. This grid is the one that preserves with higher precision the gravity signal linked to the major geologic structures of the research area and that are known to have deep roots – São Francisco craton, Parnaíba basin and the Borborema plateau being good examples of those structures. These types of structures, along with the large fault zones systems in the area, have dimensions that are clearly inserted in the resolution of the gravity grid (0.1ºx0.1º – 11x11 km). In Figure 5.1.4.4 we present the gravity disturbance grid after applying the downward continuation with the approximate locations of the mentioned geological structures.

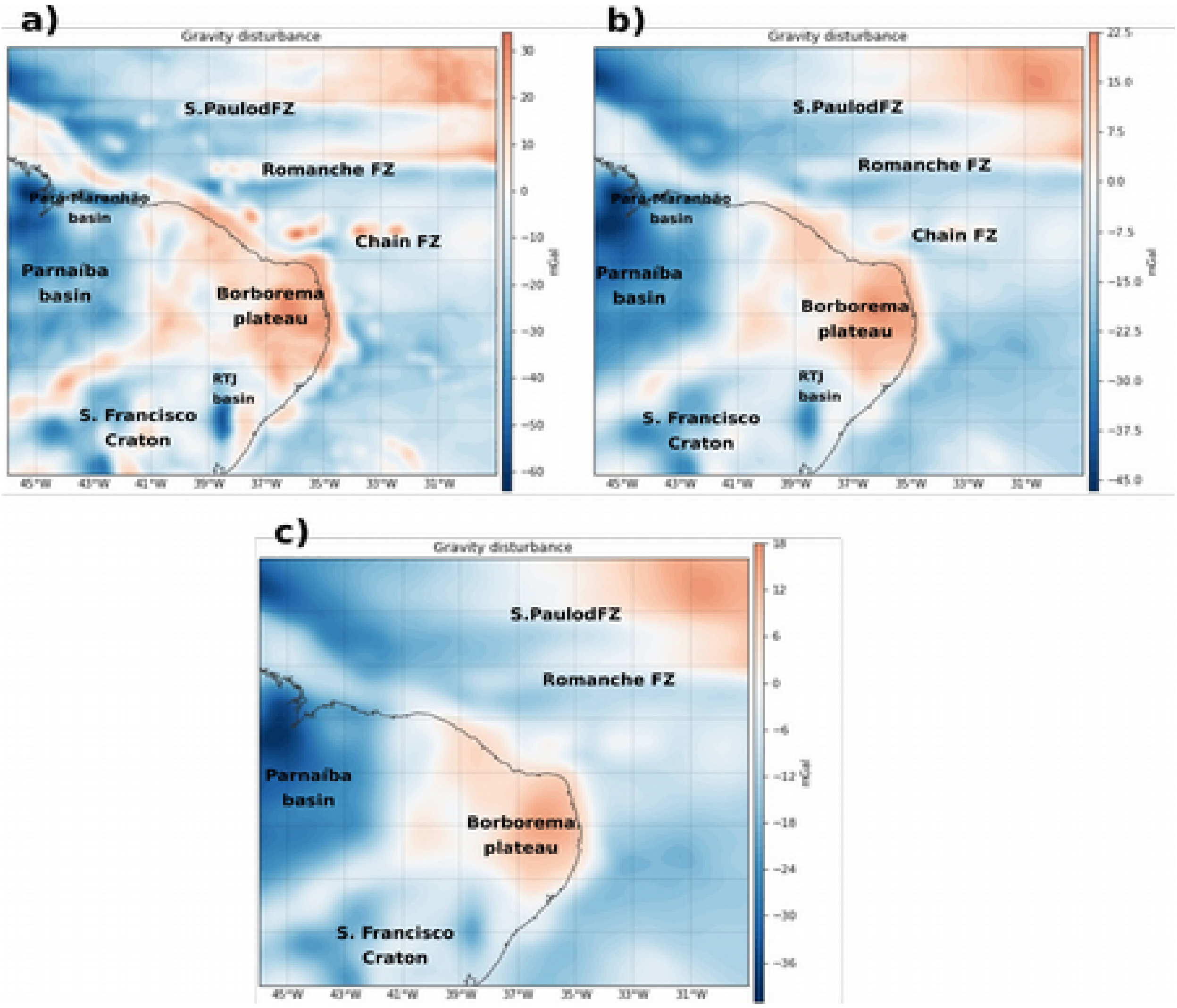

Figure 5.1.4.4 – Gravity disturbance grids for the research area obtained with applied downward continuation of: a) 25 km; b) 50 km; c) 75 km

From the raw gravity grid at 25 km height (Figure 5.1.4.1-a) we can observe a variation of 324 mGal between the minimum and maximum for the research area with a S-N trend. This trend is caused by the latitude variation where the values close to the Equator reach a minimum and increase with latitude. The fact that the Coriolis force is at its maximum at the Equator, has a negative impact on the gravity attraction because it acts in an opposing direction.

When the reference Earth correction is applied, we obtain the grid presented in Figure 5.1.4.4-a. The variation between the maximum and minimum values is of 90 mGal and the S-N trend vanishes completely. At this point we observe the clear influence of the big terrain structures like the chain of mountains and plateaus on land and the seamounts or volcanoes in the ocean. From this result, we move to the terrain correction.

6.1.5. Retrieve the Bouguer Anomaly

Gravity disturbance

As described previously, preceding the 3D inversion of the data, we need to calculate the Bouguer anomaly generated by the Moho for our research area. In practice the calculation of the gravity disturbance (Figure 5.1.4.4-a) using equation 5.1.1.1 is taking the measured values to the geoid level.

Simple Terrain correction

The terrain correction is about removing the topographic effect from the gravity signal. Because the research target is at regional scale and the raw gravity data is satellite measured, we do not need to apply the full terrain correction. In another words, we do not take into account the influence from topography of surrounding terrain to a particular measure as it would be done for full terrain correction but solely remove effect of land masses and the water layer. To calculate this correction using equation 5.1.1.3, we use topographic values from the ETOPO1 model at a 0.1x0.1° resolution and assume a density value of 2670 kg/m³ for land and -1630 kg/m³ for water – ρ_{water}-ρ_{rocks} = 1040-2670 = -1630 kg/m³. The Bouguer plate is an infinite flat plate with finite thickness and density value. Where excess of mass (for example, a chain of mountains) exits the terrain correction is thus positive while a lack of mass (for example, the water layer) leads to a negative correction as observed on Figure 5.1.5.1. This correction is removed to calculate the Bouguer anomaly so that both excess and lack of mass will cancel out.

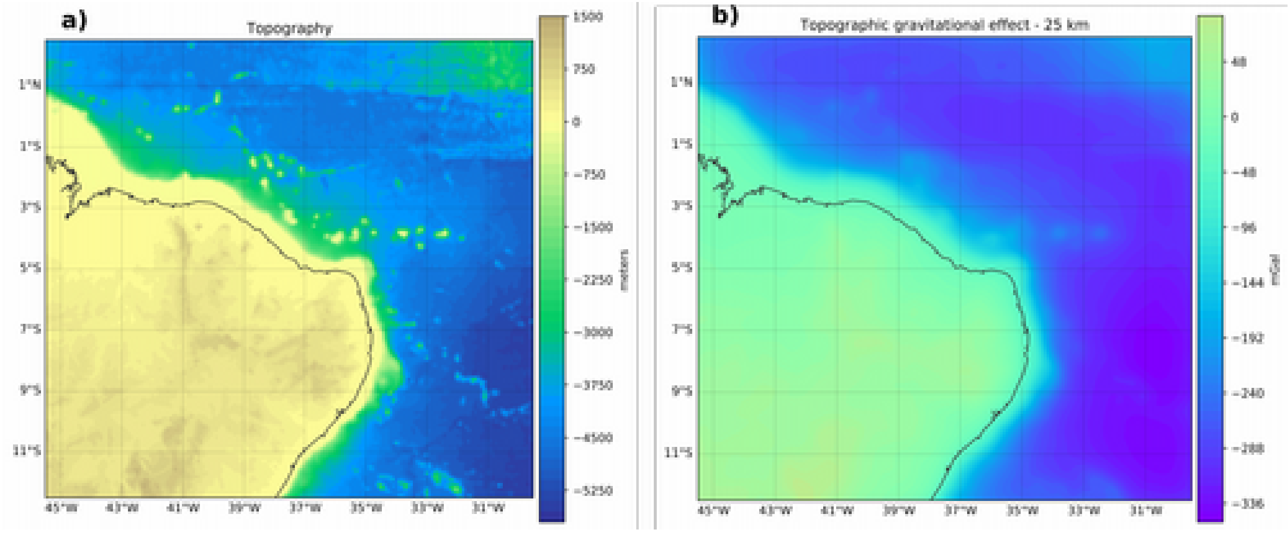

Figure 5.1.5.1 – a) Topographic grid with 0.1x0.1° resolution from ETOPO1 model, downloaded from ICGEM website; b) Topographic effect on the measured gravity values (mGal) – negative in the ocean environment and positive in the land environment

The Bouguer anomaly for our research area is shown in Figure 5.1.5.2 with a range of [-96; 336] mGal, being mainly negative on land and positive in the ocean and with a quite short horizontal transition at the margins.

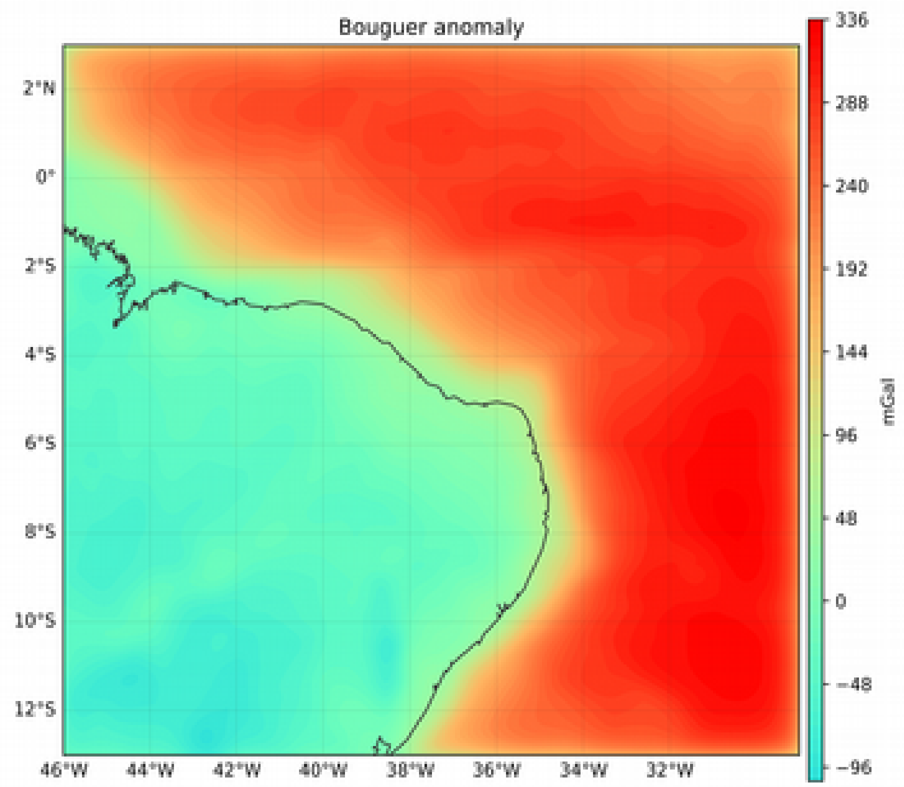

Figure 5.1.5.2 – Bouguer anomaly (mGal) for the research area

Bouguer anomaly for the Moho discontinuity

The calculation of the Bouguer anomaly that would correspond to a particular layer is explained in section 5.1.1. We first calculate the Bouguer simple correction for that layer (equation 5.1.1.3), with density and thicknesses values that correspond to that layer. Secondly, we remove that effect from the full Bouguer anomaly value by using equation 5.1.1.2. These calculations are done to each layers above the Moho discontinuity that is considered by CRUST1.0 model in a layer-striping approach.

The CRUST1.0 model considers 3 sedimentary layers and 3 crustal layers, above the Moho discontinuity. For the research area, the thicknesses of each those layers are presented in Figures 5.1.5.5 and 5.1.5.6 – sedimentary and crustal layer thickness respectively.

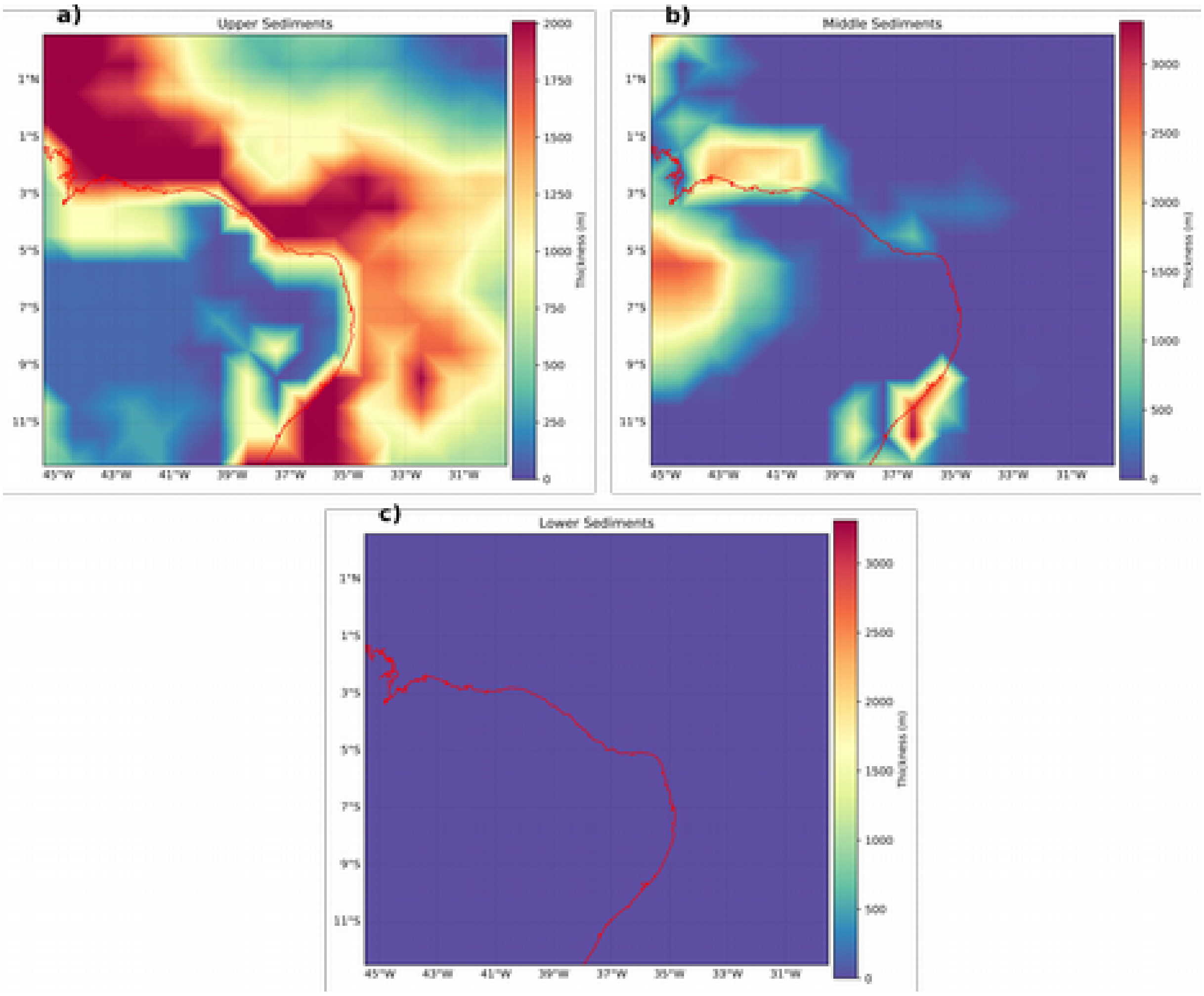

Figure 5.1.5.3 – Thicknesses of each sediment layer given in CRUST1.0 model (m). a) Thickness of upper sediments (m); b) Thickness of middle sediments (m); c) Thickness of lower sediments (m)

For the research area we can see that only the first two layers of sediments need to be considered. The middle sediments layer add up to the upper sediment layer for the offshore of Pará-Maranhão and Barreirinhas basin, the Amazon river mouth, the bay close to S. Luís do Maranhão, Ilha de Santana, S. Francisco river mouth and Alagoas basin. For example, with this two layers, the offshore of Pará-Maranhão and Barreirinhas basins comprise almost 4500 m of sediments.

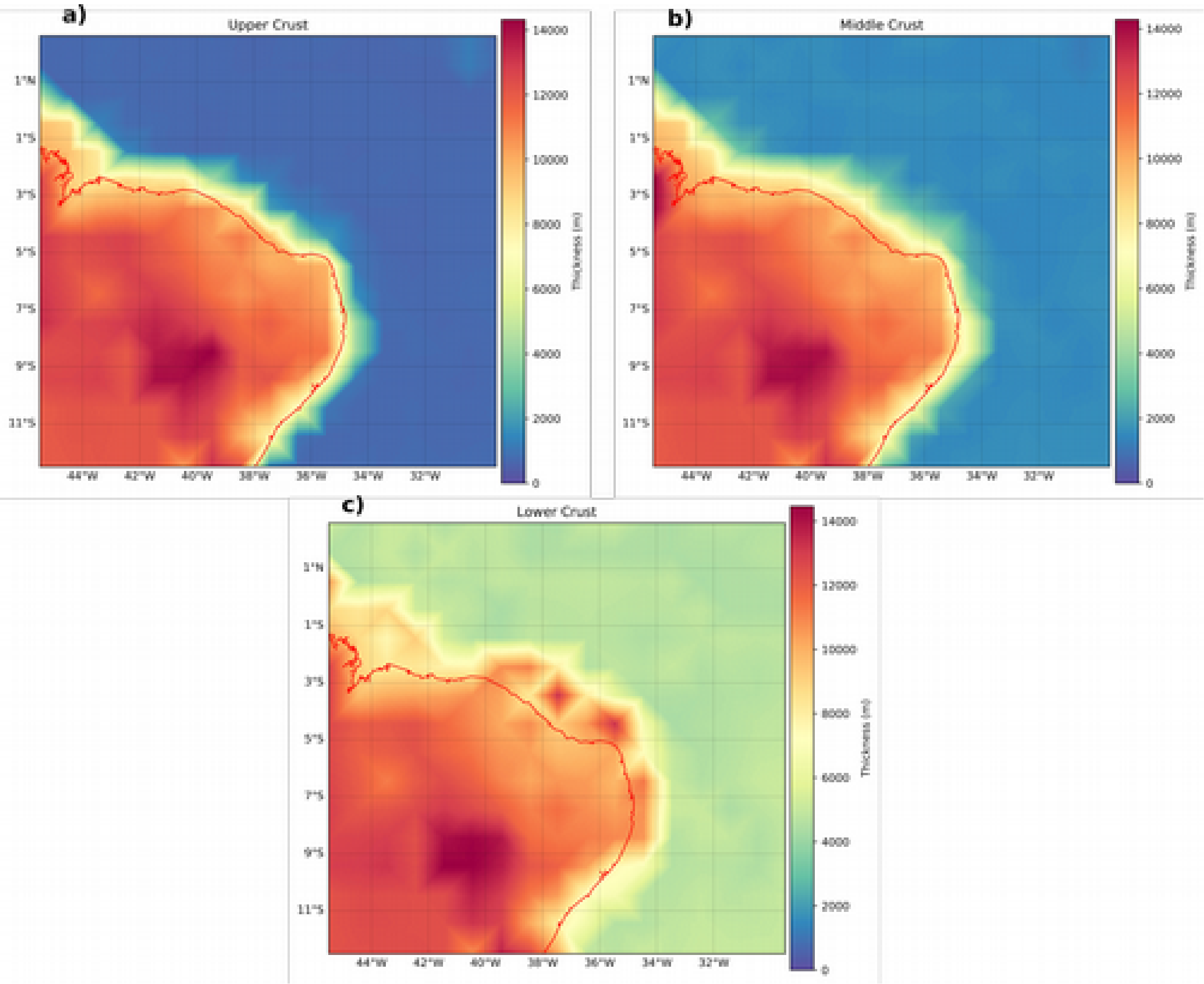

Figure 5.1.5.4 – Thicknesses of each crustal layer given in CRUST1.0 model (m). a) Thickness of upper crust (m); b) Thickness of middle crust (m); c) Thickness of lower crust (m)

Regarding the crustal layers (Figure 5.1.5.4), all three layer thickness need to be taken into account. All the crustal layers present a clear contrast land/ocean with very thick continental crust (reaching 14 km depth at certain locations), thin oceanic layers (between 0 km and 4 km depending on the layer) and a short horizontal transition between the two environments. Adding up the thicknesses of the three crustal layers, we end up with a continental crust that varies between 26 km and 42 km, an oceanic crust that varies between 2 km and 6 km and a transitional crust that varies between 18 km and 26 km.

The research area has a very complex geology with units and structures that range from the Archean to the Cretaceous age. This complexity explains the large variation of the thickness of the crustal layers.

The variation of the density values for the same layers are presented in Figures 5.1.5.5 and 5.1.5.6. These values are also taken from the CRUST1.0 model.

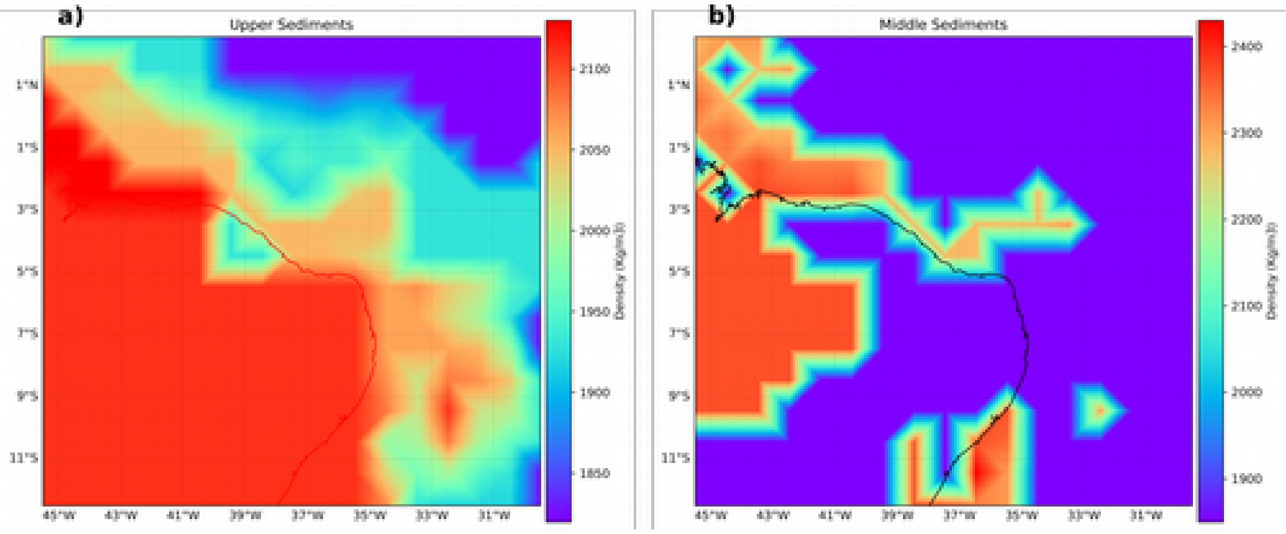

Figure 5.1.5.5 – Density of each sediment layer given in CRUST1.0 model (Kg/m^3). a) Density of the Upper sediments layer (kg/m^3); b) Density of the Middle sediments layer (kg/m^3)

The density distribution for the two sediment layers ranges between [1850; 2100] Kg/m^3 for the upper layer and [1900; 2400] Kg/m^3 for the middle layer. While we have a SW-NE trend of decreasing density for the upper layer, for the middle layer we have denser sediments in the same areas where they are thicker and that correspond two known basin – Parnaíba or Alagoas/Sergipe, for example.

Where there is no information regarding density values for a particular layer considered by CRUST1.0 model, by default, 0 Kg/m^3 is the value considered by the model. This means that very sharp variations and high contrasts of density would happen for several points within the area and, as consequence, create artifacts. To solve or diminish this problem but, at the same time, avoid to create other artifacts, the empty density values where replaced by the minimum value found within a particular layer. By doing that, the contrast between neighboring points is smoothed without adding new potential artifacts.

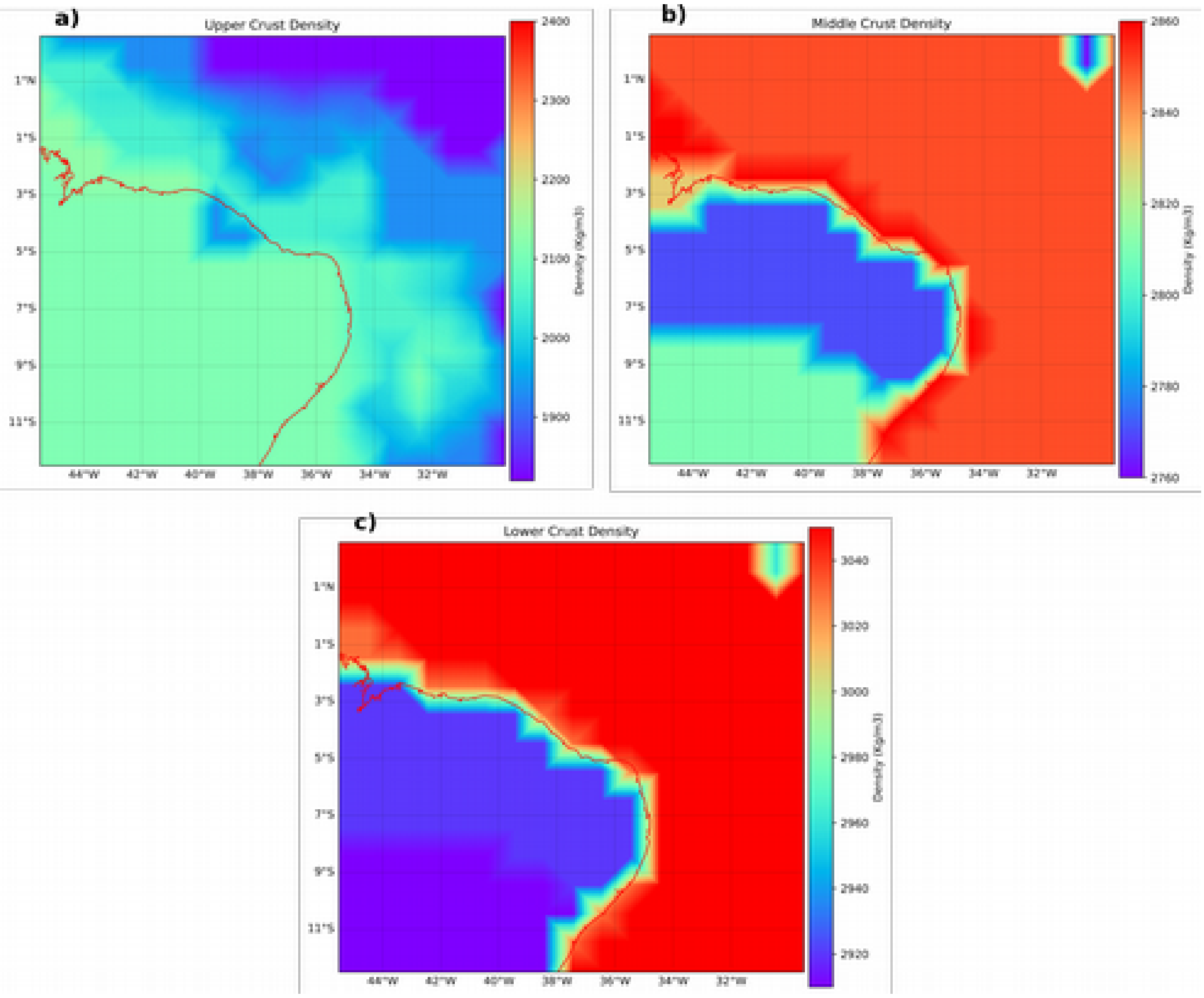

Figure 5.1.5.6 – Density of each crustal layer given in CRUST1.0 model (Kg/m^3). a) Density of the Upper Crust layer (kg/m^3); b) Density of the Middle Crust layer (kg/m^3); c) Density of the Lower Crust layer (kg/m^3)

For the density distribution of the crustal layers, three principal characteristics need to be mentioned – for the upper layer we have a trend SW-NE of progressively less denser crust that varies between [1900; 2400] Kg/m^3; the middle and lower crust present a clear continent/ocean contrast, being the continental crust less dense; and for the middle crust, the density for the Parnaíba and Borborema area is lower then the continental structures to the south.

The Figures 5.1.5.7 and 5.1.5.8 correspond to the density contrast considered to each layer. This contrast is found by considering a reference density value for each layer and subtract to this value the density in each point of the grid. There is no reason to consider different reference density values for different sediment layers since we have a resolution of 0.1x0.1° (about 10 km x 10 km) and do not have precision within the data to consider small density differences between sediment layers. So we have considered a reference value for all the sediments layers – 2670 Kg/m³ – and another to all the crustal layers – 3050 kg/m³. Is this density contrast that allows to calculate the gravitational effect of each layer or, in another words, what is the contribution to the Bouguer anomaly of a particular layer.

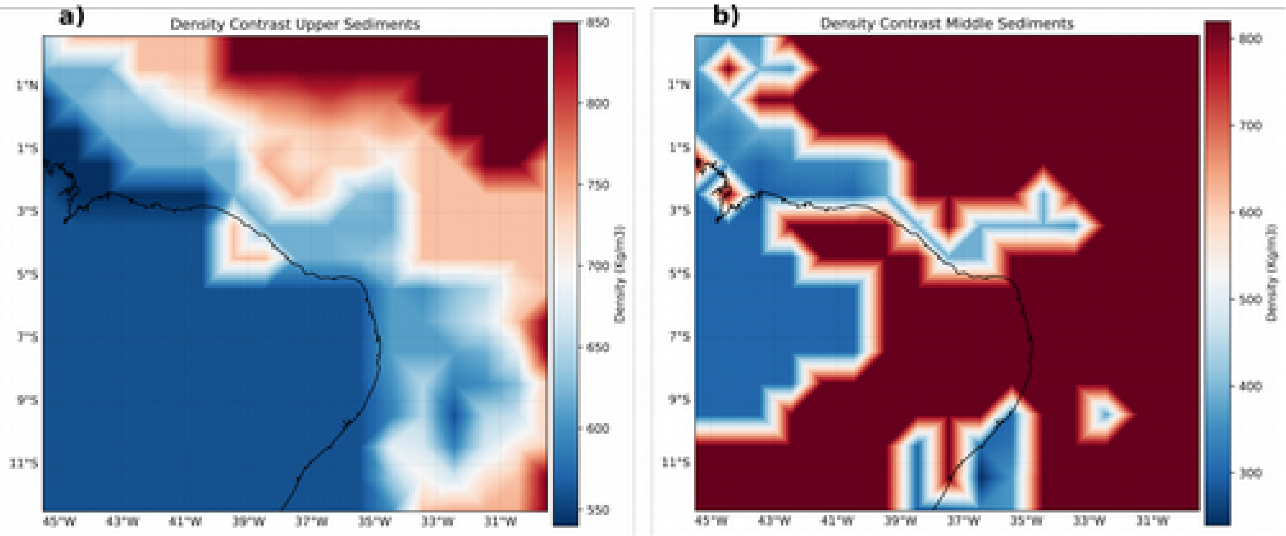

Figure 5.1.5.7 – Density Contrast of each sediment layer – Reference Density value of 2670 kg/m³. a) Density Contrast of the Upper sediment layer (kg/m³); b) Density Contrast of the Middle sediment layer (kg/m³)

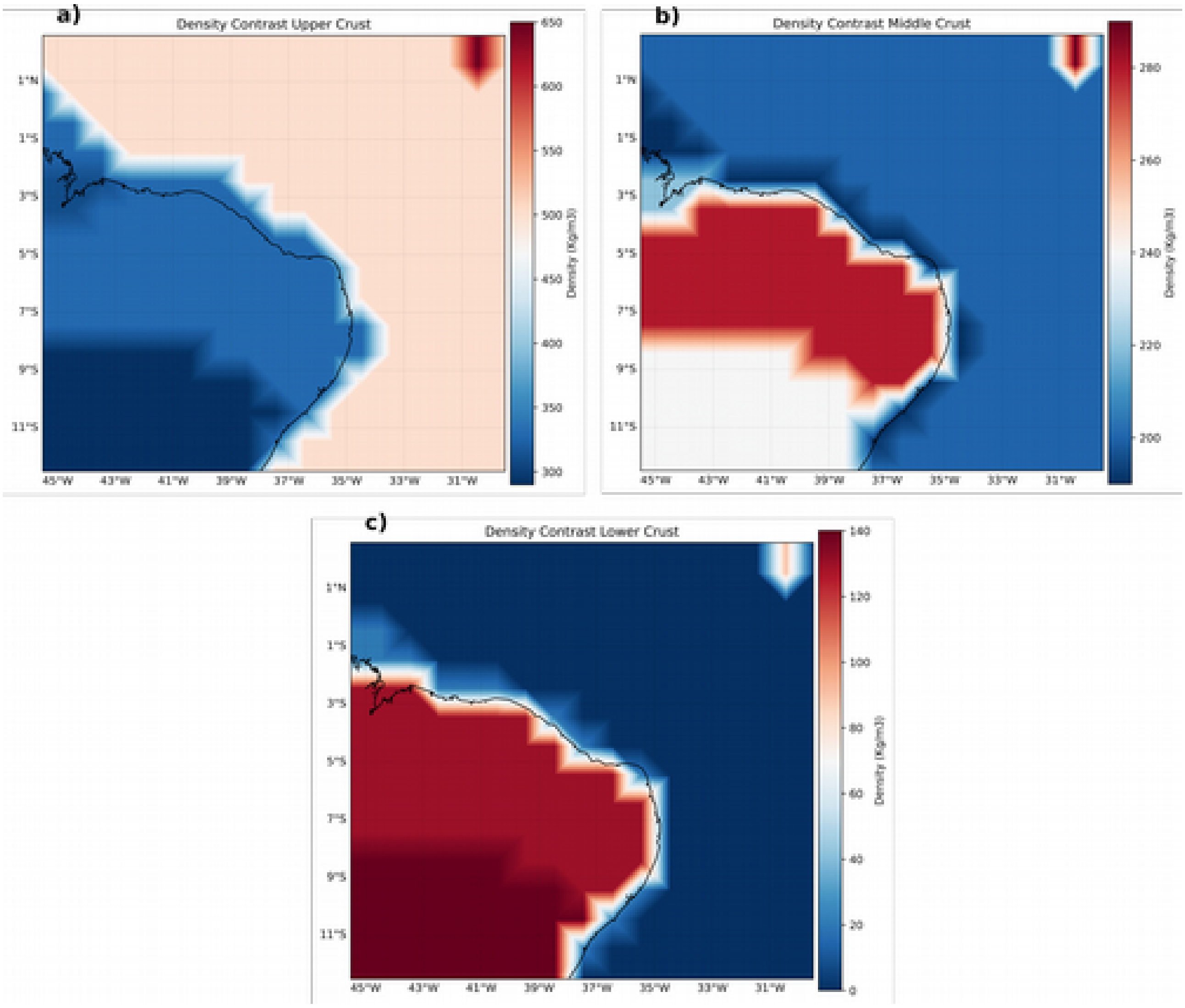

Figure 5.1.5.8 – Density Contrast of each crustal layer – Reference Density value of 3050 kg/m³. a) Density Contrast of the Upper Crust layer (kg/m³); b) Density Contrast of the Middle Crust layer (kg/m³); c) Density Contrast of the Lower Crust layer (kg/m³)

The distributions and trends related to the density contrast correspond, to each layer, to the ones described previously. Where we have higher values of density we have a lower contrast and were we have lower density values we have higher contrast. Following the density distribution, it is clear that the ranges for the density contrast are quite large either within sediments (550 kg/m³ between maximum and minimum value) as within crustal sediments (650 kg/m³, between maximum and minimum values).

The gravitational effect is calculated by equation 5.1.1.3 and is the value that corresponds to each layer and that will be subtracted to the full Bouguer anomaly so we can obtain the gravity anomaly values that correspond to the Moho discontinuity and the remaining material under it.

Figures 5.1.5.9, 5.1.5.10 and 5.1.5.11 correspond to the gravitational effect to each considered layer and the total gravitational effect for sediments and crust.

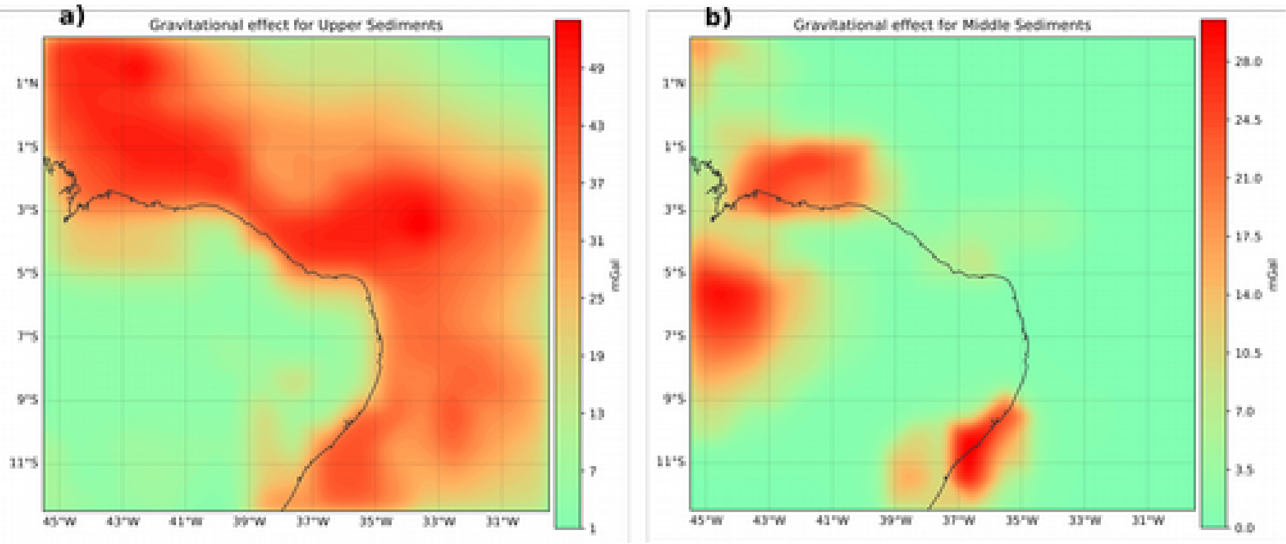

Figure 5.1.5.9 – Gravitational effect of each sediment layer (mGal). a) Gravitational effect of the Upper sediment layer (mGal); b) Gravitational effect of the Middle sediment layer (mGal)

The upper sediment layer has a gravitational effect that is stronger for the land/ocean transition, reaching values between 30 to 49 mGal. The gravitational effect of the upper sediments on continent is practically non existent, being coherent with the fact that there is no or a very thin layer in this area. Regarding the middle sediments layer, the relevant gravitational effect is clear for three areas – Parnaíba basin, Equatorial margin and Alagoas/Sergipe basin. These values – with a maximum of 28 mGal – will add up to the ones for the upper sediments and the total gravitational effect corresponding to the sediment layers will range between [1.5; 69.0] mGal, as shown in Figure 5.1.5.11-a.

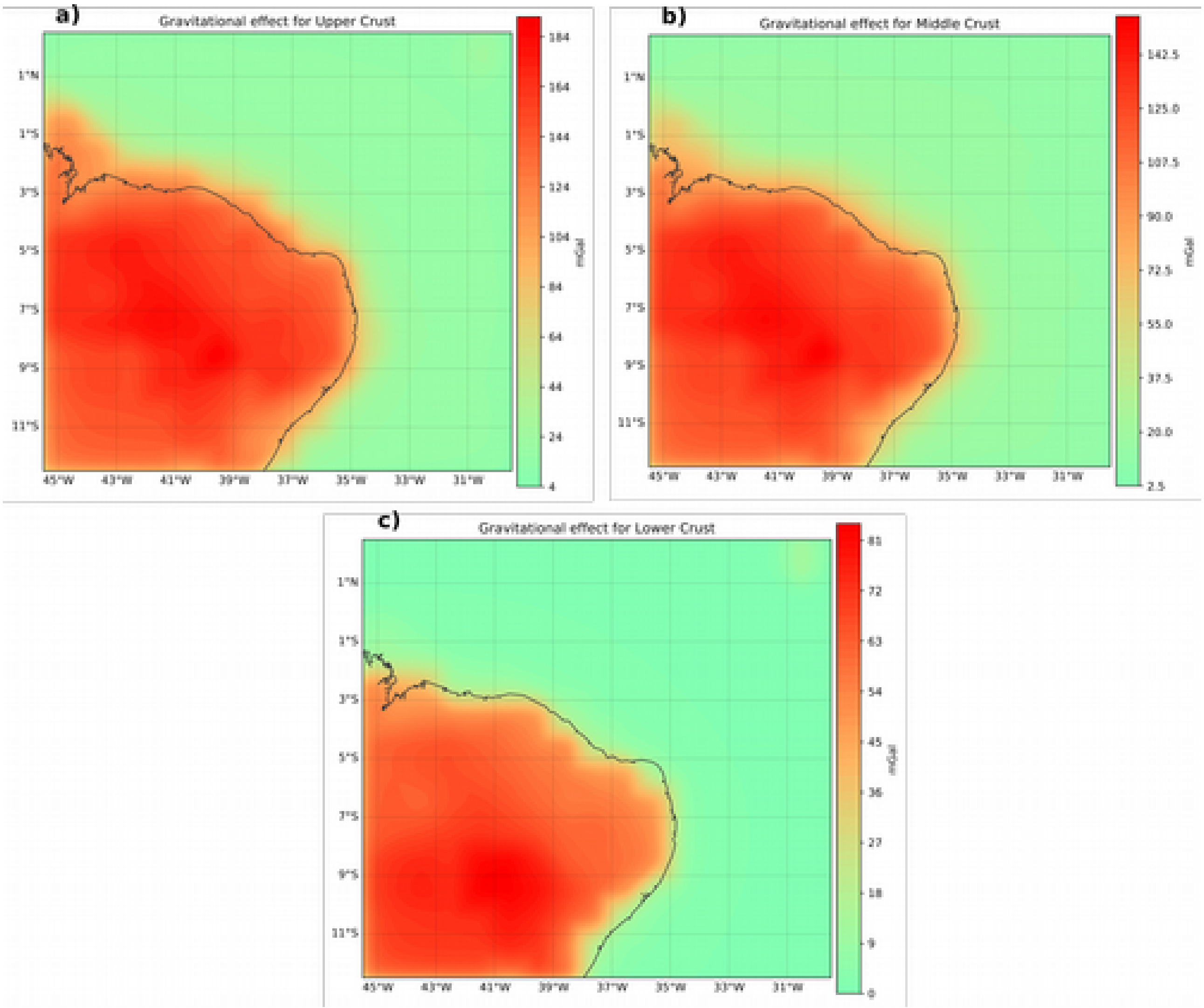

Figure 5.1.5.10 – Gravitational effect of each crust layer (mGal). a) Gravitational effect of the Upper crust layer (mGal); b) Gravitational effect of the Middle crust layer (mGal) ; c) Gravitational effect of the Lower crust layer (mGal)

Regarding the crustal layers, presented in Figure 5.1.5.10, the range of decreases from the upper crust to the lower crust, agreeing with the fact that we have similar thicknesses but progressively denser values. The gravitational effect of all the crustal layers can be described as a high contrast land/ocean with high anomaly values for the continent and very low or no value for the ocean. A feature to mention is the fact that upper and middle crust gravitational effect extends to the beginning of the transition zone while for the lower crust the variation is sharper, being the gravitational effect focused on the continent. When the gravitational effect of each crustal layer is added up, we obtain the total gravitational effect of the crust – Figure 5.1.5.11-b.

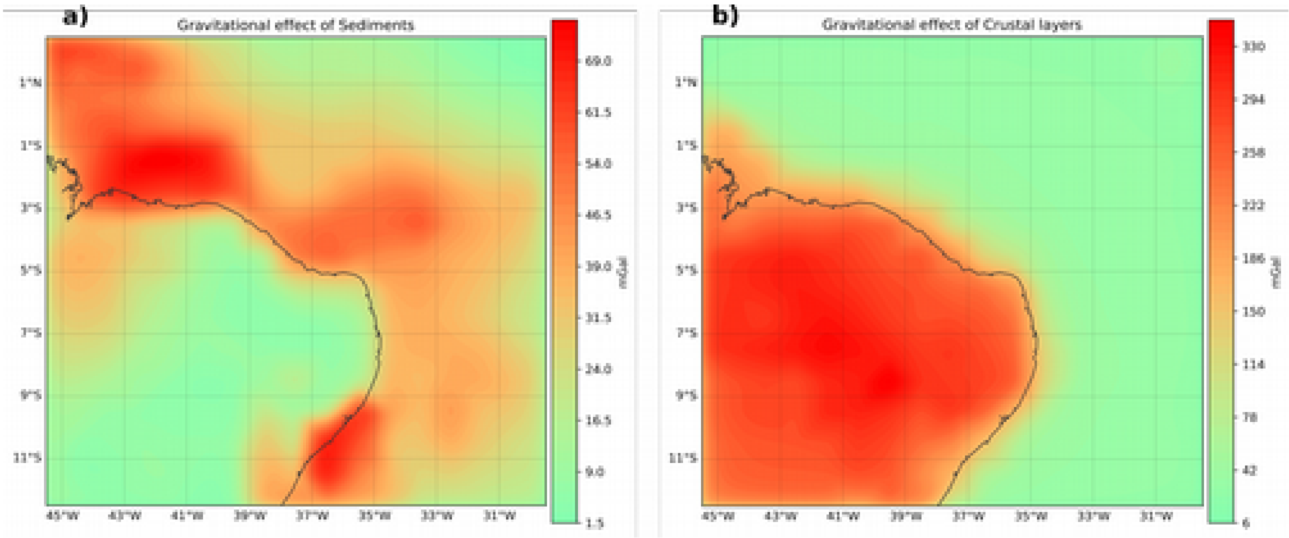

Figure 5.1.5.11 – Total gravitational effect of Sediments and Crust (mGal). a) Sum of all the sediment layers (mGal); b) Sum of all crustal layers (mGal)

In Figure 5.1.5.12 we present the Sediment free Bouguer anomaly (Figure 5.1.5.12-a) and the Sediment and Crust free Bouguer anomaly (Figure 5.1.5.12-b). These values are obtained using equation 5.1.1.2.

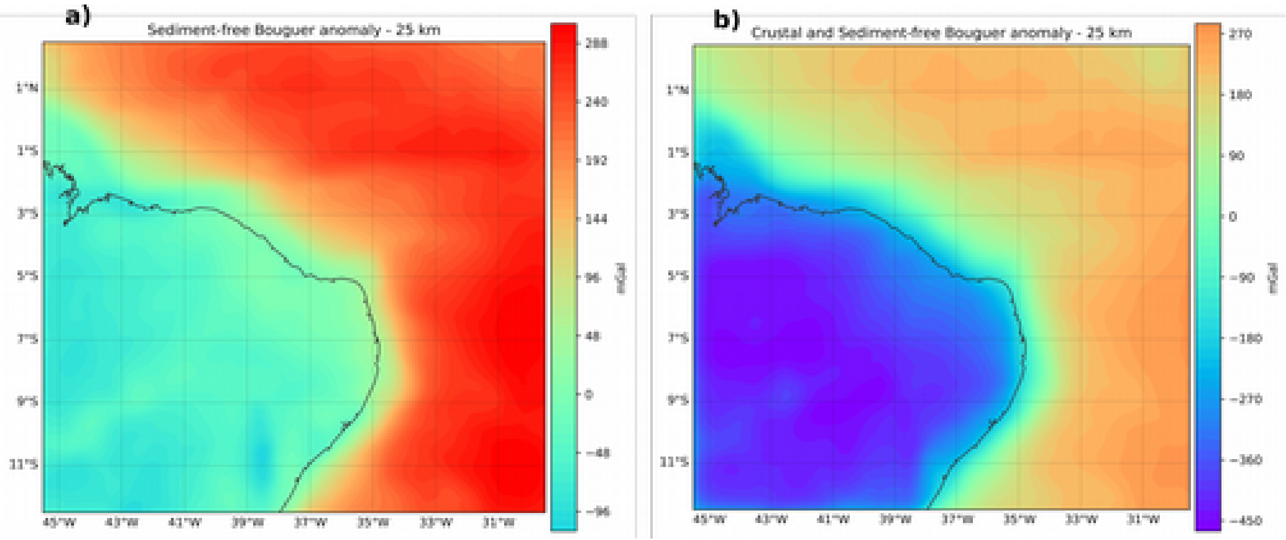

Figure 5.1.5.12 – Bouguer anomaly (mGal) for the studied area. a) Sediment free Bouguer anomaly (mGal); b) Sediment plus Crust free Bouguer anomaly (mGal)

The Bouguer anomaly obtained in Figure 5.1.5.12-b is the grid that will be used to perform the inversion and obtain the estimation of the depth of the Moho discontinuity. This grid contains the Bouguer anomaly that corresponds to the contribution of the masses distribution located around the reference Moho discontinuity.

When we remove the gravitational effect of the sediment layers, we obtain the grid in Figure 5.1.5.12-a. If we compare this grid with the one presented in Figure 5.1.5.2 we see that the sediment layers have a greater weight over the ocean environment, decreasing the maximum Bouguer anomaly from 336 mGal to 288 mGal. The removal of the gravitational effect of the crust has almost the opposite effect over the Bouguer anomaly, meaning that the maximum Bouguer anomaly decreases from 288 mGal to 270 mGal in the ocean environment but on land the minimum Bouguer anomaly decreases from -96 mGal to -450 mGal. The much larger thickness of the continental crust when compared with the oceanic one is the main explanation for this result.

5.1.6. Inversion setup and results

The concepts linked with the 3D inversion of the Bouguer anomaly with seismic constrain are described in section 5.1.1. In this section the practical steps taken are described and the results of the inversion will be presented. However a more detailed discussion of those results will be presented in the next chapter, Results and Discussion.

Having the Bouguer anomaly grid (Figure 5.1.5.12-b) and the seismic points (Figure 5.1.3.1), the first step of the inversion is to define the setup of the inversion. The area, the resolution of the grid, the high of the grid and the initial Moho depth are defined. The first two are the same as the ones used for the processing the gravity grid. The high of the grid is, in this case, 25 km since it provides the best wave-length resolution without degrading the hyper-parameters.

The Bouguer anomaly grid is split in two. One half is used to calculate the hyper-parameters and the other half is used to preform the inversion of the gravity data.

The inversion is preformed with the Gauss-Newton formulation, giving the tolerance value (0.2) and the maximum number of iterations (25).

A range of values is defined for each hyper-parameter. For the regularization parameter (μ) the range is log([-10; -2]) evenly spaced by a total of 16 values. This interval is chosen taking into account the asymptotically decrease of the mean square error. For the reference level parameter (Δz_{ref}) the range is [-45; 2.5; -15] km, meaning that 11 different depth values are tested. Finally, the density contrast parameter ($\Delta\rho$) have a range between [500; 50; 1200] Kg/m^3, comprising 14 different density contrast values tested.

The regularization parameter is calculated using 15 km as reference level and 600 kg/m^3 as density contrast. The estimated value is then use in the second cross-validation to find the density contrast and the reference level that better fit the data.

The obtained results to each combination is compared with the test data set and the best solution is the one with smallest cross-validation score. This solution will be used as the inversion solver for the next cross-validation – reference level and density contrast. Finally, the estimated models are scored against the seismic constrains.

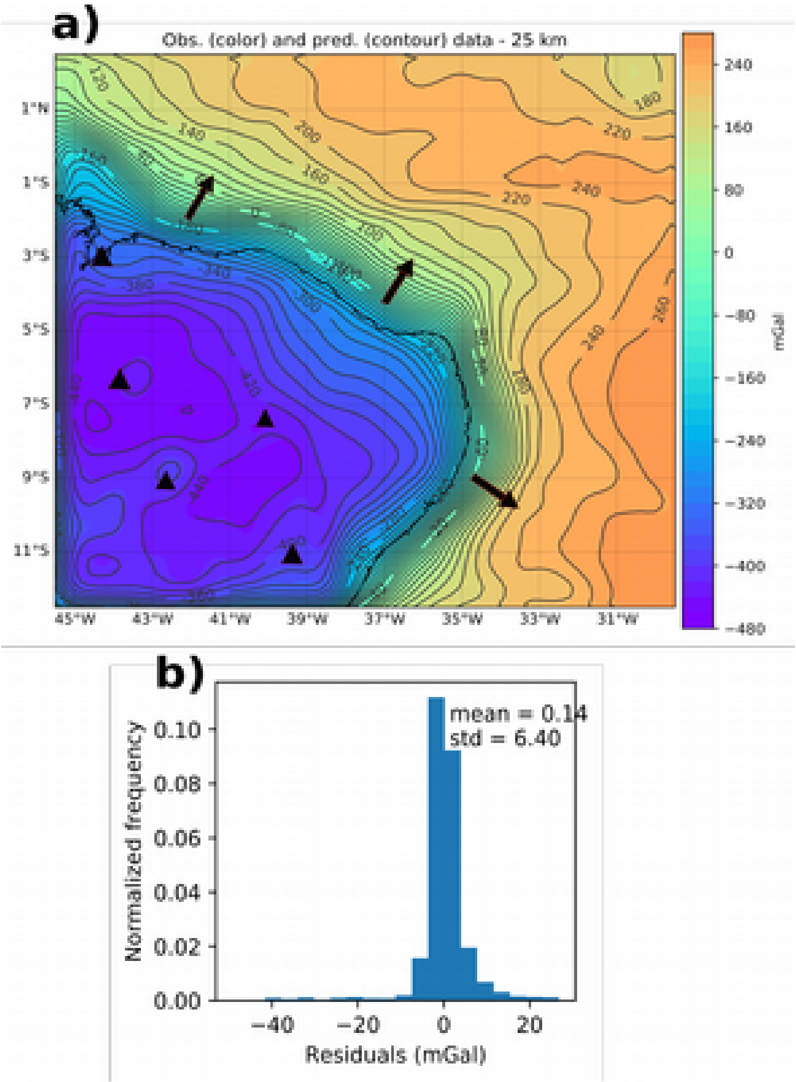

Figure 5.1.6.1 – Inversion result of the Bouguer anomaly for the Moho discontinuity. a) Observed (color) and predicted (contour) Bouguer anomaly for the Moho discontinuity (mGal) (triangles: location of cratons or deep basins; arrows: sharpness of the predicted Bouguer anomaly); b) Residuals between the original Bouguer anomaly and the result from the inversion

As it is possible to observe from Figure 5.1.6.1-a, the inversion of the gravity data (contours) has a really good match with the observed data (color). Also, in Figure 5.1.6.1-b, the residuals have a mean value of 0.14 mGal and a standard deviation of 6.40 mGal, showing that the fit between the real and inverted Bouguer anomaly for the Moho discontinuity is quite good.

The greater mismatch between the two is located in areas where cratons or very deep basins are located (black triangles in Figure 5.1.6.1). Also, it is clear from the contours, the sharp variation of the anomaly in the transition from land to ocean (highlighted by the black arrows in Figure 5.1.6.1).

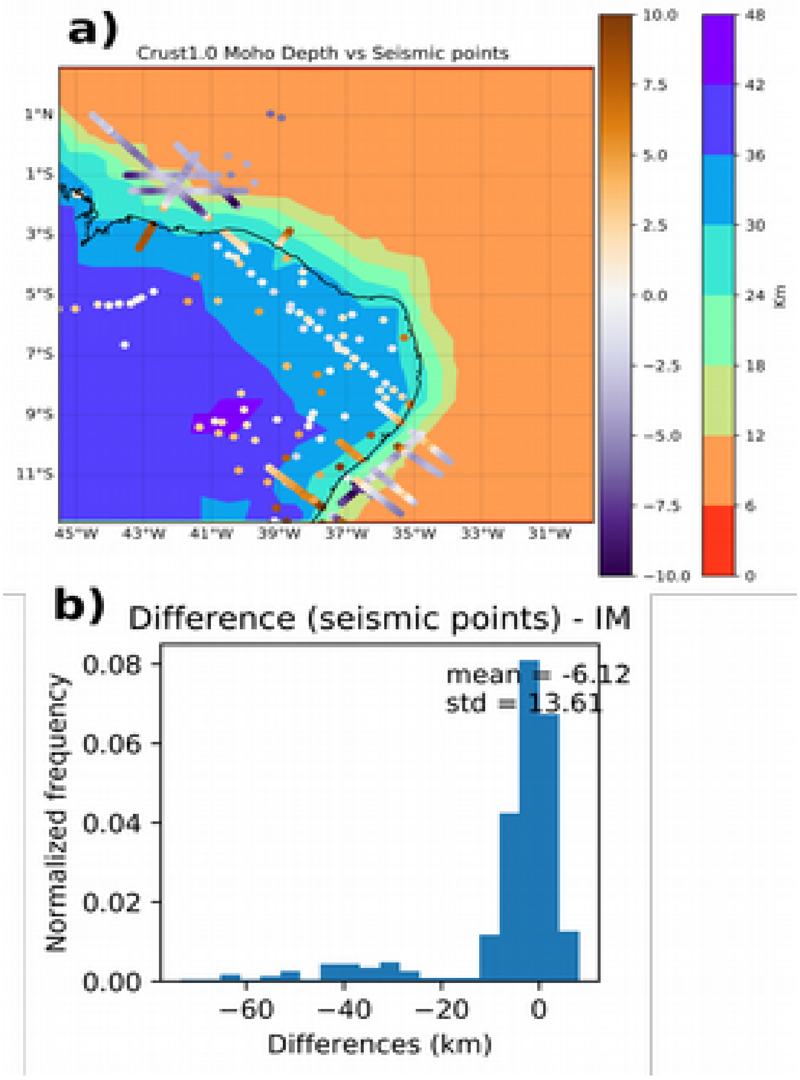

Figure 5.1.6.2 – Initial Moho depth model. a) Moho depth (given by the sum of the interpolated layers) from CRUST1.0 (background rainbow color) and Moho depth difference between CRUST1.0 and seismic stations in the research area (points with blue/brown color scheme); b) Histogram of the distribution of the differences between seismic points and initial model

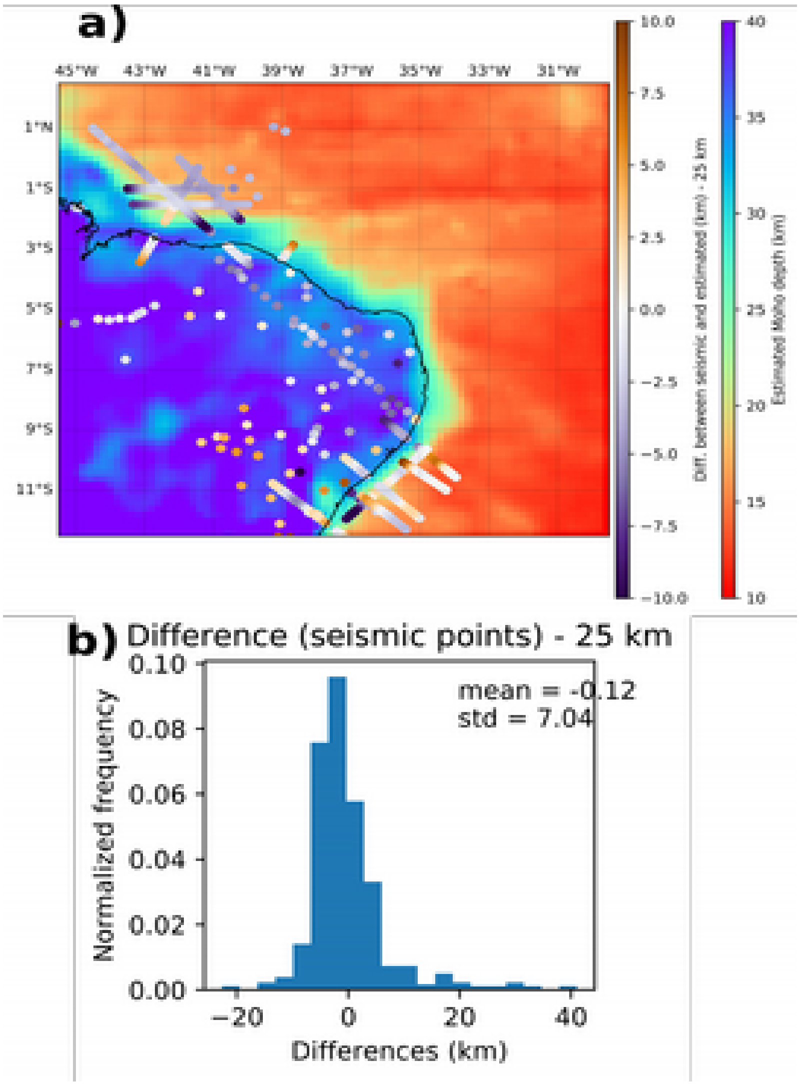

Figure 5.1.6.3 – Inversion result of the Moho depth. a)Estimated Moho depth (km) from the inversion of the Bouguer anomaly Moho – rainbow color scheme – and difference between estimated depth with Moho depth points (km) given by seismic data – blue/brow color scale; b) Histogram of the distribution of the differences between seismic points and the inversion result

If we compare the Moho depth given by the sum of the CRUST1.0 with the depth given by the seismic stations (Figure 5.1.6.2) we can see that we start from a quite good initial model, in particular for the stations on the continent. However, when we compare with the result inversion (Figure 5.1.6.3) we can see improvement at stations offshore and also for some locations in the continent as is the case for the Pará-Maranhão basin or the Recôncavo-Tucano-Jatoba basin. By comparing the results given by the histograms for the initial model (Figure 5.1.6.2-b) and the inversion result (Figure 5.1.6.3-b), the mean value and the standard deviation decrease significantly. The mean value decreases from -6.12 km, in the initial model, to -0.12 km, in the inversion; the standard deviation from 13.61 km, in the initial model, to 7.04 km, in the inversion. However we still observe the biggest differences along the continent to ocean transition.

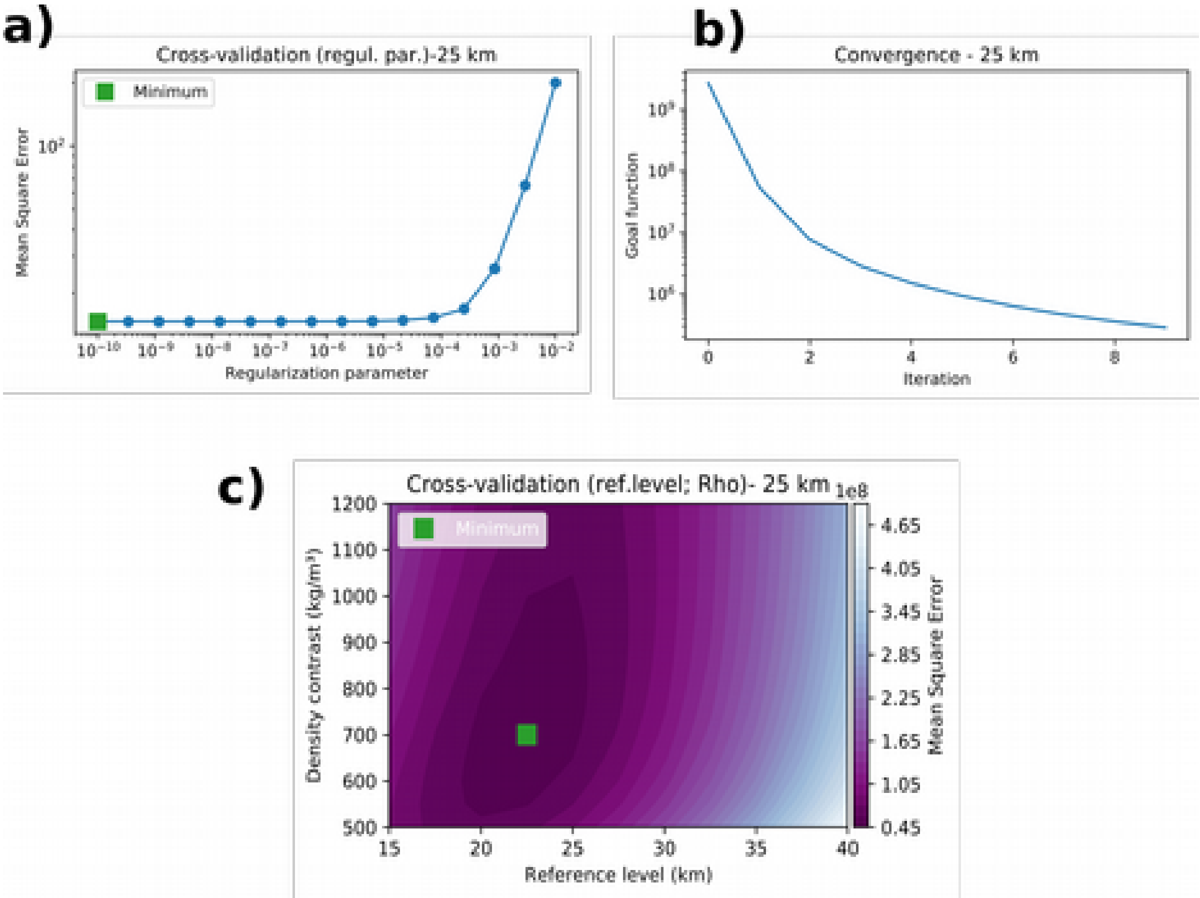

Figure 5.1.6.4 – Hyper-parameters evaluation and dispersion of data after inversion. a) Regularization parameter (µ); b) Convergence of the inversion; c) Mean square error associated with density contrast (Δρ) and reference level (z_{ref})

Analyzing the hyper-parameter results from Figure 5.1.6.4 we observe that we have a stable regularization parameter (µ) with a low mean square error (Figure 5.1.6.4-a), a convergence of the goal function (Figure 5.1.6.4-b) ensuring a stable inversion and the lower mean square error – 0.45 - is given for a density contrast (Δρ) of 700 km/m³ and a reference level of 22.5 km depth for the Moho discontinuity.

This gives a range of 525 kg/m³, actually within the ranges that we have when calculating the Bouguer anomaly. Being true that within that range there are values for the density contrast that do not seem plausible, we also need to take into account that there are layers withing the CRUST1.0 (in particular for the crust) that may have to low density values.

As mentioned before, this value for the density contrast should be considered with caution since it is quite high for a contrast between sediment plus crust density with lithospheric mantle.

However, we have the same mean square error for lower values (minimum 525 kg/m³) that better fit the average values that we can find in the bibliography (Afonso et al., 2019; Maystrenko and Scheck-Wenderoth, 2009). Also, the found range is within the density contrast variations shown, for sediment and crustal layers, of CRUST1.0 model.

Regarding the gravity residuals (Figure 5.1.6.1-b) we observe a very low dispersion – mean=0.14 mGal; standard deviation=6.40 mGal - confirming the results observed in Figure 5.1.6.1-a. Finally, the dispersion of the depth difference between the Moho given by the inversion of the gravity data and the Moho given by the seismic points has a mean of -0.12 km; and a standard deviation of 7.04 km. In spite of obtaining quite significant differences for several points, the general results are quite encouraging specially because some of those differences have straightforward explanations, like the transitions Land/Ocean with very narrow necking zones.

5.2. Reverse Time Migration (RTM)

5.2.1. Concepts and principles

The Reverse Time Migration method was first developed in the 1980’s decade and has been extensively used to image the sub-surface of the Earth.

One of the most effective ways to map sub-surface structures and properties is the seismic imaging. The RTM method is one of the most effective since is the only one that is capable of using all the seismic wave types. The fact that the evaluation of the image quality is done in the same space where the images are formed is another advantage as opposed to approaches of modeling and inversion that search for the solution in the model space but evaluate the solution fitness in the data space (Zhou et al., 2018).

Regardless the migration method used, the concept of migration is to place the different structures that constitutes the Earth sub-surface in their proper position, vertically and horizontally. There are different approaches to implement it. Depending on the seismic data set characteristics, a migration approach can be more suitable then other.

We can separate the different approaches in two general groups: Time and Depth. From a simple point of view, we can say that:

- Time Migration implies that we consider that the rays that travel inside the Earth medium have strait paths between the source, the medium and then to the receiver
- Depth Migration implies that we consider that the rays that travel inside the Earth medium have curved paths between the source, the medium and the to the receiver.

We can apply the migration technique before or after stacking the seismic data. If we apply before we call it a Pre-Stack Migration, if we apply after the processing and stacking the data, we call it Post-Stack Migration.

The RTM method is part of the Depth migration category. When first developed it was applied as a Post-Stack Migration (Edip Baysal et al., 1983; Baysal et al., 1984; McMechan, 1983; Whitmore, 1983), but quickly moved to Pre-Stack Migration (Chang and McMechan, 1987). With 40 years of developed work with RTM, at present day there is a multitude of different applications and formulations of the method. Following (Zhou et al., 2018), we can sub-categorize the method in first and second generation RTM. The first generation comprises all the applications of the method that include only first arrivals waves - (Baysal et al., 1984; Chang and McMechan, 1994, 1987;

Chang and McMECHAN, 1990; McMechan, 1983) – and the second generation comprises full waveform, meaning the inclusion of multiples - (Chang and McMechan, 1994; Sun and McMechan, 1988; Youn and Zhou, 2001). There is work developed for different imaging conditions, to different reflection data types and configurations, different geological targets and environments and a detailed description and compiled bibliography can be found in (Zhou et al., 2018). However there are very few examples of the application of the RTM method to Wide Angle Seismic (WAS) data acquired with Ocean-Bottom Seismometers (OBS) and Land Station Seismometers (LSS) - (Górszczyk et al., 2019; Kamei et al., 2012; Nakanishi et al., 2008; Schnürle et al., 2006; Shiraishi et al., 2022). The low folds in the OBS deployments with wide spacing is the main explanation for such few applications of the method to this type of data. Imaging shallow subsurface structures is usually done in high-resolution reflection profiles with multichannel seismic streamer data (MCS) surveys. However, this kind of surveys frequently fail to image the deep crustal structures due to the limited length of the streamer. Also, these surveys are not always available due to restrictions of using streamer cables, limitations related to mammals or protected areas on the survey locations or even weather conditions. Being able to image the deep crustal layers through RTM method from WAS data can be a valuable addition to seismic data processing and imaging. We can consider that the applied RTM method to the chosen profiles – MC5 and SL04 – is part the first generation RTM using the acoustic seismic wave. A detailed description of the applied method is done in the following paragraphs.

Mathematical background

The term that contemplates the time of propagation in the acoustic seismic equation, does not have a sense of positive or negative values. This means that the path taken by a particular ray can be traced back to the source by simply reverse the time to zero.

First we compute the forward propagating wavefield for each defined time step. Then, we restore the energy back to the respective sources by back-propagating the wavefield imposing the recorded signal as boundary condition for the same time steps. By correlating the forward and backward propagating wavefield for each saved time step, we image the horizons at their true vertical and horizontal positions.

In the case of pre-stack experiments, the shot profile reverse-time migration consists of a non-reflective two-way wave equation modeled with a finite difference (FD) method of the scalar acoustic wave equation. The method implemented is described in steps (Baysal et al., 1984; Nolet, 1986; Shiraishi et al., 2022). By adopting the source-receiver reciprocity on the relation between airgun shots and OBS's for each spacial coordinate in the model (x in equations 5.2.1.1, 5.2.1.2 and 5.2.1.3), the down going wavefields – $F_i(x,t)$, equation 5.2.1.1 – are extrapolated forward in time from OBS locations (X_{OBSi} (i=1,2,…,M), equation 5.2.1.1).The up going wavefields – $B_i(t,x)$, equation 5.2.1.2 – are extrapolated backwards in time from airgun shot locations (X_{shotj}, equation 5.2.1.2) (e.g. Schnürle et al., 2006; Shiraishi et al., 2022):

1. We forward propagate a shot wavefield – $F_i(t,x)$ - in time (t: 0 → T) to out past all horizons (backward sorted), based on the scalar wave equation with a migration velocity – C(x) – and a source function – s(t) – from the i^{th} OBS location – x_{OBSi} (i=1,2,…,M). The $d(x-x_{OBSi})$ is the Dirac delta function:

$$\left\{\frac{1}{C^2(x)}\frac{\partial^2}{\partial t^2}-\nabla^2\right\}F_i(t,x)=s(t)\delta\left(x-x_{OBS_i}\right) \qquad (5.2.1.1)$$

2. Back propagate the recorded wave field – $B_i(t,x)$ - at the same time interval (t: T → 0) by treating the seismic traces of the i^{th} OBS record – $D_{i,j}(t,x_{shotj})$ – as a boundary condition at the sea surface:

$$\left\{\frac{1}{C^2(x)}\frac{\partial^2}{\partial t^2}-\nabla^2\right\}B_i(t,x)=\sum_{j=1}^{N}D_{i,j}\left(t,x_{shotj}\right) \qquad (5.2.1.2)$$

3. Imaging – I(x) – by adding through all time steps the two wave field’s product for each grid point. The imaging condition for the zero instance in the time domain can be represented by:

$$I(x)=\sum_{i=1}^{M}\int_{0}^{T}F_i(t,x)B_i(t,x)\,dt \qquad (5.2.1.3)$$

Finally we obtain the subsurface image along the entire profile by stacking the individual image sections from all OBS records (Baysal et al., 1984; Nolet, 1986; Shiraishi et al., 2022).

5.2.2. Data preparation (Individual OBS/LSS results as examples)

The WAS data acquired on OBS and LSS stations were prepared taking into account similar steps – Table 5.2.2.1.

Action (sequential)	**OBS**	**LSS**
Apply gain to scale the data	$1x10^{-6}$	No
Apply mute to eliminate water multiple	Yes	No
Butter-worth filter (in time)	f_{stop}(low)=0.5; f_{pass}(low)=4; f_{pass}(high)=32; f_{stop}(high)=48; zerophase=0	f_{stop}(low)=0.5; f_{pass}(low)=4; f_{pass}(high)=32; f_{stop}(high)=48; zerophase=0
Apply gain two times In offset	Yes	Yes
Butter-worth filter (in depth)	f_{stop}(low)=1; f_{pass}(low)=4; f_{pass}(high)=12; f_{stop}(high)=18; zerophase=0	No
Mute multiples	According with first multiple picking	In offset, until 28s with a taper of 24

Table 5.2.2.1 – Sequential processing steps to prepare the WAS data for the forward problem of the RTM method

After applying the described steps in table 5.2.2.1, the data sets to each station are ready and comprise all types of data – Figures 5.2.2.1 and 5.2.2.2.

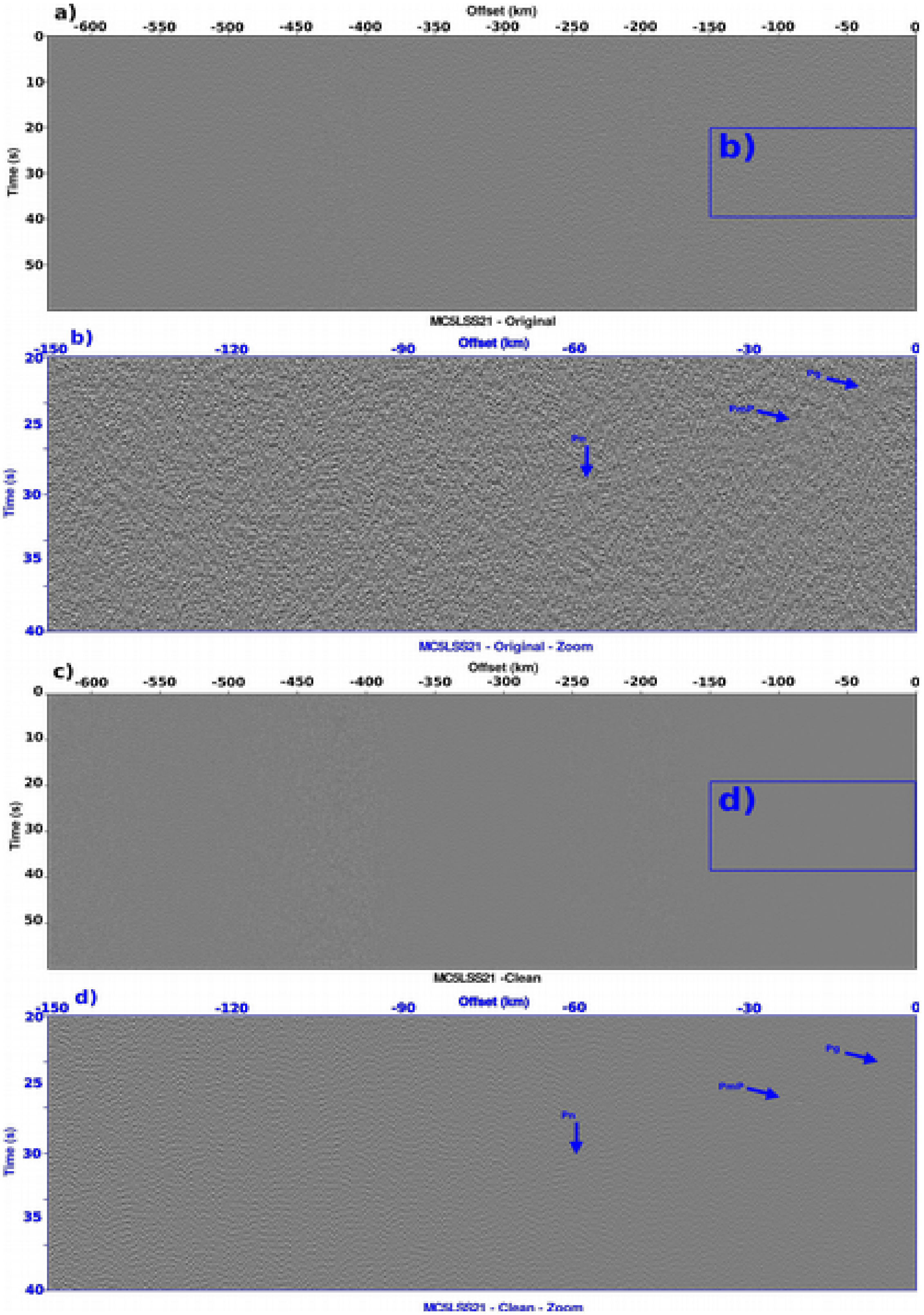

Figure 5.2.2.1 – Original data and processed data for MC5LSS21. a) MC5LSS21 raw data for the entire offset range and 59 s interval; b) Zoom on MC5LSS21 (blue square on a)) with annotation of presence of all types of waves (blue arrows); c) MC5LSS21 processed data for the entire offset range and 59 s time interval; d) Zoom on MC5LSS21 processed data (blue square on c)) with annotation of presence of all types of waves (blue arrows)

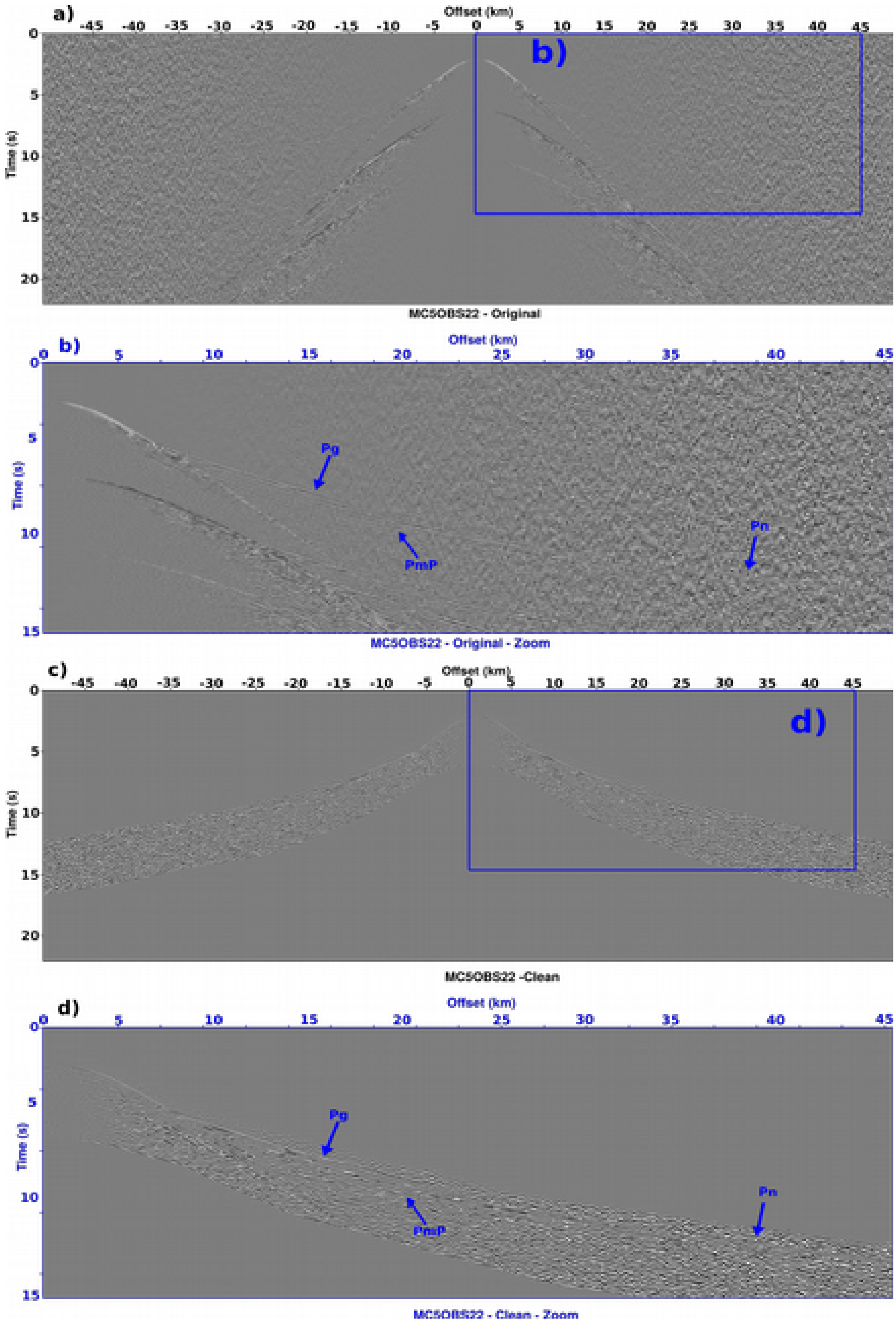

MC5OBS22 - Original

MC5OBS22 - Original - Zoom

MC5OBS22 -Clean

MC5OBS22 - Clean - Zoom

Figure 5.2.2.2 – Original data and processed data for MC5OBS22. a) MC5LSS22 raw data for 100 km offset and 22 s interval; b) Zoom on MC5OBS22 (blue square on a)) with annotation of presence of all types of

waves (blue arrows); c) MC5OBS22 processed data for 100 km offset and 22 s time interval; d) Zoom on MC5OBS22 processed data (blue square on c)) with annotation of presence of all types of waves (blue arrows)

The data processing done for each station aims to filter noise and the multiples present in each station. The differences in the processing steps between OBS and LSS stations are explained by the intrinsic characteristics of the stations and their location (there are no water layer or water multiples in the land stations, for example), but also due to the horizontal distance between the stations and the shooting. The shooting started at MC5OBS44 (and SL04OBS01 for SL04 profile) and ended at MC5OBS05 (and SL04OBS01 for SL04 profile), meaning that the energy recorded by the LSS stations traveled longer distances and crossed different layers before reaching the station when compared with the OBS stations. In Figures 5.2.2.1 and 5.2.2.2, the original and processed data are presented for MC5OBS22 and MC5LSS21. Within the zoomed Figures 5.2.2.1-b and d; 5.2.2.2-b and d; it is possible to see that the processing steps taken are efficient on removing the random noise and multiples but keep all the different wave types present – reflected and refracted waves for different interfaces that are crossed by the traveling rays.

5.2.3. The velocity models

The layered RayINVR (Zelt and Smith, 1992) velocity model corresponding to each profile (MC5 and SL04) used to perform the RTM were previously obtained by applying a procedure of two-dimensional forward ray-tracing followed by a damped least-squares travel time inversion – Figure 5.2.3.1.

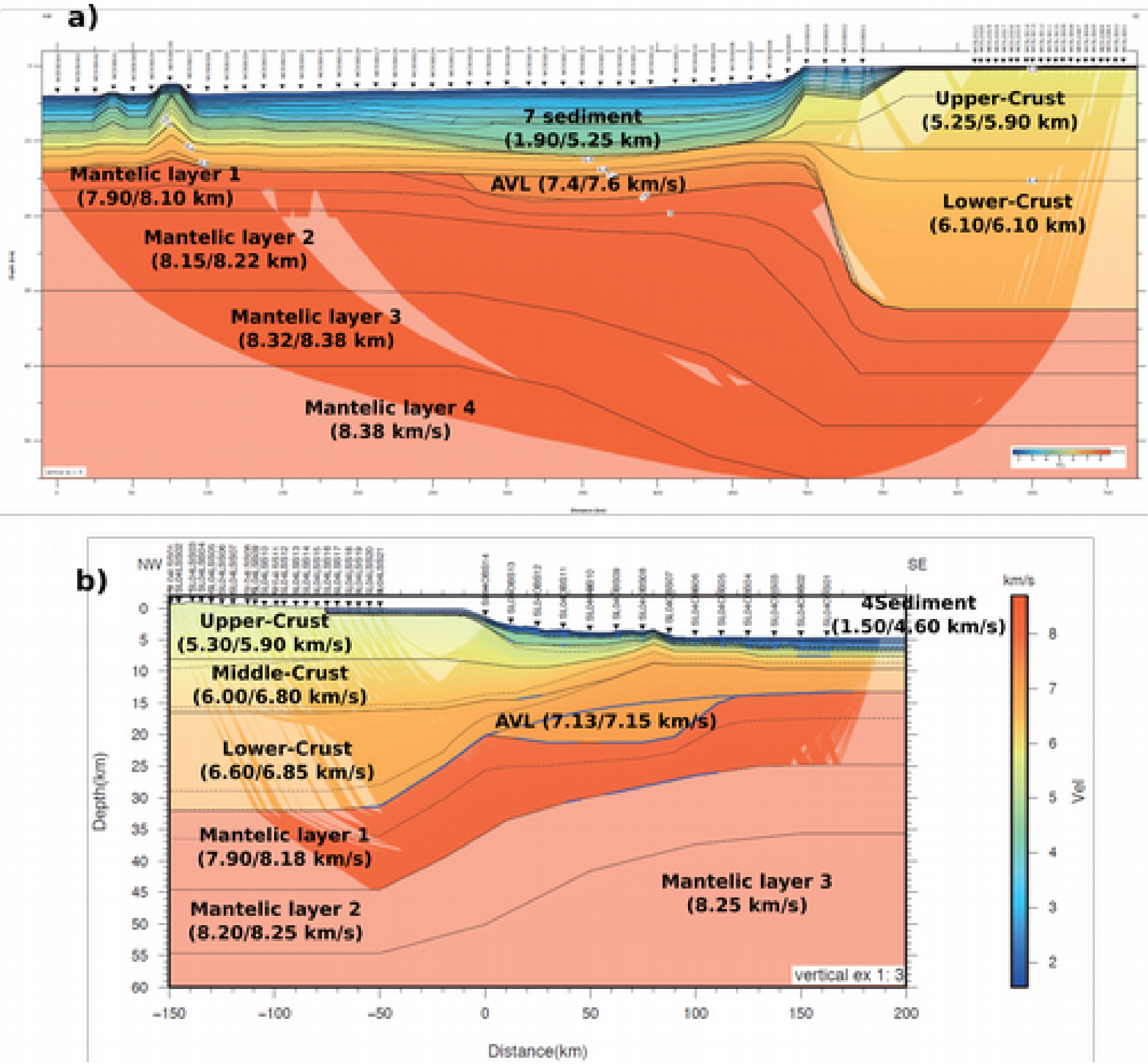

Figure 5.2.3.1 – Layered RayINVR velocity models. a) MC5 (adapted after Schnürle et al., 2023); b) SL04 (adapted after Aslanian et al., 2016)

To ensure sufficient resolution with limited dispersion and spacial aliasing, the optimal grid-spacing needs to be established. This grid-spacing was implemented in the 10th order 2D finite difference acoustic modeling. Given the acquisition footprint, the horizontal grid spacing chosen is that of the shot spacing, i.e. dx=150 m. The recorded OBS data is sampled at 4 ms, and provided ample sampling for a vertical grid spacing dz=25 m. A grid with of 100 km (+/- 50 km offset) was selected in order to reach a depth of 25 km of imaging.

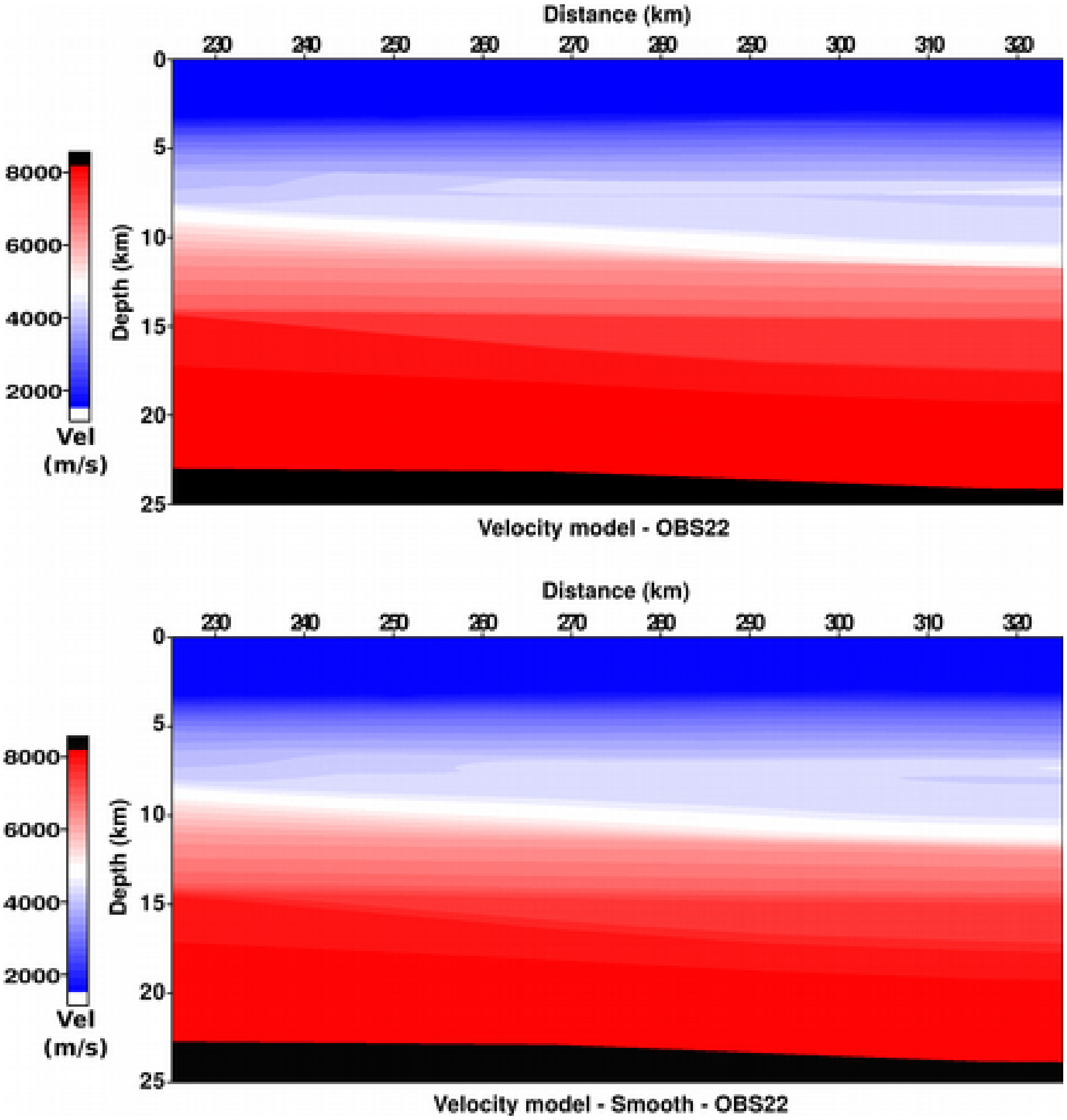

Figure 5.2.3.2 – Velocity models for MC5OBS22 with 100 km offset (-50 to 50 km) and 25 km depth. a) Regular grid velocity model; b) Smoothed velocity model

The layered RayINVR velocity models was converted into regular grids, the grids are cut in order to fit the section where the individual RTM stations are placed and a damped least squares smoothing was applied – Figure 5.2.3.2. Applying the smoothing to the velocity model is essential in order for the migration technique to work and avoid artifacts generated by sharp variations of velocity for neighboring points.

5.2.4. Perform the RTM for individual stations

With the smoothed velocity model, we back-propagate the recorded wavefield from the forward problem and use it as a boundary problem. Leaving only the top boundary , where the marine shots are placed, as a free surface and all the other as absorbing boundaries, the wavefield is back-propagated with no limitation on the incidence angle of each wave and saving 50 time steps in order to visualize the back-propagation in a small movie.

Next, by preforming the correlation between the results of the forward problem and the backward problem, we obtain the RTM result for each station.

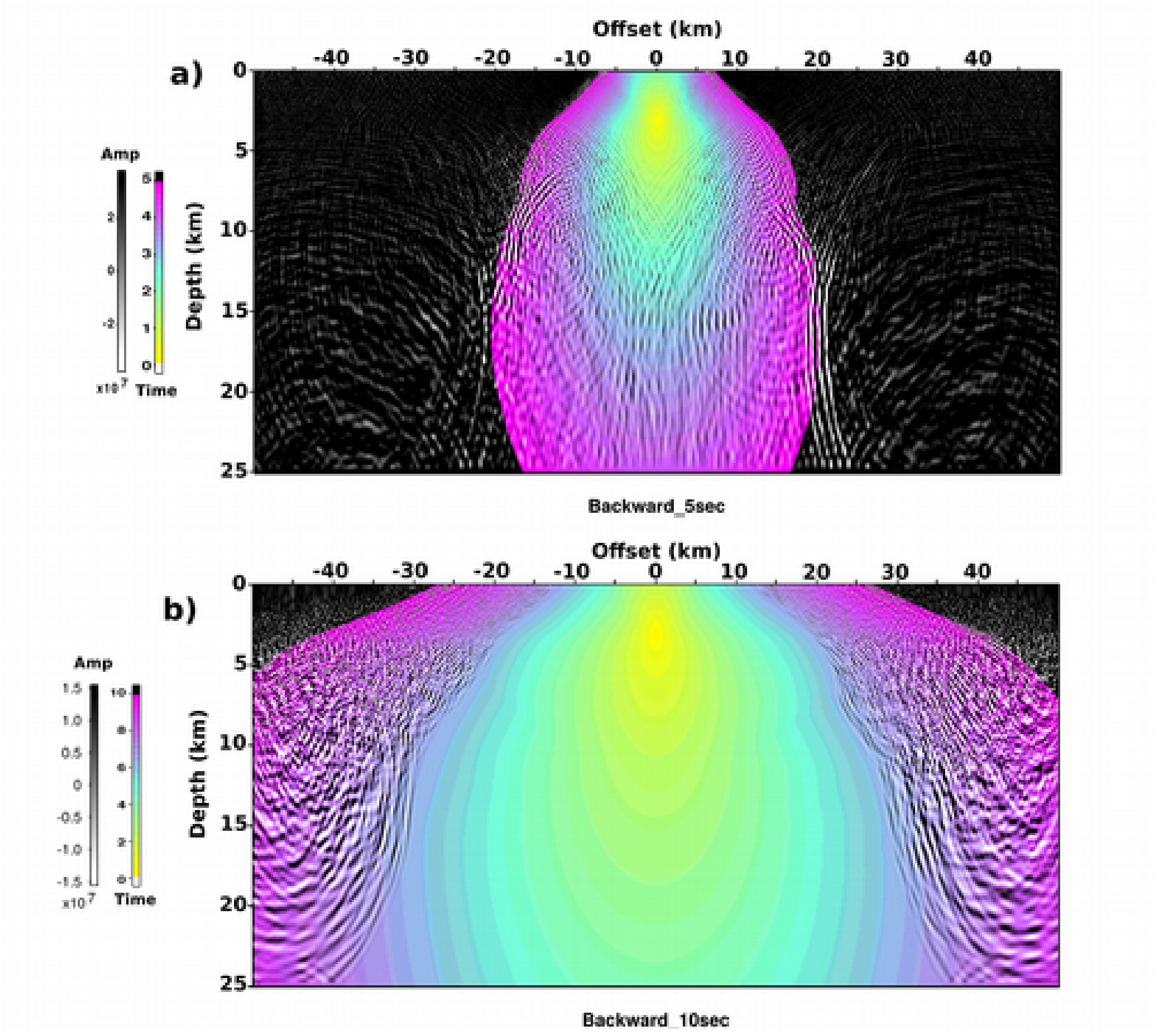

Figure 5.2.4.1 – Backward propagation of the wavefield for MC5OBS22. a) 5 seconds time step; b) 10 seconds time step

Regarding the content that is being saved to each time step in the backward propagation wavefield, Figure 5.2.4.1 is an example of two of those time steps. All the wavefield that is within the time envelope for a particular time step is saved. However, it will be the coherent signal that propagates at the edges of each time envelope (magenta/black limit on Figure 5.2.4.1) that will positively correlate with the forward wavefield and give the final RTM result for each station.

The RTM is preformed to each station and a dip filter is applied to remove artifacts that are generated due to the remaining noise within the data and the non coherent wavefield that is saved within each time step and that the correlation is not able to remove with success.

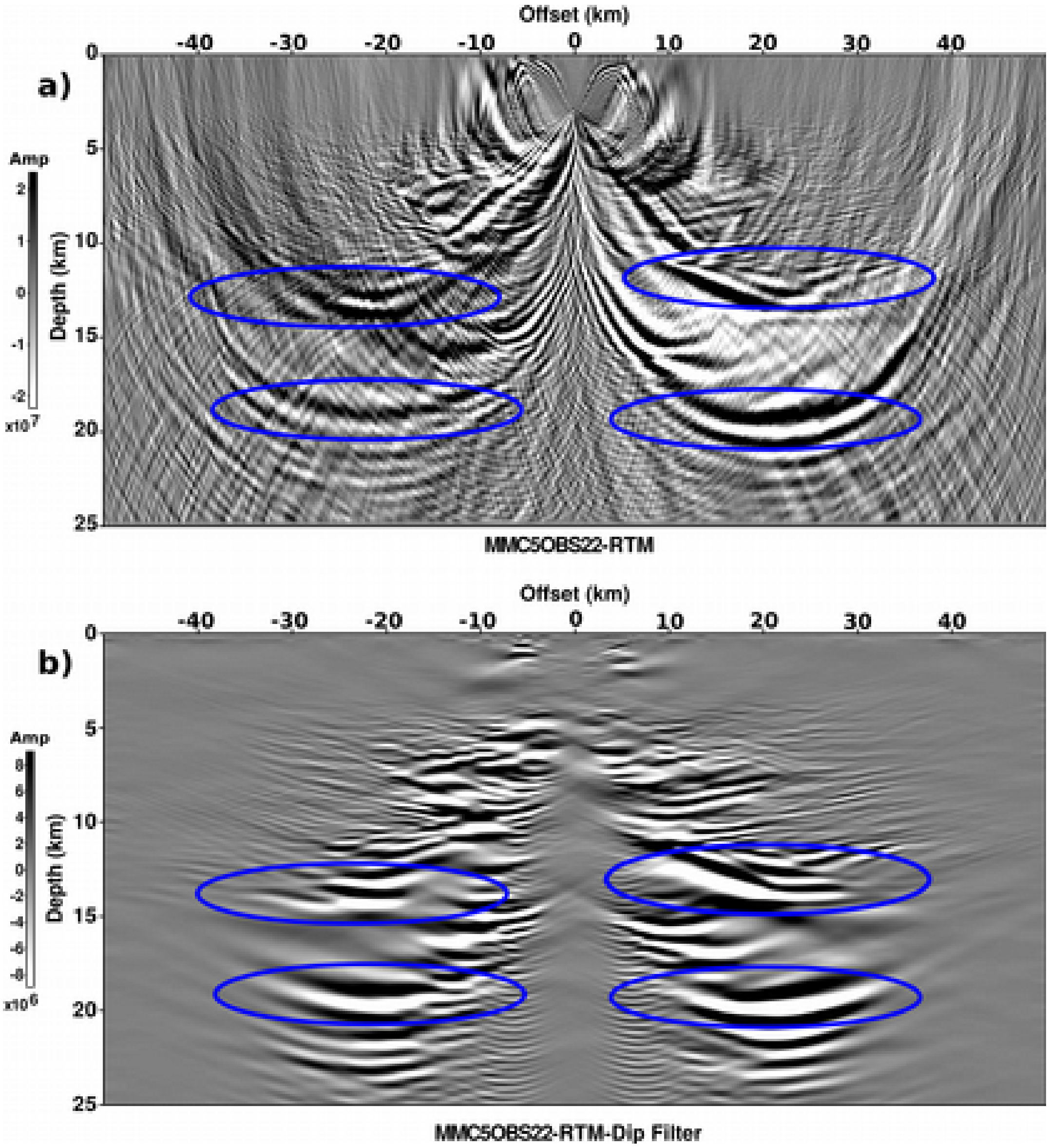

Figure 5.2.4.2 – RTM result for MC5OBS22 station with 100 km offset and 25 km depth. Some of the obtained refractors are highlighted with blue ellipses. a) Without dip filter; b) With dip filter

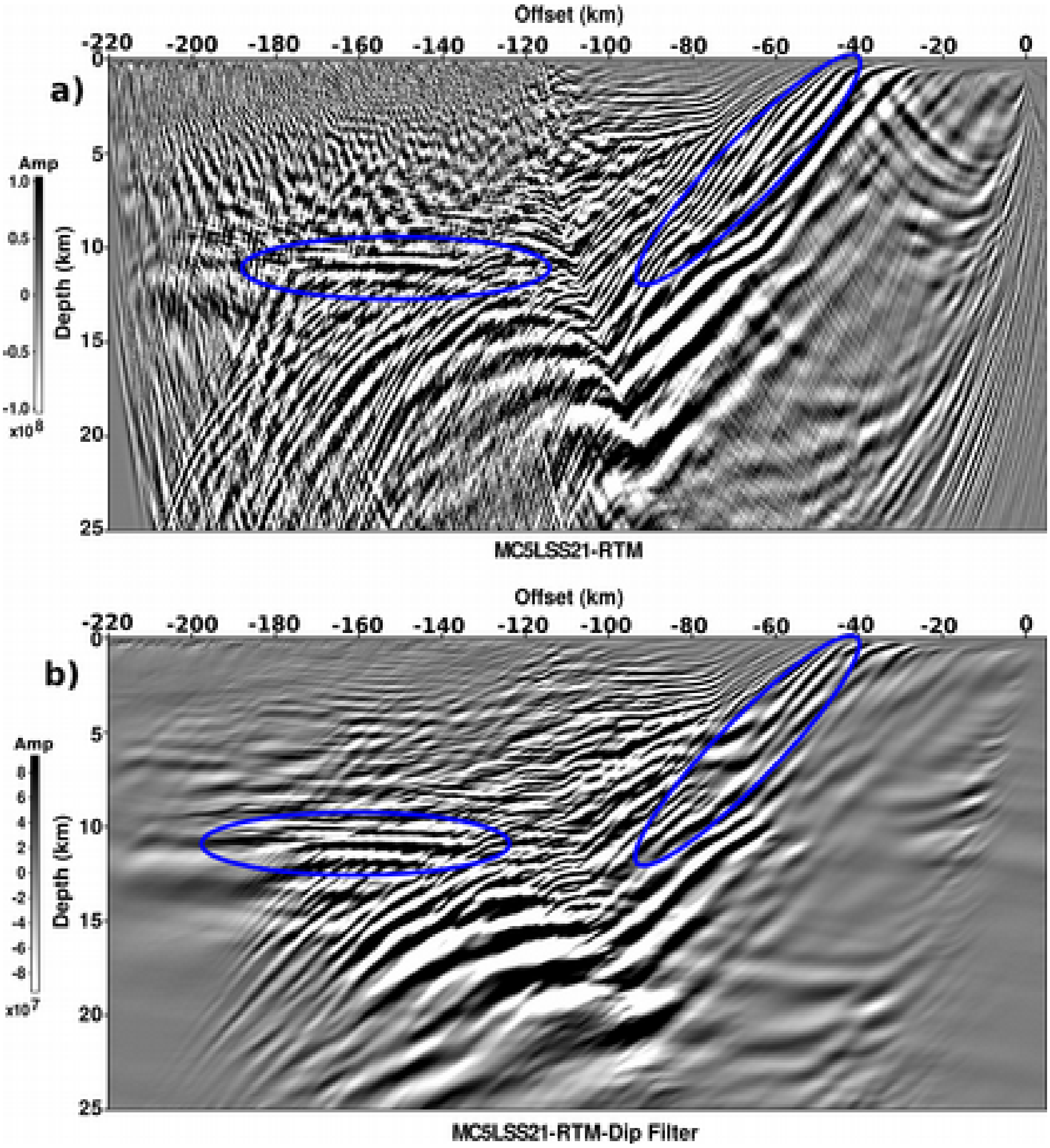

Figure 5.2.4.3 – RTM result for MC5LSS21 station with 220 km offset and 25 km depth. Some of the obtained refractors are highlighted with blue ellipses. a) Without dip filter; b) With dip filter

Figures 5.2.4.2 and 5.2.4.3 show the individual RTM result for MC5OBS22 and MC5LSS21 stations, respectively. When we compare the original result with the one where the dip filter was applied (a and b) for each Figure) we can see that we have the same reflectors/refractors in the same horizontal and vertical positions, meaning that the filter does not change the results but simply allow to have more clear results.

The offsets taken into account in the OBS stations are different from the ones in the LSS stations. While 100km offset is considered for the OBS stations, for the LSS stations we have 220 km of offset. Due to the fact that the shooting has stopped at MC5OBS05 (500 km model distance in Figure 5.2.3.1-a), the energy needs to travel a long distance within the Earth surface to reach the land stations and, because of that, we needed to take into account the maximum energy possible. Also, the main goal of performing the RTM for the LSS stations was to image the necking zone, which is exactly the area that does not have any stations directly above due to the very shallow and long shelf.

There is, at least, 1order difference in amplitude between OBS and LSS stations that are presented in Figures 5.2.4.2 and 5.2.4.3. In this particular case, the amplitude within the LSS station is higher then the amplitude within the OBS. This difference progressively increases as we move to LSS stations located more in land. The amount of energy that reaches the land stations decreases meaning that the amplitude of the obtained refractors also decreases. This difference reveals the uncertainty of the instrument sensibility corrections, coupling and near surface effects, and propagation energy loss that we apply: the true energy imaging remains slightly inaccurate.

Contribution of the different types of waves

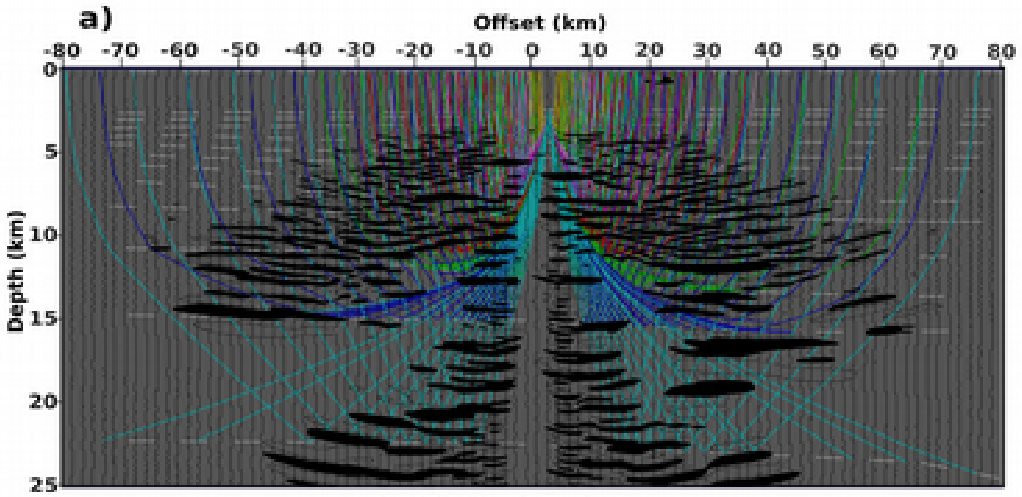

MC5OBS22 - Reflected waves

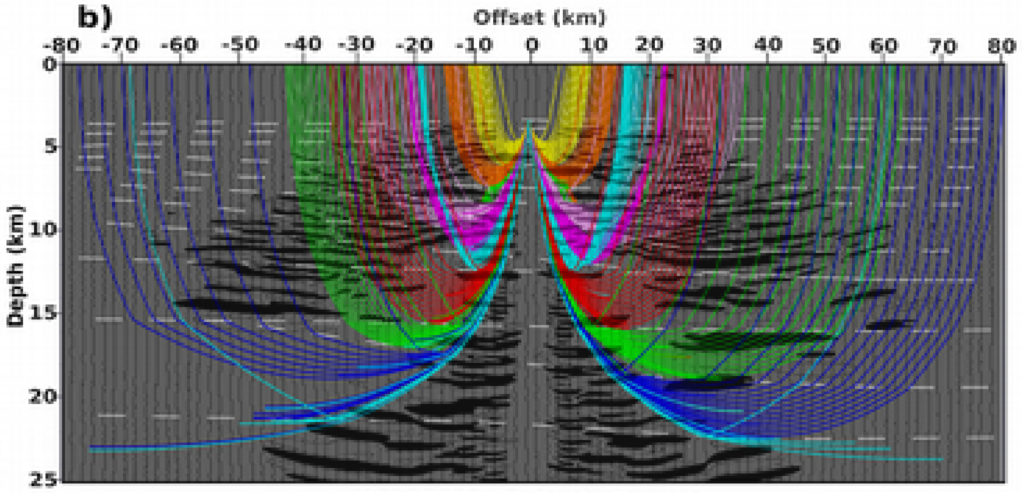

MC5OBS22 - Refracted waves

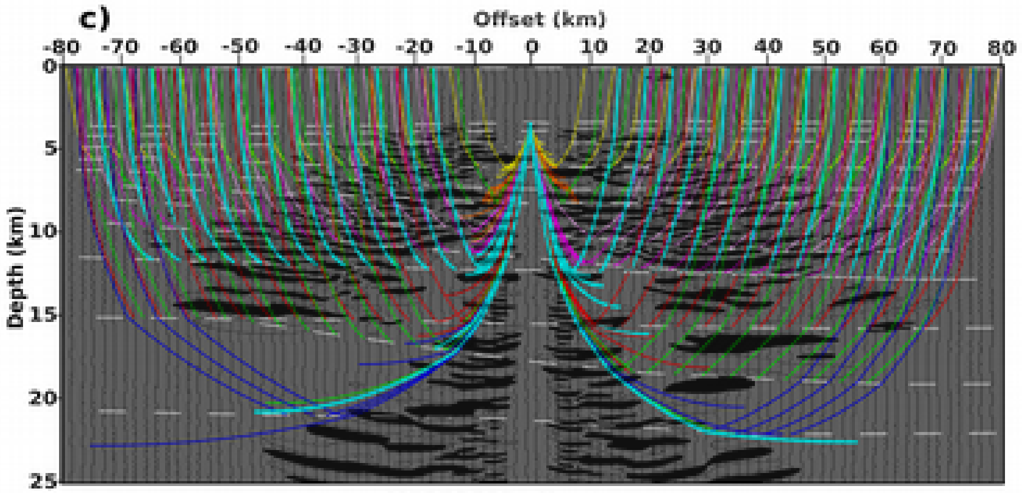

MC5OBS22 - Head waves

Figure 5.2.4.4 – RTM result for MC5OBS22 with the different ray types tracing overlaid - P-waves. a) Reflection waves; b) Turning waves; c) Head Waves

From the analysis of the individual RTM results, there is a feature that is quite relevant for the success of the application of the method to the WAS data. That feature is the contribution of the turning-waves and head-waves wavefields.

Usually the RTM method regards mostly the reflection content of the wavefield since is these types of waves that have a tight correlation with the boundaries between layers. But the truth is that within the traveling wavefield, we have all types of waves and they are all considered in the method, since it does not make any assumptions on the type of propagation wavefield. In Figure 5.2.4.4 we present for MC5OBS22 station, the three major types of rays that we record for only P-wave field: i) reflected wavefield (Figure 5.2.4.4-a); ii) turning wavefield (Figure 5.2.4.4-b); head wave wavefield (Figure 5.2.4.4-c).

A reflected wave is generated when an incident wave encounters a change in velocity and is converted into a reflected wave that travels back with a certain angle (reflection angle). A turning wave is generated by the same velocity change but is transmitted to the layer bellow with a certain angle (refraction angle) and travels within that layer before returns to the receiver. The head wave for a particular layer is generated when the incident wave hits the boundary of that layer at the critical angle and a refracted wave is propagated at the maximum possible angle (90º) traveling along the boundary that was hit.

If it is true that both refracted and reflected waves are capable to provide information about the depth of a certain layer, it is also true that only the turning waves and head waves can provide horizontal information about those velocity changes for offsets above the critical angle. In fact, Figure 5.2.4.4 is an example of the importance of the turning and head-wave (Figure 5.2.4.4-b and c) content within the wavefield. We can see that for short offsets – 0 to 20 km – most of the reflectors/refractors are crossed by both types of waves. However, as we move to offsets up to 50 km to 70 km, the majority of the refractors/reflectors are crossed only by the turning waves and/or head waves – dark blue, red and green rays, for example. Also, in depth, some of the obtained reflectors/refractors are more clearly imaged due to the refracted waves – Moho discontinuity (dark blue rays) or AVL (red rays).

5.2.5. RTM Stack

The stack of the individual RTM results is done according to the common depth point (CDP). The stacking process is the same for OBS and LSS stations but they are independent. We obtain a stacked result for all the OBS stations and another for the LSS stations. Due to the amplitude differences between RTM results in OBS and LSS stations, building a stack for OBS and LSS stations of the same profile requires the normalization of the amplitudes for the entire set of stations. This means that we may loose refractors that have a geological interpretation meaning or that we create artifacts. However, because we have overlapping offsets, we can combine both results by building a joint figure.

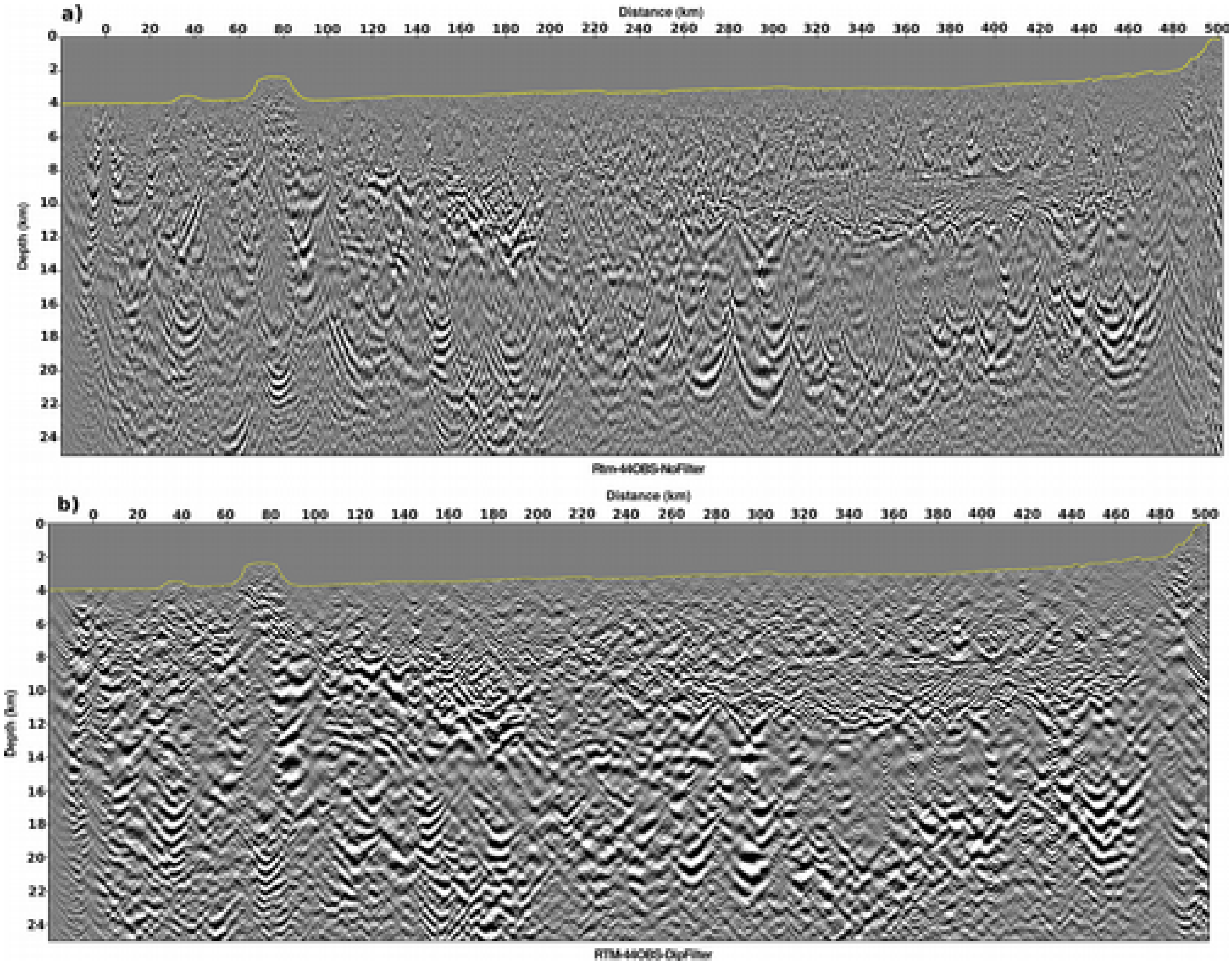

Figure 5.2.5.1 – RTM stack result for the 44 OBS stations of profile MC5. a) No dip filter applied; b) With dip filter (1:6 vertical exaggeration)

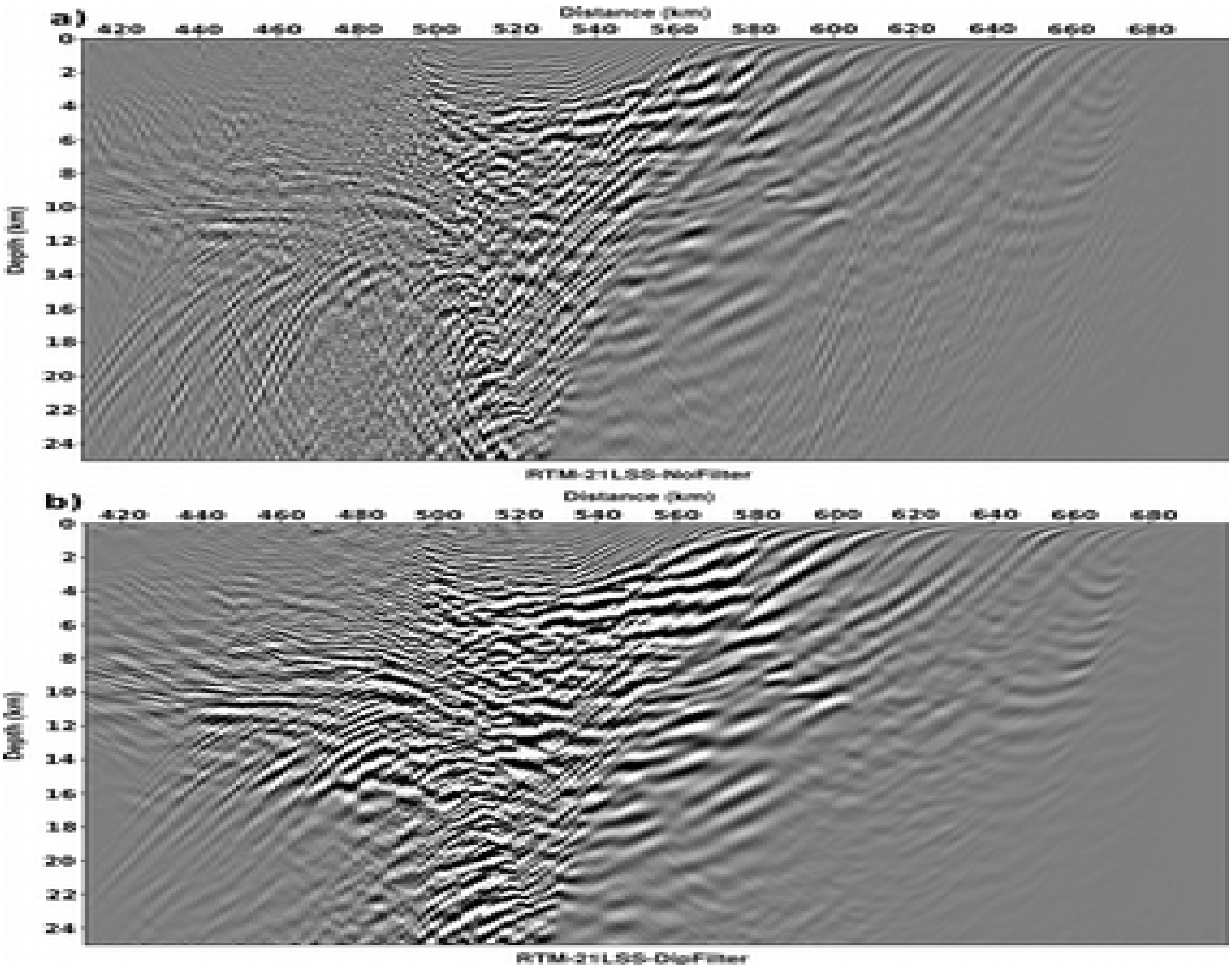

Figure 5.2.5.2 – RTM stack result for the 21 LSS stations of profile MC5. a) No dip filter applied; b) With dip filter (1:6 vertical exaggeration)

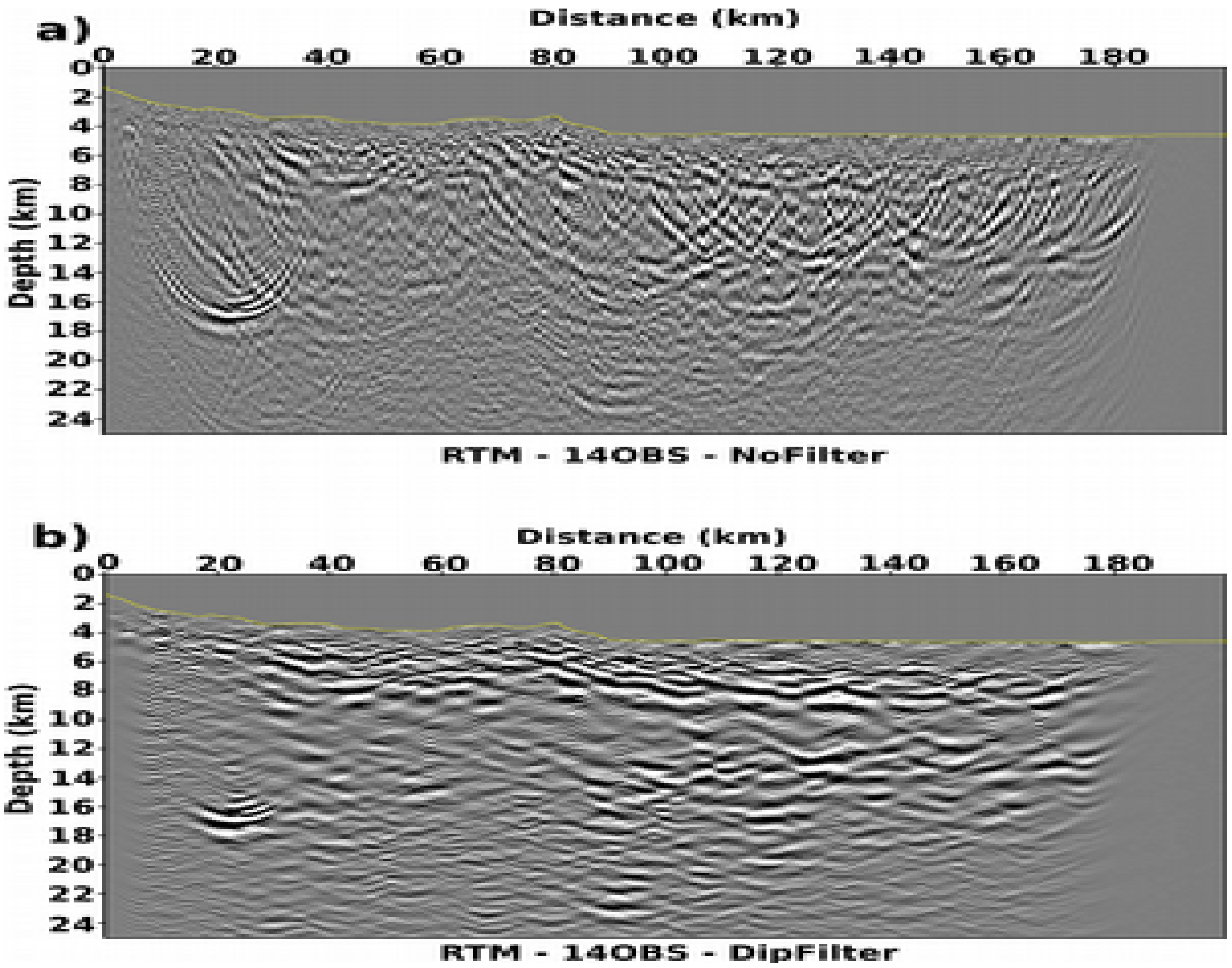

Figure 5.2.5.3 – RTM stack result for the 14 OBS stations of profile SL04. a) No dip filter applied; b) With dip filter (1:3 vertical exaggeration)

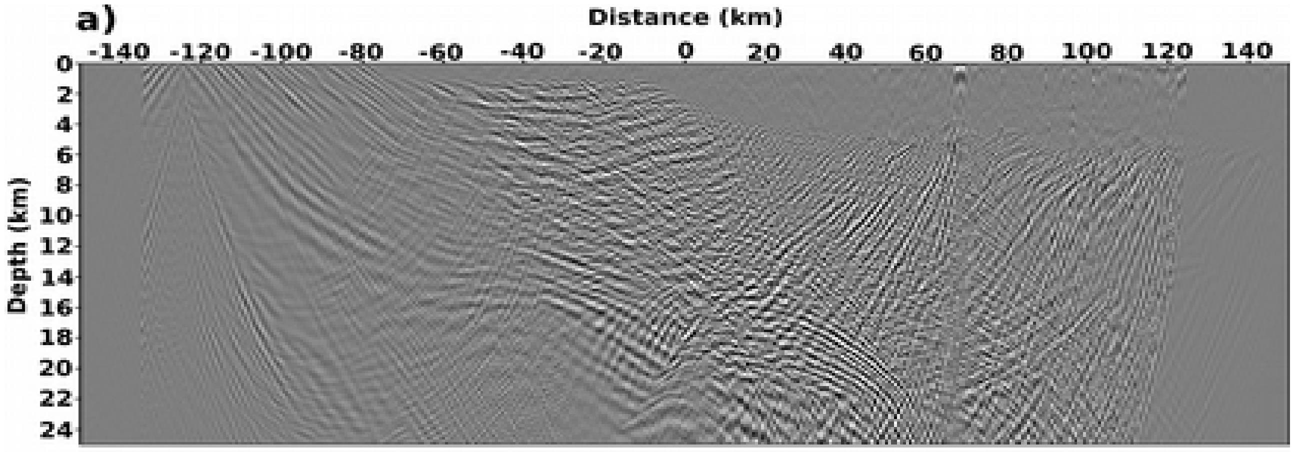

RTM - 21LSS - NoFilter

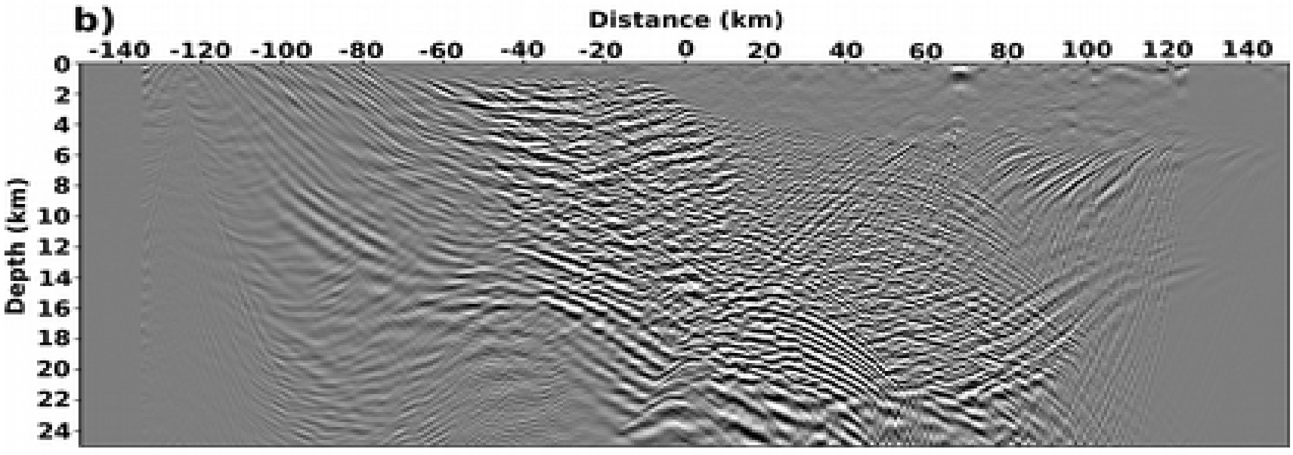

RTM - 21LSS - DipFilter

Figure 5.2.5.4 – RTM stack result for the 21 LSS stations of profile SL04. a) No dip filter applied; b) With dip filter (1:3 vertical exaggeration)

Comparing the stacked results with and without applying the dip filter – Figure 5.2.5.1 to 5.2.5.4 – we can see that, as described before, the purpose of this filter is to remove the refractors with large dip inclinations that remain after correlating the forward and backward images. The filter is kept quite open in order to keep the result as close as the original but easier to analyze.

5.2.6. The different Vp/Vs equations – Horizontal OBS channel

The RTM method was also applied and tested for the horizontal channels of the 44 OBS stations of MC5 profile.

The propagation of shear (S-waves) and compressional (P-waves) are sensible to different physical characteristics of the material that compose the subsurface. This means that, a joint interpretation of P and S wave content may provide more information on the composition of the subsurface then the P-wave content alone (Holbrook et al., 1992).

If we are able to retrieve, using the same method, a resulting image that contains characteristics regarding the wavefield that is forward propagated as P-wave content and backward propagated as S-wave content, can provide elements on the characterization of the Poisson ratio and provide additional knowledge about the subsurface of the research area.

The rotation of each OBS station was previously done and, since is outside the scope of this work, the process to obtain the rotated OBS stations is not described.

The steps taken to obtain the individual and stacked RTM result are very similar to the ones described in the previous sections. The main difference is, when performing the RTM to each OBS station, we need to convert the P-wave velocity model into a S-wave velocity model.

The conversion of the velocities was done testing 4 different equations/relations that correlate the P-wave (V_P) and S-wave (V_S) velocities:

(Holbrook et al., 1992)

$$V_S = \frac{V_P}{\sqrt[2]{3}} \tag{5.2.6.1}$$

(Castagna et al., 1985)

$$V_S = 0.8621 V_P - 1.1724 \tag{5.2.6.2}$$

(Castagna et al., 1993)

$$V_S = -0.05509 V^2_P + 1.0168 V_P - 1.0305 \tag{5.2.6.3}$$

(Brocher, 2008, 2005)

$$V_S = 0.7858 - 1.2344 V_P + 0.7949 V^2_P - 0.1238 V^3_P + 0.006 V^4_P \tag{5.2.6.4}$$

The relation between P-wave and S-wave velocities is highly dependent on the lithology of the material that compose the subsurface. The pressure, porosity and temperature conditions at which the materials are exposed also have an influence on the propagation velocity of a wave through a certain material. Because of all those variables, a precise relation between those two velocities does not exist and several empirical relations were tested and developed depending on a set of lithologies of a certain research area or relations developed for different categories of materials. The constant ratio presented in equation 5.2.6.1 (Holbrook et al., 1992; Kvarven et al., 2016) has an application for crystalline rocks that usually compose the crust. The relationship presented in equation 5.2.6.2 was developed by Castagna et al., 1985 for clastic silicate rocks. In their study, different laboratory data and in-situ data were used, taking into account different levels of porosity and pressures. Among those data were water saturated sediments, making this relation plausible to test for our research area. Few years later, the same author (Castagna et al., 1993) developed another set of relations for different lithologies where, among them is equation 5.2.6.3, applicable to sandstones, limestones, shale and dolomite rocks. Finally, Brocher et al. (2005, 2008) reached the relation presented in equation 5.2.6.4 by plotting thousands of wave velocity data for a wide range of lithologies from unconsolidated sediments to very low porosity igneous rocks. This relationship is valid for V_P velocities between [1.5; 8.5] km/s. In (Maleki et al., 2014), several of these relationships were tested in the Iranian Province of Khuzestan, onshore of the Ahwaz region near the Iran-Iraq frontier. Their research area was mainly composed by limestones, dolomite, sandstone, shale and Marl.

The same type of approach was taken in this study, and these different relationships were tested for the 44 OBS stations since the composition of the research area is very complex and contains not only different materials but also, in depth, different water saturation (porosity).

Converted Velocity model

As previously done, for each station, a velocity model with 100 km offset and 25 km depth was used. In this case, using each of the relationships presented, the grid P-wave velocity model was converted to S-wave velocity model.

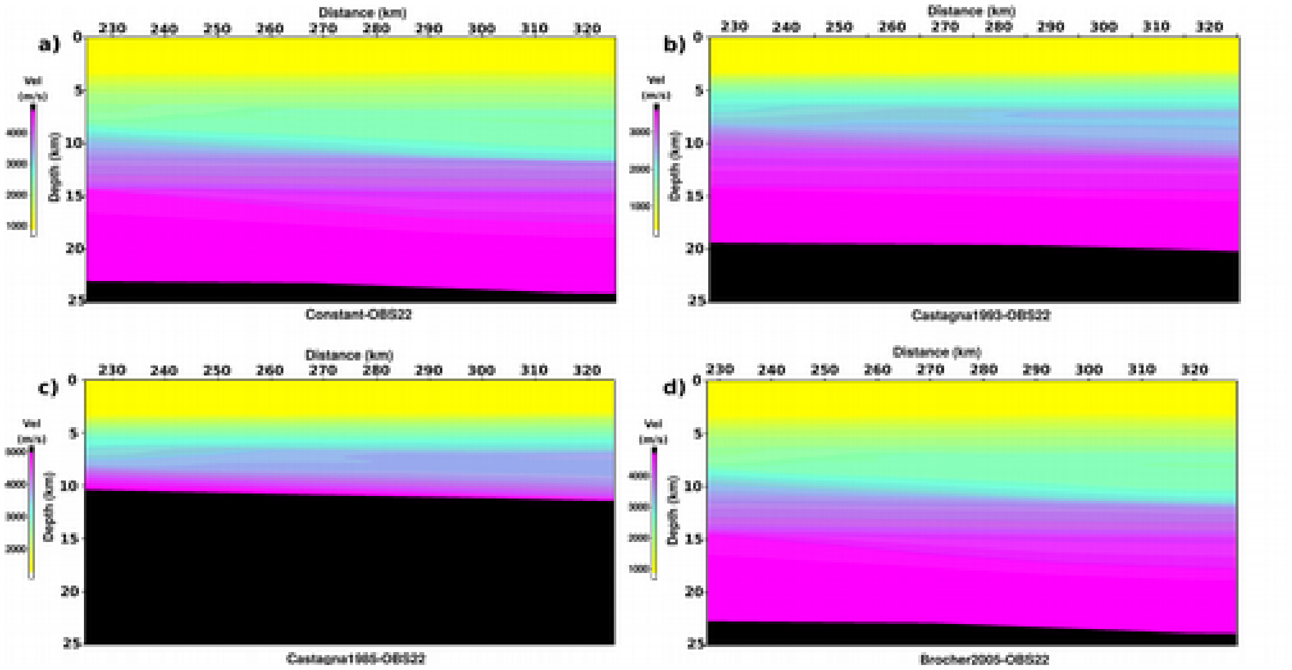

Figure 5.2.6.1 – S-wave velocity grid for MC5OBS22, converted from P-wave velocity grid. a) Converted using constant relation 5.2.6.1 (Holbrook et al., 1992); b) Converted using relation 5.2.6.2; c) Converted using relation 5.2.6.3 (Castagna et al., 1993); d) Converted using relation 5.2.6.4 (Brocher et al., 2005, 2008)

The different S-wave velocity grids obtained with the different V_P/V_S relationships are presented in Figure 5.2.6.1, for MC5OBS22. As we can observe, the relationship given by Castagna et al., (1985) are the one that have a sharper vertical velocity gradient. This relationship (Figure 5.2.6.1-c) gives velocities greater then 5 km/s for depths greater then 10 km. Having S-wave velocities greater then 5 km/s at these depths is not plausible (Kennett and Engdahl, 1991) and, because of that, will not be considered to perform the RTM. Regarding the other relationships, the constant ratio (Figure 5.2.6.1-a) and the Brocher et al. (2005, 2008) (Figure 5.2.6.1-d) have similar ranges and similar vertical gradients. The relationship from Castagna et al. (1993) has a narrower range but the vertical gradient is sharper for that range. Since the differences, regarding the velocity model, are hard to distinguish, the RTM was performed for these three relationships.

RTM individual results

The application of the RTM method to the horizontal channel of each considered OBS needs to take into account the slower propagation velocity of the S-waves. This means that these waves arrive later then the P-waves. Because of that, the time interval considered to preform the RTM is greater, approximately 30 s. Also, the only multiples that were removed were the water multiples.

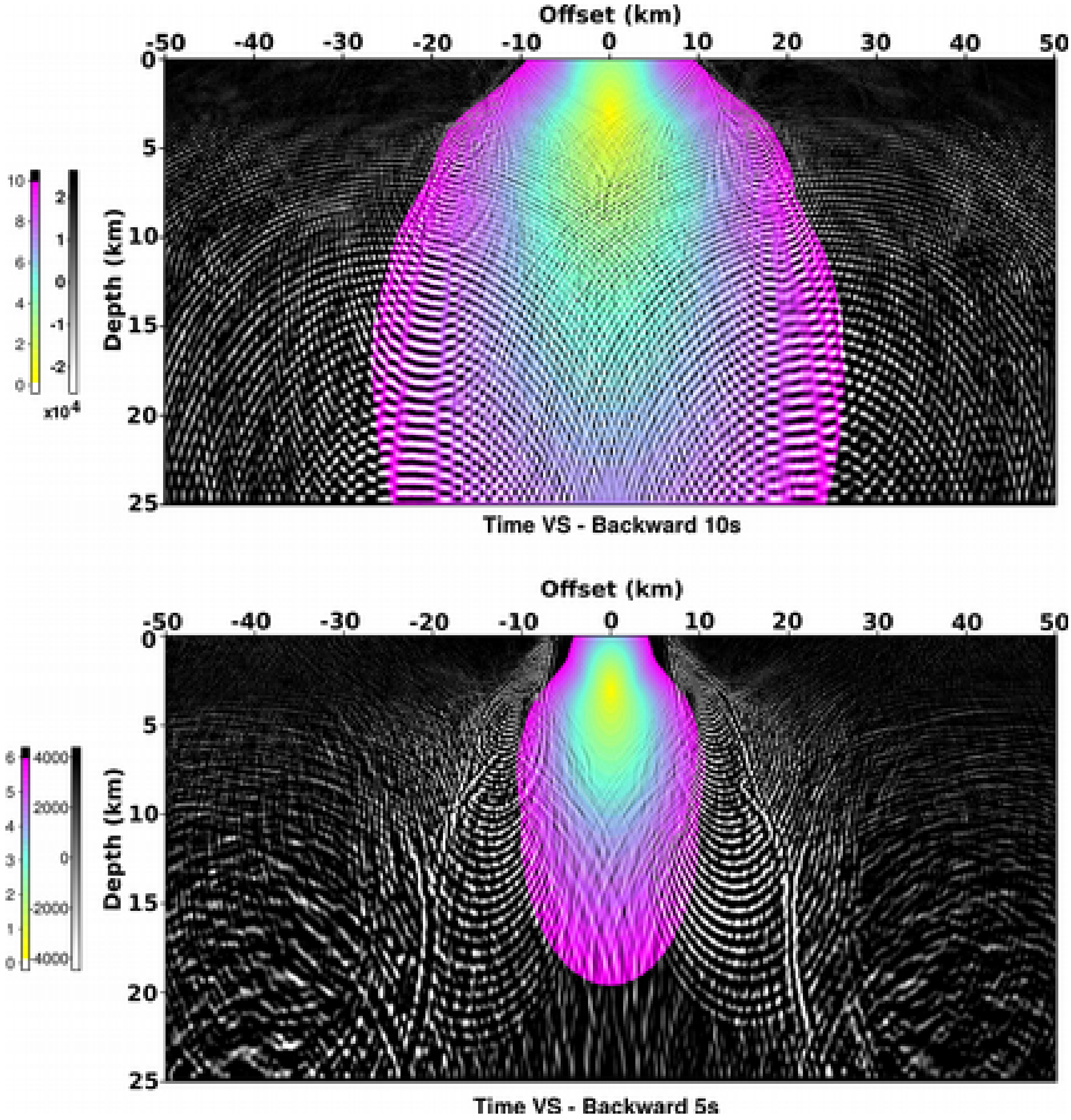

Figure 5.2.6.2 - Backward propagation of the wavefield for MC5OBS22. a) 10 seconds S-wave time step; b) 5 seconds S-wave time step

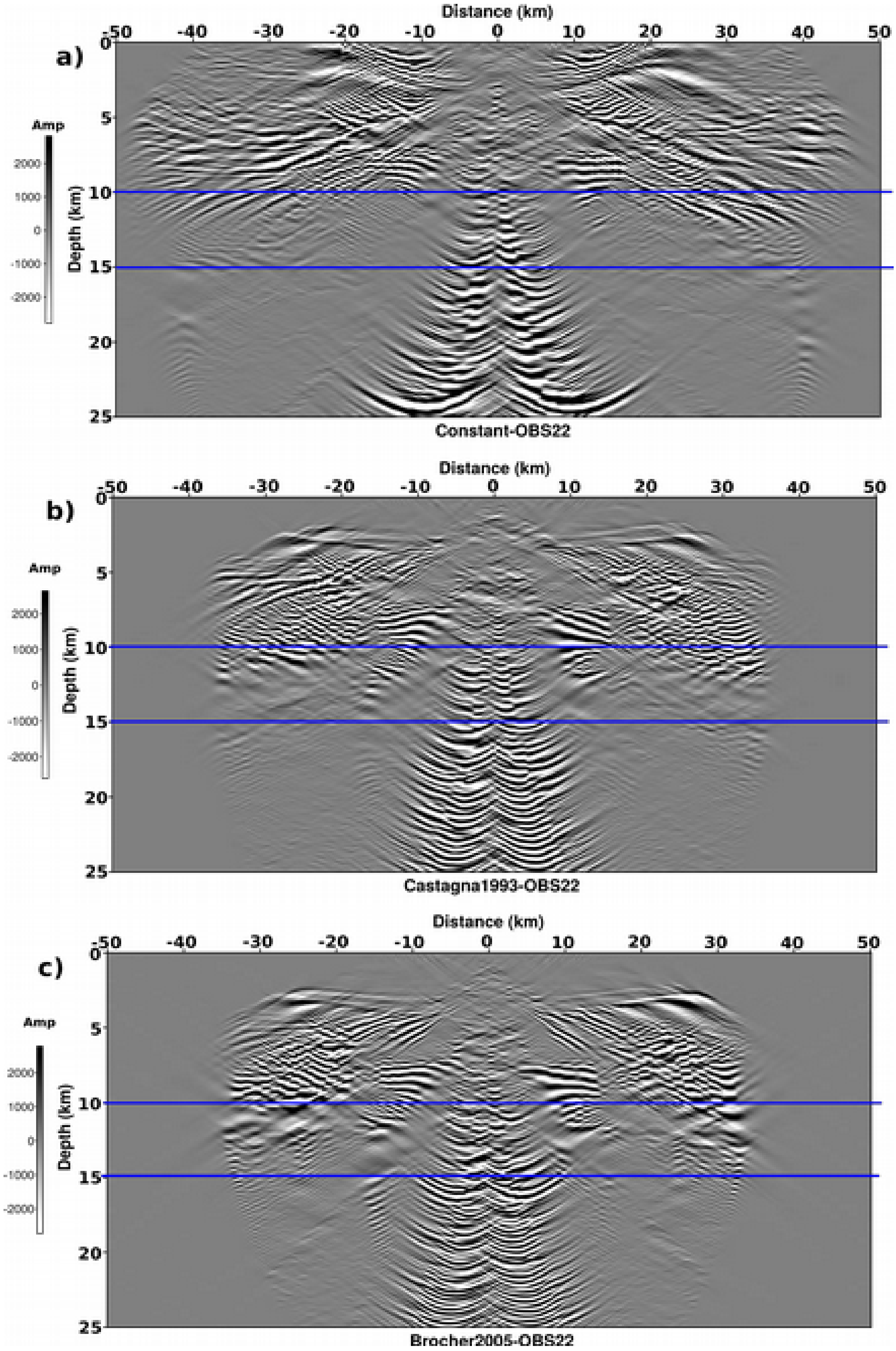

Figure 5.2.6.3 – RTM individual result for MC5OBS22. a) Using constant V_P/V_S ratio; b) Using relation 5.2.6.3 (Castagna et al., 1993); c) Using relation 5.2.6.4 (Brocher et al., 2005, 2008)

For the radial component, the forward propagation is done within the S-wave velocity model but the backward propagation within the P-wave velocity model. As mentioned before, the S-wave velocity is lower the P-wave meaning that we need not only to take into account a larger time interval but also to consider the signal with potential multiples. As shown in Figure 5.2.6.2, the signal that is recorded for each considered time step is different from the one recorded for the vertical component (Figure 5.2.4.1). The strength of the coherent signal within the time envelope is lower and noisier. Also, it is clear from the time envelope saved that the signal recorded reaches much shorter offsets.

The RTM result for MC5OBS22 with the three different V_P/V_S relationships is presented in Figure 5.2.6.3. The obtained result for the constant ratio (Figure 5.2.6.3-a) is the one where the greater offsets are reached (50 km). In terms of depth, all the relationships allow to retrieve similar refractors for the first 10 km. However, is the Brocher et al. (2005, 2008) relationship (Figure 5.2.6.3-c) that seem to allow to retrieve deeper refractors (between 10 km and 15 km). None of the relationships allow to return refractors deeper then 15km. The refractor retrieved, for the constant ratio, at 25 km depth is only for short offsets and it may be an artifact due possible reflectivity of the bottom boundary.

Contribution of the different types of waves

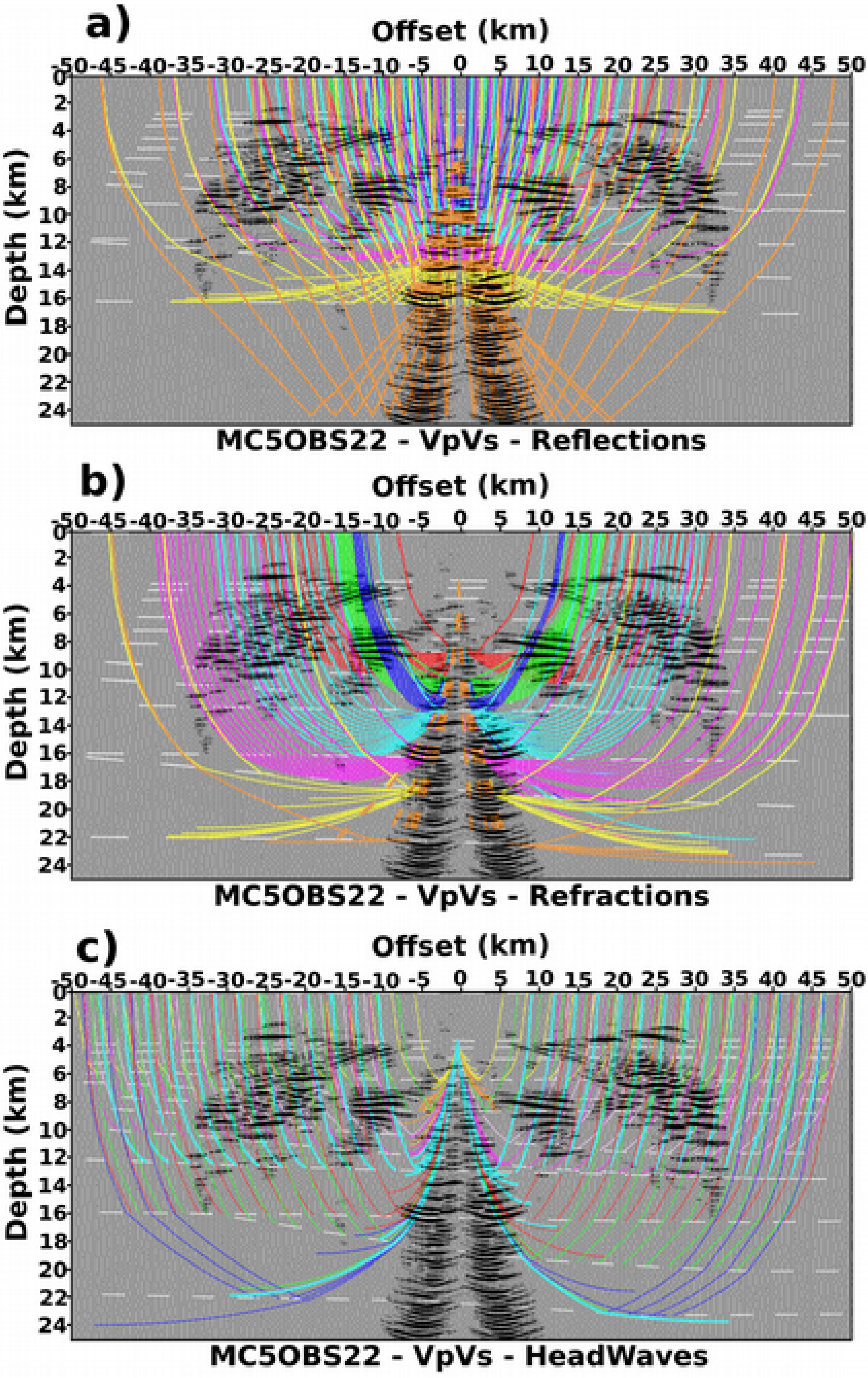

Figure 5.2.6.4 - RTM result for MC5OBS22 with the different ray types tracing overlaid - P-S-waves. a) Reflection waves; b) Turning waves; c) Head Waves

As we did for the vertical component, the analyses of the type of waves that are contributing for the RTM result was done for the radial component. As mentioned before, the RTM usually relies on the reflected wavefield. However, the applied method does not make any assumptions on this issue having, by principle, all types of waves within the propagating wavefield.

In the case of the radial component and as previously explain within this chapter, the wavefield traveling back to the Earth is a P-wave field but the wavefield traveling from the Earth to the stations is a S-wave field. In order to symbolize that, the traveling rays corresponding to each layer are traveling down as P-waves and they convert to S-waves as they hit the boundary of that layer and travel back up to the station as S-waves are presented for MC5OBS22 in Figure 5.2.6.4.

In Figure 5.2.6.4 we present the same different ray types as we presented for the vertical component: i) reflected rays (Figure 5.2.6.4-a); ii) turning rays (Figure 5.2.6.4-b); iii) head waves (Figure 5.2.6.4-c).

The first feature that needs to be mentioned is that the offsets covered by the S-waves are very short (between 5 km to 10km) and is almost only the reflected wavefield (Figure 5.2.6.4-a) that allows to retrieve deeper reflectors.

We retrieve reflectors/refractors up until 35 km offsets (to each side of the OBS) and 12 km depth even if we do not seem to have S-wave field traveling within those offsets. This means that either the P-waves traveling down to the Earth have a radial component that allows the correlation with the S-wave field or that the long offsets results are obtained due only to the correlation between P-wave field traveling down and upward.

Despite the possible explanation for retrieving reflectors/refractors at shallower depths and long offsets, we need to keep in mind that, in order to obtain a reflector/refractor, there needs to be a conversion of a wave at that offset for a particular layer. In the case of the radial component, we have a P-wavefield traveling down back to the Earth and then having the waves traveling in S-wavefield back to the OBS station, meaning that we are obtaining all the correct distances horizontally and vertically. If we take a closer look to the head-waves ray path (Figure 5.2.6.4-c), we observe that these are the only rays that convert at each layer where we obtain refractors/reflectors. If we consider that each of those rays travel down to the Earth as a P-wave and, as it hits the boundary, travels horizontally as a guided S-wave and back to the OBS also as an S-wave, the retrieved reflectors/refractors obtained at 30 km offset and up until 12 km depth, are easily explained. One can argue that, if that is the explanation for those reflectors/refractors, how come we do not obtain results for deeper layers. In fact, the majority of the rays traveling for deeper layers (red, cyan and dark blue) do not reach the OBS.

By comparing the results for the radial component (Figure 5.2.6.4) with the ones for the vertical component (Figure 5.2.4.4) at MC5OBS22, the relevance of the wavefield content becomes quite clear. While the method is able to retrieve reflectors/refractors in depth and offset for the vertical component, this is not true for the vertical component, where the depth and the extent of the refractors/reflectors is significantly shorter. We can argue that the method stops to be able to retrieve those refractors/reflectors, once the refracted wavefield stops to propagate in both or one of the directions, something that is quite clear in the radial component where for depths greater then 10/12 km we only have reflected wave paths and we stop to have turning waves, the head waves are very few and some of them are not able to reach the surface. This is in clear contrast with the vertical component where, because we have turning and head waves up until greater depths, we are able to retrieve the refractors/reflectors up until 20km depth but they become progressively shorter in offset after 15 km depth being in agreement with the progressively loss of refracted content.

RTM stacked result

The stacked result for each relationship was performed with the same parameters described in the previous section.

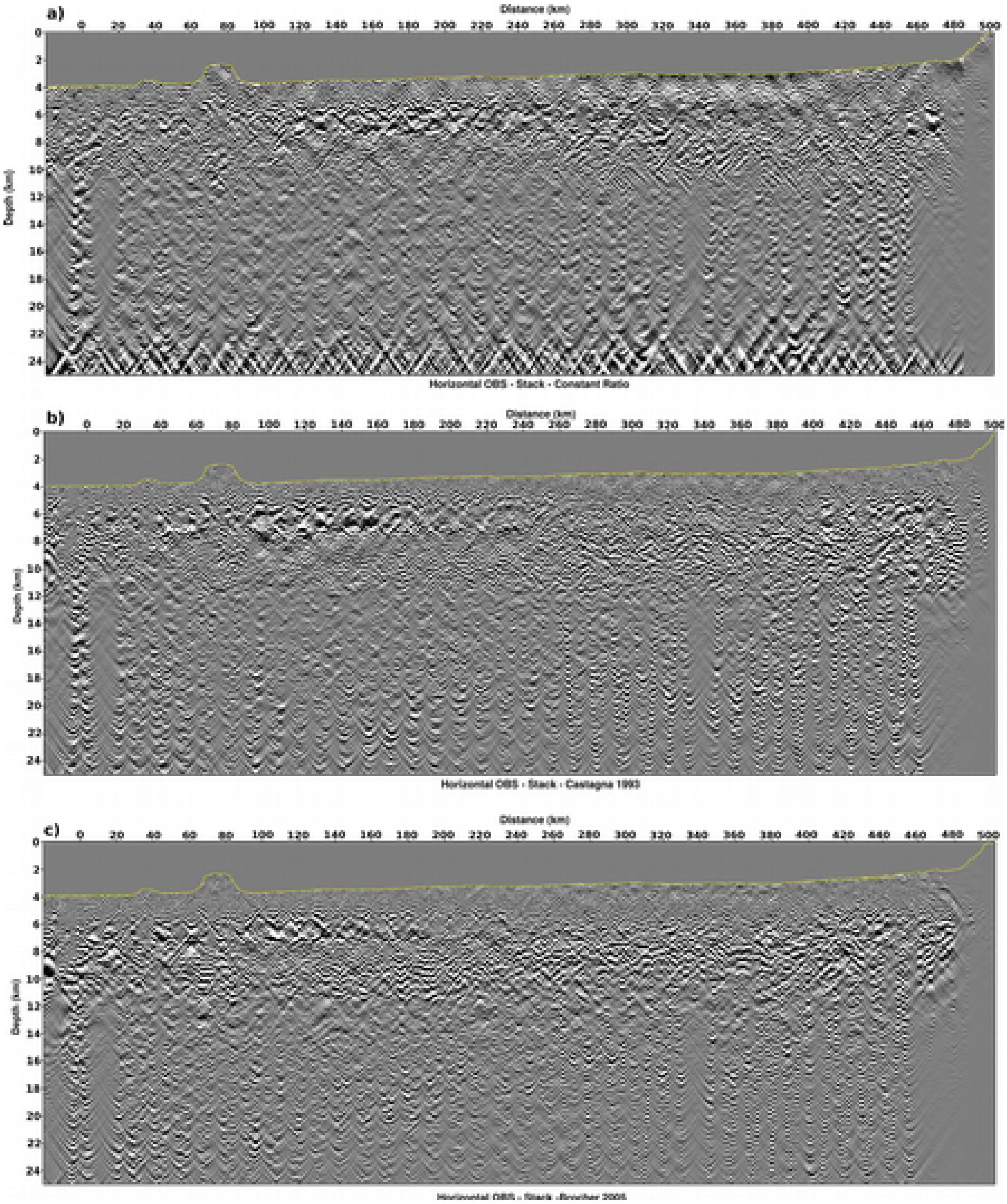

Horizontal OBS - Stack - Constant Ratio

Horizontal OBS - Stack - Castagna 1993

Horizontal OBS - Stack -Brocher 2005

Figure 5.2.6.5 – RTM stacked result for the 44 OBS stations of MC5 profile. a) Using constant V_P/V_S ratio; b) Using relation 6.2.6.3 (Castagna et al., 1993); c) Using relation 6.2.6.4 (Brocher et al., 2005, 2008)

As it is possible to observe from Figure 5.2.6.5, in the stacked result for the horizontal radial channel of the 44 OBS stations on profile MC5, the obtained refractors are much harder to follow in offset and they reach much shallower depths when compared with the results for the vertical channel. Further interpretations and results will be presented in later sections.

6. Results and Discussion

In this chapter the results obtained from the developed and applied methods are presented along with their discussion. The direct results from each method are described and discussed in light of their coherence, potential to retrieve knowledge from the application of the methods and previous knowledge of the area.

The structure of the chapter is equivalent to the one found in the Methodology chapter. We recall, in Figure 6.1, the major structures and profiles of the research area.

The process and results of the merging of the three profiles shown in Figure 6.1 will also be presented and discussed. Then the 3 profiles are integrated with the 3D gravity inversion results, giving relevance to the goal of having a regional overview and interpretations of such a long profile (almost 1800 km) that comprise to necking zones correlated with the opening of the ocean and also adding purpose to the 3D gravity inversion.

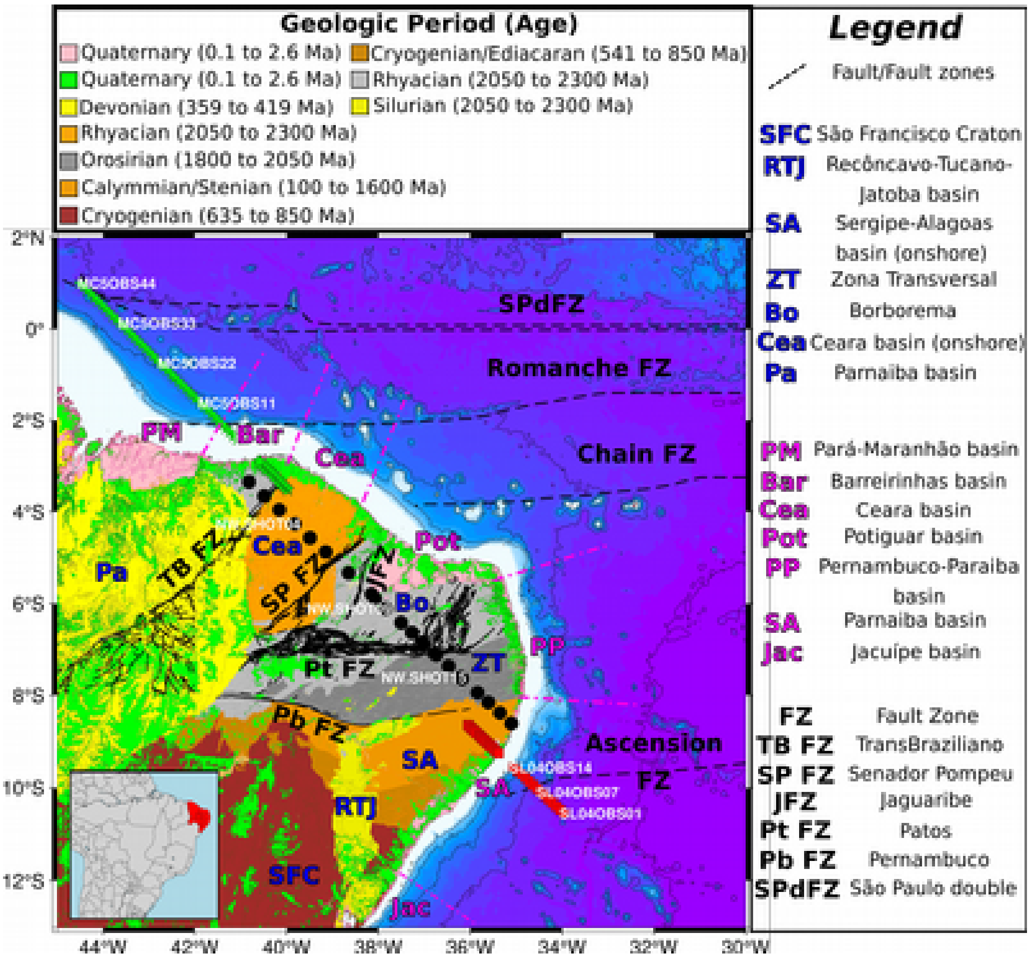

Figure 6.1 – Geology of the research area and studied profiles. (Green stars – MC5 profile from the MAGIC experiment; Black dots – NW profile of the INCT-ET project; red squares – SL04 profile from the SALSA experiment)

6.1. 3D Gravity inversion

The first results to be presented will be the 3D gravity inversion for the entire research area, recalling the Figures 5.1.6.2 and 5.1.6.3 and integrating those results with the regional geology and geodynamic context. Following those results, we will present the 2D profiles from MAGIC experiment and the northern part of the SALSA experiment We will compare the seismic Moho depth of those profiles with the gravity Moho depth given by the gravity.

Then we will present the process and results of merging the three profiles – MC5, NW/INCT-NE and SL04 - into a single combined 2D profile of almost 1800 km in length. This will give the opportunity to discuss the geodynamics of the opening of the Atlantic ocean in two distinct places that are the Central segment and the Equatorial segment. The merge was done over a line that best fits all the WAS profiles that are sub-parallel to each other.

6.1.1. Regional results

The 3D gravity inversion with the seismic points constraints has two main elements that are essential to understand: i) the inversion of the Bouguer anomaly alone returns an average reference Moho depth (z_{ref}) with a direct link with the density contrast ($\Delta\rho$) that best fits the transition between the crust (including sediments) with lithospheric mantle; The reference Moho depth retrieved from the inversion is 22.5 km and the density contrast of 700 kg/m^3, for the entire research area; ii) the inversion of the that anomaly together with the seismic points constraint calculates the variation and consequent geometry of the Moho discontinuity depth around that reference level.

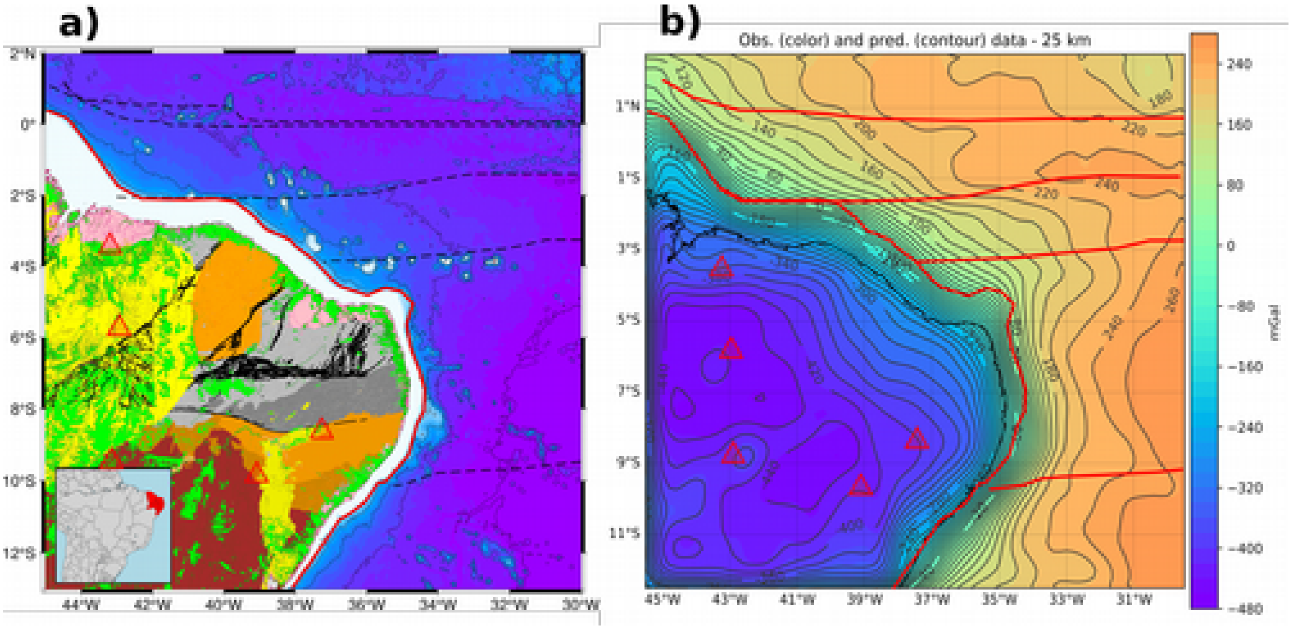

Figure 6.1.1.1 - Inversion of the Bouguer anomaly result against geology features of the research area. a) Main geological features of the research area (for a complete description of each feature see Figure 7.1-a); b) Bouguer anomaly inversion (color – observed Bouguer anomaly; contour – predicted Bouguer anomaly). Red triangles – points where the predicted and observed Bouguer anomaly have a miss match; Red lines – sketch of the limit of the continental platform and main offshore faults

The fit between the observed and predicted (inversion) Bouguer anomaly for the Moho discontinuity (Figure 6.1.1.1-b) is really good where the gravity residuals have a mean of 0.14 mGal and a standard deviation of 6.40 mGal. The red triangles placed in both images of Figure 6.1.1.1, detail the locations where we found the biggest miss-fits such as transitions between different geological terrains and main tectonic fault zones. The platform shelf and major fault zones are shown by the red lines.

The sketch of the platform shelf and the major fault zones, in the offshore environment, show that these structures have a major influence in the Bouguer anomaly with a progressively increasing anomaly where the contours are perpendicular to the fault areas and, within the platform shelf area, the contours follow it’s shape. The size of these structures clearly influence the gravity signal but, most importantly, they have an influence in depth and in the geometry of deeper layers as is the case of the Moho discontinuity.

We can not forget that we are analyzing the gravimetric signal that is directly connected with the structures that are deeper then the Moho discontinuity. This means that the fault systems present within the research area may have a strong influence at depth and a part on the shaping those layers.

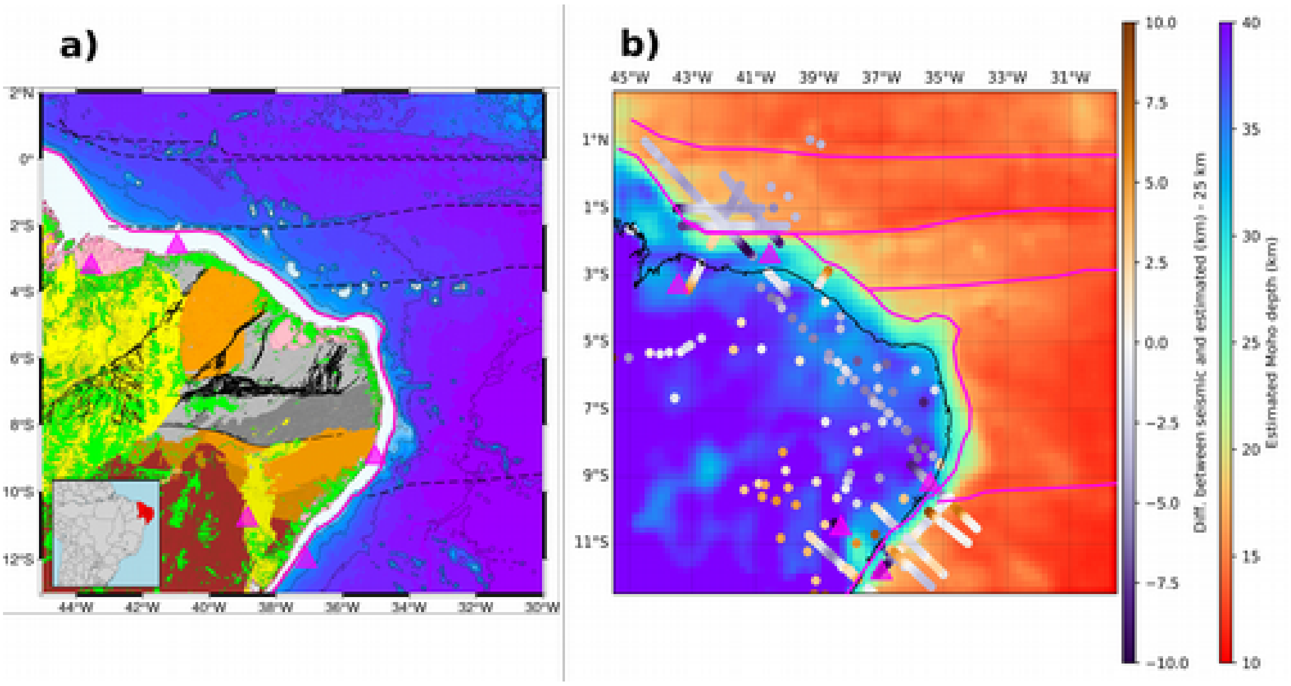

Figure 6.1.1.2 – Estimated Moho depth compared with given depth by seismic points against geology features of the research area. a) Main geological features of the research area (for a complete description of each feature see Figure 7.1-a); b) Estimated Moho depth result from gravity inversion with seismic point constrain. Pink triangles – points where the miss match between Moho seismic depth and Moho gravity depth is higher; Pink lines – sketch of the limit of the continental platform and main offshore faults

The Moho depth result retrieved from the gravity inversion with the seismic constraints and comparison with the Moho depth given by the seismic points (Figure 6.1.1.2-b) and also with the geology (Figure 6.1.1.2-a) are presented. From a general point of view we find a pattern where we have miss matches ranging from -7.5 km to 7.5 km between the Moho depth given from the seismic points and the Moho depth given by the gravity inversion. There are bigger differences to areas that correspond to land/ocean transitions (necking zone). However, if we compare these results with the initial difference between seismic points and Moho depth given by CRUST1.0 (Figure 5.1.6.2-a) we can see that, for some of this locations, the values improved or have similar absolute differences (for example the land stations for MC4 and MC5, on the Equatorial margin – Figure 6.1.1.2-a, pink triangles. The difference between the seismic points and the gravity inversion along line in Borborema province (corresponding to NW/INCT-NE profile – Figure 6.1, black circles) and the points in the surrounding area seem to increase. However, they become all overestimated giving coherence, less dispersion and removing outliers. The standard deviation and the mean values for the initial model (Figure 5.1.6.2-b) and the inversion (Figure 5.1.6.3-b), clearly decrease. There are several fault zones on land too whom the inversion responds and being one of the reasons for the fluctuation of the Moho depth and being more coherent with the seismic points in terms of trend. The 2D profiles analysis in the next section, we will show this feature more clearly.

As in Figure 6.1.1.1, the pink lines represent the sketch of the platform shelf and the oceanic fault zones. We find that two of the places where we have the biggest miss match correspond to the same places mentioned before – the transition between the Recôncavo-Tucano-Jatoba basin and the São Francisco craton; the transition between the Parnaíba basin and the Pará-Maranhão basin. However all the other highlighted locations concern the continental margin. In the next sections, we going to analyze the accuracy of the inversion in more detail along the 2D seismic profiles, where the inversion is most constrained.

6.1.2. Profile analysis

Three 2D seismic profiles – MC5, NW/INCT-ET profile and SL04 - can be assembled as a unique reference profile of 1800 km in length spanning from the Equatorial Atlantic ocean, through the North-East Brazilian continent to the central South Atlantic ocean. Their location is shown in Figure 6.1. The results presented in Figure 6.1.2.1 allow to have a overall perspective of the Moho discontinuity geometry, possible explanations for miss fits such as the geological structures present, and the consistency of the method. For each profile we added the coast limit (land to ocean transition in red dotted lines) and the major fault zones that the profiles cross (in black dashed lines). We also have the OBS stations crossings for the MAGIC and SALSA experiments (red rectangles) where gravity and seismic Moho depth values were added, for those crossings.

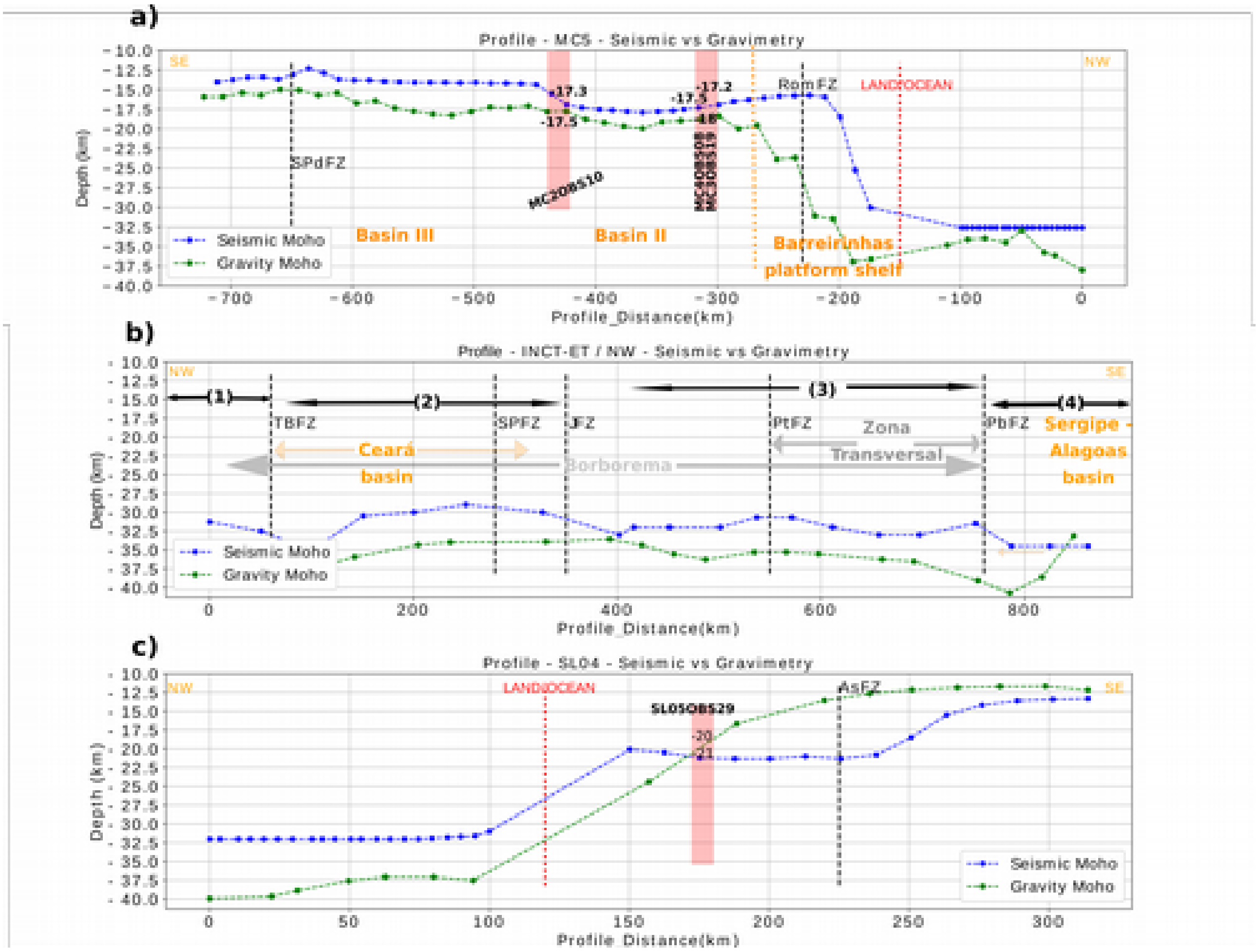

Figure 6.1.2.1 – 2D comparison of the Moho depth variation given by Gravity inversion and Seismic points. a) MC5 profile from the MAGIC experiment; b) NW Profile from INCT-ET project; c) SL04 profile from the SALSA experiment. Red dotted lines: land to ocean transition; Black dashed lines - major fault zones that the profiles cross; Red squares - OBS stations crossings for the MAGIC and SALSA experiments where gravity and seismic Moho depth values were added for each profile. **(the horizontal scale is different between profiles – corresponds to the length of each profile)**

Along MC5 profile (Figure 6.1.2.1-a), we obtain quite a good match between gravity and seismic Moho either on land as or deep sea (between 0.5 km and 5 km), except in the necking zone (12 km) between -150 and -250 km distance. This large miss-match may happen by a combination of following reasons: 1) the necking zone is very sharp, where the Moho depth goes from approximately 32/35 km depth to 16/18 km within a -60/70 km horizontal distance; 2) the necking zone is not in isostatic equilibrium, an element that has a great influence in the gravity anomaly values but is not considered in the inversion; 3) one unique value of density contrast may not be sufficient to properly invert areas with such sharp variations.

Between -250 and -425 km, both Moho are relatively flat, the gravity Moho lies about 1 km deeper then the seismic Moho, which is about 17.5 km depth. The seismic Moho sharply rises 2.5 km at -450 km. From that distance until -720 km, the seismic Moho is flat at 15 km depth while the gravity Moho undulates around 16-18 km. Reaching the volcanoes structures and the marked SPdFZ the gravity Moho approaches the depths of the seismic points.

If we take into account the velocity model available for this profile (Figure 2.1.2-a; (Schnürle et al., 2023)), this -450 km distance corresponds approximately to the end of the Basin II limit to the NW, entering the Basin III and where upper and lower crust thicken up until the volcanic structures, respectively. Even thought the difference between the two Moho depth is small, the fact that they have different trends for Basin III may allow us to argue about the nature of the crust. Recalling Figure 2.1.2-a, where the nature of the crust is analyzed for this profile, the crust is interpreted as a combination of the middle lower continental crust overlaid by a highly magma-intruded crust, making it distinguishable from the crust in Basin II. Taking into account that the main parameters to calculate the Bouguer anomaly is the thickness and the density for a particular layer, that the Bouguer anomaly progressively decreases in the profile direction (Figure 6.1.2.1-a) and the crustal velocities (Schnürle et al., 2023) are lower for Basin III, the fact that there is a bigger difference between the two Moho discontinuities may be explained by either an average lower density crust and/or a lack of isostatic equilibrium due to the volcanic structures.

Along the NW/INCT-NE on land profile (Figure 6.1.2.1-b), we may distinguish four different areas (numbered withing Figure 7.1.2.1-b): 1) Northwest shoreline up to the TransBrasiliano Fault Zone, the seismic and gravity Moho are sub-parallel until 100 km distance. The Moho has a dipping trend from 31 km to 35 km (seismic depth); 2) TransBrasiliano Fault Zone to Jaguaripe Fault Zone – Ceará basin – where the Moho range is 31 km and 35 km (seismic depth) where, the unique point at 35 km lies close to the TBFZ; 3) Jaguaribe Fault Zone and Pernambuco Fault Zone – Borborema Plateau and Zona Transversal, location where the variation is between 31 km and 33 km (seismic depth) ; 4) Pernambuco Fault Zone to Southeast shoreline – Sergipe-Alagoas basin, where we find a constant seismic Moho at 34 km (seismic depth) and a gravity Moho that shallows steeply to reach a depth similar to the seismic one. The Moho depths within each of these four areas are within the intervals considered in several previous studies. This sub-division is sustained by superficial geology characterization, geochemical characterization or seismic velocity properties (Almeida et al., 2015; AMARAL, 2010; da Silva et al., 2021; Dias et al., 2015; dos Santos et al., 2008; Lima et al., 2015; Rosana M. N. Luz et al., 2015; Oliveira, 2008; Osako et al., 2011; Pacheco Neves, 2021; Padilha et al., 2014; Soares et al., 2010; Van Schmus et al., 2011). In R.M.N. Luz et al. (2015) and Rosana M. N. Luz et al. (2015), where receiver functions studies were performed to characterize the boundary between crust and lithospheric mantle, we have the following depths for the same areas – 1) 30 km to 32 km 2) 30 km to 35 km; 3) 30 km to 32 km; 4) 30 km to 37 km. In (Osako et al., 2011), a gravimetric study acquired along the same line as the NW/INCT-NE seismic profile, we find the following depths: 1) 28 km to 32 km; 2) 30km to 32 km; 3) 28 km to 30 km; 4) 30 km.

One feature on the land profile is the results obtained for the Borborema plateau area (between the Patos and Pernambuco Fault zone – Figure 7.1.2.1b) where the thickening of the crustal layers is significant and well documented (De Oliveira and De Medeiros, 2012; Gusmão De Oliveira et al., 2023; R.M.N. Luz et al., 2015). Within the different authors (Gusmão De Oliveira et al., 2023) the thickening of the crust is between 4 km to 8 km. From our results, the depth of the Moho discontinuity, given by the gravity inversion, deepens from 35 km depth to 38-40 km depth between Patos Fault zone and the Pernambuco Fault Zone and then shallows rapidly but it is not followed by the seismic Moho that has a variation of 1.5 to 2.5 km for the same area.

The last profile, SL04 (Figure 6.1.2.1-c), we obtain similar mismatch on land (with differences lower or equal to 5 km), with a deeper gravity Moho and a shallower gravity Moho offshore. Across Alagoas basin and the Ascension Fault Zone, the Moho depth given by the seismic is deeper than the gravity one. Oceanward the fit improves, possibly due to a simpler nature of the crust. In this case, we obtain a gravity Moho depth geometry that smoothly becomes shallower from the beginning of the necking zone (36 km) up to the end of the Ascension Fault Zone (15 km) and then follows horizontally at the shallow depths. The discrepancy observed between the necking zone and the oceanic domain can be related to the presence of an anomalous velocity layer overlying the interpreted seismic Moho. If we consider a Moho at the top of the AVL, the fit between the two Moho improves significantly. As a consequence, this could indicate that the AVL is from altered mantellic nature. However, this feature will be further discussed when we present the other profiles of the SALSA experiment, further in this section.

Figure 6.1.2.2 – Comparison between gravity and seismic Moho depth for all the 2D profiles from MAGIC experiment. a) Zoom of the MAGIC experiment area and each profile location; b) MC1 profile; c) MC2 profile; d) MC3 profile; e) MC4 profile; Red dotted lines: land to ocean transition; Black dashed lines - major fault zones that the profiles cross; Red squares - OBS stations crossings for the MAGIC experiment where gravity and seismic Moho depth values were added for each profile. **(the horizontal scale is different between profiles since it is particular of each profile length)**

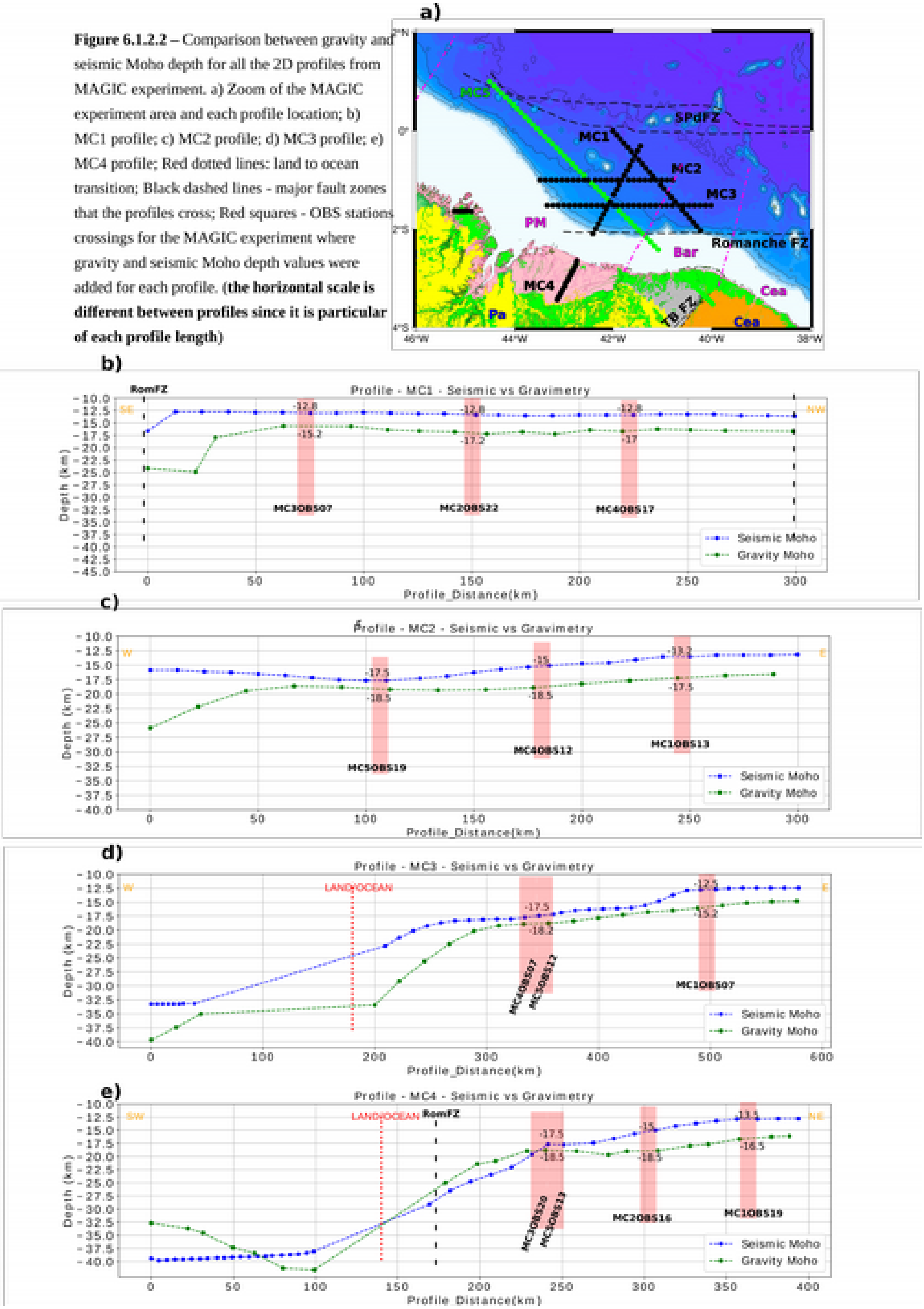

In Figure 6.1.2.2 we present the comparison between the seismic Moho depth and the gravity one for all the other profiles of the MAGIC experiment, along with their location (Figure 6.1.2.2-a). There is a consistent difference of 2.5 km to 3.5 km between the seismic and gravity Moho depths for the points that are in oceanic environment. This difference is also characterized by the fact that the gravity Moho depth is always deeper then the one obtain from the seismic points. This consistent difference may be related primarily with a poor initial approximation of the crustal layers thicknesses (in particular the lower crust) by CRUST1.0 (Figure 5.1.6.2-a) that takes into account a total thickness that varies between 2 km to 4 km for purely oceanic environment and between 16 km to 20 km in the a transition land/ocean environment. Even if the density contrast remains practically the same for the entire area of MAGIC experiment, the considered thickness values for the crustal layers has, as direct consequence, the overestimation of the Moho depth given by the gravity inversion and a resulting gravity Moho depth consistently deeper then the seismic Moho depth. This difference is quite clear and larger for MC1 (Figure 6.1.2.2-b) and MC2 (Figure 6.1.2.2-c). In the case of MC1 profile, interpreted by Moulin et al., (2021), the crust is of proto-oceanic nature (Figures 2.1.1 and 2.1.2) with a thickness of 5-7 km and a bottom depth limit of almost 15 km. This interpretation clearly miss matches the initial Moho depth and even if it is true that the gravity inversion improves the depth of the gravity Moho for this profile, it is not capable to give a better result, possibly due to the unique density contrast value. For the MC2 profile, interpreted by Aslanian et al., (2021), the crust nature is interpreted as continental crust underlain by a possible upper lithospheric mantle or lowermost continental crust up until the crossing with the MC4 profile (Figure 6.1.2.2-c), followed offshore by proto-oceanic crust. After the necking zone, both Moho discontinuity depths become closer up until the crossing with profile MC5 and from that point forward (W-E direction in Figure 6.1.2.2-c) the difference grows and becomes stable with a 3-3.5 km difference. This behavior re-enforces the poor initial approximation of the Moho depth by CRUST1.0 but it also restricts the area for that poor approximation. From this analyses, we may argue that in domains between unthinned continental crust and real oceanic crust, or close to fault zones the crustal nature is far more complicated that is supposed by CRUST1.0 model. This type of WAS data should be integrated in a future CRUST model since they are essential to better understand this complex areas.

The match between both Moho depths is clearly better for MC3 profile, with a average difference of 1-2 km (Figure 6.1.2.2-d). This profile has a W-E direction and runs closer to the Barreirinhas platform shelf, parallel to the Romanche Fault zone. The larger difference limit (2 km) is reached after the interpreted limit of the beginning of the proto-oceanic crust, giving sense to the described behavior and possible justifications for the obtained results for MC1 and MC2.

A closer look at MC4 profile (Figure 6.1.2.2-e), a profile that crosses all the others in a oblique direction (approximately SW-NE) to the platform shelf, actually brings coherence to the previous discussion points. The differences between both Moho depths becomes larger just before the crossing with MC2 profile and that difference is maintained for the crossing with MC1 and beyond in the NE direction. Another interesting feature of this profile is the fact that is the one where the both Moho depths have the best fit in the necking zone, starting at the land stations closer to the shore. It is the profile where the results of the gravity inversion clearly improve the geometry of the Moho in the transition land/ocean. The obtained results imply that the Moho depth at this location is actually shallower then the neighboring locations. Recalling the crustal interpretation of this profile (Figure 2.1.2-b), it is clear that the lower continental crust thins more rapidly when compared with the other profiles and is underlain by a anomalous velocity layer interpreted as altered lowermost continental crust or upper lithospheric mantle. A potential explanation for this thinning and anomalous velocity layer may be that, at the beginning of the opening of the equatorial margin, there was not enough crustal material in the pull-apart opening direction (E-W) and a more ductile crustal/mantellic material was exhumed from this area contributing to the formation of the deep-sea basin basement.

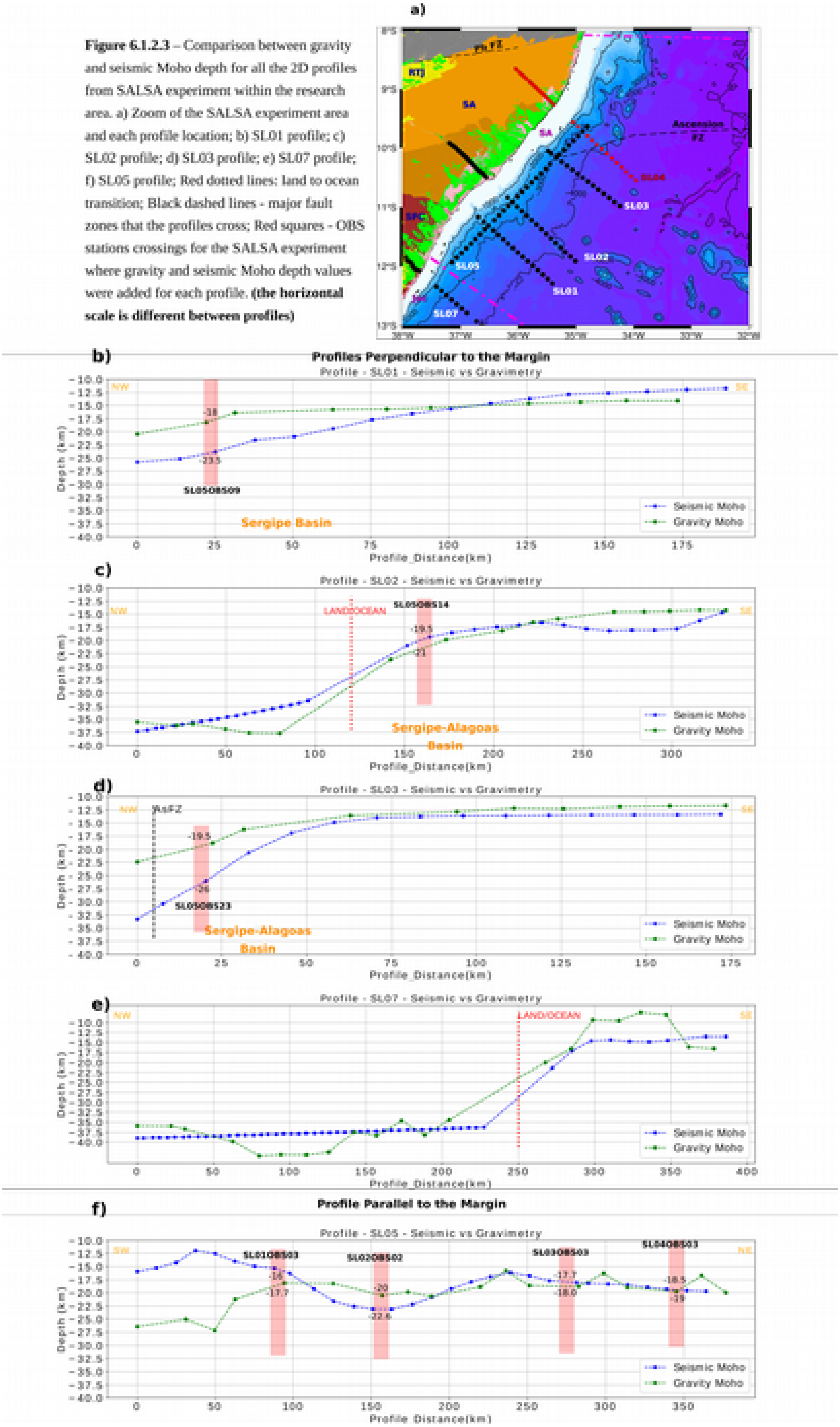

Figure 6.1.2.3 – Comparison between gravity and seismic Moho depth for all the 2D profiles from SALSA experiment within the research area. a) Zoom of the SALSA experiment area and each profile location; b) SL01 profile; c) SL02 profile; d) SL03 profile; e) SL07 profile; f) SL05 profile; Red dotted lines: land to ocean transition; Black dashed lines - major fault zones that the profiles cross; Red squares - OBS stations crossings for the SALSA experiment where gravity and seismic Moho depth values were added for each profile. **(the horizontal scale is different between profiles)**

The 2D profiles from SALSA experiment that are located within the research area, are presented in Figure 6.1.2.3. We need to distinguish SL05 profile from the remaining profiles since it has a different orientation and the stations are located parallel to the margin just after the platform shelf. Also, this profile crosses other profiles – SL01 to SL07 – in the necking zone and is particularly useful to evaluate the coherence and robustness of the method. The crossing points are marked with red rectangles in each profile (Figure 6.1.2.3) with the respective value of seismic and gravity Moho depth at those points. We find that, for those crossing points, the difference between the two Moho is consistently close to 0.5 km difference.

The match between seismic and gravity Moho depth is quite good for the SALSA profiles, in particular for profiles SL02 and SL03. The difference has a miss-fit between 0.5 km to 1.5 km, being within the lower limits of the difference found for the MAGIC experiment profiles. As discussed previously for the MAGIC profiles, there is a clear poorer initial model of the Moho depth that the inversion is not capable to improve in the MAGIC experiment region, that explains the miss match between gravity and seismic Moho for the MAGIC area and that may also explain the better fit for the SALSA experiment profiles, where the initial model for the Moho depth is slightly better (Figure 5.1.6.2-a). Also, the oceanic to continental crust transition in more clear and abrupt for the SALSA area when compared with the MAGIC area. Finally, the gravity Moho depth, for the MAGIC profiles, is consistently overestimated (deeper then the values given by the seismic points), while in the SALSA experiment profiles, we do not have the same pattern.

We may question if there is a relation with the intrinsic characteristics of the crustal layers for the MAGIC profiles when compared with the SALSA profiles. The dynamic of the opening of the two parts of the margin – MAGIC and SALSA areas - is quite different. As a matter of facts, on one hand, after the Tucano rift aborted (Berriasian/Valanginian – 145-139 Ma), the Jacuipe, Sergipe and Alagoas margin segments underwent a strike-slip phase between the Barremian and the Albian times (Evain et al., 2023). Afterwards, the opening progressed to a direction perpendicular to the margin. As a consequence, those margin segments are characterized by a sharp necking zone and oceanic crust immediately oceanward with the exception of the SL07 and SL08 in the Jacuipe basin, where an anomalous velocity zone is intercalated (Evain et al., 2023; Figure 2.2.5-a). On the other hand, the Para-Maranhão margin opened as a pull-apart bounded to the north by the SPdFZ and to the south by Barreirinhas and RomFZ. Consequently, the Para-Manhão margin is characterized by wider necking zone directly followed by a exhumed continental crust basement.

On SL03 profile, a 5 km miss-fit of the two Moho depths is observed. The miss-fit smoothly decreases to almost 0 km at 50 km distance (the entire necking zone). Oceanward the fit is within the inversion accuracy. A similar miss-fit is observed on SL05 at the crossing with SL03.

The SL02 and SL01, parallel to SL03 and SL04 but further SW (Figure 6.1.2.3-a), image the end of the Alagoas basin and the Sergipe basin. The miss match within the SL01 is, on average, 2.5 km. The miss match in the necking zone is very large (about 5 km) up until 40 km distance (crossing SL05 at 25 km distance). It may be explained by the observed thick anomalous velocity layer (Figure 2.2.3-b) (Pinheiro et al., 2018; Aslanian et al., 2015, 2023) within the necking zone, that is also imaged and interpreted by Evain et al. (2023) for the same region in SL05 profile. As for the Sergipe basin the miss match between the two Moho progressively decreases almost to zero. In the oceanic domain the miss match progressively increases to 2 km. As for SL02 profile, the match between the two Moho discontinuities is quite good with an overall difference of 1 km. The largest miss fit reaches 5 km at 80 km distance; it coincides with the drastic thinning of the upper crust and the development of an up to 8 km thick Sergipe basin (Figure 2.2.3-a). The second largest miss fit of up to 3.5 km is located between 225 km and 325 km (Figure 6.1.2.3-c), with an anomalous velocity zone and a volcano structure at its center.

The SL02 profile presents similarities to SL04 profile. For instance, on land the upper crust thins abruptly leaving space for the deposition of the Sergipe-Alagoas basins: up to 5 km thick while 8 km thick in the Sergipe basin. The AVL along SL02 raises the same questioning about the nature that composes the AVL as in SL04. Weather the AVL is composed by altered lower crust or mantle, the inversion is solely dependent on the density contrast with the “normal” mantle and does not allow to determine the nature. The differences between seismic and gravity Moho may be explained by a combination of factors: i) the complex geology on land, with the older Sergipe-Alagoas belt transitioning to the Cenozoic Sergipe-Alagoas basins (Figure 6.1.2.3-a); ii) sharp continent/ocean transitions in terms of geometry of the layers but also their intrinsic characteristics; iii) the fact that the inversion does not take into account the isostasy equilibrium and only considers a unique density contrast value.

The SL07 profile is characterized by a flat and smoothly rising seismic Moho for the continental domain (Figure 6.1.2.3-f; between 0 to 225 km distance). For the same distance, the gravity Moho undulates around the depths of the seismic Moho, excepting between 50 to 140 km distance, where it goes deeper for 2.5/3 km. This distance corresponds to the crossing of the Recôncavo-Tucano-Jatoba basin. According with Aslanian et al. (2023) strong seismic reflectors within the bottom of the lower crust suggest a flat Moho with large depocenters in the basins above and highly deforming the top of the upper crust. In what concern the gravity Moho result, we may argue that, on one hand we can have a thinner upper crust at that location that would allow the gravity Moho result to be closer to the seismic Moho or, on the other hand, a deeper and bending Moho that accommodated the formation of the Basin. On the oceanic domain, our research area only has the first part of the seismic points of SL07, ending just after the interpreted AVL (Figure 2.2.4). For this part of the profile, the miss-fit between seismic and gravity Moho is related with the AVL where, if we consider a Moho overlain the AVL the match between the two Moho would be clearly improved.

The depth variation shown in SL05 profile (Figure 6.1.2.3-e) contributes to the interpretation of a highly segmented margin for the SALSA experiment. Following this profile in the SW-NE direction (crossing first SL01 and SL04 last), there is a very large difference between gravity and seismic Moho of approximately 10 km that rapidly decreases just before the crossing of this profile with SL01 profile. This part of the SL05 profile, Evain et al. (2023), observe a high anomalous velocity and low density lithospheric mantle. According with Loureiro et al. (2023) and Aslanian et al. (2023), this anomaly is described as the prolongation of the “boutonneire” to the NE identified at the Camamu triple junction in the SALSA profiles to the SW. A low density of the lithospheric mantle in this area implies a lower density contrast between crustal and mantellic layers. Since the inversion considers a unique value for the density contrast and that value is quite high (700 kg/m³), this miss match is easily explained and actually re-enforces the interpretation done by Evain et al., (2023) for that area. For the remaining SL05 profile, the difference between the two Moho discontinuities varies between 1.5 km and 4 km and we can distinguish, at least, two areas:

1) the variation of the Moho between 100 km and 200 km (the crossing with SL01 and just after the crossing with SL02 – Figure 6.1.2.3-e). In this area the gravity Moho is shallower then the seismic Moho with a maximum difference of 1.5 km, and while the latter has a parabolic shape, the gravity Moho is mostly flat. This area corresponds to an interpreted thicker crust underlain by a normal lithospheric mantle (Evain et al., 2023). When compared with the Jacuipe segment where the difference is, on average, 10 km between 0 km and 100 km, in the Sergipe segment the difference is, on average, 2.5 km.

2) the variation of the Moho discontinuity between 200 km to the end of the profile, at 380 km (crossing SL03 and SL04 – Figure 6.1.2.3-e). Within this area the SL05 profile is crossing the end of the Sergipe basin, crossing the entire Alagoas basin and ending after the Ascension Fault Zone in the extreme NE of the SALSA experiment area. According to Evain et al. (2023), this area is characterized by a low dip deeper Moho towards the NE, with a progressive thickening of the lower

crust that is more pronounced after crossing profile SL04. An anomalous high velocity and low density mantellic layer is interpreted from the velocity model. The difference of 4-4.5 km between the two Moho discontinuities is fairly constant within this area, the gravity Moho being deeper then the seismic Moho. Their trend is also similar even if the gravity Moho presents some localized outliers.

From a general point of view, we may correlate a better fit between the seismic and gravity Moho with a simpler crustal structure and a worst fit with a more complex crustal structure – both in space as in composition. Also that the inclusion of the WAS profiles play a relevant role in the comprehension of the crustal structure not only within the applied method but should be taken into account in a possible review of the CRUST1.0 model – in the study area and other locations where this type of profiles are available.

Sub-parallel profiles

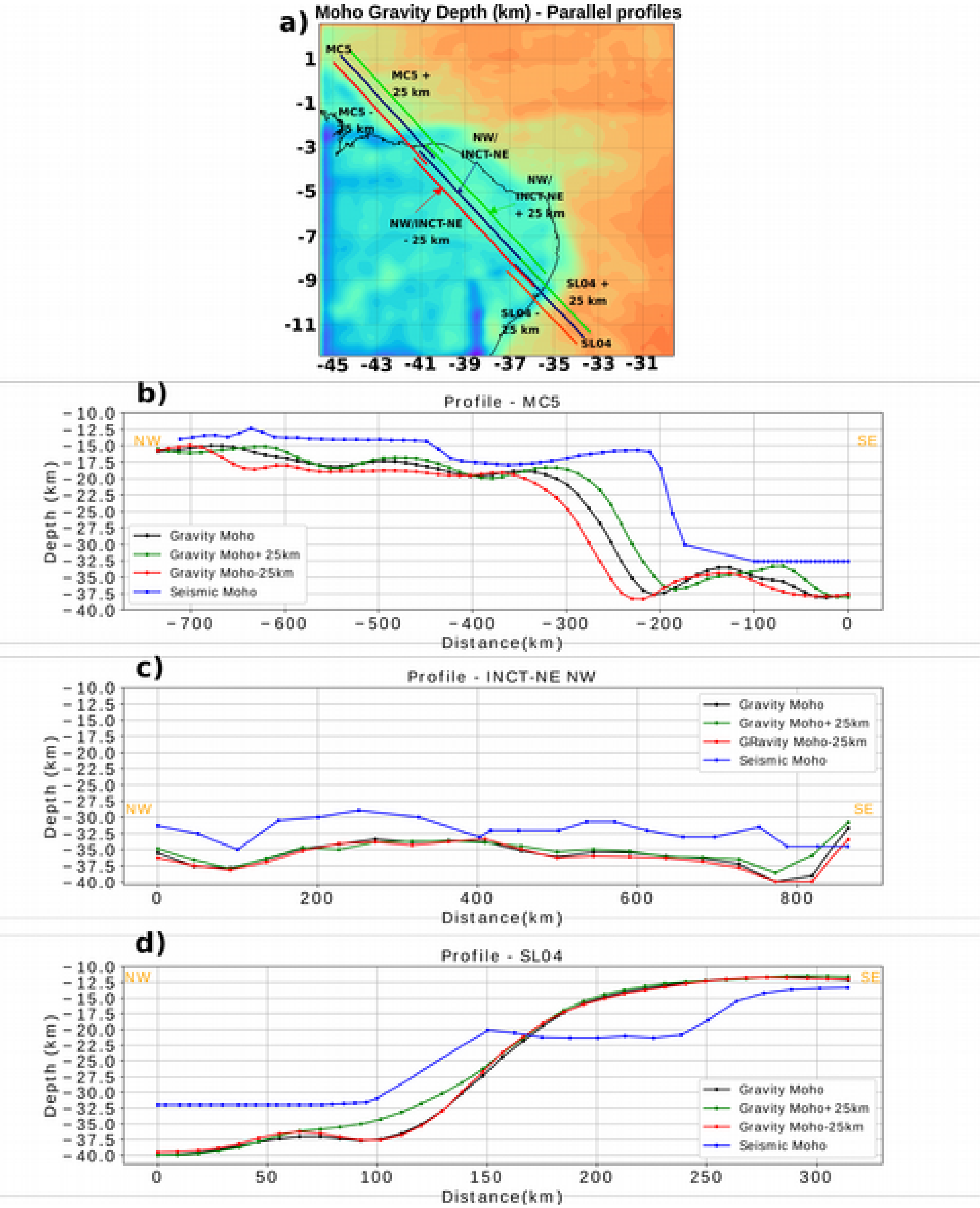

Figure 6.1.2.4 – Comparison of 3 parallel gravity Moho depth profiles with seismic Moho depth. a) Profiles location; b) MC5 profile; b) INCT-NE NW profile; c) SL04 profiles **(the horizontal scale is not the same between profiles since it represents the profile length)**

In Figure 6.1.2.4 we present a comparison of the seismic depth Moho (blue lines) for each profile – MC5, INCT-NE NW, SL04 – and 3 gravity Moho depth – one located on top of the seismic Moho (black lines), one 25 km to the Southeast (green lines) and another 25 km to the Southwest (red lines).

The CRUST1.0 model is 3D and, because of that, no sharp variations were expected. However, it was important to verify that the applied method did not create artifacts. By plotting these parallel profiles we can verify that, regardless the profile location, we do not observe any sharp variation of the gravity Moho depth or artifact between parallel profiles, showing coherence of the method. The necking zone in MC5 and SL04 have similar width and shape. The NW/INCT-NE and SL04 profiles share 100 km in length of overlap: both present a lateral Moho depth variation towards SW (green line, Figure 6.1.2.4-b and c).

Perpendicular profiles

To finalize the 2D profiles analysis, we extracted 35 profiles, perpendicular to the line (red line, Figure 6.1.2.5-a) that best fit the merge of the three independent profiles (MC5,NW/INCT-NE and SL04). These profiles are 50 km apart from each other and are 500 km in length.

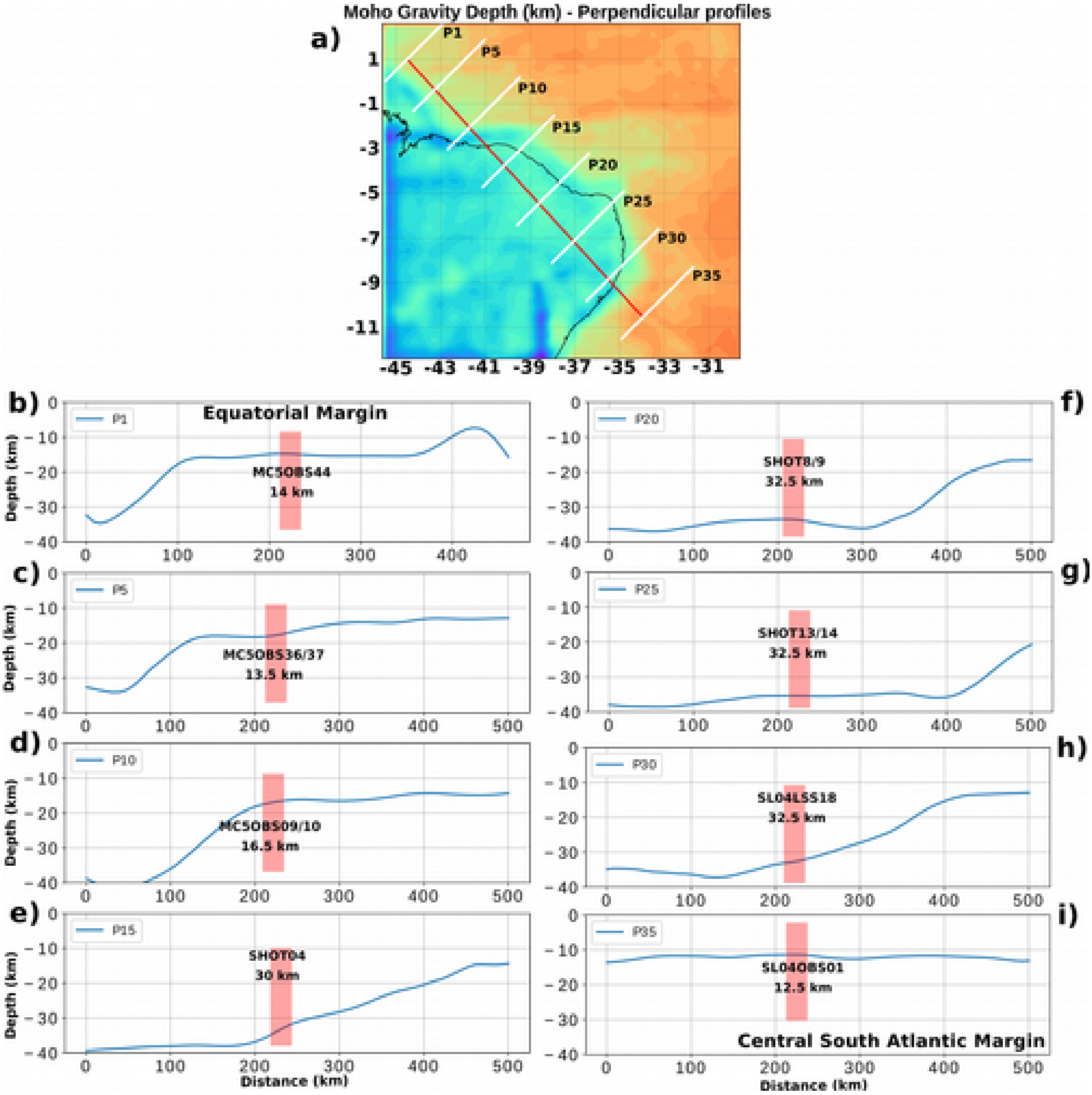

Figure 6.1.2.5 – Variation of the gravity Moho depth for different profiles perpendicular to the line that combines MC5, INCT-NE NW and SL04 . a) Location of each profile; b) P1; c) P5; d) P10; e) P15; f) P20; g) P25; h) P30; i) P35; Red rectangles – Location of the crossings of each perpendicular profile with MC5, INCT-NE NW and SL04 and the annotation of the seismic depth registered is the WAS profile at the crossing

In Figure 6.1.2.5 (b to i), 8 of the 35 profiles are shown, to provide examples of the progressively changing Moho discontinuity geometry from the Equatorial Atlantic to the Central South Atlantic margins . Also, the purpose of these profiles is to evaluate the ability of the method of distinguishing different geometries of a layer and may give some clues on the related geodynamic processes.

The Moho depth in continental domain varies between 42 km and 32 km depth, responding to the different structures present. Regarding the oceanic domain we have a variation between 10 km and 15 km. The Moho depth in the region of the SALSA experiment (Figure 6.1.2.5-h and i) is shallower when compared with the one found in the MAGIC experiment region (Figure 6.1.2.5-b, c and d). The difference is of 1 km to 2.5 km.

The observed variations along these 35 profiles re-enforces the idea that margins have a great diversity in architecture and that they are segmented at the first order by the geodynamic context in which they were formed and that influenced their mode of formation. For example, normal versus oblique/strike-slip opening, exhumation of lower continental crust versus proto-oceanic/oceanic spreading. It also gives robustness to the applied method showing that the method may be applied to other regions as an exploration tool when planning new seismic acquisition, for example.

6.1.3.3. Merged Model

One of the goals of this research project was to build a 2D regional seismic interpretation of the kinematics and dynamics by merging the three sub-parallel profiles – MC5, NW/INCT-NE and SL04 – in a unique profile of almost 1800 km in length. This merged profile could be one of the few combined interpretations that cross such an important piece of the geodynamic history correlated with the opening of the South and Equatorial Atlantic Ocean. The published work for each of the three profiles are a crucial part to accomplish this goal: (Aslanian et al., 2023, 2021, 2016, 2009; J. Tavares et al., 2012; Lima et al., 2015; Moulin et al., 2021, 2015, 2010, 2005; Pinheiro et al., 2018; Soares et al., 2011, 2010; Loureiro et al., 2023; Schnürle et al., 2023, Evain et al., 2023).

The data gathered from the LSS stations in MC5 and SL04 can be compared and combined with the stations belonging to the INCT-ET profile since the are sub-parallel with 100 km and 150 km of lateral separation. We need to take into account several factors while merging these profiles: I) the curvature of the Earth; II) the merged profile considers the great circle that best fits all the stations; III) the merged profile crosses the margins with an oblique angle.

We had access to the three independent velocity models that were developed for each of the profiles. Each of those velocity models were obtained based on their independent data set but all of them used the same processing and technique – rayINVR, two dimensional forward ray tracing followed by a damped least-squares travel time inversion (Zelt, 1999; Zelt and Smith, 1992). In order to merge the three models, we also used the tools that are part of rayINV.

Gravity and Load anomaly from rayINV – individual profiles

Among the tools from the RayINVR package developed by (Zelt and Smith, 1992) there is the gravmod package that calculates the Free Air anomaly and the load anomaly for a given 2D velocity model that is defined by polygons. The 2D model is extended laterally, to both sides, by the full distance of the model (by default), where the added polygons have the same characteristics as the polygons at the edge of the profile. This extension of the model intends to give stability to the inversion by creating a constant platform of velocity and depth for each layer to prevent boundary artifacts.

The velocity polygons are converted into density contrasts according with the relationship given by Ludwig et al. (1970), and the Free Air gravity anomaly is calculated taking into account each of those polygons. The load anomaly (given in bar) is calculated by multiplying each density contrast by the thickness of each polygon. This anomaly, evaluates the isostatic equilibrium along the profile. If the value is zero (or close) we have isostatic equilibrium since it means that we have a pressure force balance between the blocks that are above the lithospheric mantle (the reference level where the pressure force is considered the same) and the mantle itself.

In Figures 6.1.3.1, 6.1.3.2 and 6.1.3.3 we present the density model obtained by the conversion of the seismic velocity, the observed and calculated free air anomaly and the load anomaly for each of the MC5, NW-SE/INCT-NE and SL04 profiles. The observed free air anomaly is obtained from satellites (Sandwell et al., 2014). The lateral extension of each of these models is the default one, meaning that each of them is extended to each side by the same total distance of the concerning profile (for example, MC5 has a 740 km horizontal length so, the inversion of velocity into density considers a 740 km lateral prolongation of the model to each side).

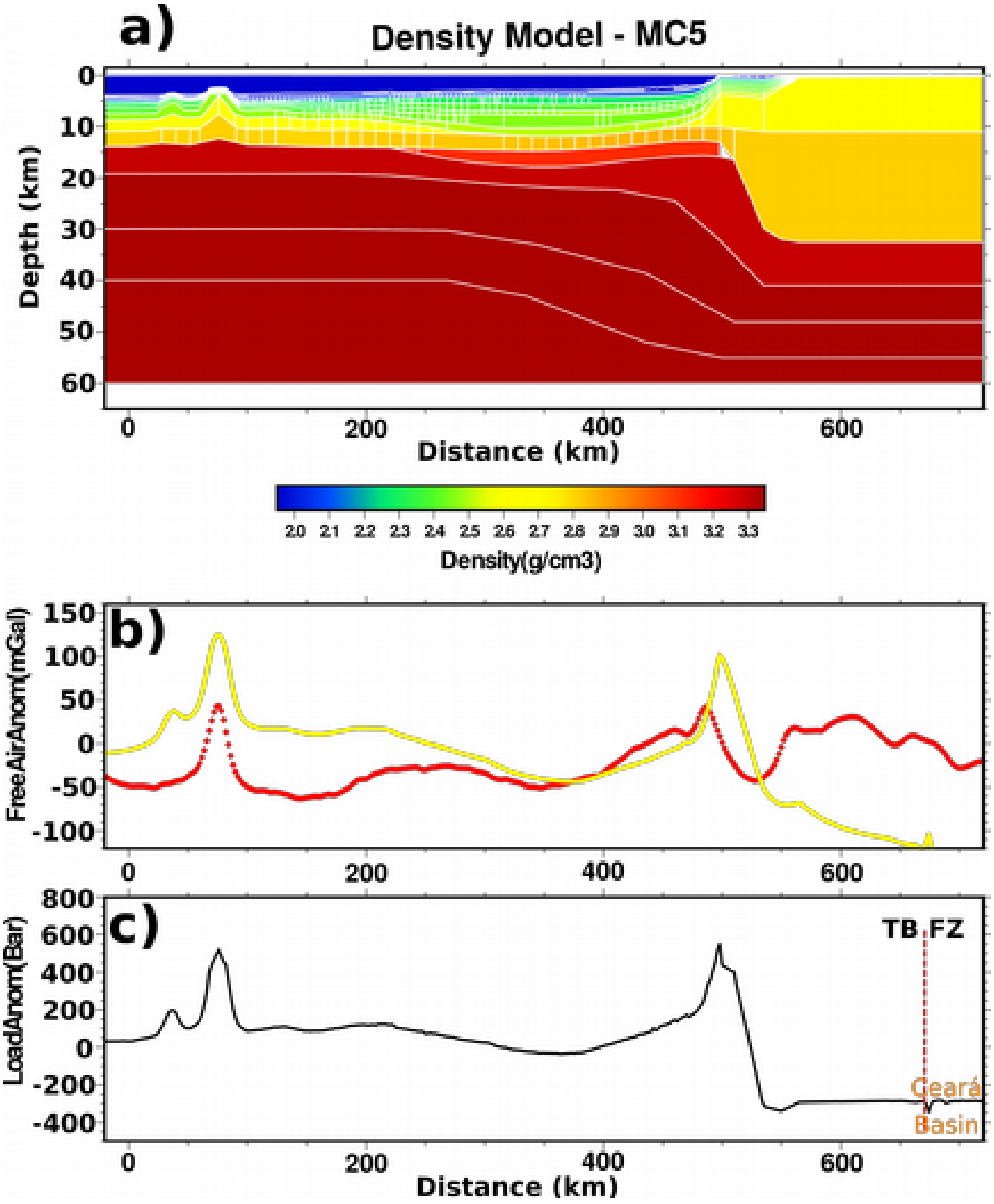

Figure 6.1.3.1 – MC5 profile density model obtained by the conversion of the velocity model. a) Density model; b) Free Air Anomaly (mGal) – observed in red and modeled in yellow; c) Load anomaly (Bar)

There is a significant difference between the observed and calculated free air anomaly for MC5 profile (Figure 6.1.3.1-b). However, the free air and load anomaly for MC5 profile (Figure 6.1.3.1-b and c) clearly shows that we have a large variation in two locations – for the volcano structures and for the necking zone – showing that they are not in isostatic equilibrium. Also, for the continental area (between 550 and 700 km), we have a negative load anomaly. This feature may be explained by the way the load anomaly is calculated. In order to calculate this value, a reference depth for isostatic equilibrium is considered. Having a significantly higher crustal thickness in this area, the load anomaly will be negative. Another possibility is the actual influence of two geological features in this area: the TransBrasiliano fault system close to the end of the profile (675 km) and the transition, on land, into de Ceará Basin.

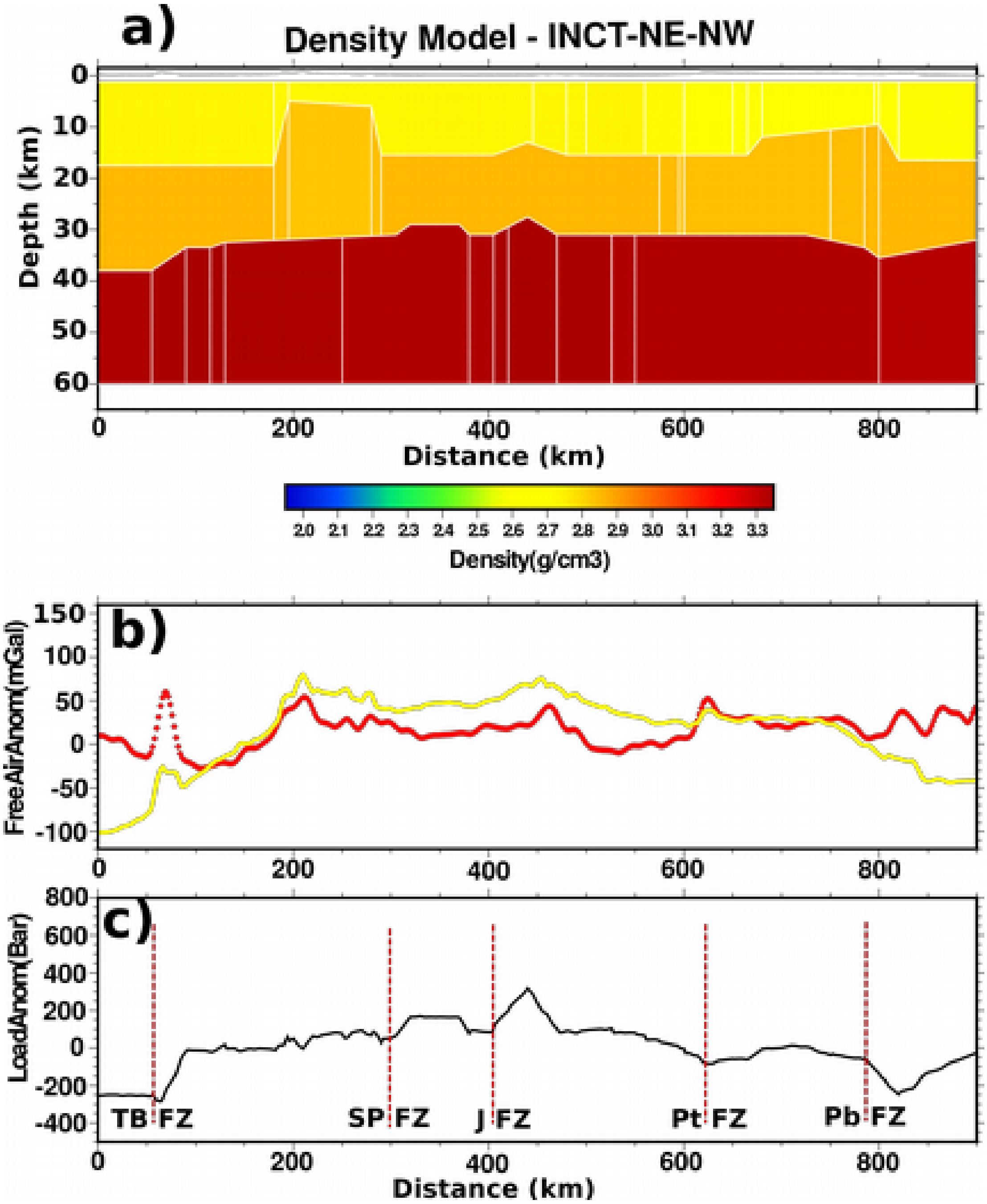

Figure 6.1.3.2 – NW/INCT-NE profile density model obtained by the conversion of the velocity model. a) Density model; b) Free Air Anomaly (mGal) – observed in red and modeled in yellow; c) Load anomaly (Bar)

For the land profile (Figure 6.1.3.2), the load anomaly floats around 0 Bar with exception of the edges of the model and for the interval [300; 450] km. This means that there is isostatic equilibrium for the majority of the region considered in the profile. The range of the load anomaly between 0 and 150 km distance in of the same order as the one found for the MC5 profile (Figure 7.1.3.1). For the interval [300; 450] km, where there is a positive load anomaly of, approximately, 200 to 350 Bar corresponds to the Senador Pompeu and Jaguaripe Fault zones. Within this area, the middle and lower crust are at shallower depth. Being denser then the upper crust, that impacts the load anomaly by making it positive at that location.

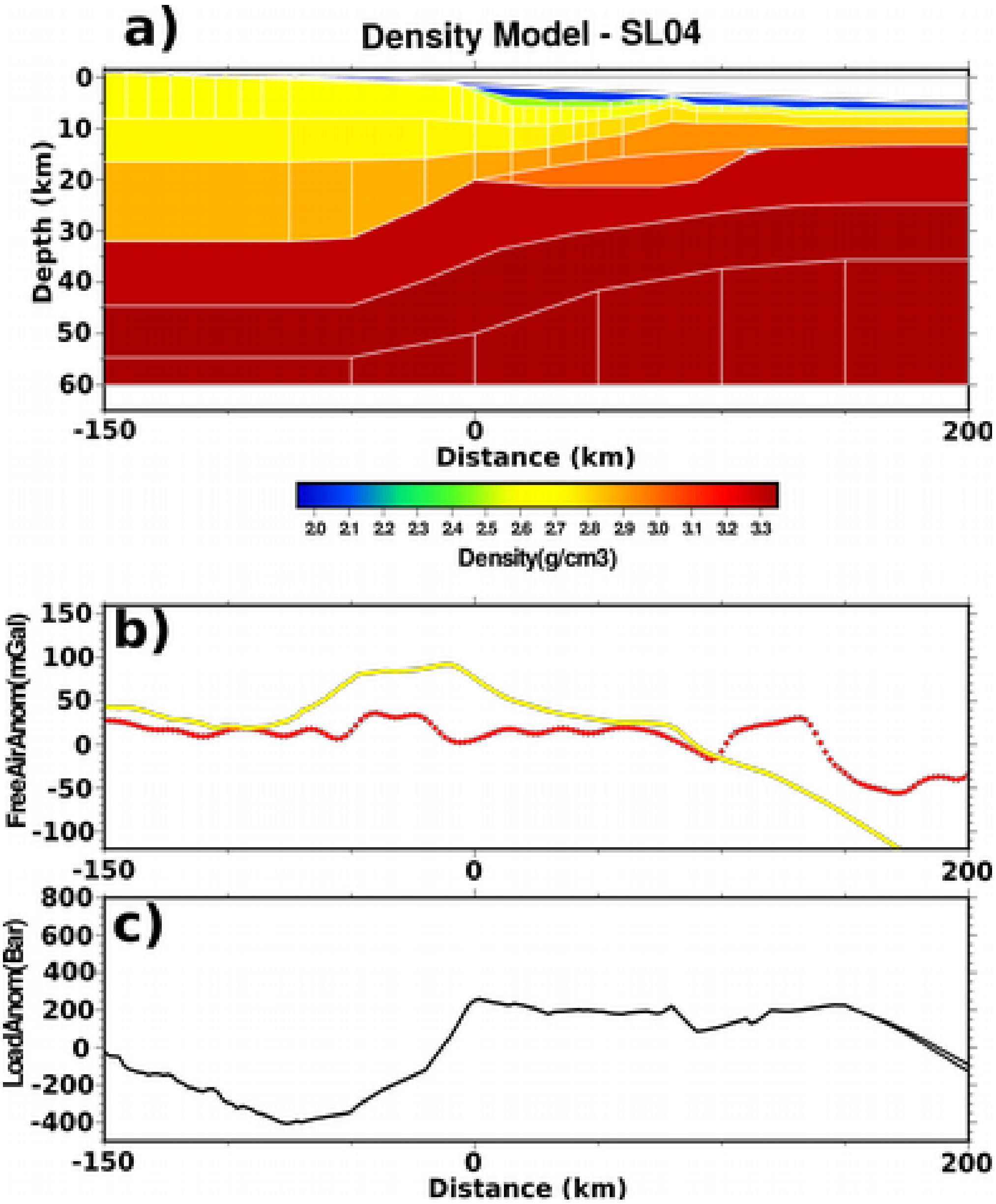

Figure 6.1.3.3 – SL04 profile density model obtained by the conversion of the velocity model. a) Density model; b) Free Air Anomaly (mGal) – observed in red and modeled in yellow; c) Load anomaly (Bar)

Finally, for the SL04 profile (Figure 6.1.3.3-c), we do not seem to have isostatic equilibrium for almost the entire profile, except the very edges. However, taking into account the uncertainties associated with the conversion of seismic velocities into densities, we can consider that the system is in equilibrium, taking into account an variation interval of [-200; 200] Bar. As for MC5, the variation of the load anomaly for the necking zone in SL04 is quite significant but approximately half of the variation that we obtain for MC5 profile. The positive load anomaly after the necking zone may be related with the volcano structures and AVL present.

The analysis of the load anomaly for each profile helps to explain some of the miss fits obtained with the 3D gravity inversion. As mentioned before, locations with sharp variations of the Moho depth, as is the case of the passive margins, may need a more detailed and/or accurate density contrast. Also, having a parameter or a process that considers the isostatic equilibrium and integrate the calculation of the load anomaly into the 3D gravity inversion may improve the applied method.

Combining the three profiles

As a first approach, we wanted to make the minimum changes as possible to the original models. To do that, we kept all the layers, matched the ones that had a correspondence and shifted each model distance that would correspond to the OBS and LSS stations for a unique profile. The best fit that takes into account all the stations is the red line shown in Figure 6.1.2.5-a.

The second step was to have a closer look at the overlapping areas of the profiles and make decisions on how to merge the layers in the transition areas, based on the published data of the land profile and on the WAS data from SL04 and MC5. Synthetic data were generated for the merged profile at the locations where we have overlapping stations, so we could compare the synthetic result with the WAS data and evaluate the merged model robustness.

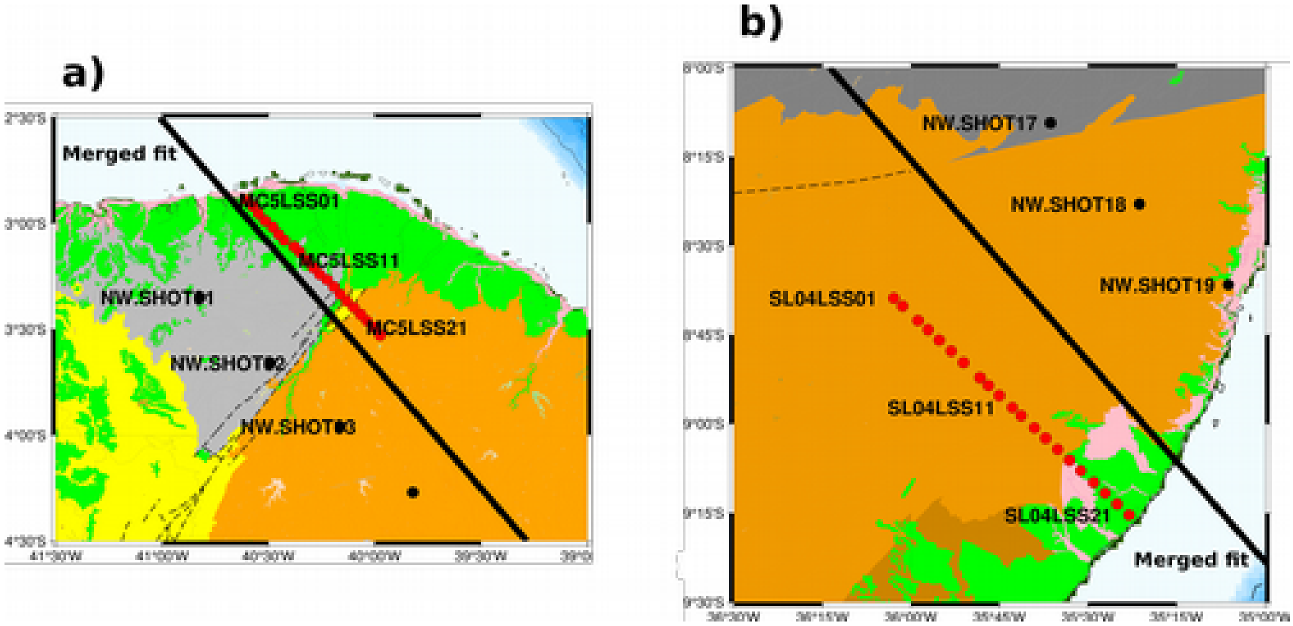

Figure 6.1.3.4 – Zoom on the locations of the land stations of the 3 profiles and their position regarding the merged fit profile (black full line). a) Overlap between land stations of MC5 and NW/INCT-NE profiles; b) Overlap between land stations of SL04 and NW/INCT-NE profiles

As we can see from Figure 6.1.3.4, the land stations of MC5 and SL04 profile have a overlap with two of the shots of the NW/INCT-NE profile each (Shot 1 and 2; Shot 18 and 19, respectively). In respect to the merged line fit, the land stations of MC5 are much closer to the line and the land stations of SL04 are, more or less, at the same distance as the ones from NW/INCT-NE profile. The shot 18 from the NW/INCT-NE failed during acquisition (Lima et al., 2015; Soares et al., 2011, 2010), meaning that we can not use this shot location to compare the results from each profile.

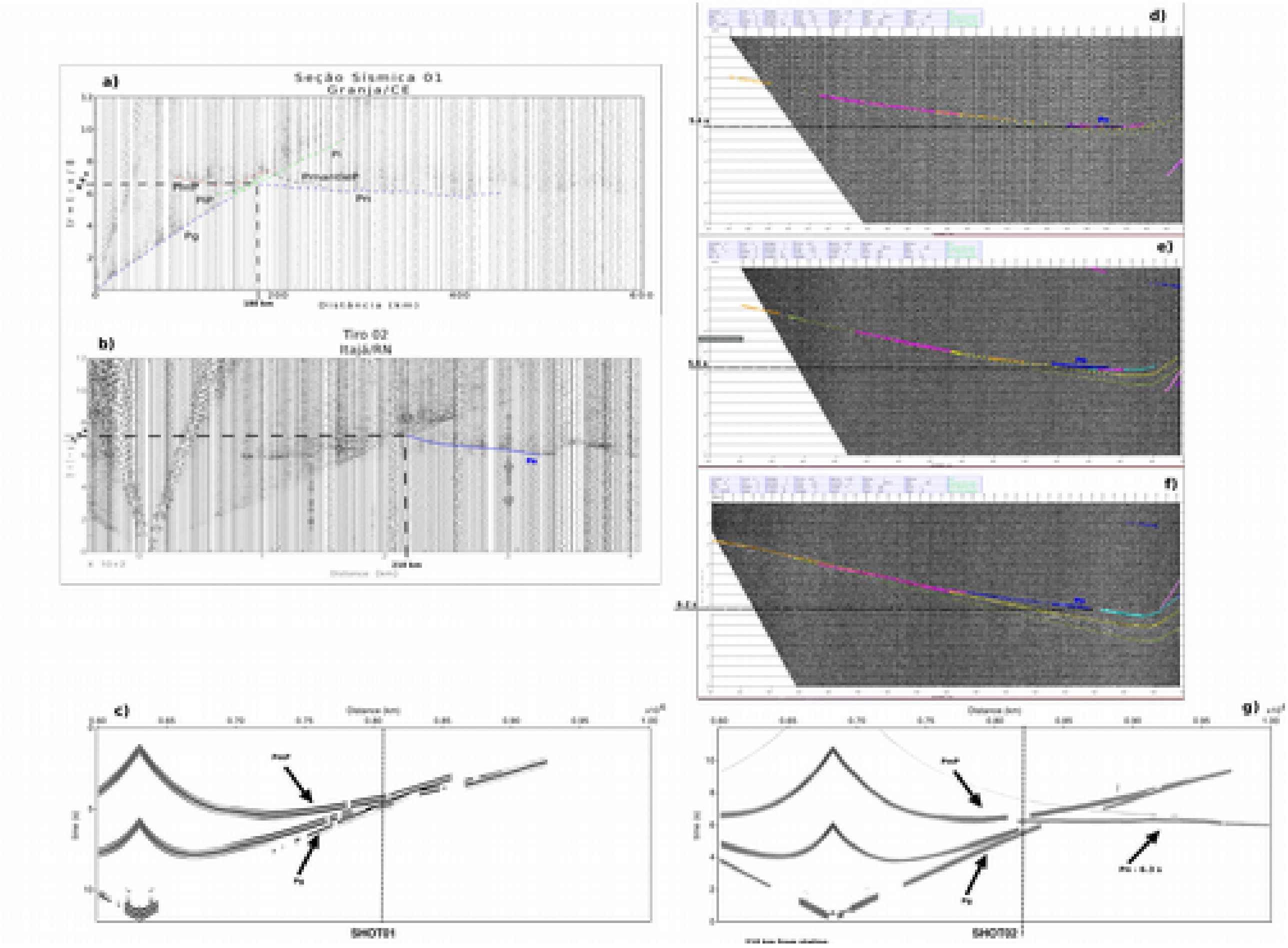

Figure 6.1.3.5 – Wide angle seismic data from NW-SE INCT-NE profile: a) Shot 01; c) Shot 02 (Soares et al., 2011, 2010); Wide angle seismic data from MC5 profile: d) MC5LSS01; e) MC5LSS11; f) MC5LSS21; Synthetic wide angle seismic data for the merged model at the same locations as NW-SE INCT-NE profile: c) Shot 01; g) Shot 02

The wide angle seismic data concerning the overlap of the profiles MC5 and NW/INCT-NE profiles are presented in Figure 6.1.3.5. In all the images, the Pn onset arrival time and associated offset is market with black dashed lines .

When we compare the results from the two shots of the NW/INCT-NE profiles (Figure 6.1.3.5-a and b) with the ones for the land stations of MC5 (Figure 6.1.3.5-d to f), the quality of the arrivals is better for the land stations of MC5 mostly due to the density of the marine shooting.

Comparing the synthetic results of shot 01 (Figure 6.1.3.5-c) with the real data for the same location (Figure 6.1.3.5-a), we do not observe a Pn propagation on the synthetics and the Pn propagation for the real data is quite unclear. Regarding the land stations on MC5 profile (Figure 6.1.3.5-d and e), closer to the synthetics, the Pn propagation is quite clear.

For the synthetic shot 02 (Figure 6.1.3.5-g), the obtained arrivals are quite similar to the ones obtained for the real data. However, the arrival time for the Pn differs between real data on NW/INCT-NE profile, MC5 land stations and synthetic. While for the synthetic we obtain an onset arrival time of approximately 6.3 s, we observe an arrival time of 5.8 s for MC5LSS01 (the station closer to this location), and approximately 7.0 s for NW/INCT-NE profile .

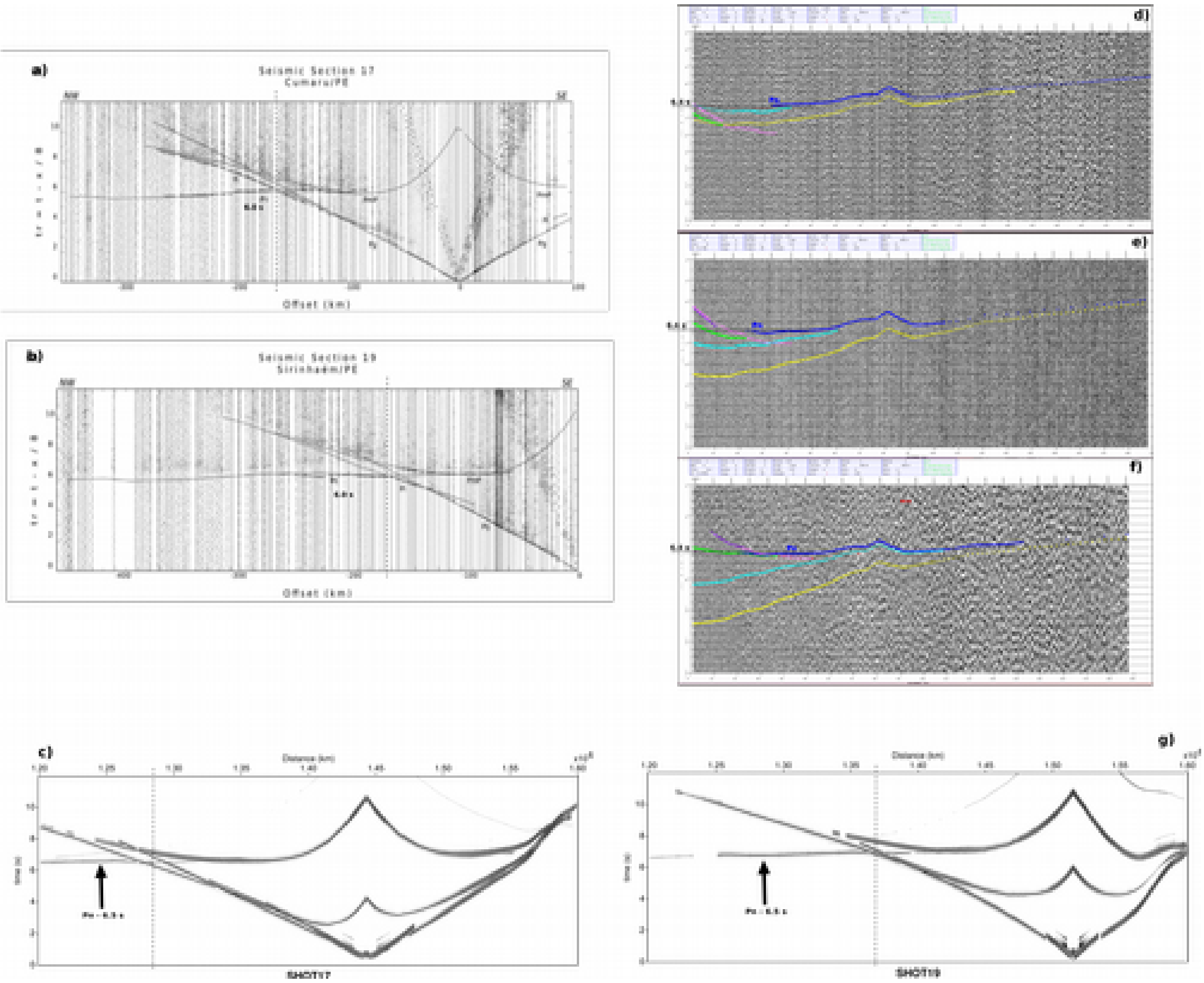

Figure 6.1.3.6 – Wide angle seismic data from NW-SE INCT-NE profile: a) Shot 01; c) Shot 02 (Soares et al., 2011, 2010); Wide angle seismic data from MC5 profile: d) MC5LSS01; e) MC5LSS11; f) MC5LSS21; Synthetic wide angle seismic data for the merged model at the same locations as NW-SE INCT-NE profile: c) Shot 01; g) Shot 02

Regarding the other overlapping side of the model, between SL04 land stations and shots 17 and 19 of NW/INCT-NE profile, we have similar general results – Figure 6.1.3.6. The amplitude of arrivals for Pg and PmP may be comparable for both set of stations (Figure 6.1.3.6-a, b, d, e and f) but the Pn is much clear for the SL04 land stations and is also in better agreement with the results of the synthetic shots.

3D gravity inversion results – Merged profile

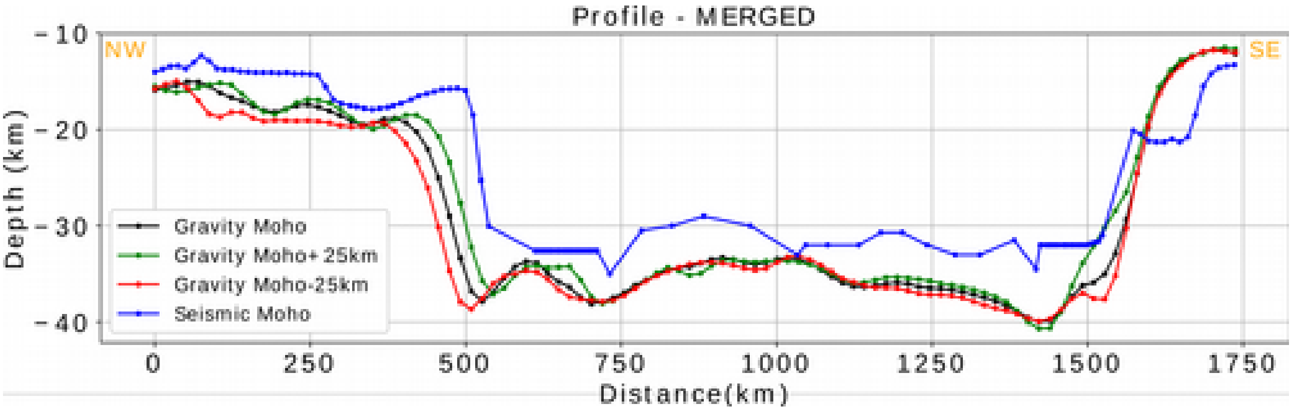

Figure 6.1.3.7 – Gravity Moho depth versus Seismic Moho depth for the merged profiles

The Moho depth given by the 3D gravity inversion for the merged profile is presented in Figure 6.1.3.7. In this figure, we compare the seismic Moho depth (blue line) with the gravity Moho depth (black line) and two other parallel profiles 25 km apart from the original (green line – 25 km NE of the merged profile line; red line – 25 km SW of the merged profile line).

The parallel profiles taken from gravity Moho depth tells us that the lateral variation is not sharp but has a progressive variation in the MC5 profile region, going from deeper (Figure 6.1.3.7, red line) to shallower (Figure 6.1.3.7, green line) in the SW-NE direction. In what concerns the continental part of the merged profile there is no significant differences between the profiles. Finnaly, for the SL04 profile region we have the same variation as for MC5 but only for the necking zone.

The consistency between the sub-parallel profiles with smooth variations, helps to understand that, in spite of the lateral distance between the land stations between each profile, the merge of the seismic profiles and its interpretation can be done at a regional scale.

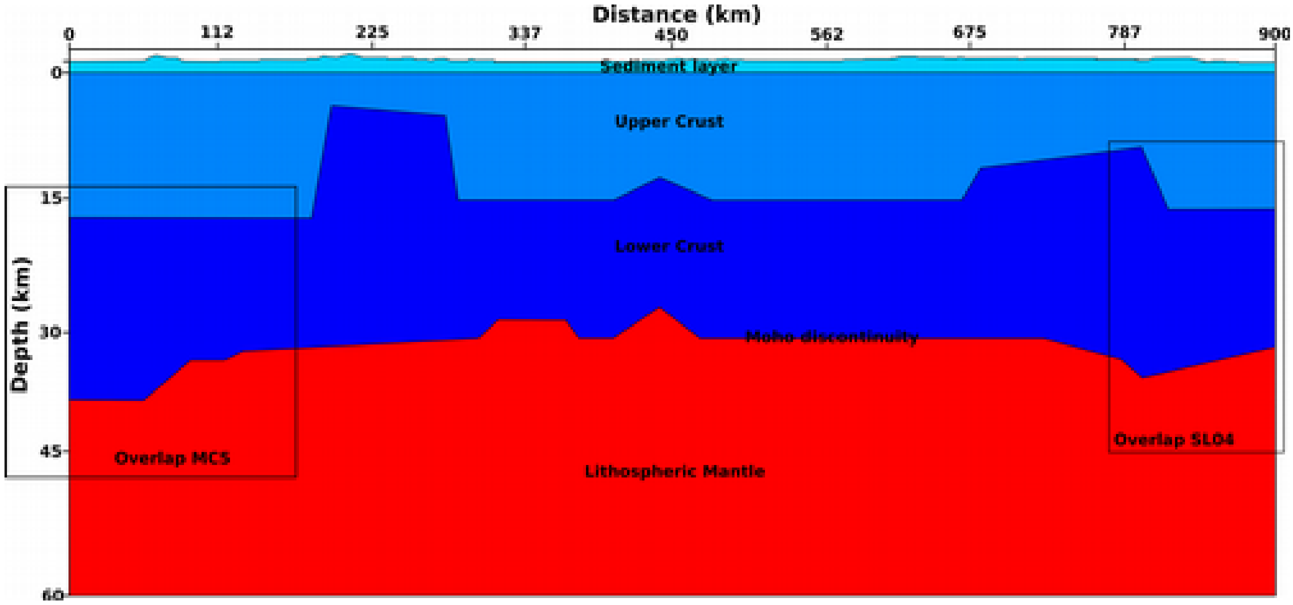

Figure 6.1.3.8 – NW/INCT-NE velocity model used for the merged model

Taking into account the results from the overlapping land stations, their comparison with the synthetic generated and the velocity model for the NW/INCT-NE profile (Figure 6.1.3.8), the overlapping lengths of the merged model, we preferred to attribute more relevance to the information given by the land stations of MC5 and SL04, in particular for the deeper layers like the lower crust and Moho discontinuity where the land stations from MC5 and SL04 present clear refracted waves arrivals when compared with the land stations from the land profile where we mostly find reflected wave arrivals.

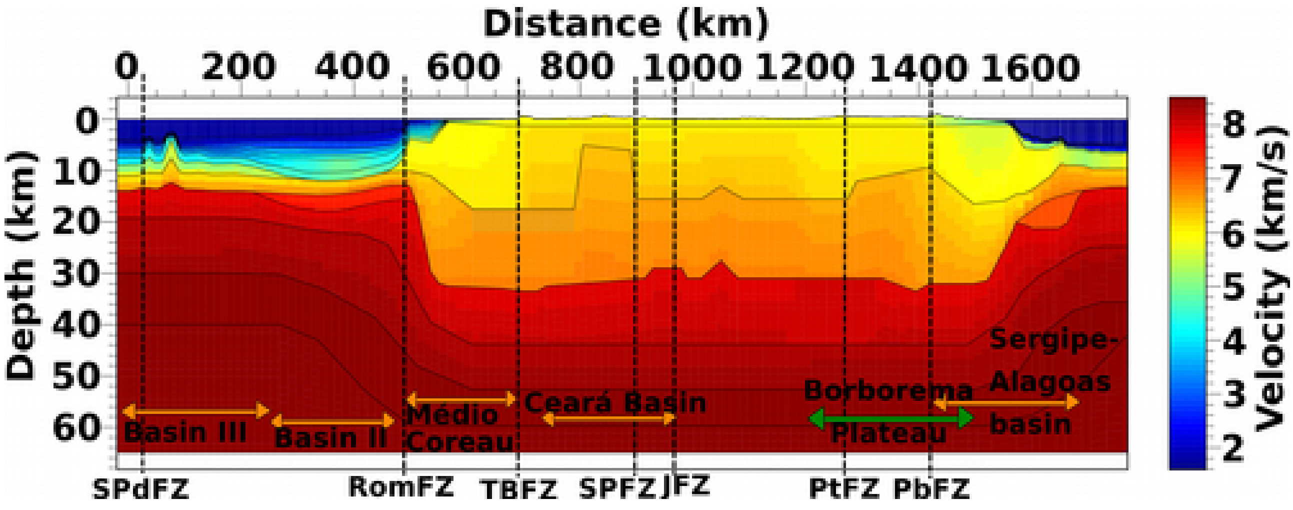

Figure 6.1.3.9 – Merged velocity model of 1770 km in legth, starting in the Equatorial margin (MC5 - 0 km distance), crossing the Borborema Province (NW/INCT-NE profile – 600 to 1500 km distance) and ending in the Central segment of the South Atlantic Ocean margin (SL04 – 1770 km distance) . Black dashed lines -

Fault/Fracture Zones crossing the profiles; Orange arrows - Basins crossed by the profile; green arrow – location of the Borborema Plateau.

The merged velocity model is presented in Figure 6.1.3.9. When merging the 3 profiles, we can see that the major features adapted or changed were: 1) the connection between profiles for the Moho discontinuity was kept smooth; 2) the top of the lower crust of MC5 was connected with that of NW/INCT-NE profile along a smooth slope instead of an abrupt step; 3) the middle crust layer on the SL04 side was removed connecting the lower crust of SL04 and NW/INCT-NE profile resulting in a velocity gradient similar to the upper+middle crust original model ; 4) the mantellic layers, that are not imaged on the land profile, were kept tabular in this area, and the velocities are the ones from MC5 and SL04; 5) no other velocity values were changed.

The first feature to notice from the merged profile (Figure 6.1.3.9) are the differences in geometry of the two deep sea basins. While on the SL04 profile side, the oceanic crust is reached shortly after the necking zone (1675 km), the entire deep sea basin along MC5 was interpreted as being floored by exhumed continental crust (Figure 2.1.2-a, Basin III – 0 to 275 km) together with altered lower crust/mantle in the AVL located underneath (Basin II – 275 to 500 km).

For the MC5 profile side, the Moho discontinuity deepens sharply from approximately 15 km to 32 km depth, in about 50 km horizontal distance (necking zone – 500 km to 550 km distance). The sediment layers pinch out at the edge of the continental boundary and the top of the upper crust rises from 12 km to 1 km depth. The upper crust possibly collapsed towards the deep sea basin along a listric fault. Landward, the upper-lower crust boundary deepens from 12 km to 20 km between 500 and 625 km.

The Central South Atlantic margin imaged on the SL04 side and the Equatorial Atlantic margin imaged on the MC5 side also have, surprisingly, but strikingly similarities: i) the top of the upper crust deepens from 2 to about 8 km between 1500 to 1650 km; its geometry also suggests seaward collapse part of the upper crust; ii) similarly the base of the upper crust shallows from 18 to 12 km over the same distance; iii) in this necking zone the Moho rises from 32 to 15 km depth between 1525 to 1700 km, slightly seaward then the upper crust; iv) A final feature that simultaneously distinguish and makes the two margins comparable, is the presence of an anomalous velocity layer (AVL) at each margin. They are clearly different in shape and the AVL on the Central margin has lower velocity value.

The difference between the margins becomes more obvious when considering the distinct geodynamic movements associated with their opening (see Geological context chapter). The central margin (which rifting started earlier) is described as a divergent margin system in a first phase

(Evain et al., 2023) where the margin is formed perpendicular to the profile direction. At the Equatorial margin, the opening system is described as a pull-apart system (Moulin et al., 2010,2021; Aslanian et al., 2021; Schnürle et al., 2023). In what concerns the merged profile, the margin is formed as a strike-slip/transform controlled by the Romanche fracture zone.

As in what concerns the continental part of the profile (between 600 km and 1450 km – Figure 6.1.3.9), the model shows a very thin sediment layer, followed by a thick crustal package about 30 km thick above tabular lithospheric mantellic layers. The velocity gradient, in depth, is quite smooth except for the necking zone in the central margin where we have upper crust velocities up until the first third of the lower crust. The lateral velocity variation in the upper crust insignificant, where the central part of the profile has a faster upper crust when compared with the margins, and the equatorial margin has a faster bottom upper crust when compared with the central margin. There is some correlation with the Fault Zones that cross the profile. The fault zones in the Borborema province (continental part of the profile) seem to affect mainly the crustal layers. The intra-continental faults are consistent with the crustal segmentation. The geometry of the Moho discontinuity and the lithospheric mantellic layers is not clearly linked to the fault zones.

6.2. Reverse-Time Migration

The first results to be considered will be the different stack results compared with the velocity models that served as base to the application of the method. An integration of the OBS and LSS stations stack results is presented also in order to be able to discuss the importance of the method and its contribution to the knowledge of the research area.

Finally the stacked result of the radial component of the 44 OBS stations of MC5 profile will be presented in comparison with the velocity model used and the potential contribution of these results when combined with the vertical component RTM.

6.2.1. Stacked results for vertical channels

In order to discuss the stacked results obtained for the vertical channels, shown in the Methodology chapter (Figures 5.2.5.1-b and 5.2.5.2-b), we need to combine the two stack results (OBS + LSS stations) and overlay them over the respective velocity model profile.

As mentioned in section 5.2.5, there are differences in amplitude that do not allow us to perform the RTM for the entire set of stations (OBS and LSS ensemble) and, because of that, the combined result is a joint image of the two separated results.

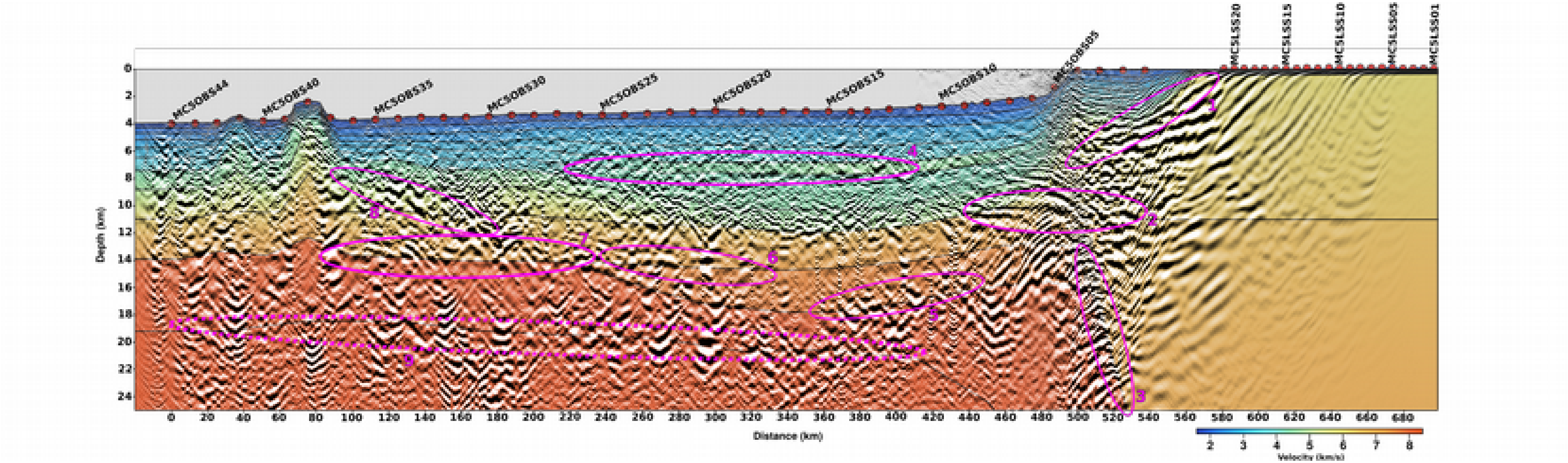

Figure 6.2.1.1 – Combined stacked RTM result of the 44 OBS plus 21 LSS stations, overlaid with the velocity model, for MC5 profile (1:3 vertical exaggeration)

From Figure 6.2.1.1, several refractors/reflectors can be identified and linked to different structures. Due to the significant contribution of the refracted wavefield that compose the stacked result, we can observe that many refractors/reflectors that we obtain travel within the layers - close to the top limit of each layer - instead of corresponding, exactly, to the layers boundaries. The refractors/reflectors with more strength and continuity are the ones corresponding to the basement, the Moho discontinuity and the upper/lower crust on land. The basement can be identified between 10 km and 12 km depth for almost the entire length of the profile, being less clear between 210 km and 260 km model distance (MC5OBS24 to MC5OBS28). The Moho discontinuity refractors can be identified between 14 km to 17 km for almost the entire oceanic environment (Figure 6.2.1.1, pink ellipse 7) and the deepening (necking zone) is clearly imaged by the land stations at 520 km model distance (Figure 6.2.1.1, pink ellipse 3). The strength of the refractors in the necking zone that is imaged by the land stations, allows to distinguish the basement progressively shallower (Figure 6.2.1.1, pink ellipse 1) but also a clear distinction between lower and upper crust (Figure 6.2.1.1, pink ellipse 2). The refractors within the lower crust have continuity as we move ocean-ward, connecting with the basement ones.

The anomalous velocity layer can also be identified at 14 km depth between 250 km to 300 km distance (Figure 6.2.1.1, pink ellipse 6) and 400 km to 475 km were its edge connects with the lower crust (Figure 6.2.1.1, pink ellipse 2). At 5-6 km depth, within the basin, between 275 km to 450 km distance, the higher velocity volcanic ash layer refractors are present (Figure 6.2.1.1, pink ellipse 4). The refactors under the volcanic structures between 25 km and 140 km are strong but the connection with the velocity layers is harder to do. However, there seems to be a continuous dipping set of refractors/reflectors between 80 km to 200 km (Figure 6.2.1.1, pink ellipse 8) that connect the top of the Moho discontinuity with the base of the volcanic structure (8 km to 14 km). We may interpret this result as the volcanic structure to have a deeper root connecting mantellic layers directly with the volcano. These dipping refractors may explain the interpretation done by Schnürle et al. (2023) (Figure 2.1.2-a) in this area with a highly intruded top layer crust but contradict the interpretation of that intruded crust being underlain by a middle crust. Those refractors suggest a mantellic intrusion within the crust, starting close to the limit of basin II (220 km model distance – Figure 6.2.1.1, 7 and 8 pink ellipses) and possibly propagating until the end of the volcanic structures. Recalling the 3D gravity inversion results and discussion done for this same profile (Figure 6.1.2.1-a), it is for this same area, where the gravity and seismic Moho have a bigger difference, suggesting that there is a difference for the crust nature due a difference in thickness or density when compared with the neighboring areas. The retrieved gravity Moho is deeper then the seismic one meaning that or either the layers above are thicker or have a higher density value. This result combined with the strong amplitude dipping reflectors/refractors obtained, re-enforce the interpretation of, at least, a highly intruded crustal package. Consequently, it questions the position of the marked SPdFZ or, at least, its width. Taking into account this interpretation, it is possible that the volcanic structures are within the SPdFZ and not before it.

There is refractors/reflectors at deeper depths then the Moho discontinuity (Figure 6.2.1.1, pink ellipse 9). However, the lack of continuity between them makes it hard to debate if they may correspond or not to a layered lithospheric mantle.

Apart from the interpretation of the nature of the crust in Basin III, discussed previously, the obtained results have a very good match with the velocity model and with the geologic structures that are described in previous chapter, the Geologic setting and in previously published work (Aslanian et al., 2015; Gonçalves et al., 2023; Moulin et al., 2021; Schnürle et al., 2023).

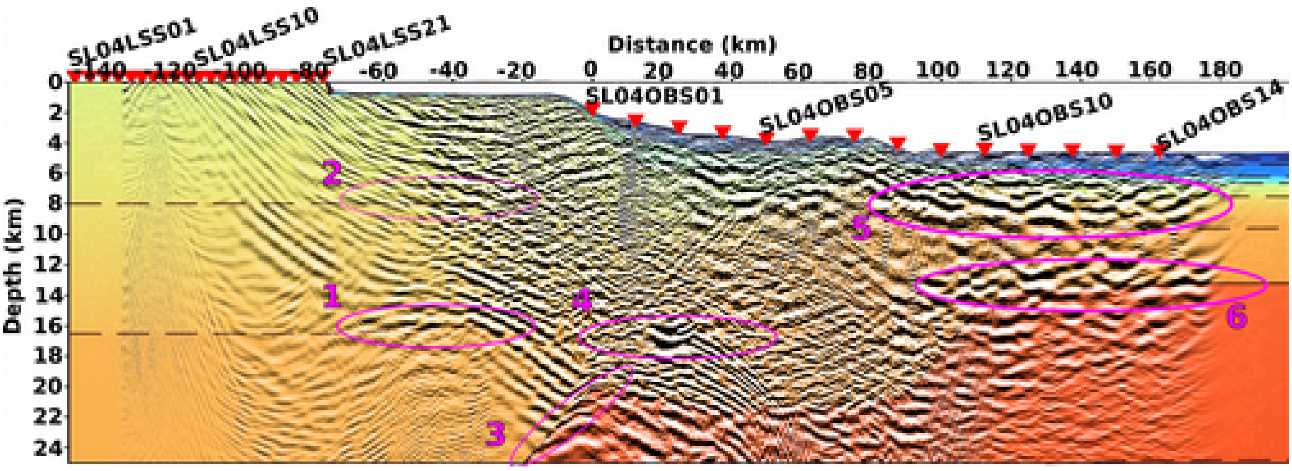

Figure 6.2.1.2 – Combined stacked RTM result of the 14 OBS plus 21 LSS stations, overlaid with the velocity model, for SL04 profile (1:3 vertical exaggeration)

The combined RTM stack result for profile SL04 is presented in Figure 6.2.1.2. This profile is much shorter in length (350 km, 14 OBS plus 21 LSS stations) when compared with MC5 (720 km) but, apart from that and the intrinsic characteristics of the sub-surface, the spacing between stations and the overall acquisition geometry is the same.

The strongest refractors/reflectors have a correspondence with the basement and upper crust (Figure 6.2.1.2, pink ellipse 5), and the Moho discontinuity (Figure 6.2.1.2, pink ellipse 6). They are particularly clear and continuous for the half of the OBS most offshore (SL04OBS07 to SL04OBS 14). For the other half of the OBS stations (SL04OBS01 to SL04OBS07), while the refractors/reflectors that correspond to the basement and the upper crust remain clear and continuous, those that should correspond to the Moho discontinuity become very weak or disappear.

In the necking zone, mostly imaged by the RTM stack result of the 21 LSS stations, there is clear refractors/reflectors that distinguish middle crust from lower crust (Figure 6.2.1.2, pink ellipse 1) at 16 km depth, between -60 km to -20 km model distance and also the dipping of the Moho discontinuity (Figure 6.2.1.2, pink ellipse 3) at 18 km depth, between -20 km to 0 km model distance. We may also argue that there is a distinct set of refractors/reflectors between the upper crust and the middle crust (Figure 6.2.1.2, pink ellipse 2) at 8 km depth, between -50 km to -30 km model distance. However, the RTM result for the land stations is not only weaker in amplitude when compared with the one obtained for MC5 profile, but is also have more dipping refractors/reflectors and diffraction's that impairs the result. One key feature imaged by the land stations is the clear signature of refractor/reflectors just above the dipping of the Moho discontinuity (Figure 6.2.1.2, pink ellipse 4), between 16 km to 20 km depth, at 0 km to 40 km model distance, that connect with the unique reflector/refractor given by the RTM result of the OBS stations that re-force the presence of an anomalous velocity layer just above the Moho discontinuity, described in previous published work (Aslanian et al., 2016; J.M. Pinheiro et al., 2018).

The quality of the results obtained by the RTM method is quite remarkable, specially taking into account the characteristics of the acquisition for both profiles. Two profiles where there is a large spacing between stations (about 12.5 km), an asymmetry regarding acquisition since there is only shooting offshore (between SL04OBS14 and SL04OBS01) meaning that the land stations only register the signal coming from one side and an asymmetry regarding the geologic geometry where one side of the profile has quite sharp variations of layer geometry and the other side almost flat layers. All these characteristics are described as ones that stops the RTM method to be efficient for WAS data type (E. Baysal et al., 1983; Chang and McMechan, 1994; Chang and McMECHAN, 1990; Zhou et al., 2018) and the reasons why there is such few previous examples of the application of the method (Gonçalves et al., 2023; Schnürle et al., 2006; Shiraishi et al., 2022). The success of the method applied to these type of data certainly has a connection with the intrinsic characteristics of the sub-surface of the research area but the fact that we do not make any assumptions of the propagating wavefield, allowing all types of waves to propagate, and conclude that we have a major contribution of the refracted wavefield, seems to be the crucial elements for the success of the method. Recalling Figures 5.2.4.4 and 5.2.6.4 (Methodology chapter), we see that there is a major difference on wave type contribution for the vertical channel (Figure 5.2.4.4, MC5OBS22) and the radial channel (Figure 5.2.6.4, MC5OBS22). For the first one we have several refractors/reflectors that are obtained mostly due to the presence of the refracted content. For the second one, the main contribution of the refracted wavefield is the P-head-wave conversion when hitting a boundary and traveling as an S guided wave back to the OBS station. Because those guided waves are very sparse or absent beyond a certain depth, we retrieve reflectors that may extend in offset but are at shallow depths and the deeper ones have very short offsets because they are entirely dependent on the reflection wavefield. In the next section we will analyze the stacked results for the radial channel of the 44 OBS stations of profile MC5, and we will be able to discuss the effect of lacking in refracted wavefield content.

6.2.2. Stacked results for horizontal OBS components

As mentioned in the previous chapter, in order to go a little bit further in the capacity of the RTM method to image the sub-surface when applied to WAS data, we applied it to the radial channel of the 44 OBS stations of the MC5 profile.

In order to convert the P-wave velocity model into S-have velocity model, different empiric relations were tested, described and discussed in the previous sections. The discussion was based on the individual station RTM results. In this section we will present the stacked result obtained with the different empirical relationship.

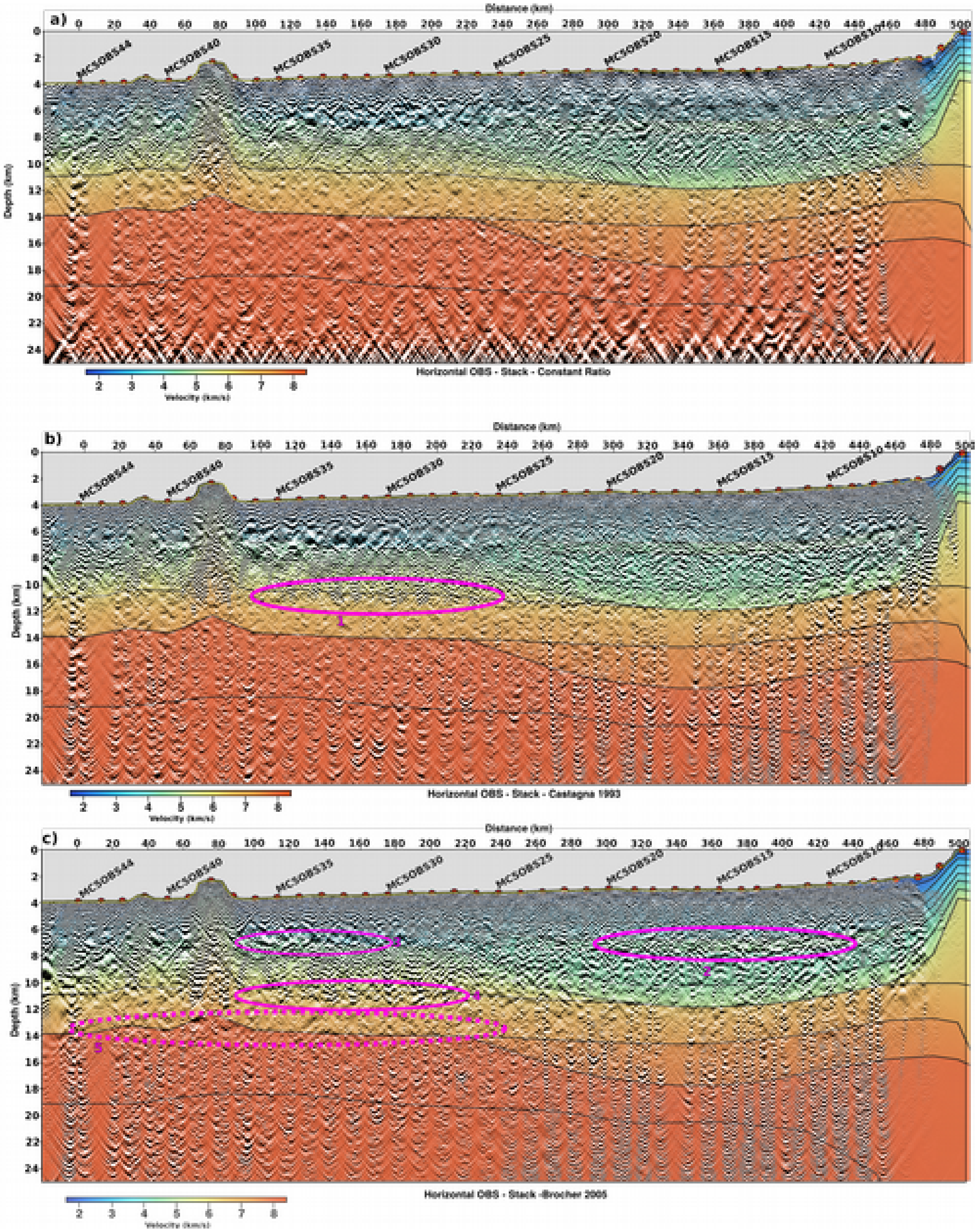

Figure 6.2.2.1 – RTM stack result for the radial component of each 44 OBS stations of MC5 profile. a) Velocity model converted with a constant Vp/Vs; b) Velocity model converted with Vp/Vs empirical relationship given by Castagna et al. (1993); c) Velocity model converted with the Vp/Vs empirical relationship given by Brocher et al. (2005) (1:3 vertical exaggeration)

From the stacked RTM results for each empirical relationship, presented in Figure 6.2.2.1, the first obvious feature is the poor overall quality obtained, specially if we compare with the obtained results for the vertical channel. As mentioned in section 5.2.6 , for the radial component, we mostly obtain reflection wavefield content and that limitation clearly impacts the stacked results as impacted each individual results (shown in section 5.2.6). The reflectors are not only very limited in offset extent, but also in depth. The results within the layers above the basin may be interesting but there is other methods that can add to the evaluation and interpretation in a much more efficient manner. For depths greater then the basement, the reflectors are sparse and in general weak making their interpretation quite difficult.

Comparing the three RTM stacked results we can see that, for the constant Vp/Vs relationship (Figure 6.2.2.1-a), the quality of the reflectors is very poor, is not able to retrieve coherent reflectors deeper then 7 km and the main coherent feature is for a sediment layer at 6/7 km between 120 km to 200 km.

Next, we have the RTM stacked result using the Vp/Vs relationship presented in Castagna et al. (1993) (Figure 6.2.2.1-b). Adding to the reflectors retrieved at the same location, mentioned in the previous paragraph, within this result, we also find some coherent reflectors that match the upper/lower crust boundary close to the volcanic structures (Figure 6.2.2.1-b, pink ellipse 1).

Finally, the RTM stacked result retrieved using the Vp/Vs relationship presented by Brocher et al. (2005, 2008) (Figure 6.2.2.1-c) is the best result from the three, following the results obtained for the individual stations (Section 5.2.6, Figure 5.2.6.3). We can identify the volcanic ash layer within the deeper part of the basin (Figure 6.2.2.1-c, pink ellipse 2), the same set of reflectors identified in the other two images close to the volcanic edifice (Figure 6.2.2.1-c, pink ellipse 3), the boundary between upper and lower crust (Figure 6.2.2.1-c, pink ellipse 4) and also a set of weak but quite coherent reflectors just above the Moho discontinuity boundary (Figure 6.2.2.1-c, pink ellipse 5).

Given the quality of the results, we can clearly state that the empirical relationship that allow to retrieve the best overall results is the one given by Brocher et al. (2005, 2008). The most interesting feature is the recovered reflectors next and under the volcanic structure. As in the RTM stacked result obtained for the vertical channel, there seems to be a set of reflectors that distinguish the upper and lower crust in this area when compared with the neighboring and that dips up until the Moho discontinuity. The presence of the São Paulo double Fracture zone may explain the vertical movement and also the presence of volcanic structures. However, the contour of this fracture zone is marked to the Northwest of the volcanoes. It seems plausible to, at least, question the extent of this fracture zone, as discussed for the vertical component RTM result.

6.2.3. RTM versus PSDM

The ability of the RTM method, when applied to WAS data, to retrieve results that have a correspondence with the structures described in previous published work and even being able to add knowledge to that work is a very relevant element and allows to achieve one defined goals. However, another main goal of the application of the RTM method to this type of data was to know if the method was able to image deeper sub-surface structures, being the Moho discontinuity and lithospheric mantle, within the range of depths that makes the method a useful tool for future studies and research work.

In order to understand and discuss the ability of the method to image deeper sub-surface layers and in what degree the retrieved result contribute to the comprehension and interpretation of a given WAS data profile, we have compared the results of the RTM method with the results of Pre-Stack Depth Migration (PSDM) method, applied to multichannel seismic streamer (MCS) data survey acquired for the same profiles.

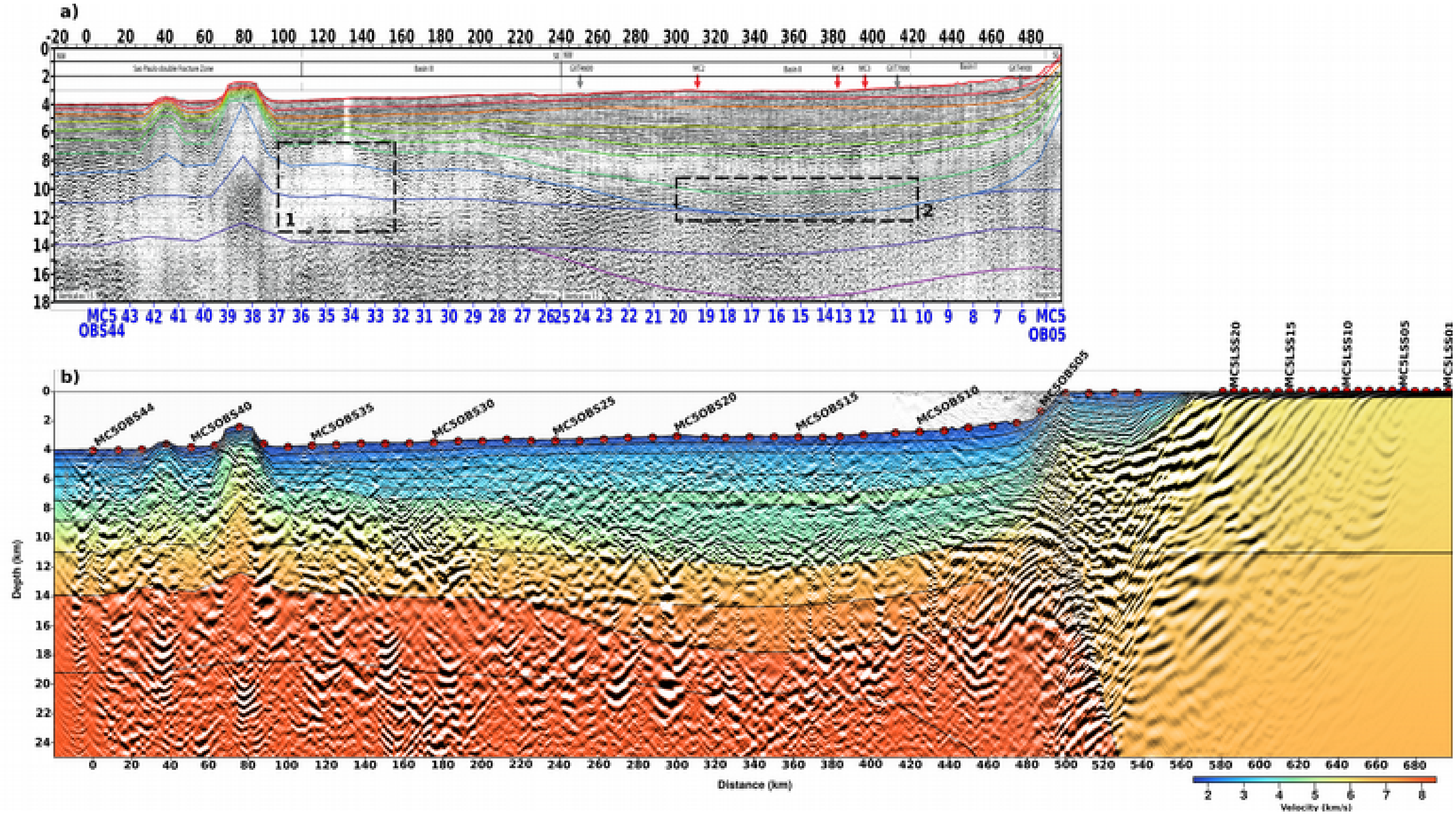

Figure 6.2.3.1 – Comparison between PSDM and RTM results for MC5 profile. a) Pre-stack Depth migration result for the MCS data for MC5 profile (image adapted from Aslanian et al., 2015); b) RTM result for the WAS data for MC5 profile (1:3 vertical exaggeration)

The MCS data profile was only acquired offshore meaning that we can only compare the PSDM result (Figure 6.2.3.1-a) with the WAS data for the 44 OBS stations (Figure 6.2.3.1-b). By having both results at the same scale and next to each other, as presented in Figure 6.2.3.1, it is quite clear that we need to separate the shallower layers up until the basement and the deeper ones. From a general point of view the PSDM result, for the layers within the basin, have a considerably higher quality then the RTM result for the same layers. However, as we move deeper, the PSDM result is not able to retrieve with the same quality and clarity as the RTM.

The reflectors highlighted in the black rectangle (2) in Figure 6.2.3.1-a, correspond to the basement and to the upper crust and their accuracy and quality is similar to the ones for the RTM (Figure 6.2.3.1-b). On the other hand, as we move offshore, to the other black rectangle (1), while the reflectors in the PSDM completely vanish, the RTM is able to retrieve those refractors/reflectors.

The RTM result (Figure 6.2.3.1-b) is clearly superior to the PSDM result (Figure 6.2.3.1-a) for the deeper layers, since we can only clearly identify the Moho discontinuity, the anomalous velocity layer and even some deeper refractors/reflectors that may correspond to lithospheric mantle with the RTM method.

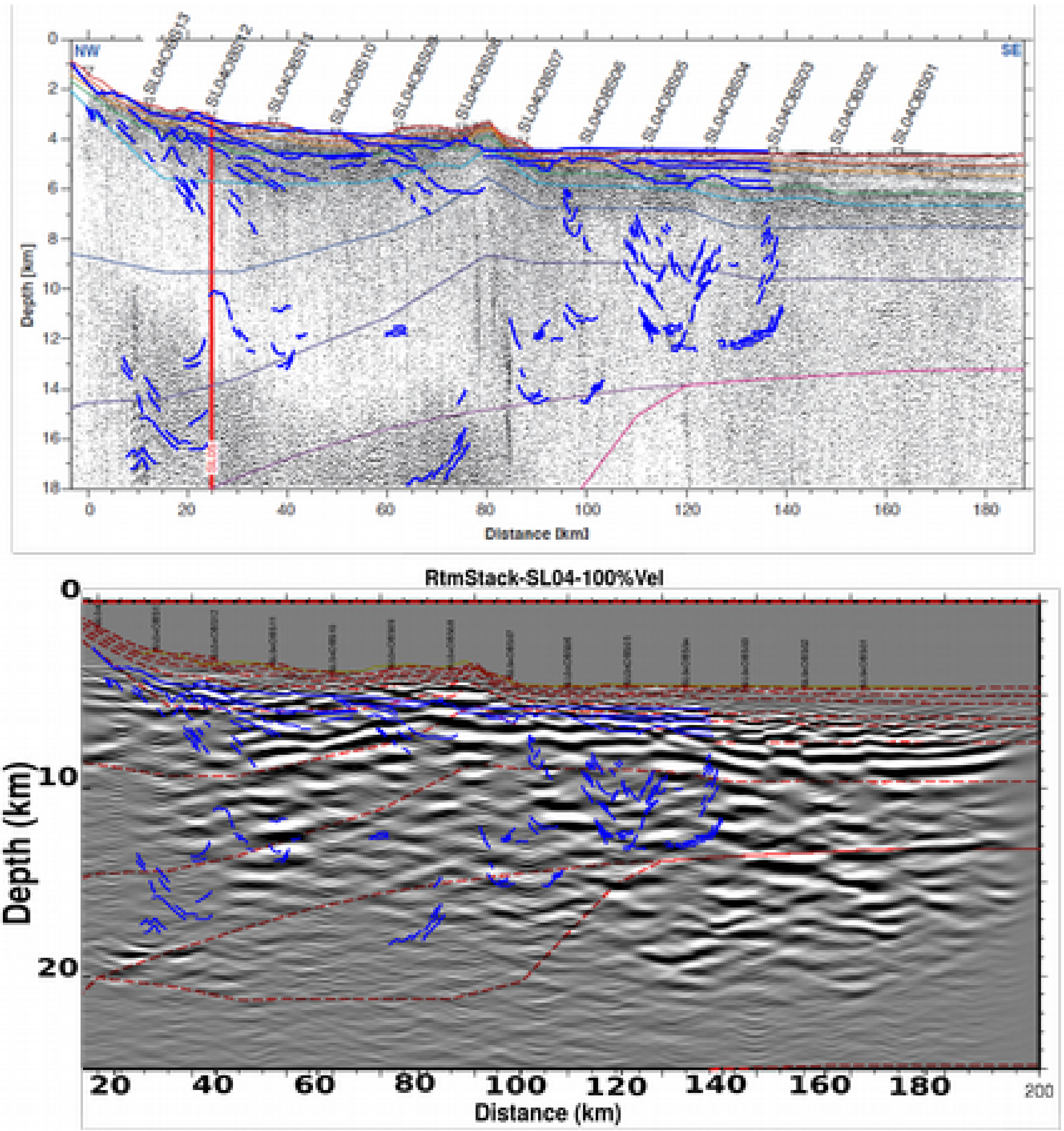

Figure 6.2.3.2 – Comparison between PSDM and RTM migration method. a) PSDM results of the MCS streamer data for profile SL04 with overlaid ION-GXT 2400 interpreted line-drawing – blue lines, which location overlaps the SL04 profile from SL04OBS14 to SL04OBS03; b) RTM results of the WAS data for profile SL04 with overlaid ION-GXT 2400 interpreted line-drawing – blue lines. Red dashed lines – velocity model layers (vertical exaggeration 1:6) (adapted from Gonçalves et al., 2023)

When we compare the PSDM results (Figure 6.2.3.2-a) of MCS streamer data and the RTM results (Figure 6.2.3.2-b) of the WAS data for SL04 profile and also overlay the interpretation of the ION-GTX-2400 line (an industrial survey conducted by ION with a ~12 km long streamer at the same location), we can easily see that for shallow depths – up until the basement – we obtain quite similar results. However, for deeper layers, the PSDM results are insufficient to obtain crustal layers and the Moho discontinuity: refractors or reflectors are absent or mostly imperceptible for depths greater then 8-10 km (Figure 6.2.3.2-a). On the other hand, in the RTM results (Figure 6.2.3.2-b), we can identify refractors related with the crustal layers and the Moho discontinuity matching the discontinuous interpretation of the ION-GTX-2400 line.

The comparison of the PSDM with RTM brings to light the utility of the RTM method when applied to WAS data. These comparisons also show that the results obtained with RTM are trustworthy, but also that we can easily obtain an image of the sub-surface with only WAS data, as previously done by Shiraishi et al. (2022).

6.2.4. Velocity Evaluation

Assess the sensibility of the RTM method to small velocity variations is another relevant element to evaluate the robustness of the method. Velocity variations of -4%, -2%, 2% and 4% were performed to the velocity model grid for each set of OBS stations (44 OBS in MC5 profile and 14 OBS in SL04 profile). Also, vertical velocity profiles were taken in order to help this evaluation.

The velocity variation percentage is the same for all the layers within the velocity profile until the depth considered for the RTM method (25 km depth). This means that the all the velocity values within the velocity grid were increased or decrease accordingly with the mentioned percentages.

This type of evaluation was done for the OBS stations because is were we have more accuracy in terms of data acquisition and were we have symmetry for the wavefield that propagates.

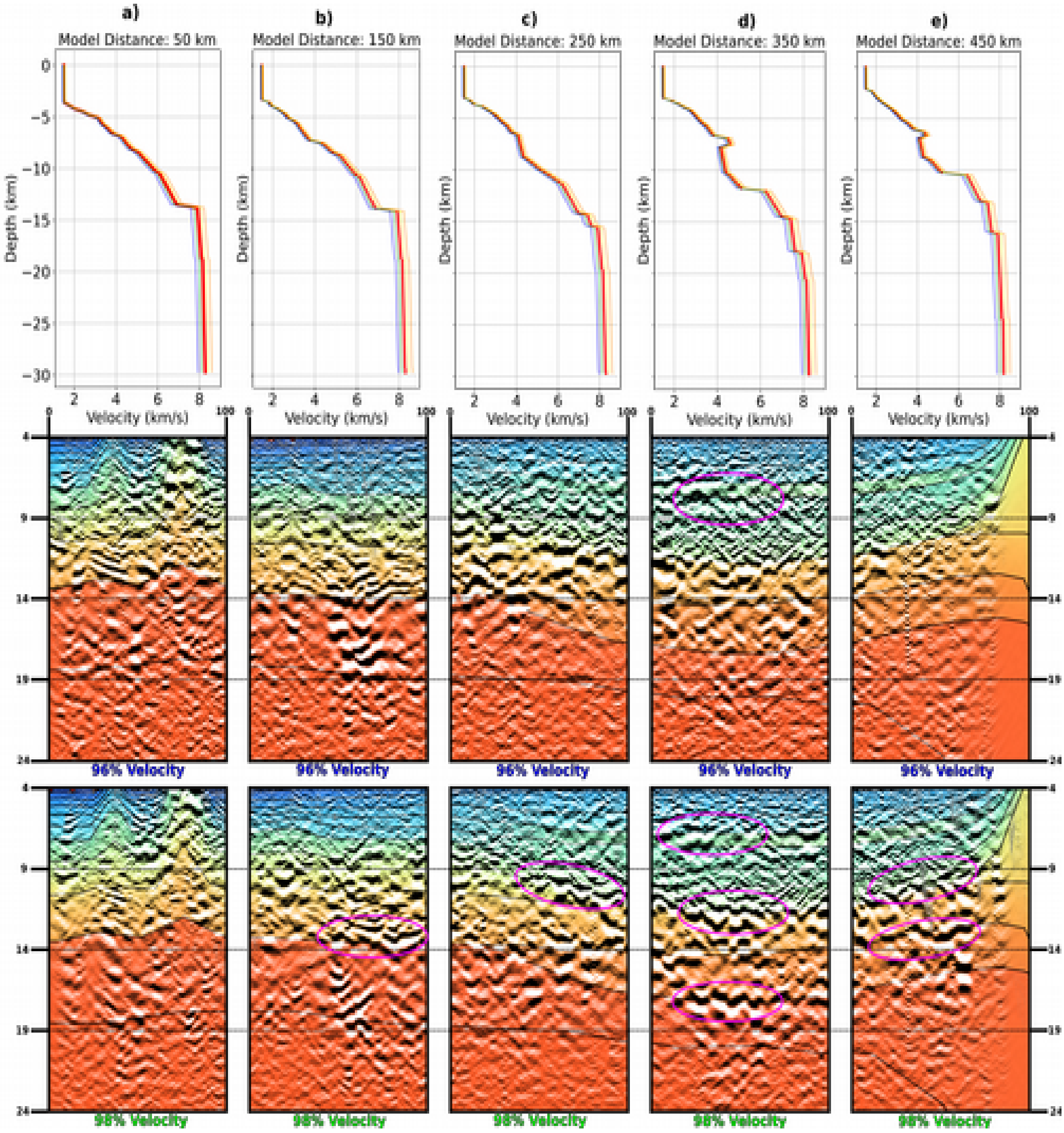
a)
Model Distance: 50 km
b)
Model Distance: 150 km
c)
Model Distance: 250 km
d)
Model Distance: 350 km
e)
Model Distance: 450 km
Depth (km)
0
−5
−10
−15
−20
−25
−30
2
4
6
8
Velocity (km/s)
0
100
4
9
14
19
24
96% Velocity
98% Velocity

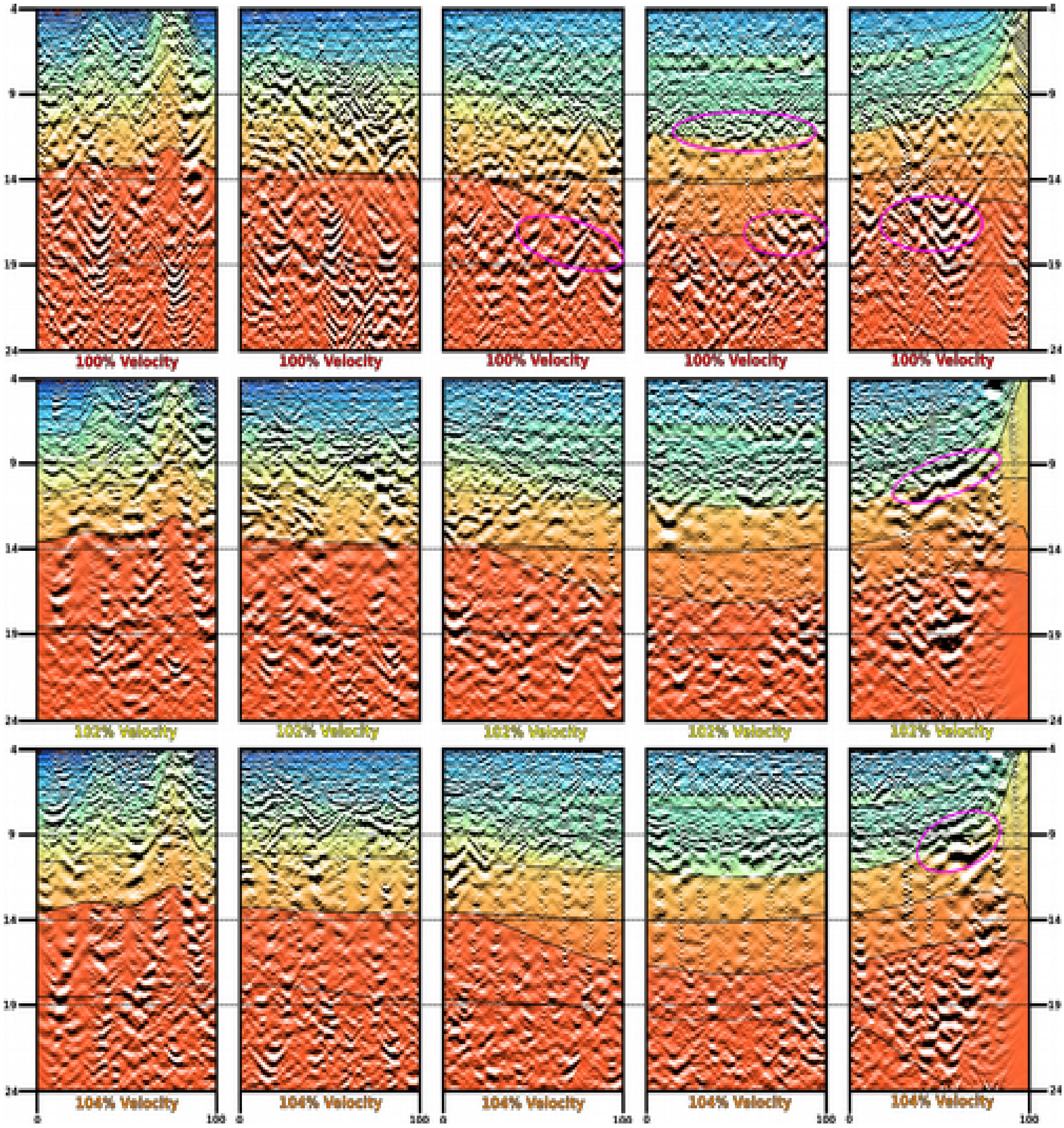

Figure 6.2.4.1 - Effect of the variation of the velocity grids – -4%, -2%, +2% and +4% of the original – on the RTM results of MC5 profile and vertical velocity variation profiles for different model distance: a) 50 km; b) 150 km; c) 250 km; d) 350 km; e) 450 km; RTM results overlaid by each velocity model for different model distance: a) 50 km ; b) 150 km ; c) 250 km ; d) 350 km ; e) 450 km. Vertical exaggeration 1:6

From the vertical velocity profiles presented in Figure 6.2.4.1 for each model distance (50 km; 150 km; 250 km; 350 km and 450 km) we can see that the velocity changing is uniform throughout the MC5 profile (Figure 6.2.4.1-a to d) and does not create any vertical variation that was not present on the original model (red line on the vertical velocity profiles, Figure 6.2.4.1).

Also, the quality of the RTM results is quite similar trough out the profile, being coherent with the previous point. On the other hand, the major feature that we observe is the different strengths of the refractors depending on the velocity model used. In the case of the MC5 profile, we observe that the basement and Moho refractors are quite good for the original velocity model but seem stronger for a velocity model that has 98% of the velocities of the original one. For the other velocity models – 96%, 102% and 104% - the same refractors are quite weak or even absent.

Another feature to mention is the response of the method to the sharper velocity variations. There is sharper velocity variations at approximately 14 km depth (Figure 6.2.4.1-a and b) and at 7/10 km depth (Figure 6.2.4.1-d and e) that we can easily distinguish from the vertical velocity profiles for those horizontal distances. The link between this vertical variations is not clear, in particular for the 14 km. However for the shallower variations for horizontal distances of 350 km and 450 km, the refractors/reflectors that concern the volcanic ash layer in the basin are stronger for the 98% velocity model and the basement for the 102% and 104%.

A slower velocity model seem to have a stronger effect over the shallower refractors/reflectors and a higher velocity model hover the deeper ones.

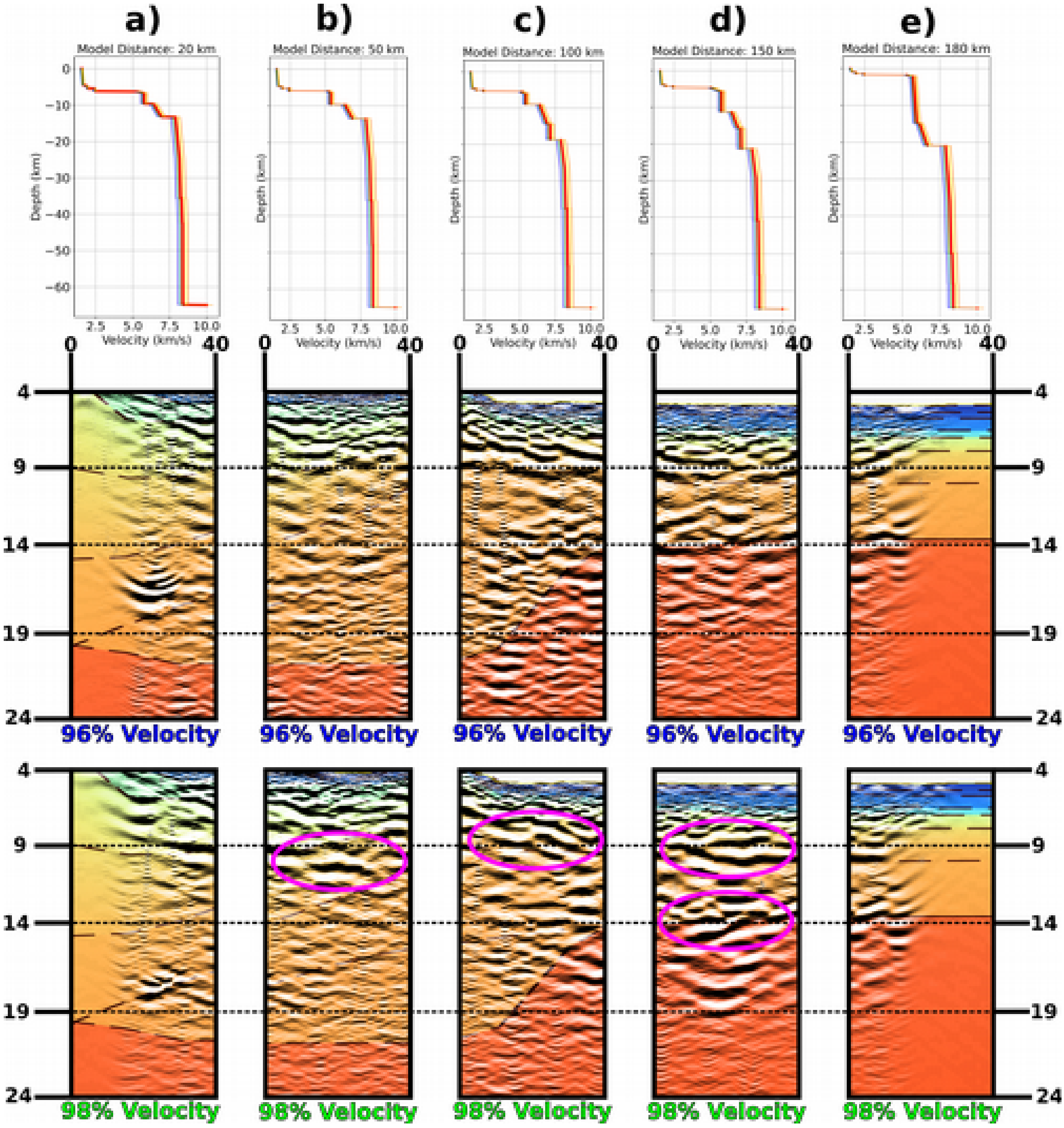
a)
b)
c)
d)
e)
Model Distance: 20 km
Model Distance: 50 km
Model Distance: 100 km
Model Distance: 150 km
Model Distance: 180 km
Depth (km)
Velocity (km/s)
2.5
5.0
7.5
10.0
0
−10
−20
−30
−40
−50
−60
0
40
4
9
14
19
24
96% Velocity
98% Velocity

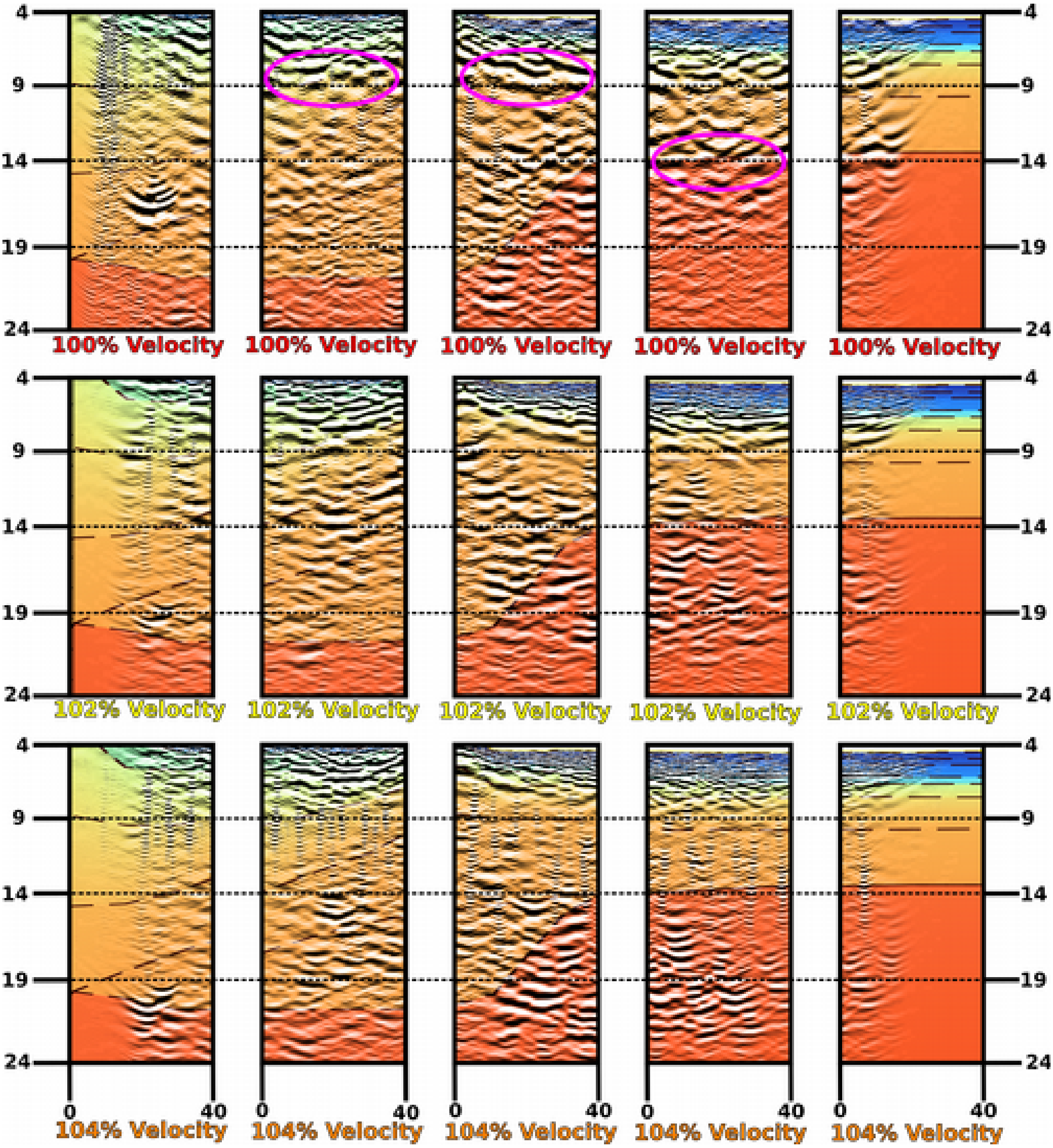

Figure 6.2.4.2 - Effect of the variation of the velocity grids – -4%, -2%, +2% and +4% of the original – on the RTM results of SL04 profile and vertical velocity variation profiles for different model distance: a) 20 km; b) 50 km; c) 100 km; d) 150 km; e) 180 km; RTM results overlaid by each velocity model for different model distance: a) 20 km ; b) 50 km ; c) 100 km ; d) 150 km ; e) 180 km. Vertical exaggeration 1:6

The same type of evaluation was done for the 14 OBS stations of SL04 profile – Figure 6.2.4.2. In general, the results are quite similar to the ones obtained for MC5 profile. We lose the reflectors/refractors for higher velocity models and they seem less affected with the slower velocity models.

The refractors/reflectors obtained for the basement and Moho discontinuity seem slightly stronger for the original velocity model but they are also quite good for the 96% and 98% velocity models (Figure 6.2.4.2-b, c and d).

The sharp velocity variation at 9/10 km depth (clear for all vertical velocity profiles in Figure 6.2.4.2) have a link with the variation of the strength of the obtained reflectors/refractors for the basement and crust. It is possible that also has an effect over the ones present within the basin but we do not have enough resolution to infer any differences for these depths.

There are a few reasons that can explain the different RTM results depending on the velocity model: (i) in spite of the ratio of velocity scaling is a few percent, the cumulative velocity difference from the seafloor to the target depth may have a strong effect on the focusing of the refractions (Shiraishi et al., 2022); (ii) the sensitivity to velocity structures could be high because of low folds of wide-angle data obtained with a spacing between OBS stations (Shiraishi et al., 2022); (iii) the uncertainty associated with the velocities of each layer, in particular the deeper ones; (iv) the geometry of the layers may contribute to the obtained results since, for example, for model distance of 250 km and 96% of the velocity model – MC5, Figure 6.2.4.1 – and model distance 50 km and 96% of the velocity model – SL04, Figure 6.2.4.2 – we obtain stronger refractors for the basement and Moho, respectively. For both cases, the layers have a stronger dip for those distances.

The fact that the method responds to small variations of velocity and that seems to be a link with sharper variations and also the geometry of the sub-surface, give robustness to the method meaning that it is sensible the velocity contrasts present within a certain model. On the other hand, it does not change abruptly give the velocity variations meaning that is within the associated error of the picking and also of the velocity model.

7. Conclusions

3D gravity inversion with seismic constraints

The original 3D gravity inversion with a seismic constraint developed by Uieda et al. (2017) is a powerful tool to estimate the Moho depth in a continental environment and within a large study area. The application of the method to the study the Northeast Brazilian passive margins broadens the scope of application of the method but also demanded a set of changes to the original approach. A higher resolution gravity grid was used (0.1x0.1º) along with the interpolation of each thickness and density values in each layer given by CRUST1.0 model. Where there was no information about the density value at a certain location within CRUST1.0 model the value was changed to the minimum value given for that layer. This change allowed to avoid artifacts due to abrupt changes in density between neighboring points. Instead of only considering the sedimentary layers, we have also considered the three crustal layers to calculate the Bouguer anomaly at the Moho, by applying a layer-striping approach. Given the presence of two contrasting domains (continental and oceanic), considering all the layers above the Moho discontinuity, meaning a crustal structure that respect a minimum geology, was essential to retrieve its geometry with more accuracy.

The main limitation of the method is the poor constrain of the density contrast across the Moho. By only considering a unique value for the density contrast, the inversion is not capable to retrieve better estimations of the depth of the Moho discontinuity in areas with sharp variations of crustal thickness and density, as it is the case across the passive margins. However, the error evaluation for the density contrast versus Moho reference depth (Figure 5.1.6.4-c), it is calculated during the estimation of the hyper-parameters, show that a large set of density values can be considered to produce a good fit of the Moho Bouguer anomaly (Figure 5.1.6.1).

The crustal thickness values given by CRUST1.0 model was also a limitation, specially offshore. While the values in the continental domain provide a good initial fit (Figure 5.1.6.2-a), in the oceanic domain the misfit is generally too high and impair the inversion process to retrieve better estimations for the Moho depth. This is particularly significant in the Equatorial margin, where the initial thickness of the crustal layers are too high and impair a better fit from the inversion.

The level of consistency and robustness of the method is high since the inversion results allow to distinguish and evaluate different geometries of the Moho discontinuity within a complex geological area and interpret them taking into account the geodynamic context of each area and postulate on the geological processes that occurred (Figures 6.1.2.1, 6.1.2.2 and 6.1.2.3).

The layer-striping approach along with the increase in resolution of the grids and the enlargement of the pool of seismic points, the geometry of any crustal layer can be estimated by this method, given that we have thickness and density values for the layers above the targeted one, along with depth values given by the seismic points.

The method can be applied within two main perspectives: i) to bring new insights on the knowledge concerning the geometry of a crustal layer and the geodynamic processes associated; ii) as a first approach in a research area, where a data acquisition is planned, in order to give insights on the locations where those data should be acquired.

Reverse Time Migration

By applying the RTM method to two 2D-WAS profiles, as developed by Schnürle et al. (2006), we have shown that the results retrieved are significant to the interpretation of deep crustal layers. We retrieved continuous reflectors/refractors concerning the basement, crust and the Moho discontinuity.

The application to land stations showed that valuable knowledge can be retrieved, in particular when combined with the marine OBS stations . Alone, the stacked result for the two sets of LSS stations (Figures 5.2.5.2 and 5.2.5.4) gives some insights on the geometry of the crustal layers on the continental domain. Moreover, when we combine those results with the ones for the OBS stations (Figures 6.2.1.1 and 6.2.1.2), we are able to follow the geometry of those layers from continental to oceanic domains. By combining the two results we are able to image the crustal layers of the necking zone in the passive margins, essential to understand the geodynamic processes involved during the formation of the margins.

We have extended the application of the method to the radial component of the OBS stations of MC5 profile, so we could measure the capacity of the method on retrieving results from shear-waves propagation. For our velocity model, we have tested different empirical relationships to convert acoustic Vp into shear-wave Vs velocities, concluding that the one given by Brocher et al. (2008) provides the best results (Figures 5.2.6.3-c and 6.2.2.1-c). We were not able to retrieve continuous and strong reflectors/refractors for the deeper crustal layers: The method stops to be effective for depths greater then 10/12 km.

The evaluation of the individual results of MC5OBS22 for the radial component (Figure 5.2.6.4) together with the vertical component (Figure 5.2.4.4), highlight the essential importance of refracted/head-wave content on the propagating wavefields. From these results, it becomes clear that the success of the method, when applied to WAS data, is that no limitations should be imposed in the types of rays that propagate within the forward or backward problem. The two results clearly show that, once we stop to have refracted content propagating in one of the directions, we do not obtain refractors/reflectors.

Following Gonçalves et al. (2023), by comparing the marine streamer PSDM results with the OBS RTM (Figures 6.2.3.1 and 6.2.3.2), we were able to confirm that we can better image the deeper crustal layers by using RTM applied to wide-angle data and also obtain the refractors that correspond to the shallower layers. We also showed that the method is trustworthy and quite useful when the MCS streamer data are not available at the target depths, or can not be at all acquired.

By making variations of the overall velocity model between -4% and 4% (MC5 – Figure 6.2.4.1; SL04 – Figure 6.2.4.2), we have showed that the method is quite sensitive to velocity changes but may also be explained by the geometry of the target interfaces and, finally, with the uncertainties in the velocity of the deeper layers.

The general results have significance and are an important contribution for the seismic interpretation of the studied areas. The method allows to retrieve the main structures of the subsurface and reach depths that other migration techniques are not capable of. The method can be applied as a complement to other methods (PSDM or P-wave velocity modeling) and confirm or not the obtained results. It can be applied as a tool to retrieve the characteristics of deeper layers when only WAS data are available.

Geologic/Geodynamical insights

From an broad perspective, the results from the two applied methods confirm the geologic and geodynamic interpretations achieved by previous authors (Almeida et al., 2015; Aslanian et al., 2021, 2023; Lima et al., 2015; Loureiro et al., 2023, 2018; Moulin et al., 2021, 2010; Osako et al., 2011; Pinheiro et al., 2018; Schnürle et al., 2023) in what concerns the Northest Brazilian passive margins. Nevertheless, the obtained results bring some new knowledge and understanding in what concerns the opening of the two margins:

i) For the different profile locations where anomalous velocity layers were interpreted (Figures 2.2.2-a; 2.2.3 and 2.2.4), the gravity and seismic Moho have a consistent miss-fit that would be significantly improved if we consider the AVL overlying the Moho discontinuity (Figures 6.1.2.1-c; 6.1.2.3-c and f) . Since the 3D gravity inversion considers a density contrast between the crustal plus sediment layers and typical mantle, we can not make conclusions over the nature of the AVL. However, given the consistency of the results for the depth and shape of the gravity Moho, the identified AVL are most probably related with lithospheric mantle processes.

ii) The depth variation of the Moho on the continental domain for profile MC4 (Figure 6.1.2.2-e) re-enforces the interpretation of the presence of exhumed continental crust in the oceanic domain in the Para-Maranhão/Barreirinhas basins due to the lack of sufficient crustal material in the opening direction (E-W) of the Equatorial margin.

iii) the RTM results for MC5 profile (Figures 6.2.1.1) question the nature of the crust in Basin III (Figure 2.1.2-a) and the position of the SPdFZ by showing dipping reflectors/refractors connecting the Moho discontinuity to the base of the volcano structures.

iv) The merge of MC5, NW/INCT-NE and SL04 wide-angle seismic profiles into one unique profile of almost 1800 km in length brings to light a striking similarity between the Equatorial and the Central margin of the South Atlantic Ocean (Figure 6.1.3.9). This project allowed to confirm previous interpretations reached in the two areas and the significant difference between the geodynamic processes in the two margins, as for instance the main difference the nature/origin of the identified AVL.

8. Bibliography

Afonso, J.C., Salajegheh, F., Szwillus, W., Ebbing, J., Gaina, C., 2019. A global reference model of the lithosphere and upper mantle from joint inversion and analysis of multiple data sets. Geophysical Journal International 217, 1602–1628. https://doi.org/10.1093/gji/ggz094

Almeida, Y.B., Julià, J., Frassetto, A., 2015. Crustal architecture of the Borborema Province, NE Brazil, from receiver function CCP stacks: Implications for Mesozoic stretching and Cenozoic uplift. Tectonophysics 649, 68–80. https://doi.org/10.1016/j.tecto.2015.03.001

AMARAL, W.D.S., 2010. Análise Geoquímica, geocronológica e termobarométrica das rochas de alto grau metamórfico, adjacentes ao arco magmático de Santa Quitéria, NW da Província Borborema. Universidade Estadual de Campinas, Instotuto de Geociências Pós-Graduação em Geociências, área de Geologia e Recursos Naturais.

Asgharzadeh, M.F., von Frese, R.R.B., Kim, H.R., Leftwich, T.E., Kim, J.W., 2007. Spherical prism gravity effects by Gauss-Legendre quadrature integration. Geophysical Journal International 169, 1–11. https://doi.org/10.1111/j.1365-246X.2007.03214.x

Aslanian, D., Gallais, F., Afilhado, A., Schnürle, P., Moulin, M., Evain, M., Dias, N., Soares, J., Fuck, R., da Cruz Pessoa Neto, O., Viana, A., 2021a. Deep structure of the Pará-Maranhão/Barreirinhas passive margin in the equatorial Atlantic (NE Brazil). Journal of South American Earth Sciences 110, 103322. https://doi.org/10.1016/j.jsames.2021.103322

Aslanian, D., Gallais, F., Afilhado, A., Schnürle, P., Moulin, M., Evain, M., Dias, N., Soares, J., Fuck, R., da Cruz Pessoa Neto, O., Viana, A., Morvan, L., Mazé, J.P., Pierre, D., Roudaut-Pite, M., Rio Alves, D., Barros Junior, P., Biari, Y., Corela, C., Crozon Duarte, J.L., Ducatel, C., Falcão, C., Fernagu, P., Vinicius Aparecido Gomes de Lima, M., Le Piver, D., Mokeddem, Z., Pelleau, P., Rigoti, C., Roest, W., Roudaut, M., 2021b. Deep structure of the Pará-Maranhão/Barreirinhas passive margin in the equatorial Atlantic (NE Brazil). Journal of South American Earth Sciences 103322. https://doi.org/10.1016/j.jsames.2021.103322

Aslanian, D., Gallais, F., Evain, M., Schnürle, P., Pinheiro, J.M., Afilhado, A., Loureiro, A., Dias, N., Cupertino, J.A., Viana, A., Moulin, M., this issue. From São Francisco Craton to Jacuipe basin, passing trough the South Tucano and Recôncavo grabens: new insights from wide-angle-MCS data. Journal of South American Earth Sciences.

Aslanian, D., Moulin, M., Afilhado, A., Gallais, F., Schnürle, P., Dias, N., Benabdellouahed, M., Baltzer, A., Rabineau, M., 2015. Wide-Angle and Multi-Channel Seismic Experiment in the Maranhão–Barreirinhas-Ceará Basins (Brazil) (Field report).

Aslanian, D., Moulin, M., Evian, M., Afilhado, A., Schnürle, P., Gallais, F., Loureiro, A., Pinheiro, J.M., Klingelhoefer, F., Dias, N., Rabineau, M., Baltzer, A., Benabdellouahed, M., 2016. Wide-Angle and Multi-Channel Seismic Experiment in the Jequitinhonha-CamamúJacuípe-Alagoas-Sergipe Basins (NE Brazil) (Field report). Ifremer.

Aslanian, D., Moulin, M., Olivet, J.-L., Unternehr, P., Matias, L., Bache, F., Rabineau, M., Nouzé, H., Klingelheofer, F., Contrucci, I., Labails, C., 2009. Brazilian and African passive margins of the Central Segment of the South Atlantic Ocean: Kinematic constraints. Tectonophysics 468, 98–112. https://doi.org/10.1016/j.tecto.2008.12.016

Assumpção, M., Feng, M., Tassara, A., Julià, J., 2013. Models of crustal thickness for South America from seismic refraction, receiver functions and surface wave tomography. Tectonophysics 609, 82–96. https://doi.org/10.1016/j.tecto.2012.11.014

Baysal, E., Kosloff, D.D., Sherwood, J.W.C., 1984. A two way nonreflecting wave equation. GEOPHYSICS 49, 132–141. https://doi.org/10.1190/1.1441644

Baysal, Edip, Kosloff, D.D., Sherwood, J.W.C., 1983. Reverse time migration. GEOPHYSICS 48, 1514–1524. https://doi.org/10.1190/1.1441434

Baysal, E., Kosloff, D.D., Sherwood, J.W.C., 1983. Reverse time migration. GEOPHYSICS 48. https://doi.org/10.1190/1.1441434

Bley De Brito Neves, B., 2002. Main Stages of the Development of the Sedimentary Basins of South America and their Relationship with the Tectonics of Supercontinents. Gondwana Research 5, 175–196. https://doi.org/10.1016/S1342-937X(05)70901-1

Brocher, T.M., 2008. Key elements of regional seismic velocity models for long period ground motion simulations. J Seismol 12, 217–221. https://doi.org/10.1007/s10950-007-9061-3

Brocher, T.M., 2005. Empirical Relations between Elastic Wavespeeds and Density in the Earth's Crust. Bulletin of the Seismological Society of America 95, 2081–2092. https://doi.org/10.1785/0120050077

Castagna, J.P., Batzle, M.L., Eastwood, R.L., 1985. Relationships between compressional wave and shear wave velocities in clastic silicate rocks. GEOPHYSICS 50, 571–581. https://doi.org/10.1190/1.1441933

Caxito, F. de A., Santos, L.C.M. de L., Ganade, C.E., Bendaoud, A., Fettous, E.-H., Bouyo, M.H., 2020. Toward an integrated model of geological evolution for NE Brazil-NW Africa: The Borborema Province and its connections to the Trans-Saharan (Benino-Nigerian and Tuareg shields) and Central African orogens. Braz. J. Geol. 50, e20190122. https://doi.org/10.1590/2317-4889202020190122

Chaboureau, A.-C., Guillocheau, F., Robin, C., Rohais, S., Moulin, M., Aslanian, D., 2013. Paleogeographic evolution of the central segment of the South Atlantic during Early Cretaceous times: Paleotopographic and geodynamic implications. Tectonophysics 604, 191–223. https://doi.org/10.1016/j.tecto.2012.08.025

Chang, W., McMechan, G.A., 1994. 3-D elastic prestack, reverse time depth migration. GEOPHYSICS 59, 597–609. https://doi.org/10.1190/1.1443620

Chang, W., McMechan, G.A., 1987. Elastic reverse time migration. GEOPHYSICS 52, 1365–1375. https://doi.org/10.1190/1.1442249

Chang, W.-F., McMECHAN, G.A., 1990. 3D ACOUSTIC PRESTACK REVERSE-TIME MIGRATION1. Geophys Prospect 38, 737–755. https://doi.org/10.1111/j.1365-2478.1990.tb01872.x

Cordani, U.G., Pimentel, M.M., Araújo, C.E.G.D., Fuck, R.A., 2013. The significance of the -Transbrasiliano-Kandi tectonic corridor for the amalgamation of West Gondwana. Braz. J. Geol. 43, 583–597. https://doi.org/10.5327/Z2317-48892013000300012

da Silva, C.C., Poveda, E., da Silva Dantas, R.R., Julià, J., 2021. Ambient Noise Tomography with Short-Period Stations: Case Study in the Borborema Province. Pure Appl. Geophys. 178, 1709–1730. https://doi.org/10.1007/s00024-021-02718-x

De Oliveira, R.G., De Medeiros, W.E., 2012. Evidences of buried loads in the base of the crust of Borborema Plateau (NE Brazil) from Bouguer admittance estimates. Journal of South American Earth Sciences 37, 60–76. https://doi.org/10.1016/j.jsames.2012.02.004

Dias, R.C., Julià, J., Schimmel, M., 2015. Rayleigh-Wave, Group-Velocity Tomography of the Borborema Province, NE Brazil, from Ambient Seismic Noise. Pure Appl. Geophys. 172, 1429–1449. https://doi.org/10.1007/s00024-014-0982-9

dos Santos, T.J.S., Fetter, A.H., Neto, J.A.N., 2008. Comparisons between the northwestern Borborema Province, NE Brazil, and the southwestern Pharusian Dahomey Belt, SW Central Africa. SP 294, 101–120. https://doi.org/10.1144/SP294.6

Evain, M., Afilhado, A., Rigoti, C., Loureiro, A., Alves, D., Klingelhoefer, F., Schnürle, P., Feld, A., Fuck, R., Soares, J., de Lima, M.V., Corela, C., Matias, L., Benabdellouahed, M., Baltzer, A., Rabineau, M., Viana, A., Moulin, M., Aslanian, D., 2015. Deep structure of the Santos Basin-São Paulo Plateau System, SE Brazil: Santos Basin-São Paulo Plateau Structure. Journal of Geophysical Research: Solid Earth 120, 5401–5431. https://doi.org/10.1002/2014JB011561

Gonçalves, S., Schnürle, P., Rabineau, M., Afilhado, A., Aslanian, D., Moulin, M., Evian, M., Loureiro, A., Dias, N., 2023. Deep crustal structures with reverse time migration applied to offshore wide-angle seismic data: Equatorial and North-West Brazilian margins. Journal of South American Earth Sciences 104398. https://doi.org/10.1016/j.jsames.2023.104398

Górszczyk, A., Operto, S., Schenini, L., Yamada, Y., 2019. Crustal-scale depth imaging via joint full-waveform inversion of ocean-bottom seismometer data and pre-stack depth migration of multichannel seismic data: a case study from the eastern Nankai Trough. Solid Earth 10, 765–784. https://doi.org/10.5194/se-10-765-2019

Guiraud, R., Maurin, J.-C., 1992. Early Cretaceous rifts of Western and Central Africa: an overview. Tectonophysics, Geodynamics of Rifting, Volume II Case History Studies on Rifts: North and South America and Africa 213, 153–168. https://doi.org/10.1016/0040-1951(92)90256-6

Gusmão De Oliveira, R., Eugênio De Medeiros, W., Rodrigues Domingos, N.R., De Araújo Costa Rodrigues, M., 2023. A review of the geophysical knowledge of the Borborema Province, NE-Brazil, and tectonic implications. Journal of South American Earth Sciences 126, 104360. https://doi.org/10.1016/j.jsames.2023.104360

Haas, P., Ebbing, J., Celli, N.L., Rey, P.F., 2021. Two-step Gravity Inversion Reveals Variable Architecture of African Cratons. Front. Earth Sci. 9, 696674. https://doi.org/10.3389/feart.2021.696674

Herring, T., Schubert, Gerald, 2015. Geodesy, in: Treatise on Geophysics. Elsevier, p. 415.

Holbrook, W.S., Mooney, W.D., Christensen, N.I., 1992. The seismic velocity structure of the deep continental crust, in: Developments in Geotectonics. Elsevier.

J. Tavares, E., P. Soares, J.E., A. Fuck, R., A. G. de Lima, M.V., 2012. Modelagem de onda P e razão Vp-Vs da crosta sob a linha de refração sísmica profunda NW-SE da Província Borborema, in: Proceedings of the 5 Simpósio Brasileiro de Geofísica. Presented at the Simpósio Brasileiro de Geofísica, Sociedade Brasileira de Geofísica, pp. 1–4. https://doi.org/10.22564/5simbgf2012.164

Kamei, R., Pratt, R.G., Tsuji, T., 2012. Waveform tomography imaging of a megasplay fault system in the seismogenic Nankai subduction zone. Earth and Planetary Science Letters 317–318, 343–353. https://doi.org/10.1016/j.epsl.2011.10.042

Kennett, B.L.N., Engdahl, E.R., 1991. Traveltimes for global earthquake location and phase identification. Geophysical Journal International 105, 429–465. https://doi.org/10.1111/j.1365-246X.1991.tb06724.x

Kröner, A., Cordani, U., 2003. African, southern Indian and South American cratons were not part of the Rodinia supercontinent: evidence from field relationships and geochronology. Tectonophysics 375, 325–352. https://doi.org/10.1016/S0040-1951(03)00344-5

Kvarven, T., Mjelde, R., Hjelstuen, B.O., Faleide, J.I., Thybo, H., Flueh, E.R., Murai, Y., 2016. Crustal composition of the Møre Margin and compilation of a conjugate Atlantic margin transect. Tectonophysics 666, 144–157. https://doi.org/10.1016/j.tecto.2015.11.002

Laske, G., Masters, G., Ma, Z., Pasyanos, M., 2013. Update on CRUST1.0 - A 1-degree Global Model of Earth's Crust. Geophys. Res. Abstracts 15, 1.

Levin, S.A., 1984. Principle of reverse time migration. GEOPHYSICS 49, 581–583. https://doi.org/10.1190/1.1441693

Li, X., Götze, H., 2001. Ellipsoid, geoid, gravity, geodesy, and geophysics. GEOPHYSICS 66, 1660–1668. https://doi.org/10.1190/1.1487109

Liang, W., Li, J., Xu, X., Zhang, S., Zhao, Y., 2020. A High-Resolution Earth's Gravity Field Model SGG-UGM-2 from GOCE, GRACE, Satellite Altimetry, and EGM2008. Engineering 6, 860–878. https://doi.org/10.1016/j.eng.2020.05.008

Lima, M.V.A.G. de, Berrocal, J., Soares, J.E.P., Fuck, R.A., 2015. Deep seismic refraction experiment in northeast Brazil: New constraints for Borborema province evolution. Journal of South American Earth Sciences 58, 335–349. https://doi.org/10.1016/j.jsames.2014.10.007

Loureiro, A., Afilhado, A., Schnürle, P., Evain, M., Dias, N.A., Klingelhöfer, F., Gallais, F., Pinheiro, J.M., Soares, J.E., Fuck, R., Cupertino, J.A., Viana, A., Corela, C., Moulin, M., Aslanian, D., 2023. Imaging exhumed continental and proto-oceanic crusts in the Camamu triple junction, Brazil. Journal of South American Earth Sciences 126, 104336. https://doi.org/10.1016/j.jsames.2023.104336

Loureiro, A., Schnürle, P., Klingelhöfer, F., Afilhado, A., Pinheiro, J., Evain, M., Gallais, F., Dias, N.A., Rabineau, M., Baltzer, A., Benabdellouahed, M., Soares, J., Fuck, R., Cupertino, J.A., Viana, A., Matias, L., Moulin, M., Aslanian, D., Morvan, L., Mazé, J.P., Pierre, D., Roudaut-Pitel, M., Rio, I., Alves, D., Barros Junior, P., Biari, Y., Corela, C., Crozon, J., Duarte, J.L., Ducatel, C., Falcão, C., Fernagu, P., Vinicius Aparecido Gomes de Lima, M., Le Piver, D., Mokeddem, Z., Pelleau, P., Rigoti, C., Roest, W., Roudaut, M., 2018. Imaging exhumed lower continental crust in the distal Jequitinhonha basin, Brazil. Journal of South American Earth Sciences 84, 351–372. https://doi.org/10.1016/j.jsames.2018.01.009

Ludwig, J. W., Nafe, J. E. & Drake, C. L., 1970. Seismic refraction, in The Sea, vol. 4, 53-84, ed. Maxwell, A. E., Wiley, New York

Luz, Rosana M. N., Julià, J., do Nascimento, A.F., 2015. Crustal structure of the eastern Borborema Province, NE Brazil, from the joint inversion of receiver functions and surface wave dispersion: Implications for plateau uplift: BORBOREMA PROVINCE CRUSTAL

STRUCTURE. J. Geophys. Res. Solid Earth 120, 3848–3869. https://doi.org/10.1002/2015JB011872

Luz, R.M.N., Julià, J., do Nascimento, A.F., 2015. Bulk crustal properties of the Borborema Province, NE Brazil, from P-wave receiver functions: Implications for models of intraplate Cenozoic uplift. Tectonophysics 644–645, 81–91. https://doi.org/10.1016/j.tecto.2014.12.017

Maleki, S., Moradzadeh, A., Riabi, R.G., Gholami, R., Sadeghzadeh, F., 2014. Prediction of shear wave velocity using empirical correlations and artificial intelligence methods. NRIAG Journal of Astronomy and Geophysics 3, 70–81. https://doi.org/10.1016/j.nrjag.2014.05.001

Maystrenko, Y., Scheck-Wenderoth, M., 2009. Density contrasts in the upper mantle and lower crust across the continent-ocean transition: constraints from 3-D gravity modelling at the Norwegian margin. Geophysical Journal International 179, 536–548. https://doi.org/10.1111/j.1365-246X.2009.04273.x

McMechan, G.A., 1983. Migration by extrapolation of time-dependent boundary values. Geophys. Prosp. 31, 413–420.

Moulin, M., Aslanian, D., Olivet, J.-L., Contrucci, I., Matias, L., Géli, L., Klingelhoefer, F., Nouzé, H., Réhault, J.-P., Unternehr, P., 2005. Geological constraints on the evolution of the Angolan margin based on reflection and refraction seismic data (ZaïAngo project). Geophysical Journal International 162, 793–810. https://doi.org/10.1111/j.1365-246X.2005.02668.x

Moulin, M., Aslanian, D., Unternehr, P., 2010a. A new starting point for the South and Equatorial Atlantic Ocean. Earth-Science Reviews 98, 1–37. https://doi.org/10.1016/j.earscirev.2009.08.001

Moulin, M., Aslanian, D., Unternehr, P., 2010b. A new starting point for the South and Equatorial Atlantic Ocean. Earth-Science Reviews 98, 1–37. https://doi.org/10.1016/j.earscirev.2009.08.001

Moulin, M., Klingelhoefer, F., Afilhado, A., Aslanian, D., Schnürle, P., Nouzé, H., Rabineau, M., Beslier, M.-O., Feld, A., 2015. Deep crustal structure across a young passive margin from wide-angle and reflection seismic data (The SARDINIA Experiment) – I. Gulf of Lion’s margin. Bulletin de la Société Géologique de France 186, 309–330. https://doi.org/10.2113/gssgfbull.186.4-5.309

Moulin, M., Schnürle, P., Afilhado, A., Gallais, F., Dias, N., Evain, M., Soares, J., Fuck, R., da Cruz Pessoa Neto, O., Viana, A., Aslanian, D., 2021. Imaging Early Oceanic Crust spreading in the Equatorial Atlantic Ocean: Insights from the MAGIC wide-angle experiment. Journal of South American Earth Sciences 111, 103493. https://doi.org/10.1016/j.jsames.2021.103493

Nakanishi, A., Kodaira, S., Miura, S., Ito, A., Sato, T., Park, J.-O., Kido, Y., Kaneda, Y., 2008. Detailed structural image around splay-fault branching in the Nankai subduction seismogenic zone: Results from a high-density ocean bottom seismic survey. J. Geophys. Res. 113, B03105. https://doi.org/10.1029/2007JB004974

Neves, S.P., Monié, P., Bruguier, O., Rangel da Silva, J.M., 2012. Geochronological, thermochronological and thermobarometric constraints on deformation, magmatism and thermal regimes in eastern Borborema Province (NE Brazil). Journal of South American Earth Sciences 38, 129–146. https://doi.org/10.1016/j.jsames.2012.06.003

Oliveira, R.G., 2008. Arcabouço Geofísico, Isostasia e causas do Magmatismo Cenozóico da Província Borborema e de sua Margem Continental (Nordeste do Brasil) (PhD thesis). Universidade Federal do Rio Grande do Norte, Centro de Ciências Exatas e da Terra.

Osako, L.S., Castro, D.L. de, Fuck, R.A., Castro, N.A. de, Pitombeira, J.P.A., 2011. Contribuição de uma seção gravimétrica transversal ao estudo da estruturação litosférica na porção setentrional da Província Borborema, NE do Brasil. Rev. Bras. Geof. 29, 309–329. https://doi.org/10.1590/S0102-261X2011000200008

Pacheco Neves, S., 2021. Comparative geological evolution of the Borborema Province and São Francisco Craton (eastern Brazil): Decratonization and crustal reworking during West Gondwana assembly and implications for paleogeographic reconstructions. Precambrian Research 355, 106119. https://doi.org/10.1016/j.precamres.2021.106119

Padilha, A.L., Vitorello, Í., Pádua, M.B., Bologna, M.S., 2014. Electromagnetic constraints for subduction zones beneath the northwest Borborema province: Evidence for Neoproterozoic island arc–continent collision in northeast Brazil. Geology 42, 91–94. https://doi.org/10.1130/G34747.1

Pinheiro, J.M., Schnürle, P., Evain, M., Afilhado, A., Gallais, F., Klingelhoefer, F., Loureiro, A., Fuck, R., Soares, J., Cupertino, J.A., Viana, A., Rabineau, M., Baltzer, A., Benabdellouahed, M., Dias, N., Moulin, M., Aslanian, D., Morvan, L., Mazé, J.P., Pierre, D., Roudaut-Pitel, M., Rio, I., Alves, D., Barros Junior, P., Biari, Y., Corela, C., Crozon, J., Duarte, J.L., Ducatel, C., Falcão, C., Fernagu, P., Le Piver, D., Mokeddem, Z., Pelleau, P., Rigoti, C., Roest, W., Roudaut, M., 2018. Lithospheric structuration onshore-offshore of the Sergipe-Alagoas passive margin, NE Brazil, based on wide-angle seismic data. Journal of South American Earth Sciences 88, 649–672. https://doi.org/10.1016/j.jsames.2018.09.015

Pinheiro, J. M., Schnürle, P., Evain, M., Afilhado, A., Gallais, F., Klingelhoefer, F., Loureiro, A., Fuck, R., Soares, J., Cupertino, J.A., Viana, A., Rabineau, M., Baltzer, A., Benabdellouahed, M., Dias, N., Moulin, M., Aslanian, D., Morvan, L., Mazé, J.P., Pierre, D., Roudaut-Pitel, M., Rio, I., Alves, D., Barros Junior, P., Biari, Y., Corela, C., Crozon, J., Duarte, J.L., Ducatel, C., Falcão, C., Fernagu, P., Le Piver, D., Mokeddem, Z., Pelleau, P., Rigoti, C., Roest, W., Roudaut, M., 2018. Lithospheric structuration onshore-offshore of the Sergipe-Alagoas passive margin, NE Brazil, based on wide-angle seismic data. Journal of South American Earth Sciences 88, 649–672. https://doi.org/10.1016/j.jsames.2018.09.015

Rivadeneyra Vera, C., Bianchi, M., Assumpção, M., Cedraz, V., Julià, J., Rodríguez, M., Sánchez, L., Sánchez, G., Lopez Murua, L., Fernandez, G., Fugarazzo, R., The “3 Basins” Project Team, 2019. An Updated Crustal Thickness Map of Central South America Based on Receiver Function Measurements in the Region of the Chaco, Pantanal, and Paraná Basins, Southwestern Brazil. J. Geophys. Res. Solid Earth 124, 8491–8505. https://doi.org/10.1029/2018JB016811

Sandwell, D.T., Müller, R.D., Smith, W.H.F., Garcia, E., Francis, R., 2014. New global marine gravity model from CryoSat-2 and Jason-1 reveals buried tectonic structure. Science 346, 65–67. https://doi.org/10.1126/science.1258213

Schnürle, P., Gallais, F., Afilhado, A., Moulin, M., Dias, N., Soares, J., Loureiro, A., Fuck, R., Cupertino, J.A., Viana, A., Aslanian, D., 2023. Wide-angle seismic imaging of divergent and transform segments of the Pará-Maranhão-Barreirinhas-Ceará margin, NW Brazil. Journal of South American Earth Sciences 127, 104394. https://doi.org/10.1016/j.jsames.2023.104394

Schnürle, P., Liu, C.-S., Lee, C.-S., 2006. Acoustic and Shear-Wave Velocities in Hydrate-Bearing Sediments Offshore Southwestern Taiwan: Tomography, Converted Waves Analysis and Reverse-Time Migration of OBS Records. Terr. Atmos. Ocean. Sci. 17, 757. https://doi.org/10.3319/TAO.2006.17.4.757(GH)

Shiraishi, K., No, T., Fujie, G., 2022. Seismic reflection imaging of deep crustal structures via reverse time migration using offshore wide-angle seismic data on the eastern margin of the Sea of Japan. Earth Planets Space 74, 28. https://doi.org/10.1186/s40623-022-01590-w

Soares, J.E.P., de Lima, M.V., Fuck, R.A., 2010. Características sísmicas da litosfera da Província Borborema: resultados parciais do experimento de refração sísmica profunda 5.

Soares, J.E.P., Fuck, R.A., Oliveira, M.P. de, Lima, M.V. de, 2011. Descontinuidade de Moho e velocidade média da crosta sob a linha de refração sísmica profunda N-S da Província Borborema: uma aproximação por reflexões de alto ângulo, in: 12th International Congress of the Brazilian Geophysical Society & EXPOGEF, Rio de Janeiro, Brazil, 15–18 August 2011. Presented at the 12th International Congress of the Brazilian Geophysical Society & EXPOGEF, Rio de Janeiro, Brazil, 15-18 August 2011, Brazilian Geophysical Society, Rio de Janeiro, Brazil, pp. 399–403. https://doi.org/10.1190/sbgf2011-084

Sun, R., McMechan, G.A., 1988. Nonlinear reverse time inversion of elastic offset vertical seismic profile data. GEOPHYSICS 53, 1295–1302. https://doi.org/10.1190/1.1442407

Uieda, L., Barbosa, V.C.F., 2017. Fast nonlinear gravity inversion in spherical coordinates with application to the South American Moho. Geophys. J. Int. 208, 162–176. https://doi.org/10.1093/gji/ggw390

Van Schmus, W.R., Kozuch, M., de Brito Neves, B.B., 2011. Precambrian history of the Zona Transversal of the Borborema Province, NE Brazil: Insights from Sm–Nd and U–Pb geochronology. Journal of South American Earth Sciences 31, 227–252. https://doi.org/10.1016/j.jsames.2011.02.010

Whitmore, N.D., 1983. Iterative depth migration by backward time propagation, in: SEG Technical Program Expanded Abstracts 1983. Presented at the SEG Technical Program Expanded Abstracts 1983, Society of Exploration Geophysicists, pp. 382–385. https://doi.org/10.1190/1.1893867

Youn, O.K., Zhou, H., 2001. Depth imaging with multiples. GEOPHYSICS 66, 246–255. https://doi.org/10.1190/1.1444901

Zelt, C.A., 1999. Modelling strategies and model assessment for wide-angle seismic traveltime data. Geophysical Journal International 139, 183–204. https://doi.org/10.1046/j.1365-246X.1999.00934.x

Zelt, C.A., Smith, R.B., 1992. Seismic traveltime inversion for 2-D crustal velocity structure. Geophysical Journal International 108, 16–34. https://doi.org/10.1111/j.1365-246X.1992.tb00836.x

Zhou, H.-W., Hu, H., Zou, Z., Wo, Y., Youn, O., 2018. Reverse time migration: A prospect of seismic imaging methodology. Earth-Science Reviews 179, 207–227. https://doi.org/10.1016/j.earscirev.2018.02.008

COLLEGE SCIENCES
DOCTORAL DE LA MER
BRETAGNE ET DU LITTORAL

Université de Bretagne Occidentale

Titre : Caractérisation géophysique des structures crustales des marges équatoriales au nord-est du Brésil

Mots clés : Inversion gravimétrique 3D avec contrainte sismique ; Migration temporelle inverse ; Marges passives ; Sismique à grand angle ; Structures crustales profondes ; discontinuité du Moho

Résumé : Adaptation et application de la méthode d'inversion gravimétrique 3D avec contraintes sismiques à l'étude des structures crustales profondes des marges passives du nord-ouest du Brésil. Avec une approche de décapage des couches, la méthode a la capacité, la robustesse et la cohérence d'étudier la géométrie de la discontinuité du Moho dans le contexte de l'environnement des marges passives. Les résultats obtenus sont suffisamment précis pour distinguer les transitions entre les différents domaines. Ils permettent également d'identifier les différences au sein d'un même domaine lors de l'analyse de deux profils parallèles, par exemple.

Imagerie des structures de la croûte terrestre profonde avec la méthode de migration temporelle inverse appliquée à deux profils de données sismiques à grand angle. La méthode permet d'obtenir des images de ce type de structures. L'analyse des deux résultats est un outil important pour étudier la forme et la géométrie de la zone de rétrécissement, même dans les profils avec des tirs asymétriques. Elle montre également la contribution essentielle du champ d'ondes réfracté à son succès.

Fusion de trois profils sismiques grand angle subparallèles dans la région nord-ouest du Brésil en un profil unique d'une longueur d'environ 1800 km, offrant une perspective unique sur le processus d'évolution de l'ouverture de l'océan Atlantique sud. Le profil fusionné met en évidence les similitudes entre les marges équatoriale et centrale de l'océan Atlantique Sud, malgré des processus géodynamiques et des périodes d'ouverture différents.

Title : Geophysical characterization of Crustal structures from Equatorial to North-East Brazilian margins

Keywords : 3D Gravity inversion with seismic constraint ; Reverse Time Migration ; Passive margins ; Wide-Angle Seismic ; Deep Crustal Structures ; Moho discontinuity

Abstract : Adaptation and application of 3D gravity inversion with seismic constraint method to the study of the deep crustal structures of the Northwest Brazil passive margins. With a layer-stripping approach, the method has the capacity, robustness and coherency to study the geometry of the Moho discontinuity, or any other crustal layer, within the context of the passive margins environment. The obtained results have sufficient accuracy to distinguish transitions between different domains – continental domain, necking zones and oceanic domain. It is also capable to identify differences within the same domain when analyzing two parallel profiles, for example.

Imaging of deep crustal structures with Reverse Time Migration method applied to two Wide-Angle Seismic data profiles, acquired by Ocean Bottom Seismometers and Land Seismic Stations. The method has capacity to image these type of structures in the two domains. The analysis of the two results is an important tool to investigate the shape and geometry of the necking zone even in profiles with asymmetric shooting. It is also shown the essential contribution of the refracted wavefield for its success.

Merge of three sub-parallel Wide-Angle Seismic profiles in the Northwest area of Brazil into a unique profile of approximately 1800 km in length, providing an unique perspective on the evolution process of the opening of the South Atlantic Ocean. The merged profile showcases the similarities between the Equatorial and Central margins of the South Atlantic Ocean in spite of the different geodynamic processes and time of opening.